REPORT DOCUMENTATION PAGE

AFRL-SR-BL-TR-01-

0187

1. AGENCY USE ONLY (Leave blank)	2. REPORT DATE 10/08/98	3. REPORT TYPE AND DATES COVERED Final Technical Report; 06/01/93 - 11/30/97

4. TITLE AND SUBTITLE

Hypersonic Air Flow with Finite Rate Chemistry

5. FUNDING NUMBERS
PE - 61103D
PR - 3484
SA - AS
G - F49620-93-1-0373

6. AUTHOR(S)

Ian D. Boyd, Daniel A. Erwin, Ronald K. Hanson, Michael S. Holden, Joseph A. Kunc, E. Phillip Muntz

7. PERFORMING ORGANIZATION NAME(S) AND ADDRESS(ES)

Department of Aerospace Engineering
University of Southern California
854 W. 36th Pl., RRB 101
Los Angeles, CA 90089-1191

8. PERFORMING ORGANIZATION REPORT NUMBER

9. SPONSORING / MONITORING AGENCY NAME(S) AND ADDRESS(ES)

AFOSR/NA
110 Duncan Ave., Suite B115
Bolling AFB, D.C. 20332-0001

10. SPONSORING / MONITORING AGENCY REPORT NUMBER

11. SUPPLEMENTARY NOTES

AIR FORCE OFFICE OF SCIENTIFIC RESEARCH (AFOSR)
NOTICE OF TRANSMITTAL DTIC. THIS TECHNICAL REPORT
HAS BEEN REVIEWED AND IS APPROVED FOR PUBLIC RELEASE
LAW AFR 190-12. DISTRIBUTION IS UNLIMITED.

12a. DISTRIBUTION / AVAILABILITY STATEMENT
Approved for public release; distribution is unlimited.

12b. DISTRIBUTION CODE

13. ABSTRACT (Maximum 200 Words)

In this report, we present the results of a number of experimental studies and the accompanying analyses to develop and refine prediction techniques and the models that are employed in them to describe the effects of non-equilibrium flow chemistry, shock interaction, and turbulent mixing and combustion on the performance of vehicles and airbreathing engines designed to fly in the hypersonic flow regime at velocities greater than 2 km/sec. During this research program, experimental studies and analyses were conducted to:

1) Define and predict the vibrational and chemical nonequilibrium characteristics of hypervelocity flows developed in a contoured nozzle.
2) Evaluate and compute the effects of real-gas chemistry on the characteristics and properties of base flows, interaction regions resulting from shock wave/boundary layer interaction and shock/shock interaction over simple model configurations, and indented nose shapes.
3) Study the characteristics of high-temperature regions of turbulent mixing and combustion associated with scramjet operations at Mach 12. The report is divided into four sections, each of which covers separate but inter-related experimental and theoretical programs that were conducted during the present contract.

14. SUBJECT TERMS
non-equilibrium hypervelocity, flow measurements, vibrational transition probabilities

15. NUMBER OF PAGES - 234

16. PRICE CODE

17. SECURITY CLASSIFICATION OF REPORT Unclassified	18. SECURITY CLASSIFICATION OF THIS PAGE Unclassified	19. SECURITY CLASSIFICATION OF ABSTRACT Unclassified	20. LIMITATION OF ABSTRACT UL

EXECUTIVE OVERVIEW

In this report the work that has been accomplished on F49620-93-1-0373 is reviewed. The principal outcome is presented in Section I dealing with the shock tunnel tests at CUBRC under the direction of Dr. M. Holdon. Included in this section are comparisons to the many supporting calculations by Prof. I. Boyd (also see Sec. III) at Cornell. In section II instrumentation developed at Stanford and U.S.C. under the direction of Profs. R.K. Hanson, E.P. Muntz, and D. Erwin is summarized. Significant theoretical work on the properties of high temperature, nonequilibrium gases was completed at U.S.C. under the direction of Prof. J.A. Kunc and is reported in Sec. IV. The publications associated with the activities discussed in each Section appear at the end of the individual section as an appendix.

TABLE OF CONTENTS

SECTION I.

EXPERIMENTAL AND THEORETICAL STUDIES OF REAL GAS EFFECTS, SHOCK INTERACTIONS AND TURBULENT MIXING AND COMBUSTION IN HYPERVELOCITY FLOWS.

This section authored by

M.S. Holden, J. Harvey, R.C. Bergman, I.D. Boyd, and R. DeLeon.

TABLE OF CONTENTS

Table of Contents (Contd)

Table of Contents (Contd)

EXECUTIVE SUMMARY

In this section, we present the results of a number of experimental studies along with accompanying analyses. The purpose was to develop and refine prediction techniques and the models that are employed in them to describe the effects of non-equilibrium flow chemistry, shock interaction, and turbulent mixing and combustion on the performance of vehicles and air breathing engines designed to fly in the hypersonic flow regime at velocities greater than 2 km/sec. During this research program, experimental studies and analyses were conducted to (1) define and predict the vibrational and chemical nonequilibrium characteristics of hypervelocity flows developed in a contoured nozzle; (2) evaluate and compute the effects of real-gas chemistry on the characteristics and properties of base flows, interaction regions resulting from shock wave/boundary layer interaction and shock/shock interaction over simple model configurations, and indented nose shapes; and (3) study the characteristics of high-temperature regions of turbulent mixing and combustion associated with scramjet operations at Mach 12. The report is divided into five chapters, each of which covers separate but inter-related experimental and theoretical programs which were conducted during the present contract.

In Chapter 2, we describe a series of experimental and theoretical studies to investigate the flowfield characteristics over the forebody and in the base region of a sting mounted planetary probe configuration. Surface and flowfield measurements were made during three separate tunnel entries with models of identical geometries but with different instrumentation packages: one prepared by NASA and used in similar programs in a number of European and American facilities and a second prepared by Calspan-UB Research Center (CUBRC) employing a different set of instruments to measure heat transfer and pressure distribution. Comparisons have been made between the heat transfer and pressure distributions over the forebody and base region obtained in the various ground-test facilities employed in this program. In a parallel effort, computations employing DSMC and Navier-Stokes codes were made by a series of groups employing different solving techniques. The comparisons made in the non-continuum and continuum flow regimes indicated that although there was generally good agreement between the computations and measurements, there might be significant problems in accurately predicting the flow in the separation and reattachment regions of the base flow. These problems can be partially resolved by employing a hybrid Navier-Stokes/DSMC Code in the expansion region close to the edge of the base.

The experimental and theoretical studies conducted to examine real-gas effects in the nonequilibrium flow over a spherically blunted cone flare configuration conducted in this program are described in Chapter 3. The basic objective of this research was to generate a flowfield in which a stagnation region was followed by regions of expansion and recompression embodying a separated recirculation region thereby obtaining flow phenomena which could give rise to nonequilibrium effects similar to those which gave rise to problems on the space shuttle. The spherically blunted cone model employed in this study could be regarded as an axisymmetric equivalent of the centerline flowfield of the space shuttle at incidence. The selection of the experimental flow conditions and the model configuration were made in conjunction with detailed computations of the nonequilibrium flowfield using the Cornell Navier-Stokes Code. In addition to detailed measurements of heat transfer and pressure distribution, flowfield surveys were made with miniature pitot pressure rakes. However, the principal flowfield instrumentation was an electron beam apparatus coupled with spectrographic analyzer employing an Infrared radiometer/spectrometer apparatus. The results of the measurements made with this instrumentation were compared with detailed computations made with the Navier-Stokes solver. While the heat transfer and pressure measurements were in good agreement with the computations on the spherical nosetip and conical forebody, the measurements in the separated region and along the conical flare were not well predicted, possibly because of the potential presence of transition toward the end of the flare. The flowfield pitot pressure measurements were in generally good agreement with the shock position predicted from the code, as were the deductions of temperatures in the flowfield from the spectrographic data.

In Chapter 4, we present the results of experimental studies designed to examine the influence of real-gas effects on the surface and flowfield characteristics of a number of configurations which were predicted to be sensitive to real-gas effects. These included the base and separated flows discussed earlier with reference to the planetary probe and blunt cone flare studies, as well as flows where regions of shock/shock interaction on a two-dimensional cylinder and indented nose configuration where predictions indicated that flow nonequilibrium significantly influenced the levels of peak heat transfer and pressure generated in these regions. The results of the experimental studies indicated that for the flow conditions studied, real gas effects did not result in large changes in the size and properties of the separated regions in the base and comer flows over the planetary probe and blunted cone flare configuration, respectively. However, a significant increase was observed in the peak heat transfer and pressure in regions of shock/shock interaction over the cylindrical leading edge and on the indented nose shape. The results of the latter two studies supported the earlier predictions differing in this respect from similar measurements made earlier in the HEG and Cal-Tech shock tunnel facilities.

In Chapter 5, we present details of the non-intrusive optical measurements that were made to investigate the characteristics of the flow in the freestream of the Large Energy National Shock (LENS) tunnel (2.2.2), and in the shock layer of the sphere/cone/flare model. The LENS and its associated aero-thermal, aero-optical and radiation instrumentation suites were developed to evaluate the key aspects of kill vehicle performance with full-scale flight hardware under duplicated flight conditions. Modifications to the LENS facility to provide the capability to perform jet interaction studies with full-scale vehicles employing real propellants have been made and were employed in studies of the AIT kill vehicle and more generic configurations over a Mach number range between 4 and 14. Aerothermal and aero-optical performance measurements have been made on seekerhead configurations at velocities from 4,000 ft/sec to 15,000 ft/sec. Two methods of interrogation of the flow were employed - direct flow radiance and electron beam excited fluorescence measurements. The aim of the tests was to obtain data on the species concentration and on rotational and vibrational temperatures. The latter proved to be more successful. Comparisons with Navier-Stokes computations show good agreement with both temperature components just outside the boundary, but measurements made in the center of the shock layer indicate a sizable overprediction in both cases. The species concentration measurements were not successful and quantitative comparisons with the numerical results could not be made. Supplementary tests to detect the arrival of the hydrogen or helium driver gas were also inconclusive. Detection of the former was based on sensing OH, which it was assumed would be indicative of hydrogen/air combustion. No sharp rise in OH concentration was found; instead the only evidence of this compound being present suggested that it was the product of the decomposition of trace hydrocarbon contaminants. Detection of the arrival of He proved also not to be possible because of continuum blackbody radiation in the visible wavelengths, thought to originate from the reservoir/throat region of the tunnel or from minute traces of particulate.

Finally, in Chapter 6, we review the results of studies of mixing and combustion made to examine the key problems associated with air-breathing hypervelocity vehicles designed to operate up to Mach numbers of 12. Measurements of the distributions of heat transfer and pressure over a flat plate/expansion configuration are presented for a series of mixing and combusting flows generated by the burning of a vectored hydrogen jet with the 12,000 ft/sec high-pressure air flow. These studies demonstrated that it is possible to efficiently mix and combust hydrogen in high velocity flows to generate pressure rises large enough to make scramjet propulsion at such velocities a viable approach. Measurements made in these studies also demonstrated that the LENS test facility is capable of generating 5 to 6 msec of high quality air flow at velocities of 12,000 ft/sec and from 3 to 4 msec at velocities approaching 15,000 ft/sec.

During this program, close to 100 runs were made in the LENS Facility at high pressure hypervelocity flow conditions. Thirty-four runs were made during the studies with the planetary probe configuration, 37 runs were made during the studies of the flow over spherically blunted cone/flare configuration, 17 runs were made in the shock interaction studies, 14 runs were made in the flowfield measurements studies, and 21 runs were made during the studies of turbulent mixing and combustion studies at velocities of 3.6 km/sec.

1 INTRODUCTION

With the development of powerful high-speed computers and robust efficient numerical techniques to solve the Navier-Stokes equations, the prediction of simple flows over configurations such as the Space Shuttle and the Hope Spacecraft have become a practical reality. However, even in the analysis of such simple configurations, we are faced with modeling the effect of chemical nonequilibrium, boundary-layer transition, surface roughness and laminar, transitional and turbulent leeside wakes and regions of shockwave/boundary layer interaction over the control surfaces and in the interactions generated by attitude control thrusters. Such problems are significantly multiplied when the design of an air-breathing vehicle designed to fly into orbit is considered. Here, the effects of nonequilibrium must be combined with those associated with mixing and combustion, as well as techniques to cool regions associated with hot spots in the flow, such as those generated in the shock/shock interaction regions on the inlets and the three-dimensional interactions which are generated on and downstream of the fuel injector systems.

Although the major modeling problems are associated with the construction of models of turbulence and chemical kinetics for boundary layers and free shear layers subjected to strong pressure gradients and influenced by chemical nonequilibrium and combustion, there are a number of key problem areas in which modeling must be addressed if we are to predict the overall vehicle performance over the complete flow regime. In the high-Mach-number, high-temperature, low-density regime, there are important modeling problems associated with the catalytic surface/reacting gas interaction. Whereas research in low-density flows has continued at a steady pace in low-enthalpy flows, there has been almost no experimental research during the past two decades in hypervelocity (V > 10,000 fps or 3.05 km/s) flows. One of the areas of interest for small re-entry vehicles such as the Japanese Hope is the transitional flow regime between free-molecular and continuum flow. Here, flow computation using combined Navier-Stokes and DSMC codes must incorporate models of real-gas chemistry and gas/surface interaction which must be validated by experiment. The short-duration facility, in one of its various modes of operation, has been used successfully to generate the high-purity hypervelocity flows necessary to study such phenomena. Flowfield and surface diagnostics have been developed to obtain measurements in short-duration flows (1 ms), that are typical for these facilities when operated at high-temperature conditions. Thus, there are tools available for experimental study to contribute significantly to an increased understanding in this flow regime.

One of the most important areas for research in hypersonic laminar boundary-layer flows is associated with the understanding of chemical nonequilibrium and combustion effects on the size and characteristics of separated flows developed in regions of shockwave/boundary-layer interaction. Whereas solutions to the full Navier-Stokes equations have been shown to successfully describe separated regions in non-reacting hypersonic flows, nonequilibrium air chemistry or combustion in the recirculation regions provides problems that can be resolved only with combined experimental and numerical studies. In such separated flows, free shear layer transition can occur at Reynolds numbers between 10^3 and 10^4 or close to the boundaries of continuum and non-continuum flow. The

influence of nonequilibrium chemistry on hypersonic ramjet performance in laminar flows is an area for which experimental research is essential to provide the answers to critical questions. Likewise, one can have little confidence in numerical solutions to laminar combusting hypersonic flows without experimental verification. In the experimental study of such separated flows, flow duration becomes an important parameter, and test times of one or more milliseconds may be required for establishment of complex interaction flows. For this application, larger reflected shock tunnels are currently in existence that would be acceptable facilities to use, which are capable of generating test times of up to 5 ms.

Predicting boundary-layer transition to turbulent flow and the characteristics of transitional flows presents one of the formidable problems in hypersonic flows. Whereas such flows are difficult to predict at any Mach number, at hypersonic speeds, they are so extensive and have such large effects on aerothermal loads that they must be adequately described. Since the basic mechanisms of transition are not understood, only a careful combination of measurements in ground and flight tests will provide the insight required to validate the modeling of these flows. Semi-empirical transition prediction techniques such as the $(Re)^N$ method and more sophisticated techniques such as those developed by Herbert required validation on both the fundamental and correlational level. Measurements are required to define the basic instability modes associated with transition in hypersonic flow, and the mechanism involved with the gross breakdown of the laminar flow and the transition to fully developed turbulent flow, including the effects of flowfield nonequilibrium and chemistry. Extensive regions of low Reynolds-number turbulent flows in and downstream of the transition can dominate the aerothermal characteristics of hypersonic vehicles and the performance of air-breathing engines in the transitional flow regime.

The structure of turbulent boundary layers in regions of shockwave/turbulent boundary-layer interaction, and shear-layer mixing regions in hypersonic flows are strongly influenced by compressibility effects. How compressibility influences shock/turbulence interaction, flow unsteadiness and eddy shocklets, and flow structure remains to be determined. However, it is clear that accurately predicting the size and structure of turbulent flows in strong pressure gradients will require detailed insight from experimental research. The shear-layer development in mixing regions between dissimilar gases, in regions of jet injection, and also film or transpiration cooling at hypersonic speeds require extensive experimental research. Clearly, adding nonequilibrium flow chemistry and combustion to the problem, as they occur in a scramjet engine, presents a situation well beyond the current state of the art in understanding and computation.

Because of the intrinsic integrated structure of the airframe and engine for a hypersonic air-breathing vehicle, all of the problems mentioned previously are important in the design of the engine of an air-breathing vehicle. The nonequilibrium flow developed in the leading-edge flowfield will influence the flow development on the compression ramps and possibly into the inlet. Earlier experimental studies have shown that strong distortions to the inlet flows result from viscous/inviscid interaction and crossflow over compression ramps. Flow distortions can

arise from the compression ramp and cowl shocks separating the sidewall and cowl boundary layer. The sidewall boundary layer will be intrinsically transitional in nature, and predicting the flows in the presence of interacting shock waves and flow separation will be extremely difficult. Regions of shock/shock interaction on the cowl lip and leading-edge of the sidewalls will induce large leading edge heating rates as well as significant flow disturbances inside the engine. The blunt leading edges of the sidewalls and cowl will induce flow chemistry that may exert significant effects on combustion chemistry as well as the regions of shockwave/boundary layer interaction inside the engine. Two- and three-dimensional separated flows may be induced on the floor, the sidewalls, and the cowl of the engine. The characteristics of these flows must be carefully simulated in experiment and/or predicted in numerical computations. It is in these flows that there are currently no successful turbulence models. Unquestionably, various forms of film and transpiration cooling must be employed to maintain the engine integrity. Fuel injection from the engine walls and possibly struts will generate complex interacting flowfields, which again must be carefully simulated numerically and experimentally. Here, combustion and nonequilibrium turbulence and flow chemistry are all important. Without experimental verification, current models of turbulent mixing in these flows are seriously in question. Again, flow chemistry and viscous/inviscid flow interaction control the flow in, and hence the performance of, the nozzle. In these flows, relaminarization may also play an important, but poorly understood, role, which must be explored in experimental simulations.

2 EXPERIMENTAL AND COMPUTATIONAL STUDIES OF THE FLOW OVER A STING MOUNTED PLANETARY PROBE CONFIGURATION

SUMMARY

This portion of the report summarizes the results of a series of experimental studies in the LENS shock tunnel, and computations with DSMC and Navier Stokes codes. The study was done to examine the aerothermal and flowfield characteristics of the flow over a sting-supported planetary probe configuration in hypervelocity air and nitrogen flows. The experimental program was conducted in the LENS hypervelocity shock tunnel at total enthalpies of 5 and 10 MJ/kg for a range of reservoir pressure conditions from 70 to 500 bars. Heat transfer and pressure measurements were made on the front and rear face of the probe and along the supporting sting. High-speed and single shot schlieren photography were also employed to examine the flow over the model and the time to establish the flow in the base recirculation region. Predictions of the flowfield characteristics and the distributions of heat transfer and pressure were made with DSMC codes for rarefied flow conditions and with the Navier-Stokes solvers for the higher pressure conditions where the flows were assumed to be laminar. Analysis of the time history records from the heat transfer and pressure instrumentation on the face of the probe and in the base region indicated that the base flow was fully established in under 4 milliseconds from flow initiation or between 35 and 50 flow lengths based on base height. The measurements made in three different tunnel entries with two models of identical geometries but with different instrumentation packages, one prepared by NASA Langley and the second prepared by CUBRC, demonstrated good agreement between heat transfer measurements made with two different types of thin-film and coaxial-gage instrumentation.

The measurements of heat transfer and pressure to the front face of the probe were in good agreement with theoretical predictions from both the DSMC and Navier Stokes codes. For the measurements made in low density flows, computations with the DSMC code were found to compare well with the pressure and heat transfer measurements on the sting, although the computed heat transfer rates in the recirculation region did not exhibit the same characteristics as the measurements. For the 10 MJ/kg and 500 bar reservoir "match point" condition, the measurements and heat transfer along the sting from the first group of studies were in agreement with the Navier-Stokes solutions for laminar conditions. A similar set of measurements made in later tests where the model was moved to a slightly different position in the test section indicated that the boundary layer in the reattachment compression region was close to transition or transitional where small changes In the test environment can result in larger than laminar heating rates. The maximum heating coefficients on the sting observed in the present studies were a small fraction of similar measurements obtained at nominally the same conditions in the HEG shock tunnel (where it was possible for transition to occur in the base flow), and In the low enthalpy studies conducted in the NASA Langley high Reynolds number Mach 10 tunnel where the base flow was shown to be turbulent. Hybrid Navier-Stokes/DMSC calculations by Gochberg et al. (Reference 1) suggested that employing the Navier-Stokes calculations for the entire flowfield could be seriously in error in the base region for the 10 MJ/kg, 500 bar test case. Similar calculations performed by Cornell and presented here, do not indicate a serious error.

2.1 INTRODUCTION

Three years ago, as a result of discussions initiated in AGARD Working Group 18, an experimental program was conceived and designed to obtain measurements in a number of the major international high-enthalpy test facilities. The idea was to examine the flow over a standardized test article at matched test points to compare and validate the

performance of these facilities. The configuration selected as a standardized test article was a sting-mounted, blunted 70-degree cone with a flat base, which is shown in Figures 2-1 and 2-2. Measurements were to be obtained not only on the forebody but also on the base of the cone and along the sting. Thus, the rapid expansion region around the body perimeter, the wake and its associated shear layer reattachment process were all incorporated into the study. Each is recognized as being a severe challenge to current numerical prediction methods especially under conditions where real gas effects and possibly transition are present. Possibly it is for this reason this test case appears to have caught the imagination of many workers in the field. In a separate, but allied initiative, again associated with AGARD Working Group 18, experimental data was sought in low-density facilities to validate the calculations being made by various groups employing their DSMC codes. These two requirements were rolled into a test program which was conducted over a range of pressure conditions to obtain both low-density and continuum flows at total enthalpies of 5 MJ/kg and 10 MJ/kg. Originally, three high-enthalpy facilities, the HEG, the LENS and the NASA Ames shock tunnel were involved in this program. However, subsequently, the test program in the Ames facility was replaced by studies in the low-enthalpy Mach 10 facility at NASA Langley, and measurements at the F4 facility in France. Thus, the sting-mounted planetary probe configuration has become a *de facto* standard for both the comparison and calibration of high-enthalpy facilities, and the evaluation of DSMC and Navier-Stokes codes designed to compute high-enthalpy flows with real gas effects.

In this chapter of the report, we present the measurements from three sets of studies conducted in the LENS facility with two models of the planetary probe configuration of identical geometry; the first instrumented by CUBRC and the second with instrumentation provided by NASA Langley. The planetary probe instrumented by Langley has now been tested in HEG, LENS, F4 and the Langley Mach 10 tunnel. In concert with the experimental program, detailed predictions were made by a number of researchers employing the DSMC and Navier-Stokes codes. In this paper, we present comparisons between these computations and the measurements made in the LENS facility. We first discuss the objectives and design of the experimental program. The LENS facility in which our experimental studies were conducted is described and its performance and calibration are briefly discussed. Details of the two planetary probe models used in the LENS studies are presented together with the instrumentation employed to measure the pressure, heat transfer, and flowfield characteristics. We then present and discuss the measurements made in the LENS facility. The time history measurements in the baseflow region are examined to provide information on the time establishment of the baseflow. These measurements are compared with time accurate solutions to the DSMC codes for low density flows. We then present and correlate the measurements from the three entries in the LENS facility and compare measurements for nitrogen and airflows to provide an indication of real-gas effects. We then present a series of comparisons between the experimental measurements and computations in the low density and continuum regimes with the DSMC and Navier-Stokes prediction methods. We also discuss the results of predictions employing hybrid Navier-Stokes/DSMC codes. Finally, we summarize the results from both the experimental and theoretical studies.

2.2 EXPERIMENTAL PROGRAM

2.2.1 Program Objectives and Design

The studies conducted with the planetary probe model formed an important part of our program to calibrate and validate the performance of the LENS facility in high enthalpy flows. There were two main objectives of these studies. The first was to obtain surface and flowfield measurements at two sets of high-enthalpy flow conditions, 5 MJ/kg and 10 MJ/kg at stagnation pressure levels of 500 bars for the specific purpose of comparing heat transfer and pressure distributions over the forebody and in the base region of identical models tested in the HEG, LENS, and F4 high-enthalpy tunnels under nominally identical flow conditions, as well as those conducted in the Langley low-enthalpy Mach 10 tunnel. The second objective was to obtain measurements in high-temperature flows in both low density and continuum flow regimes, where vibrational relaxation and dissociation might influence the size and structure of separated base flow, for comparison with "state-of-the-art" DSMC and Navier-Stokes code solutions. The pressure levels selected for the facility comparison studies were set by the operational pressure limits of the AMES shock tunnel, while the 10 MJ/kg total enthalpy conditions was selected as a match point for all facilities and which corresponds to tailored-interface conditions in the LENS facility with a heated hydrogen driver.

2.2.2 Experimental Facilities

The LENS shock tunnel (Reference 2) is a chambered shock tunnel having a 24-foot-long driver tube with an internal diameter of 12 inches and a driven tube 8 inches in diameter, which is 60 feet long. The basic layout of the LENS facility is shown in Figure 2-3. The driver section of the tunnel is heated to 750°F and, because of hydrogen operation, is fitted with a stainless steel liner to prevent hydrogen embrittlement. The driver section of the tunnel can be operated at pressures up to 30,000 psi, and, because of its large volume, a unique high-pressure, high-flow-rate compressor was installed to provide a pumping capacity that will fill the driver in approximately one hour. The driver and heater section of the tunnel are mounted on carriages that recoil with the tunnel as it is fired. A double-diaphragm rig is used to initiate the flow. Here, two diaphragms are separated by an intermediate chamber, which is held at approximately half the driver pressure; the pressure in the intermediate chamber is rapidly increased to fire the tunnel. Diaphragms 18 inches in diameter and up to 1.25 inches thick are employed to obtain controlled bursts with the minimum amount of fragmentation. Because flowfield chemistry and cleanliness are of prime importance in this facility, driver and driven tube components that come into contact with the test gas are constructed from stainless steel. A centerbody apparatus, which employs a fast-acting plug valve to close the nozzle throat, is used to terminate the flow once the uncontaminated volume of shock-heated air has been exhausted from the reservoir region of the shock tube. The reservoir and centerbody region of the shock tunnel are lined with copper in order to prevent burning. Copper, molybdenum, tungsten or rhenium can be used for the throat section of the tunnel to prevent melting and burning. Because the high heating rates generated in the nozzle are concentrated in a relatively small region close to the throat, the major portion of the contoured nozzle can be constructed from

fiberglass. To handle the large loads generated by the recoil of the tunnel, a metal corset, which surrounds the fiberglass nozzle, is used to couple the driven tube with the test section. The test section has an internal diameter of 96 inches and has been constructed so that it can be coupled to nozzles with exit planes up to 72 inches in diameter.

2.2.3 Planetary Probe Model and Instrumentation

The two models of the planetary probe configuration employed in this test program were identical in size and geometry. A schematic diagram of the planetary probe configuration is shown in Figure 2-2. A schematic diagram of the installation of the planetary probe model for the first and second entries into the LENS facility is shown in Figure 2-4. A photograph showing the positions of the instrumentation on the sting of the model is shown in Figure 2-5. The model used in the first three entries into the LENS facility was constructed by NASA Langley and the instrumentation was constructed, calibrated and installed by CUBRC. The second model used in the fourth entry was constructed and instrumented by NASA Langley (see Horvath-Reference 3) and employed coaxial thermocouple instrumentation on the front face and thin-film platinum gages deposited on a Macor substrate on the aft face and sting. The CUBRC instrumented model was equipped with thin-film heat transfer gages together with Medtherm coaxial thermocouples on the front face of the model and platinum thin-film instrumentation on the aft face and along the sting support system. To enable us to accurately examine the time establishment of the base flow region, a significant fraction of the instrumentation was concentrated along the sting so that the length and structure of the reattachment compression region could be accurately resolved. Because of the cleanliness of the flow in the LENS facility under the high enthalpy conditions employed in these studies, we were able to employ magnesium fluoride-coated thin film heat transfer gages on the front face of the model without experiencing significant gage erosion. The addition of the Medtherm coaxial gages enabled us to examine and evaluate potential catalytic wall effects. The very low heating rates that we obtained on the sting in the low density studies (less than 0.1 BTU/ft^2/sec), required the use of special low-noise circuitry coupled with high-quality amplifiers.

The thin film instrumentation employed in these studies is capable of measuring heat transfer rates from 0.1 to 1,000 Btu/ft^2/sec with a precision of between three and five percent. Each gage was calibrated to determine its temperature coefficient and resistance prior to the studies. The properties of the Pyrex were determined from pulse heating studies for a range of temperatures, and this variation is shown in Figure 2-6. The Stanton number, Ch, based on the freestream conditions, was calculated from the following expression,

$$C_h = \frac{\dot{q}}{\rho_\infty U_\infty (H_o - H_w)} \tag{1}$$

where Ho and Hw are the total enthalpy of the free stream and the air at the wall.

The pressure transducers used in this program were piezoelectric types of a design developed by Calspan and manufactured by PCB Piezotronics, Inc. (Models 103A and 103M14). These sensors have high sensitivity, and linearity generally better than 2 percent, over an operating range of about four orders of magnitude. If the linearity was not within 2 percent, a log-log curve fit was made to the calibration data, and this resulted in all data being within 2 percent of the curve. The Model 103A transducers have a maximum pressure capability of 3 psi. The Model 103M14 transducers have a maximum capability of 100 psi. The transducers are internally compensated for acceleration to a nominal level of 0.001 psi/g.

The values of the pressure coefficients, Cp, were calculated from

$$Cp = \frac{p}{1/2\,\rho_\infty U_\infty^2} \tag{2}$$

The uncertainties in the pressure measurements associated with the calibration and recording apparatus were ±3 percent.

2.2.4 Flow Visualization

In addition to time-resolved surface measurements, high-speed movies were made with a Fastex camera running at approximately 8,000 frames/sec to examine time establishment and flow steadiness.

2.2.5 Data Recording and Reduction

All data were recorded on the 128-channel Calspan Digital Data Acquisition System (DDAS II). The DDAS n system consists of 128 Marel Co. Model 117-22 amplifiers, an Analogic ANDS 5400 data acquisition and distribution system, and a Sun SparcStation 2 computer. The Analogic system functions as a transient-event recorder in that it acquires, digitizes, and stores the data in real time. Immediately after each test run, the data was transferred to the Sun computer for processing. The Marel amplifiers provide gains up to 1,000 for low-level signals, can be AC or DC coupled to the transducers, and have selectable low-pass filters with cutoff frequencies of 300, 1,000, or 3,000 Hz. The Analogic system contains a sample-and-hold amplifier, a 12-bit analog-to-digital converter, and a 4,096-sample memory for each channel.

2.3 RESULTS AND DISCUSSION

2.3.1 Introduction

The test program for the planetary probe configuration was conducted with four entries into the LENS facility. Early in the first entry, it was found that the sting instrumentation, which was positioned based on pretest Navier-Stokes predictions, did not extend far enough downstream to encompass the entire length of the reattachment process. The model was immediately reinstrumented, and measurements were obtained for a range of pressure levels at total enthalpies of 5 MJ/kg and 10 MJ/kg. The third entry was made with the same model, but

10

with instrumentation added to the front face and along the sting to more accurately define the distribution of properties on the front face and base region of the model. For this entry, the model support system was further modified to minimize the potential upstream influence of the support system. In this and the subsequent study, the model was supported in a slightly different position in the test section. In the fourth and final entry, we employed the planetary probe model constructed and instrumented by NASA Langley. This was the identical model used in earlier studies in the HEG (Reference 4) and NASA Langley (Reference 3) Mach 10 wind tunnel, and subsequently, in the F4 facility in France. The objective of this latter study was to repeat the measurements made at the conditions employed in the earlier studies with a completely different set of instrumentation to ensure that there were no issues associated with the measurement technique.

2.3.2 Test Conditions

The experimental studies in the LENS facility were conducted at six test conditions. Measurements were made for a total enthalpy level of 5 MJ/kg for reservoir pressures of 73, 290, and 500 bars with both air and nitrogen as the test gas.

In the first of the test cases (test condition B), the reservoir conditions were selected to achieve low density flows so that direct comparisons could be made between measurements of heat transfer on the forebody and in the base region of the planetary probe with computations using the DSMC code. The freestream conditions for test case B are listed in Table 2-1. The conditions for test cases C and D were selected to achieve conditions where it was believed that computations employing either the Navier-Stokes codes or the DSMC computations could provide valid predictions for the flow. Here, air and nitrogen were used as the test gas for test cases C and D, respectively, to examine potential real-gas effects. The freestream conditions calculated for these two test cases are listed in Tables 2-2 and 2-3. The density levels for test cases A, E and F were such that fully continuum flow was developed in the forebody and base regions, and only Navier-Stokes or Navier-Stokes/DSMC hybrid methods could be practically employed to predict these flows. In fact, as discussed later, the Reynolds numbers developed under these conditions were large enough that transition from laminar to turbulent flow may have occurred in the reattachment compression region of these flows. Test conditions for test cases A, E, and F are listed in Tables 2-4, 2-5, and 2-6. The exact test conditions for each run, together with tabulations of the measurements, are presented in the CUBDAT database described in Reference 5, which is available from the First author on a CD-ROM.

2.3.3 Presentation and Discussion of the Experimental Measurements

During this test series, measurements were made over a range of Reynolds numbers for total enthalpies of 5 MJ/kg and 10 MJ/kg. At the key test conditions, we ran repeat runs for each entry into the facility, employing the Calspan-instrumented model during the first three entries and the NASA-instrumented model during the fourth entry. The measurements obtained at condition A on the forebody and base region are shown for Run 9 in Figures

11

2-7a and 2-7b and for Run 32 in Figure 2-8. Comparisons of these two sets of data are shown in Figure 2-9. Pressure and heat transfer measurements on the forebody and sting of the CUBRC-instrumented planetary probe model for the Case B test conditions are shown in Figures 2-10 and 2-11. There were no measurements made at this condition with the NASA-instrumented model. The two sets of measurements obtained for the test condition C with the CUBRC-instrumented model are shown in Figures 2-12a, b and 2-13a, b. The pressure and heat transfer measurements obtained at a similar reservoir condition, but with nitrogen as the test gas (condition D), are shown in Figures 2-14 and 2-15. Comparisons between the measurements with air and nitrogen as the test gas are shown in Figures 2-16 and 2-17 and indicate that at these low enthalpy conditions, real-gas effects (vibrational nonequilibrium, oxygen dissociation and the NO "shuffle" reactions) do not play an important role. The measurements of pressure and heat transfer obtained at the "match point" E condition with the CUBRC-instrumented model, runs 22 and 29 are presented in Figures 2-18 a, b and 2-19 a, b, and those with the NASA Langley-instrumented model are shown in Figures 2-20 and 2-21. A comparison between the two sets of measurements are presented in Figures 2-22 a, b. Next in Figures 2-23 a, b, we present the measurements obtained on the CUBRC- and NASA-Langley instrumented models in runs 26 and 34 respectively at the "match point" with nitrogen as the test gas. Comparisons between the measurements obtained on the models with two different instrumentation sets are shown in Figures 2-24 a, b and 2-25 a, b. The comparisons between the air and nitrogen data at condition E and F indicate that the baseflows are not strongly influenced by real-gas effects. A comparison between the measurements made in the LENS facility and those in the HEG shock tunnel, (Reference 4) in Figure 2-26, suggest that transition in the baseflow region may significantly influence the size of the recirculation region and the peak heating that occurs along the sting. Questions associated with transition could be explored if further studies were conducted at lower Reynolds numbers in the HEG facility.

2.3.4 Flow Visualization From High Speed Schlieren Photography

A sequence of photographs obtained with high-speed photography at 8,000 frames/sec and showed that a bow shock was established over the model in less than I millisecond and remained perfectly steady for a run time of approximately 6 milliseconds. Because of the low density of the flow in the base region, we were unable to resolve the reattachment compression process with high-speed Film.

2.3.5 Test Time and Flow Establishment

The flow establishment in regions of attached and separated flows has always been a subject of interest to the experimentalist performing studies in facilities with short flow durations. The clean and rapid start of a well-tailored shock tunnel provides an excellent facility to obtain information on the mechanism of flow establishment for separated flows which take longer than the approximately I millisecond that it takes to establish the flow through the tunnel nozzle. Past studies have correlated measurements of flow establishment in terms of number of flow lengths based on a characteristic length. Typical attached laminar and turbulent boundary layers take between

12

1.5 and 3 flow lengths (based on the characteristic length and freestream velocity) to establish. The establishment time for regions of laminar separated flows induced by compression corners and incident shocks can be as large as 10 to 20 flow lengths. However, some of the longest flow establishment times which have been observed are those associated with laminar base flow regions, and here flow lengths based on body diameter of between 25 and 50 have been recorded.

In the present study, the records from the forebody and base region instrumentation provided us with the opportunity to examine the time and mechanism for flow establishment of the baseflow region. A typical set of time history records from pressure and heat transfer instrumentation on the forebody and in the base region for the 5 MJ/kg and 500 bar reservoir conditions is shown in Figure 2-27. The pressure and heat transfer records on the face of the planetary probe indicate that the flow is established within the time to establish the steady flow in the tunnel, and there is a steady test time of up to 8 milliseconds. The end of the test time coincides with the arrival of the expansion fan causing a distinctive decrease in the pressure and heat transfer. The pressure records on the aft face of the cylinder indicate a slow rise to a plateau region taking approximately 3 milliseconds. The heat transfer to the aft face of the probe rises rapidly during the flow starting process and decreases to a slightly lower level as the baseflow region becomes established in approximately four milliseconds after flow initiation through the tunnel. The pressure records along the sting indicate that the flow well downstream of the reattachment compression region establishes quickly, but there is a slight increase in the pressure on the sting as the baseflow region increases slightly in size to reach a stable condition. This behavior is more graphically illustrated by observing the pressures ahead and downstream of the reattachment point. Upstream of reattachment, the pressure along the sting in the separated region rises as the shear layer moves slightly downstream during flow establishment. For pressure gages located initially downstream of the reattachment point, we observe an initial peak followed by a rapid decay in pressure to a steady level, which again occurs approximately four milliseconds after flow initiation or close to 13 milliseconds after the initiation of data recording. The heat transfer measurements along the sting show similar trends to those obtained with the pressure instrumentation. Well downstream of reattachment, there is an increase in heat transfer to reach a steady level, whereas in the baseflow region, the heat transfer decreases to a steady level as the flow in the base region becomes fully established. The formation of a steady flow in the base region can also be examined by plotting the distribution of pressure along the sting as a function of time, as shown in Figure 2-28. The pressure distributions for time intervals from 11.5 milliseconds to 17 milliseconds after the initiation of data recording illustrate that the separated region grows in size to reach a stable condition within four milliseconds from data rise. The growth of the separated region reduces the maximum pressure and heat transfer which are recorded in the reattachment region.

A similar set of measurements along the sting obtained for the 10 MJ/kg, 500 bar reservoir condition is shown in Figures 2-29 and 2-30. Again, it can be observed that the separated region grows during flow establishment, with a significant reduction in the heating levels in the reattachment compression region. Calculations

to examine the time-establishment of a baseflow region for the 5 MJ/kg flow condition were made by Gallis and Harvey using the Imperial College Maximum Entropy DSMC code (Reference 6). The development of the distribution of heating along the sting as a function of time is presented in Figure 2-31. It can be seen that steady values of the heat transfer along the sting are not reached until over 2 milliseconds after flow initiation. The predictions of the density contours in the baseflow region shown in Figures 2-32 a, b and 2-33 a, b also illustrate that it takes a significant time to establish the flow. From these figures, we can determine by an examination of the $p/p_\infty = 0.3$ contour, which reflects changes in the size of a recirculation immediately behind the body, that the base flow region has taken approximately 3 milliseconds to reach a steady state. The reattachment shock can be identified by the cluster of 0.4 to 0.6 contours emanating from the sting. The shock is diffuse because of the low densities in the wake; however, it plays a dominant role in the formation of the boundary layer on the sting, and hence on the heat transfer at and downstream of the reattachment point. The wake is a low density region, and the flow entering it from the forebody will not be in equilibrium due to the rapid expansion around the rim. The flow establishment time is thus determined principally by: (a) the convection of the flow in the recirculation region; and (b) the relatively slow real gas relaxation processes. Both the experimental and theoretical studies indicate that it takes 50 flow lengths to establish a steady separated flow in the baseflow region of the planetary probe.

2.4 COMPARISONS BETWEEN MEASUREMENTS AND COMPUTATIONS WITH THE DSMC AND NAVIER-STOKES CODES

2.4.1 Introduction

During the course of this work, a number of calculations have been performed by researchers in the U.S. and Europe to compare with the measurements made on the planetary probe in the LENS facility. For the measurements in low-density flows where the DSMC computational technique can yield accurate results, calculations were made by Moss, (Reference 7) Harvey and Gallis (Reference 8) and Dietrich and Boyd (Reference 9). For the 5 MJ/kg and 10 MJ/kg test cases at the 500 bar reservoir condition, calculations have been made at Cornell with a Navier-Stokes code and a hybrid Navier-Stokes/DSMC method, by Hash et al., (Reference 10), Muyiaert (Reference 11), and Chadwick (Reference 8) using different Navier-Stokes solvers. The initial series of studies was designed to provide information for fully laminar conditions over the sting-mounted planetary probe configuration for direct comparison with solutions from DSMC and Navier-Stokes codes and was selected so that there could be some overlapping over the range of applicability of these two prediction techniques. Measurements were then made at higher Reynolds numbers where transition is believed to occur in or downstream of the baseflow region. It is in these latter studies that the test case E, which is the 10 MJ/kg and 500 bar reservoir condition, falls.

2.4.2 Comparison Between Measurements with DSMC Predictions

For the lowest Reynolds number case, the flow in the forebody and base region is non-continuum, and the DSMC solution technique can be readily employed to predict the flows over the planetary probe. The first compari-

sons made with the pressure and heat transfer measurements for the test case B condition were obtained by Moss (Reference 7), Gallis and Harvey (Reference 8), and Dietrich and Boyd (Reference 9) and are compared with the data in Figures 2-34 a, b and 2-35 a, b. It can be seen from these figures that both sets of computation are in relatively good agreement and predict the features of pressure and heat transfer distribution in the baseflow region. However, while the theories are in good agreement with the measurements on the forebody, they slightly overpredict the pressure and heat transfer in the recompression region over the sting. Increasing the Reynolds number to obtain conditions close to the continuum regime over the forebody and the base region enables a comparison to be made between solutions obtained by Harvey and Gallis (Reference 8) with the DSMC code and Hash et al. (Reference 10) with their Navier-Stokes-based prediction method. These comparisons are shown in Figures 2-36 and 2-37 for the pressure and heat transfer measurements made at the LENS case C and D test conditions for the same nominal air conditions with air and nitrogen as the test gas, respectively. Again, the measurements with nitrogen and air as the test gas indicate that real-gas effects were insignificant in these flows. Here the prediction methods do not agree well in the baseflow region but give comparable results downstream of reattachment. Neither computation predicts the slower pressure and heat transfer rise measured exponentially in the recompression region of the baseflow.

2.4.3 Comparison Between Measurements with Navier-Stokes Predictions

An important set of comparisons was those between Navier-Stokes solutions and the measurements obtained for LENS cases E and F, which are at the 10 MJ/kg enthalpy and 500 bar reservoir conditions with air and nitrogen as the test gas, respectively. Test case E was developed as a match point between the various hypervelocity facilities in which the planetary probe has been tested. In particular, measurements have been obtained in the HEG and LENS shock tunnels and the "hot shot" facility Tunnel F in France at the nominal 10 MJ/kg and 500 bar test case with air. Because of the high density levels at which these studies were conducted, the flow over the front face and in the majority of the wake can be considered as fully continuum, and solutions based on the Navier-Stokes equations provide the only practical prediction technique. However, in the expansion region above the separated baseflow, the densities may be low enough that the continuum assumption in such computations is invalid, and in this region the DSMC code could be more applicable. Therefore, calculations employing the Navier-Stokes code to compute the forebody flow coupled with a DSMC method to compute the base region have been pursued. Navier-Stokes solutions to compute the flow over the planetary probe configuration for case E test conditions have been obtained by Muylaert et al. (Reference 11), Chadwick (Reference 8), and Dietrich and Boyd (Reference 9). Computations using the hybrid Navier-Stokes/DSMC method have been made by Gochberg (Reference 1) and again made by Dietrich and Boyd (Reference 9). Comparisons between the calculations of heat transfer and pressure obtained by Muylaert et al. (Reference 10) using the TINA code are compared with measurements of heat transfer rate for Run Nos. 22, 29, and 33 in Figure 2-38. The computations are in excellent agreement with the experimental measurements on the front face of the probe, but fall slightly below the measurements downstream of the reattachment region on the sting. As discussed earlier, we believe that for Run Nos. 29 and 33, the heating levels downstream of the reattachment region may be influenced by the

15

beginning of a transition process. A similar set of comparisons for the computations employing the GASP code (Reference 12) performed by Chadwick is shown in Figure 2-39. Here the computations fall slightly above the measurements during the recompression process along the sting. Finally, in Figures 2-40 and 2-41, we show the comparisons between the heat transfer and pressure measurements and computations performed at Cornell using a Navier-Stokes method. Again, we see that while predictions for the forebody are in good agreement with the measurements, the flow in the recompression region is not well predicted, and the measurements fall above the predictions downstream of the recompression region on the sting. Although discrepancies may occur between individual computations due to incorrect implementation, the differences may also illustrate a general potential weakness of the continuum codes in handling flows in which there are very rapid expansions similar to those occurring around the rim of this configuration. In this instance, a failure to compute the localized flow in the region of the rim will set inappropriate upstream conditions for the wake and reattachment flow computations, where the discrepancies may be amplified.

2.4.4 Discussion of Predictions with Hybrid Prediction Scheme

Citing problems with the validity of employing the Navier-Stokes code in the wake regions of these flows, Gochberg et al. (Reference 1) obtained computations using a hybrid method where a Navier-Stokes solution for the forebody was joined with a DSMC calculation in the wake region. Two cases were calculated: (1) the LENS case E and (2) the HEG Run 132. Again, the computations were in good agreement with the experimental measurements from the HEG and LENS facility on the forebody, as shown in Figure 2-42. However, in the baseflow, the hybrid solution predicted large levels of heating in the reattachment compression region, which more closely agreed with those obtained in the HEG facility. Measurements in the LENS facility were lower by a factor between 3 and 5, as shown in Figure 2-43. In a companion calculation, the flows were computed with a full Navier-Stokes solution employing the NEQ2D code. These predictions indicated that the separated region was significantly shorter than that found in experiment, although the peak heating levels in the reattachment region were comparable. The Navier-Stokes predictions in this paper were not in good agreement with those obtained earlier by Muyiaert (Reference 11) and Chadwick (Reference 8). The relatively poor agreement between the hybrid predictions and the experimental data prompted additional efforts employing a decoupled Navier-Stokes/DSMC approach at Cornell. Comparisons between the pressure and heat transfer measurements for the LENS case E condition with computations employing the hybrid technique and the Navier-Stokes/DSMC computation for the boundaries illustrated in Figure 2-44 are shown in Figures 2-45 and 2-46. Here it can be seen that, unlike the earlier predictions by Gochberg et al. (Reference 1), the two prediction techniques do not significantly differ, although the predictions at the end of the reattachment region employing the hybrid code are in better agreement with experiment. Again, the pressure measurements exhibited a slower return to the sting pressure than predicted by either the Navier-Stokes or hybrid codes. Clearly, further investigations are required to examine the discrepancies between the results of the two hybrid computational methods and to explore the factors that influence the accuracy of the Navier-Stokes codes in regions of highly-expanded flow.

2.5   CONCLUSIONS

Experimental studies and computations with the DSMC and Navier-Stokes codes have been made to examine the aerothermal and flowfield characteristics of the flow over a sting-mounted planetary probe configuration in hypervelocity air and nitrogen flows. In the experimental program, conducted in the LENS hypervelocity shock tunnel, surface and flowfield measurements were made at total enthalpies of 5 MJ/kg and 10 MJ/kg for a range of reservoir pressures from 70 to 500 bars. Heat transfer and pressure measurements were made with separate sets of instrumentation constructed and calibrated by CUBRC and NASA Langley, respectively. The heat transfer and pressure measurements made with these two different sets of instrumentation installed on the front and rear face of the probe and along the sting on the two models of identical geometry were in excellent agreement. High-speed and single shot Schlieren photography were also employed to examine the flow over the model and the time to establish the flow in the base region. Analysis of the time history measurements of the heat transfer and pressure indicated that the baseflow was fully established within 4 milliseconds of flow initiation or between 35 and 50 flow lengths based on freestream velocity and base height. Time-accurate calculations with the DSMC code were in agreement with these flow establishment times. Computations employing the DSMC code were found to compare well with the pressure and heat transfer measurements over the model and sting under rarefied flow conditions. Navier-Stokes solutions assuming continuum, laminar flow for the 10 MJ/kg and 500 bar reservoir conditions were in agreement with the measurements on the probe and along the sting. The maximum heating coefficients on the sting observed in the present studies were a small fraction of similar measurements obtained at nominally the same conditions in the HEG shock tunnel, where it is possible that transition occurred in the baseflow, and in the low enthalpy studies conducted in the NASA Langley high Reynolds number Mach 10 tunnel, where the baseflow was shown to be turbulent. Measurements of sting heating in the LENS facility indicate that the flow in the base recompression region is close to transitional at the match point conditions. Although the hybrid Navier-Stokes/DSMC calculations performed by Gochberg suggested that Navier-Stokes calculations could be seriously in error in the baseflow region, similar Navier-Stokes/DSMC calculations presented here by Dietrich and Boyd, did not.

2.6 REFERENCES

1.   Gochberg, L.A., Alien, G.A., Gallis, M.A. and Deiwert, G.S., "Comparison of Computations and Experiments for Nonequilibrium Flow Expansions Around a Blunted Cone," AIAA Paper No. 96-0231

2.   Holden, M.S., "Large-Energy National Shock Tunnel (LENS) Description and Capabilities" Brochure, February 1991.

3.   Horvath, T., McGinley, C., and Hannemann K., "Blunt Body Near Wake Flowfield at Mach 6," AIAA Paper No. 96-1935. New Orleans, LA.

4.   Kastell, D., Horvath, T.J., and Eitelberg, G., "Nonequilibrium Flow Expansion Experiment Around a Blunted Cone," 4th European High Velocity Database Workshop ESTEC, Noordwijk, The Netherlands (1994).

5.   Holden, M.S., Moselle, J.R., Sweet, S.J. and Martin, S.C., "A Database of Aerothermal Measurements in Hypersonic Flow for CFD Validation," AIAA Paper No. 96-4587, Norfolk, VA.

6.   Gallis, M.A. and Harvey, J.K., (1995a) "Comparison of the Maximum Entropy DSMC Code with Flowfield Measurements," AIAA Paper 95-0413, 33"* Aerospace Sciences Meeting and Exhibit in Reno, NV, January 9-12.

7.   Moss, J. N., Dogra, V. K., and Price, J. M., "DSMC Calculations for a 70° Blunted Cone at 3.2 km/s in Nitrogen," NASA TM-109181, January 1995.

8.   Holden, M.S., Chadwick, K.M., Gallis, M.A. and Harvey, J.K., "Comparison Between Shock Tunnel Measurements on a Planetary Probe Configuration and DSMC Predictions," paper presented at the 20th International Symposium on Shock Waves at California Institute of Technology, Pasadena, July 23-28, 1995.

9.   Dietrich, S. and Boyd, I.D., "A Scalar Optimized Parallel Implementation of the DSMC Technique," *Journal ofComputational Physics,'Vol.* 126, 1996, pp. 328-342.

10.   Hash, D. B., Hassan, H. A., Dogra, V. K,, and Price, J. M., "Navier-Stokes Calculations for a Spherically Blunted Cone (LENS Condition)," Presented at the 4th European High-Velocity Database Workshop, ESTEC, Noordwijk, November 24-25, 1994.

11.   Muyiaert, J. Walpot, L,, Spel, M., Tumino, G. and Steiji, R., "Non-Equilibrium Computational Analysis of Blunt-Cone Experiments Performed in the LENS and HEG Facilities, AIAA Paper No. 96-2436, New Orleans, LA.

12.   McGrory, W. D.. Slack, D. C., Applebaum, M. P., and Walters, R. W., "GASP Version 2.2 Users Guide," Aerosoft, Inc., Blacksburg, VA, 1992.

Table 2-1
Test Condition B

Shock Mach Number	Mi =	6.243
Reservoir Pressure	PO =	1075. Psia
Total Enthalpy	HO =	5.798E+07 (ft/sec)**2
Stagnation Temperature	TO =	7832. degrees R
Freestream Mach No.	M =	15.63
Freestream Reynolds No.	Re =	1.7461E+04 1/ft
Freestream Velocity	U =	10649. Ft/sec
Freestream Temperature	T =	186.7 degrees R
Freestream Pressure	P =	5.84E-04 psia
Freestream Density	RHO =	2.534E-07 slugs/ft/ft/ft
Pitot Pressure	Pitot =	1.7914E-01 psia
Wall Temperature	Twall =	5.2660E+02 degrees R
Molecular Weight	MW =	28.005
	N2 mole fraction = .9996	
	N mole fraction = .0004	

Table 2-2
Test Condition C

Shock Mach Number	Mi =	6.364
Reservoir Pressure	PO =	4222. Psia
Total Enthalpy	HO =	5.6466E+07 (ft/sec)**2
Stagnation Temperature	TO =	7.0597E+03 degrees R
Freestream Mach No.	M =	10.23
Freestream Reynolds No.	Re =	2.7093E+05 1/ft
Freestream Velocity	U =	1.0128E+04 Ft/sec
Freestream Temperature	T =	4.0731E+02 degrees R
Freestream Pressure	P =	4.0054E-02 psia
Freestream Density	RHO =	8.2404E-06 slugs/ft/ft/ft
Pitot Pressure	Pitot =	5.3966E+00 psia
Wall Temperature	Twall =	5.3320E+02 degrees R
Molecular Weight	MW =	28.94
	N2 mole fraction = 7.411E-01	
	N mole fraction = 4.710E-40	
	O2 mole fraction = 1.698E-01	
	AR mole fraction = 9.319E-03	
	O mole fraction = 1.181E-03	
	NO mole fraction = 7.859E-02	

Table 2-3
Test Condition D

Shock Mach Number	Mi =	6.4090
Reservoir Pressure	PO =	4.2080E+03 psia
Total Enthalpy	HO =	6.0915E+07 (ft/sec)**2
Stagnation Temperature	TO =	8.2014E+03 degrees R
Freestream Mach No.	M =	10.31
Freestream Reynolds No.	Re =	2.3540E+05 1/ft
Freestream Velocity	U =	1.0784E+04 Ft/sec
Freestream Temperature	T =	4.4061E+02 degrees R
Freestream Pressure	P =	3.8963E-02 psia
Freestream Density	RHO =	7.1714E-06 slugs/ft/ft/ft
Pitot Pressure	Pitot =	5.3249E+00 psia
Wall Temperature	Twall =	5.3590E+02 degrees R
Molecular Weight	MW =	28.01
	N2 mole fraction = 9.998E-01	
	N mole fraction = 1.882E-04	

Table 2-4
Test Condition A

Shock Mach Number	Mi =	6.470
Reservoir Pressure	PO =	7.5880E+03 psia
Total Enthalpy	HO =	5.8402E+07 (ft/sec)**2
Stagnation Temperature	TO =	7.2959E+03 degrees R
Freestream Mach No.	M =	10.25
Freestream Reynolds No.	Re =	4.4945E+05 1/ft
Freestream Velocity	U =	1.0327E+04 Ft/sec
Freestream Temperature	T =	4.2170E+02 degrees R
Freestream Pressure	P =	6.9402E-02 psia
Freestream Density	RHO =	1.3795E-05 slugs/ft/ft/ft
Pitot Pressure	Pitot =	9.3927E+00 psia
Wall Temperature	Twall =	5.3410E+02 degrees R
Molecular Weight	MW =	28.95
	N2 mole fraction = 7.433E-01	
	N mole fraction = 2.266E-39	
	O2 mole fraction = 1.721E-01	
	AR mole fraction = 9.321E-03	
	O mole fraction = 6.002E-04	
	NO mole fraction = 7.469E-02	

Table 2-5
Test Condition E

Shock Mach Number	Mi =	9.258
Reservoir Pressure	PO =	7.1230E+03 psia
Total Enthalpy	HO =	1.1831E+08 (ft/sec)**2
Stagnation Temperature	TO =	1.1653E+04 degrees R
Freestream Mach No.	M =	8.6545
Freestream Reynolds No.	Re =	1.3841E+05 1/ft
Freestream Velocity	U =	1.4525E+04 Ft/sec
Freestream Temperature	T =	1.1728E+03 degrees R
Freestream Pressure	P =	9.0307E-02 psia
Freestream Density	RHO =	6.3331E-06 slugs/ft/ft/ft
Pitot Pressure	Pitot =	8.5888E+00 psia
Wall Temperature	Twall =	5.3570E+02 degrees R
Molecular Weight	MW =	28.41
	N2 mole fraction = 7.357E-01	
	N mole fraction = 5.763E-11	
	O2 mole fraction = 1.564E-01	
	AR mole fraction = 9.146E-03	
	O mole fraction = 3.816E-02	
	NO mole fraction = 6.056E-02	
	NO+ mole fraction = 9.287E-09	
	E- mole fraction = 9.287E-09	

Table 2-6
Test Condition F

Shock Mach Number	Mi =	8.8590
Reservoir Pressure	PO =	7.3620E+03 psia
Total Enthalpy	HO =	1.1193E+08 (ft/sec)**2
Stagnation Temperature	TO =	1.3033E+04 degrees R
Freestream Mach No.	M =	9.3017
Freestream Reynolds No.	Re =	1.6294E+05 1/ft
Freestream Velocity	U =	1.4505E+04 Ft/sec
Freestream Temperature	T =	9.8599E+02 degrees R
Freestream Pressure	P =	8.1132E-02 psia
Freestream Density	RHO =	6.6629E-06 slugs/ft/ft/ft
Pitot Pressure	Pitot =	8.9795E+00 psia
Wall Temperature	Twall =	5.3380E+02 degrees R
Molecular Weight	MW =	27.97
	N2 mole fraction = 9.968E-01	
	N mole fraction = 3.186E-03	

Figure 2-1   70° Cone Section of Planetary Probe

$\theta = 70°$
$R_n/R_b = 0.5$
$R_c/R_b = 0.05$
$R_j/R_b = 0.083$
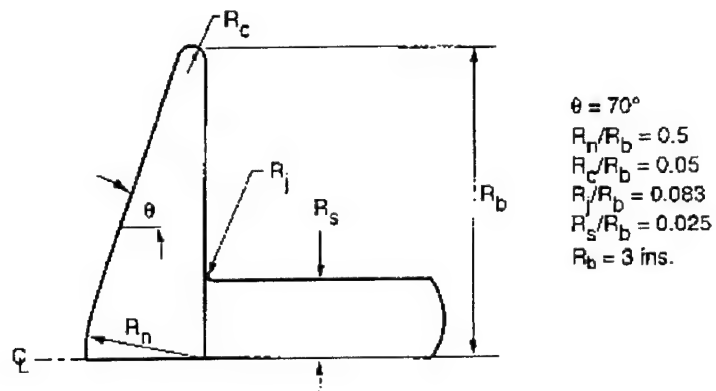$R_s/R_b = 0.025$
$R_b = 3$ ins.

Figure 2-2   Blunt Body/Wake Closure Test Model
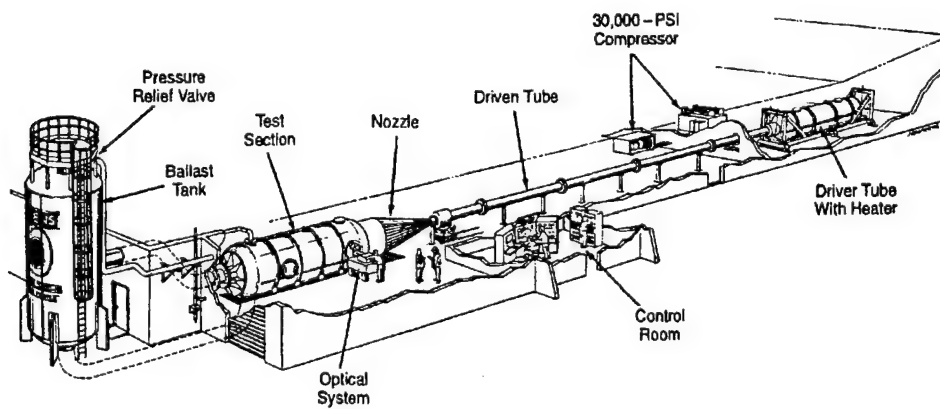
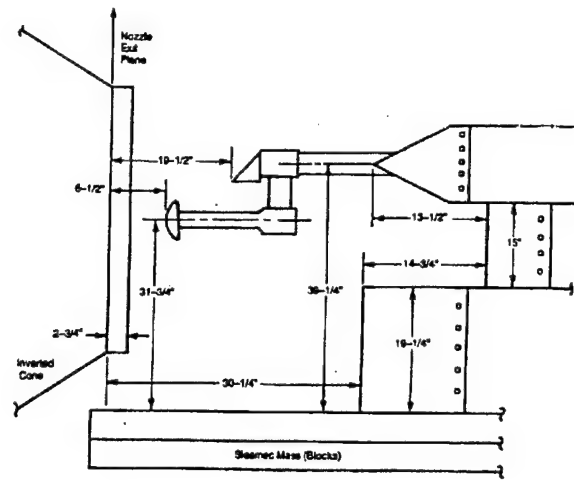

Figure 2-3   Large Energy National Shock Tunnel (LENS)

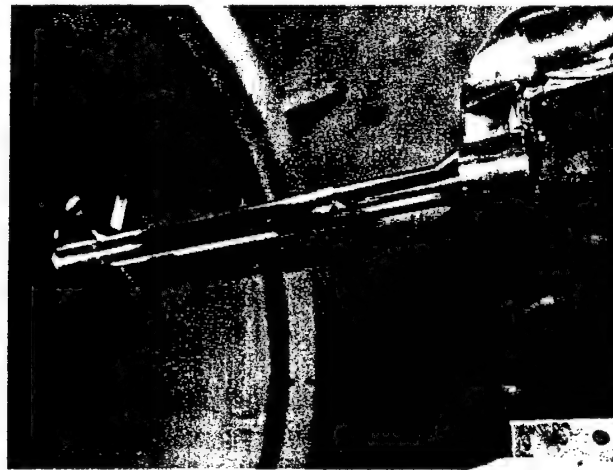Figure 2-4   Diagram of Support Section and Sting Mount with Planetary Probe

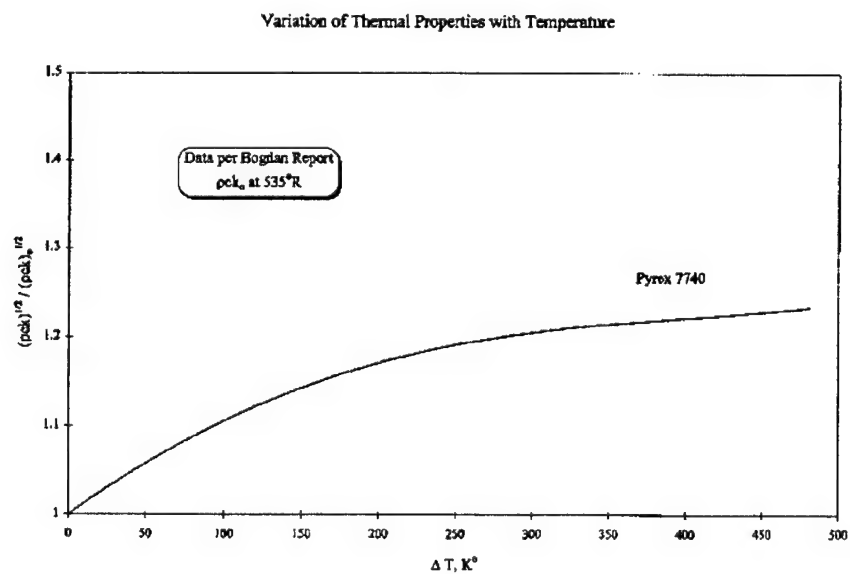Figure 2-5   Planetary Probe Installed in LENS Tunnel

Variation of Thermal Properties with Temperature

Figure 2-6   Variation of the Properties of the Pyrex Substrate with Temperature Employed in Heat Transfer Data
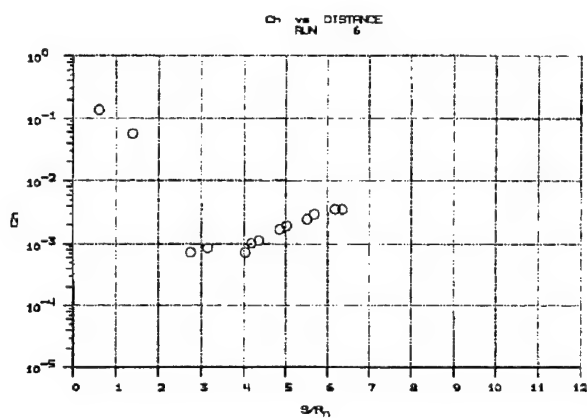Reduction Code

21
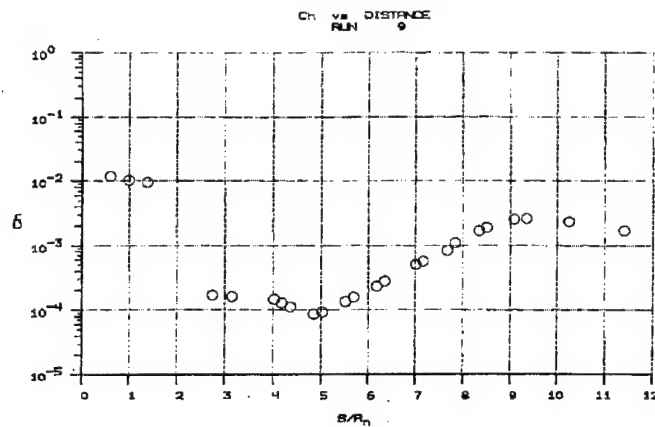
Figure 2-7a Distribution of Heat Transfer Coefficient over Planetary Probe Model and Sting for Case A Test Condition (Run 9)
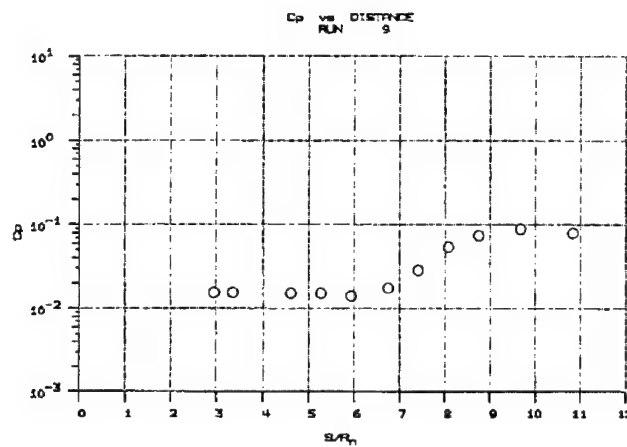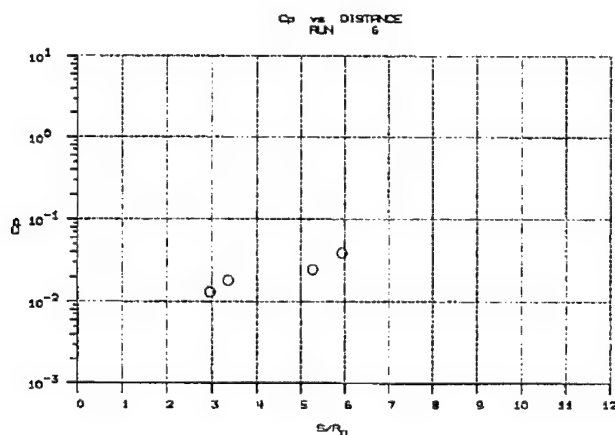

Figure 2-7b Distribution of Pressure Coefficient over Planetary Probe Model and Sting for Case A Test Condition (Run 9)
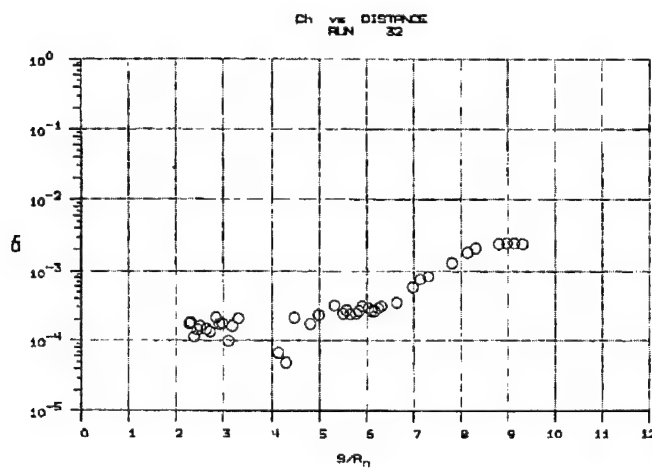
Figure 2-8 Distribution of Heat Transfer Coefficient over Planetary Probe Model and Sting for Case A Test Condition (Run 32)

22
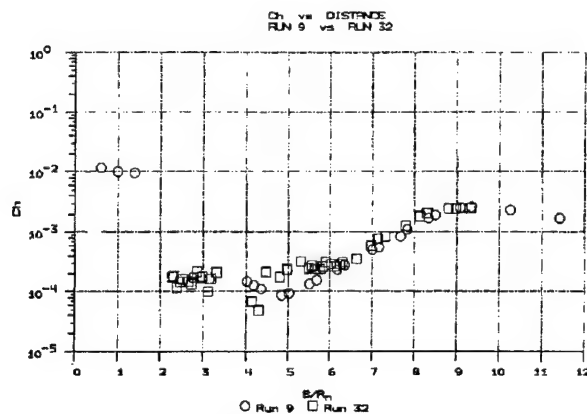
Figure 2-9   Comparison of Distributions of Heat Transfer Coefficient over Planetary Probe Model and Sting for Case A Test Condition for CUBRC and NASA Instrumented Models

Figure 2-10   Distribution of Heat Transfer Coefficient Over Planetary Probe Model and Sting for Case B Test Condition (Run 6)

Figure 2-11   Distribution of Pressure Coefficient over Planetary Probe Model and Sting for Case B Test Condition (Run 6)
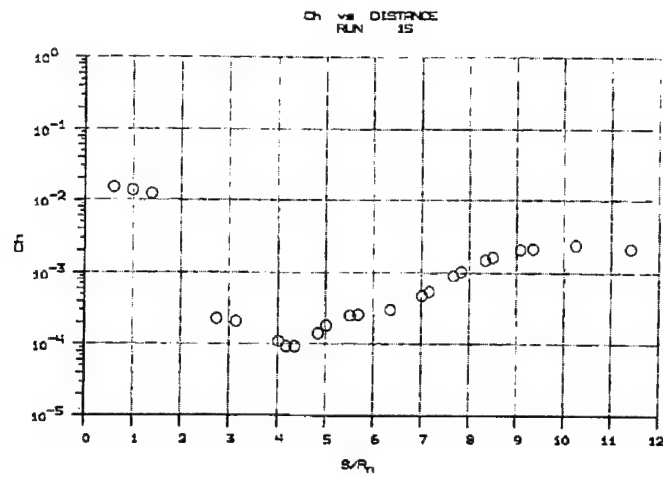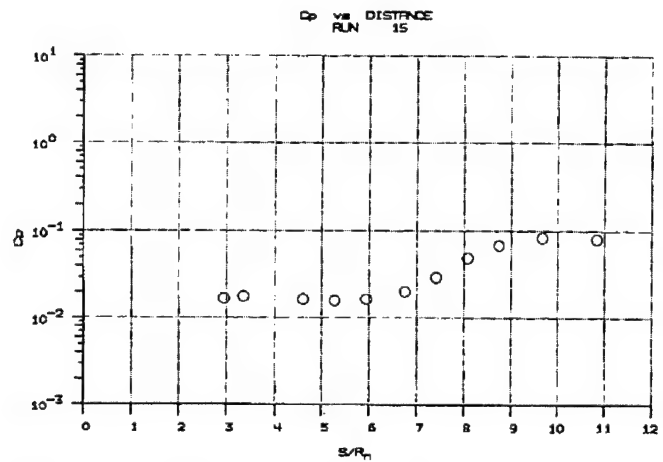
Figure 2-12a Distribution of Heat Transfer Coefficient over Planetary Probe Model and Sting for Case C Test Condition (Run 15)

Figure 2-12b Distribution of Pressure Coefficient over Planetary Probe Model and Sting for Case C Test Condition (Run 15)
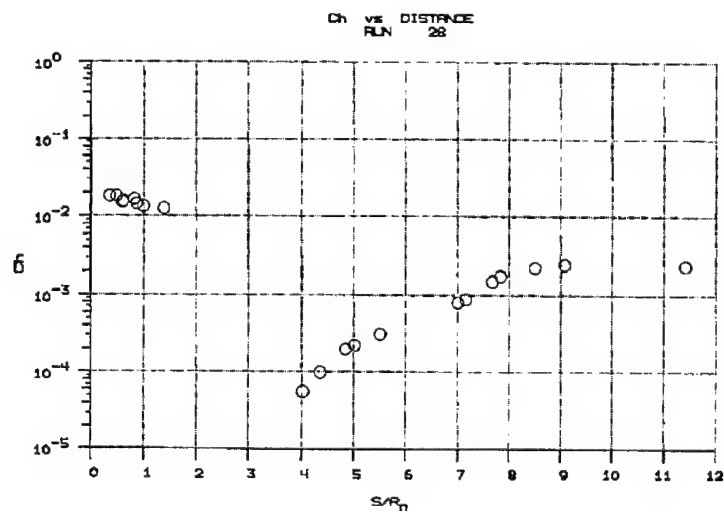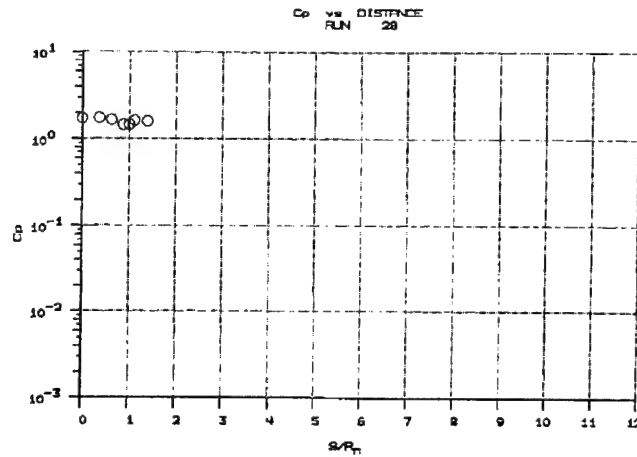

Figure 2-13a Distribution of Heat Transfer Coefficient over Planetary Probe Model and Sting for Case C Test Condition (Run 28)

24

Figure 2-13b Distribution of Pressure Coefficient over Planetary Probe Model and Sting for Case C Test Condition (Run 28)
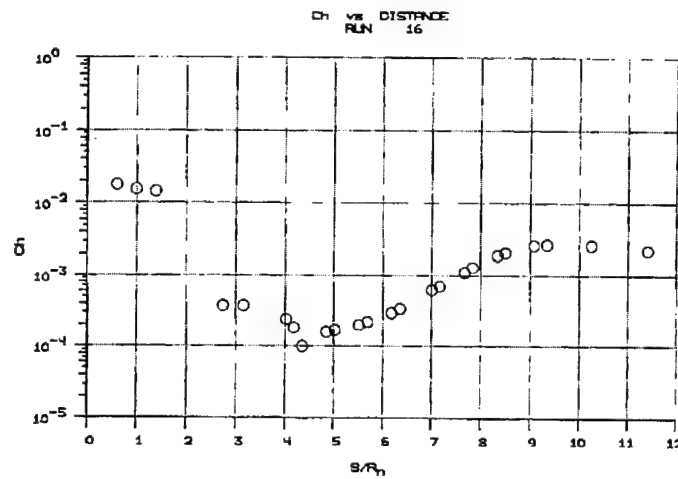

Figure 2-14 Distribution of Heat Transfer Coefficient over Planetary Probe Model and Sting for Case D Test Condition (Run 16)
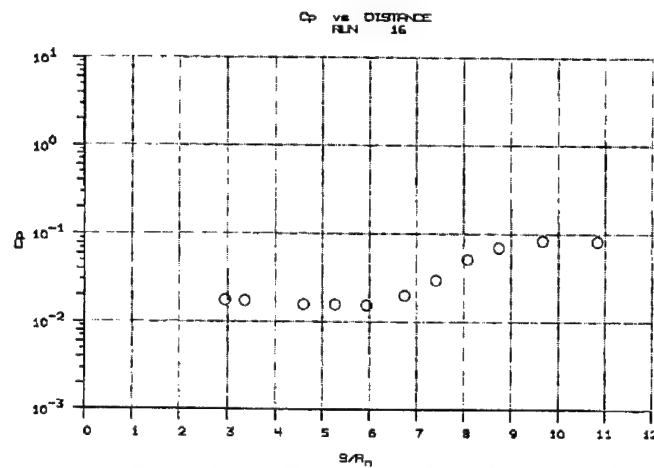

Figure 2-15 Distribution of Pressure Coefficient over Planetary Probe Model and Sting for Case D Test Condition (Run 16)
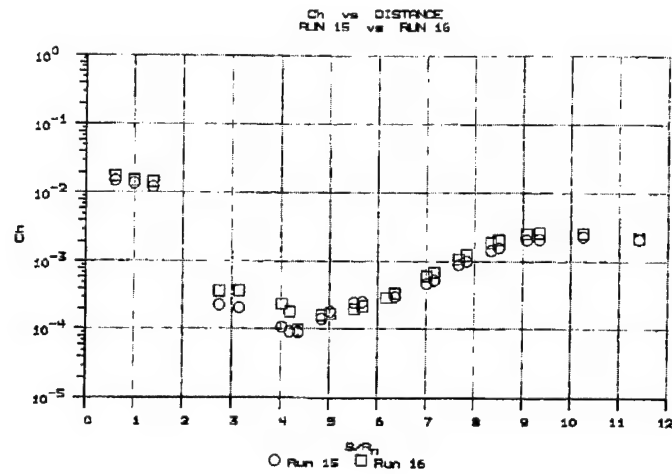
25

Figure 2-16 Comparison Between the Distribution of Heat Transfer Coefficient for Air and Nitrogen Flows for the 5Mj/kg, 500 Atmosphere Reservoir Condition
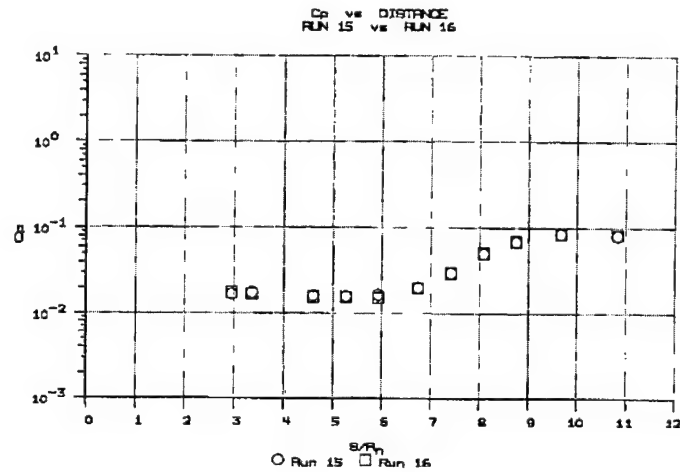

Figure 2-17 Comparison Between the Distribution of Pressure Coefficient for Air and Nitrogen Flows for the 5Mj/kg, 500 Atmosphere Reservoir Condition
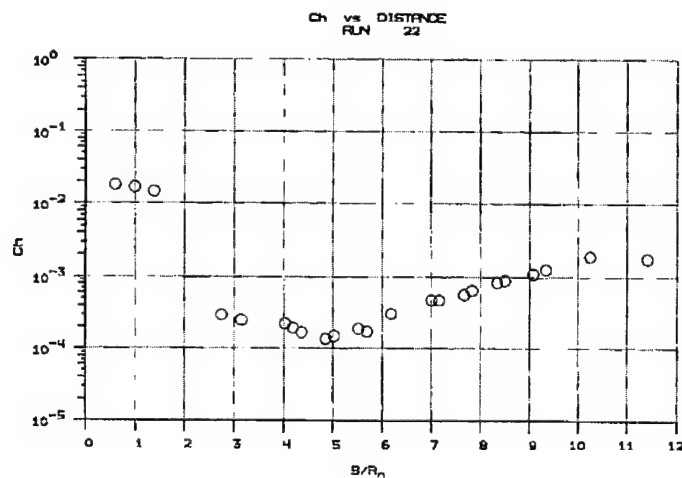

Figure 2-18a Distribution of Heat Transfer Coefficient over Planetary Probe Model and Sting for "Match Point" E Test Conditions (Run 22)

Figure 2-18b Distribution of Pressure Coefficient over Planetary Probe Model and Sting for "Match Point" E Test Conditions (Run 22)

Figure 2-19a Distribution of Heat Transfer Coefficient over Planetary Probe Model and Sting for "Match Point" E Test Conditions (Run 29)
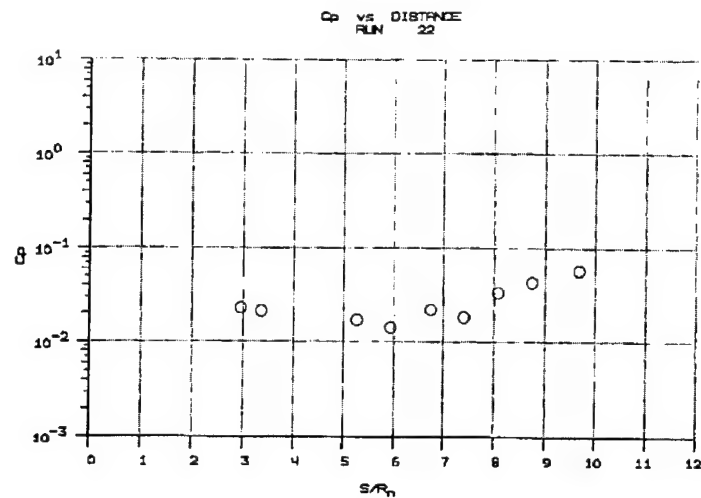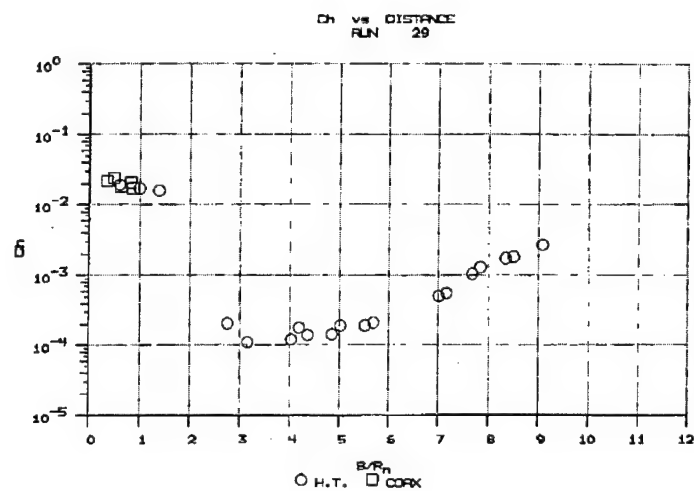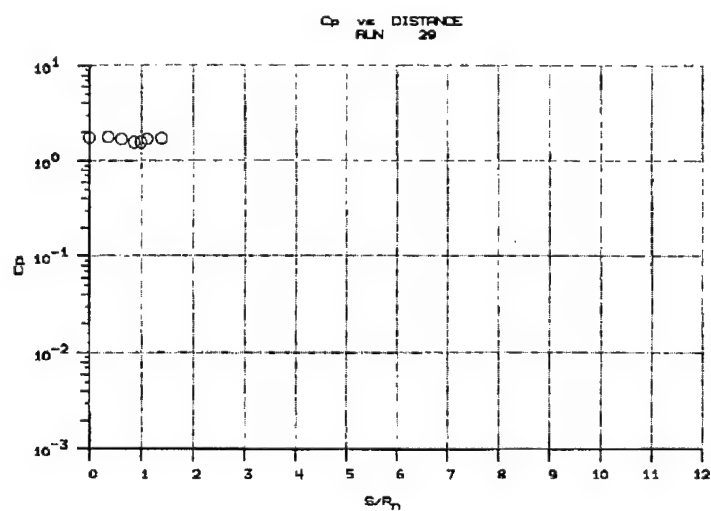

Figure 2-19b Distribution of Pressure Coefficient over Planetary Probe Model and Sting for "Match Point" E Test Conditions (Run 29)

27
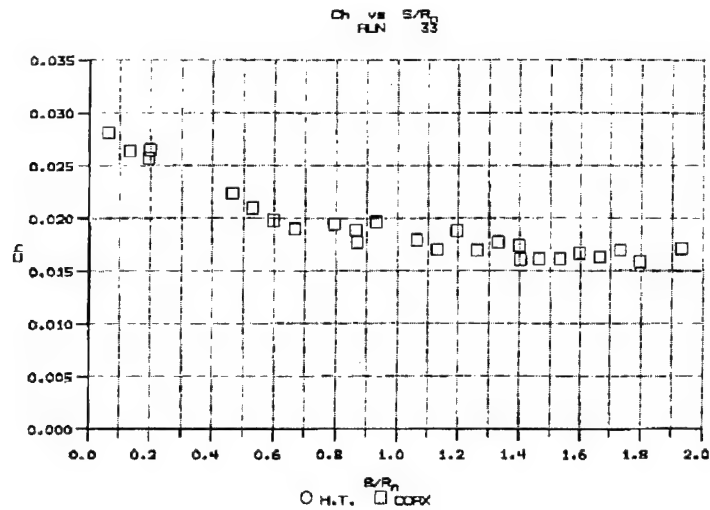
Figure 2-20 Distribution of Heat Transfer Coefficient on Front Face of Planetary Probe at "Match Point" E (Run 33)

Figure 2-21 Distribution of Heat Transfer Coefficient on Rear Face and Sting of Planetary Probe at "Match Point" E (Run 33)

Figure 2-22a Comparisons Between the Distributions of Heat Transfer Coefficient on Front Face of Planetary Probe at "Match Point" E (Run Nos. 29 & 33) for CUBRC and NASA Instrumented Models

28
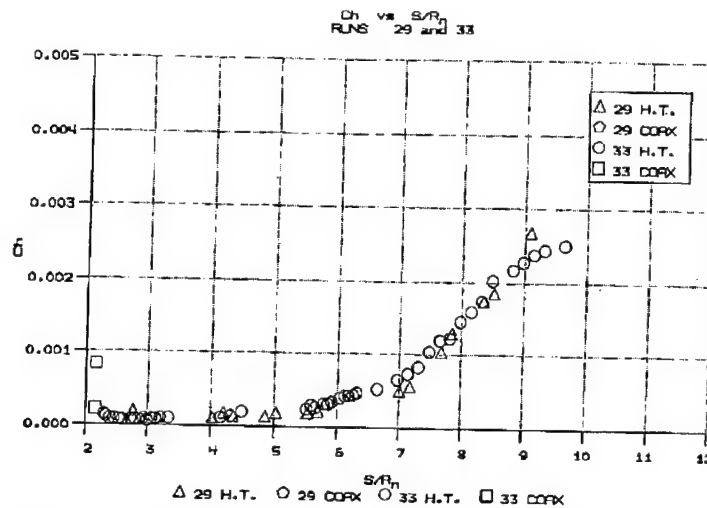
Figure 2-22b Comparison Between the Distributions of Heat Transfer Coefficient on Rear Face and Sting of Planetary Probe at "Match Point" E (Run Nos. 29 & 33) for CUBRC and NASA Instrumented Models
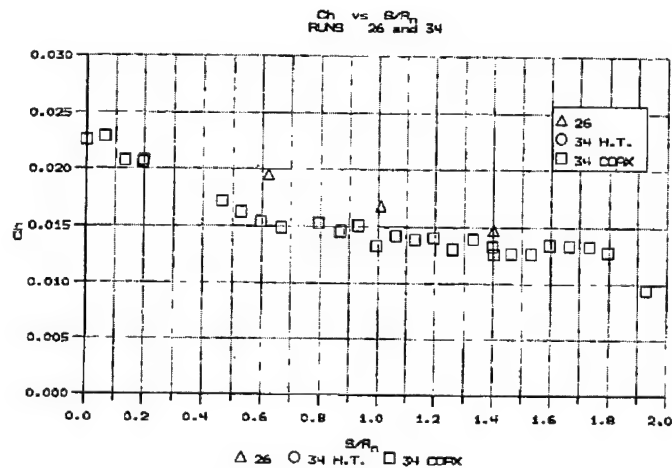
Figure 2-23a Distribution of Heat Transfer Coefficient on Front Face of Planetary Probe at "Match Point" E with Nitrogen Test Gas (Run Nos. 26 & 34) Test Condition F
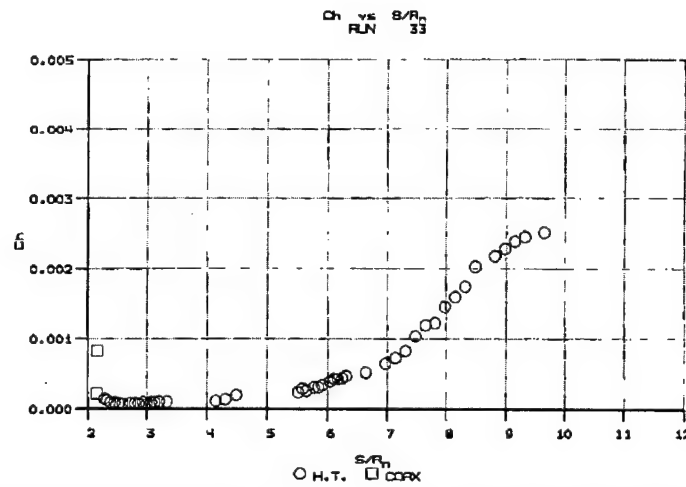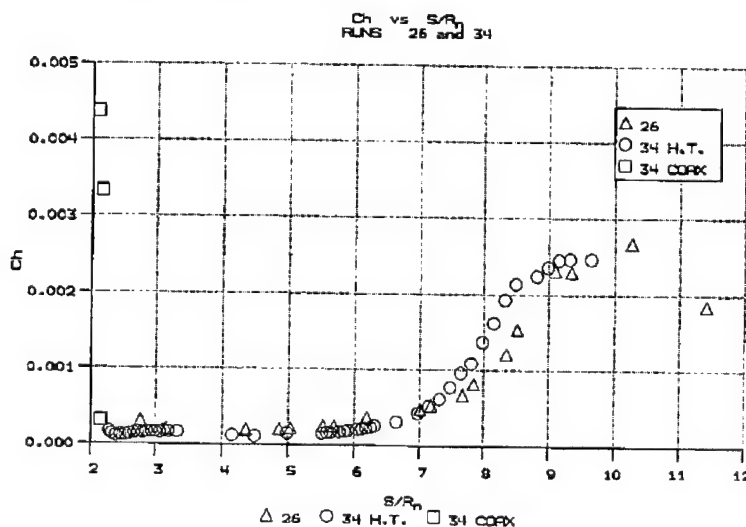

Figure 2-23b Distribution of Heat Transfer Coefficient on Rear Face and Sting of Planetary Probe at "Match Point" E with Nitrogen Test Gas (Run Nos. 29 & 33) Test Condition F
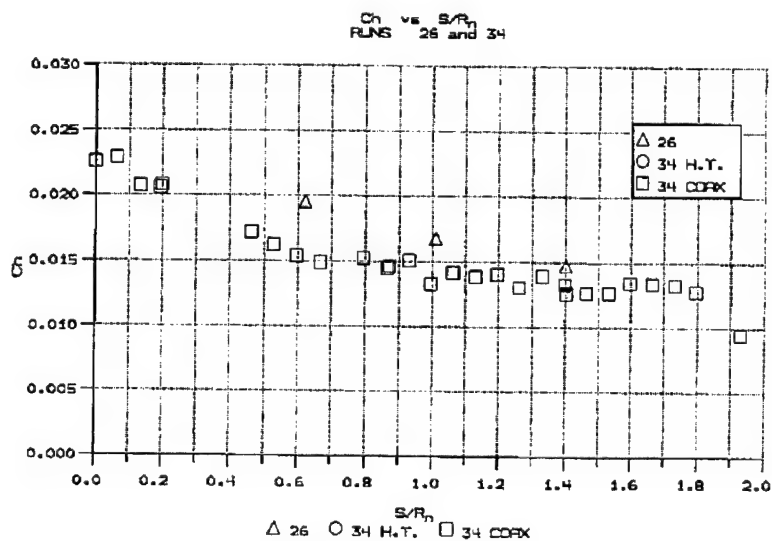
29
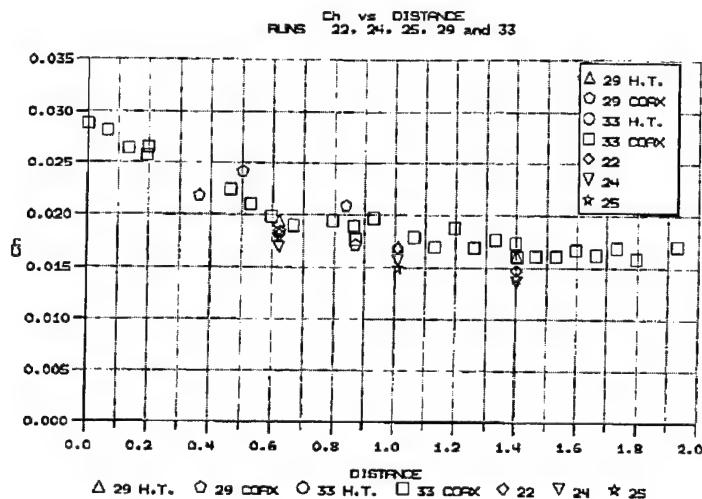
Figure 2-24a Comparisons Between all the Heat Transfer Distributions on the Front Face of the Planetary Probe at "Match Point" E (Run Nos. 22, 24, 25, 29 & 33) for CUBRC and NASA Instrumented Models
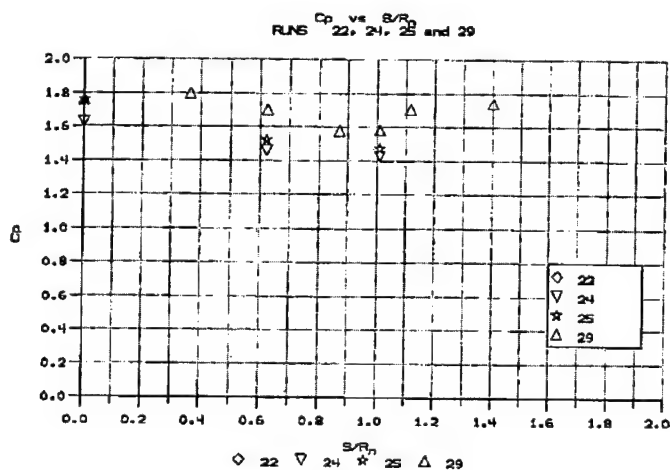
Figure 2-24b Comparisons Between all the Pressure Distributions on the Front Face of the Planetary Probe at "Match Point" E (Run Nos. 22, 24, 25, 29 & 33) for CUBRC and NASA Instrumented Models
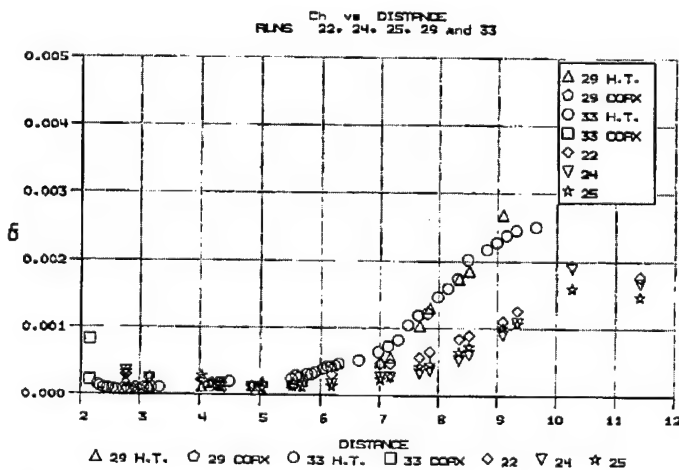
Figure 2-25a Comparisons Between all the Heat Transfer Distributions on the Rear Face and Sting of the Planetary Probe at "Match Point" E (Run Nos. 22, 24, 25, 29 & 33) for CUBRC and NASA Instrumented Models

30
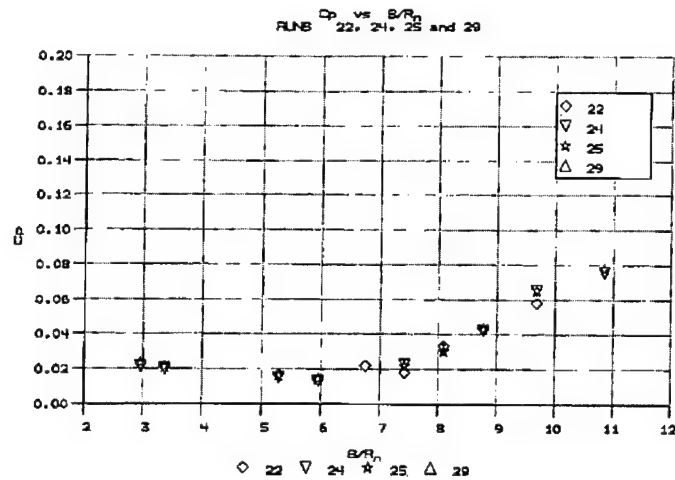
Figure 2-25b Comparisons Between all the Pressure Distributions on the Rear Face and Sting of the Planetary Probe at "Match Point" E (Run Nos. 22, 24, 25, 29 & 33) for CUBRC and NASA Instrumented Models
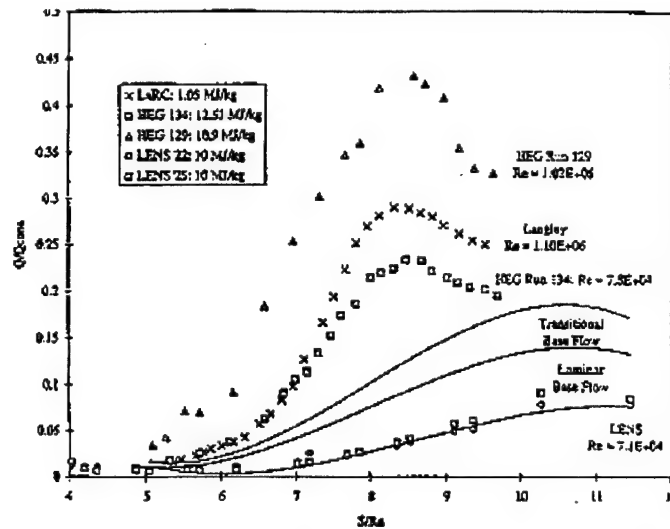
Figure 2-26 Comparison Between Measurements of Heat transfer Along the Sting Obtained in the LENS and HEG Shock Tunnels at the 10 MJ/kg Match Point
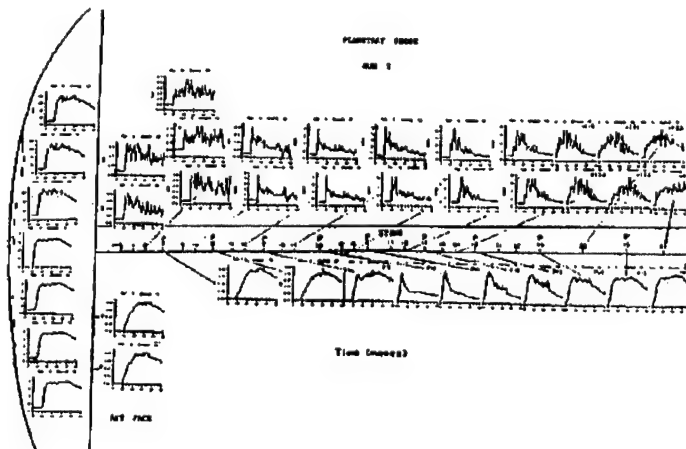
Figure 2-27 Time Establishment of Base Flow Over the Model and Sting - LENS Case A, 5 MJ/kg, 500 Atmospheres

31
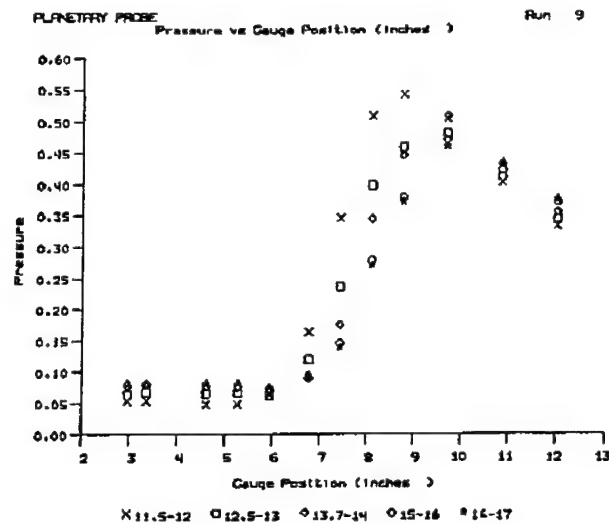
Figure 2-28 Time Establishment of Pressure Distribution Behind the Planetary Probe (Run 9)
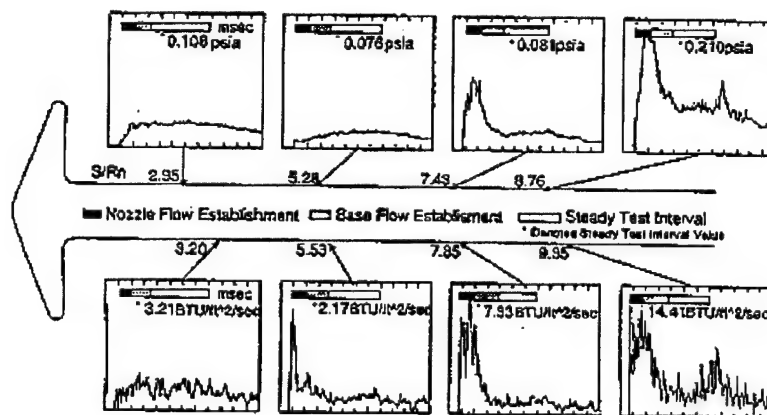
Figure 2-29 Time Histories of Pressure and Heat Transfer along Sting Behind Planetary Probe Showing Time Establishment
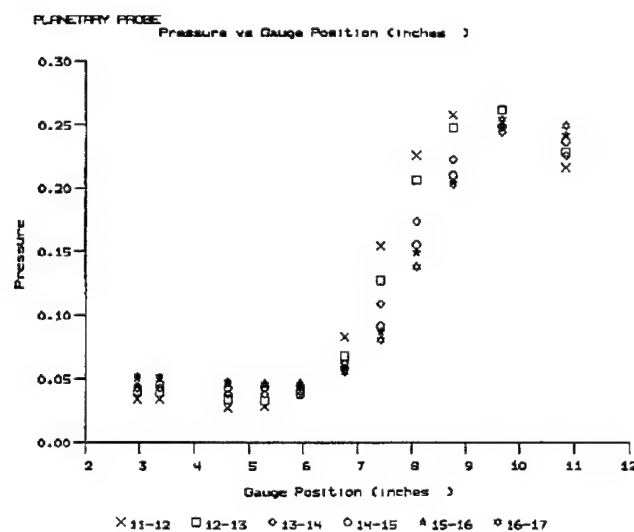
Figure 2-30 Time Establishment of Pressure Distribution Behind the Planetary Probe

32
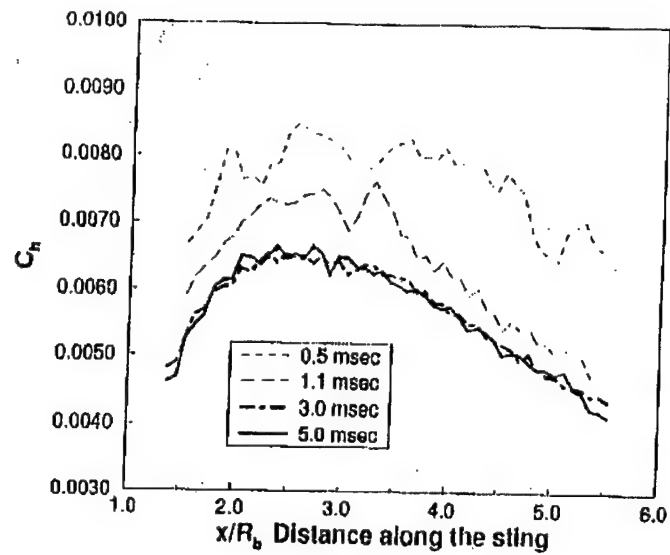
Figure 2-31   DSMC Prediction of Planetary Probe Flow Evolution of Heat transfer Along Sting
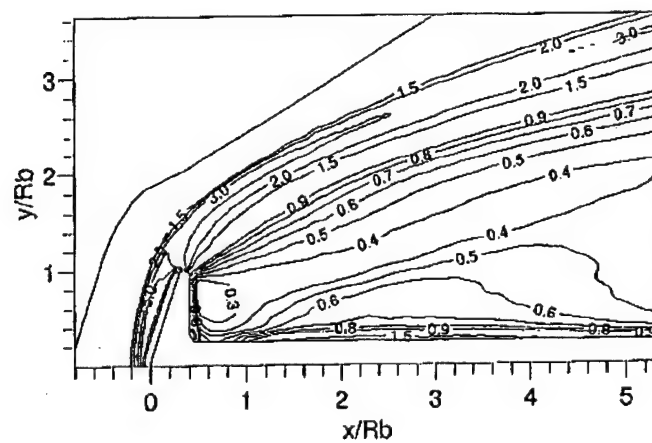
Figure 2-32a DSMC Predictions of Planetary Probe Flow Density Contour at 0.5 msec
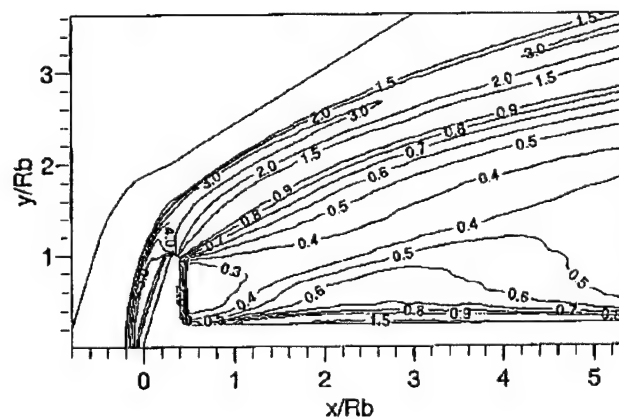
Figure 2-32b DSMC Predictions of Planetary Probe Flow Density Contours at 1.1 msec

33
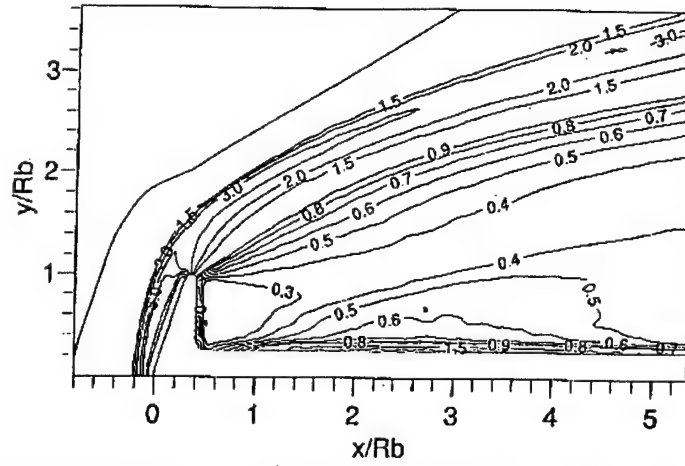
Figure 2-33a DSMC Predictions of Planetary Probe Flow Density Contours at 3.0 msecs
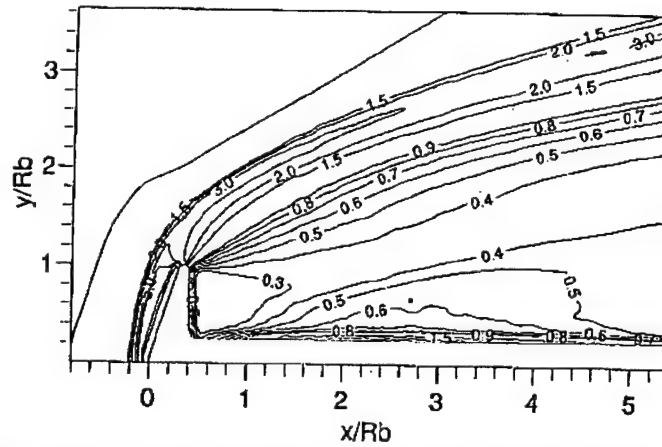
Figure 2-33b DSMC Prediction for Planetary Probe Flow Density Contour at 5.0 msec.
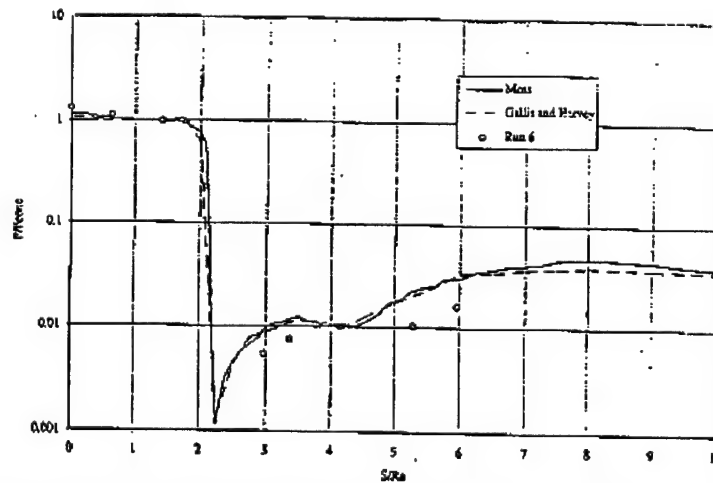
Figure 2-34a Comparison Between the Measured Pressure Distribution on Planetary Probe and DSMC Calculations by Moss (Ref. 7) and Gallis and Harvey (Ref. 6) for the LENS Case B Condition.

34
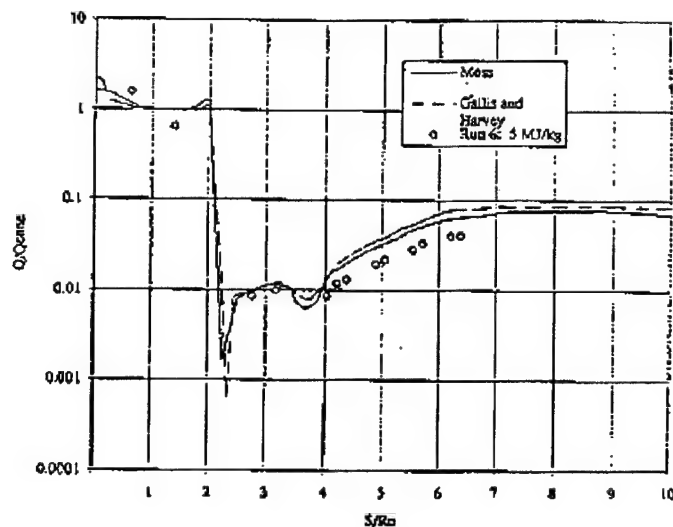
Figure 2-34b Comparison Between the Measured Heat Transfer Distribution on the Planetary Probe Configuration and Calculations by Moss (Ref. 7) and Gallis and Harvey (Ref. 6) for the LENS Case B Test Condition.
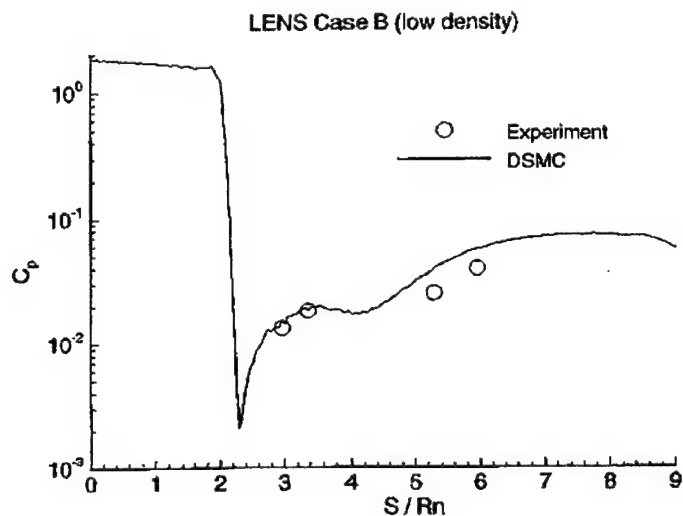
Figure 2-35a Comparison Between the Measured Pressure Distribution on Planetary Probe and DSMC Calculations by Dietrich and Boyd (Ref. 9) for the LENS Case B Condition.
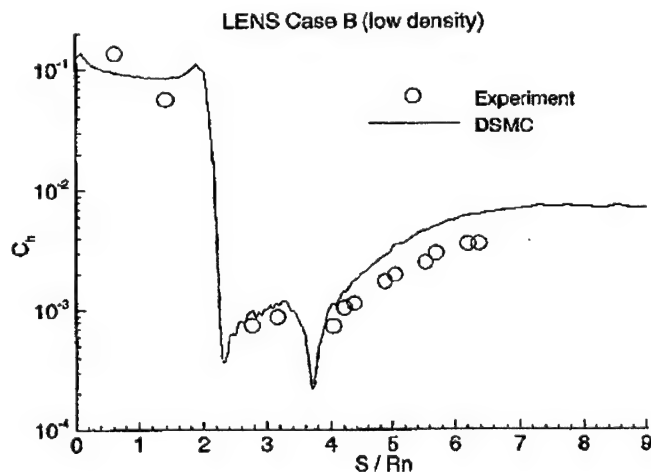
Figure 2-35b Comparison Between the Measured Heat Transfer Distribution on the Planetary Probe Configuration and Calculations by Dietrich and Boyd (Ref. 9) for the LENS Case B Test Condition

35
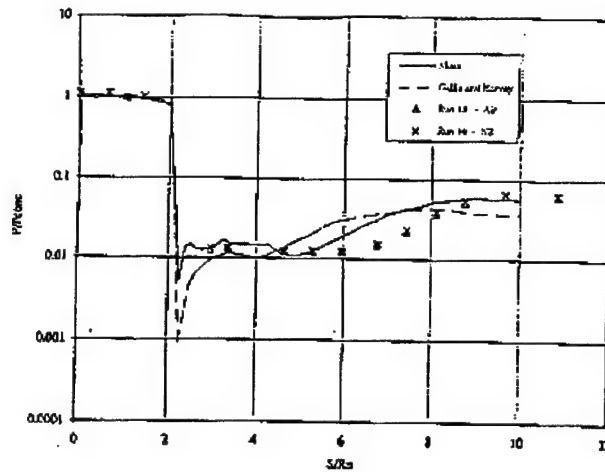
Figure 2-36 Comparisons Between the Measured Pressure Distribution and DSMC and Navier-Stokes Predictions by Gallis and Harvey (Ref 6) and Hassan (Ref. 10) for the LENS Case C Test Condition
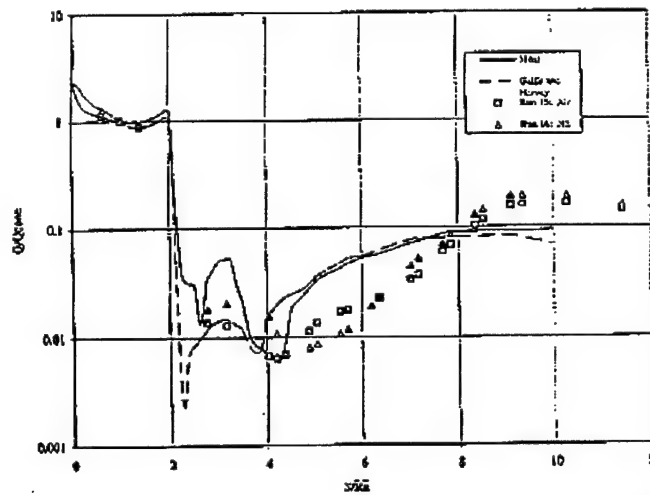
Figure 2-37 Comparisons between the Measured Heat Transfer Distribution and DSMC and Navier-Stokes Predictions by Gallis and Harvey (Ref. 6) and Hassan (Ref. 10) for the LENS Case C Test Condition
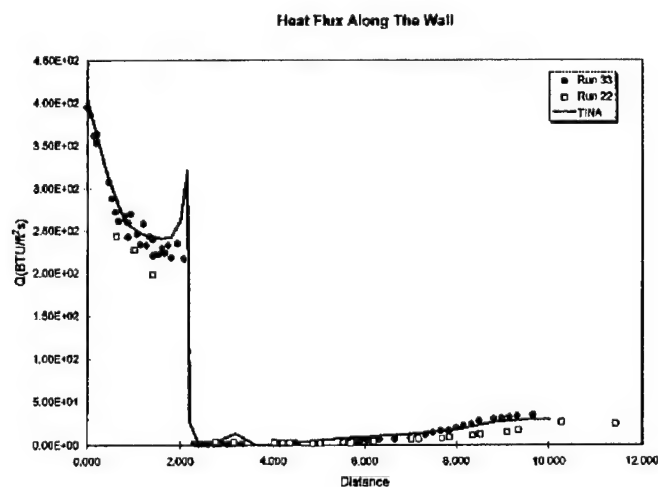
Figure 2-38 Comparison Between Calculations with "TINA" Navier-Stokes Code by Muylaert, et al. (Ref. 11) with Heat Transfer Measurements made in LENS Facility in Runs 22 and 33 at "Match Point" Case E

36
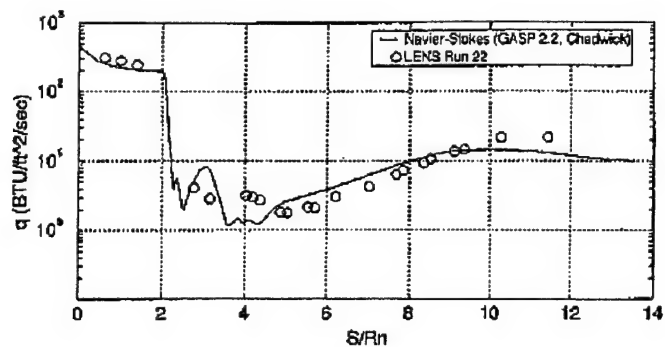
LENS Case E 500 atm and 10 Mj/kg, Heat Transfer
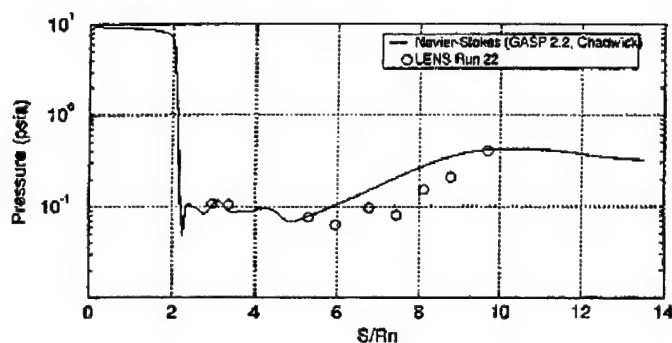
LENS Case E 500 atm and 10 Mj/kg, Pressure

Figure 2-39   Comparison Between Calculations with the GASP Navier-Stokes Code by Chadwick, et al. (Ref. 12) with Heat Transfer and Pressure Measurements made in LENS Facility in Run 22 at "Match Point" Case E
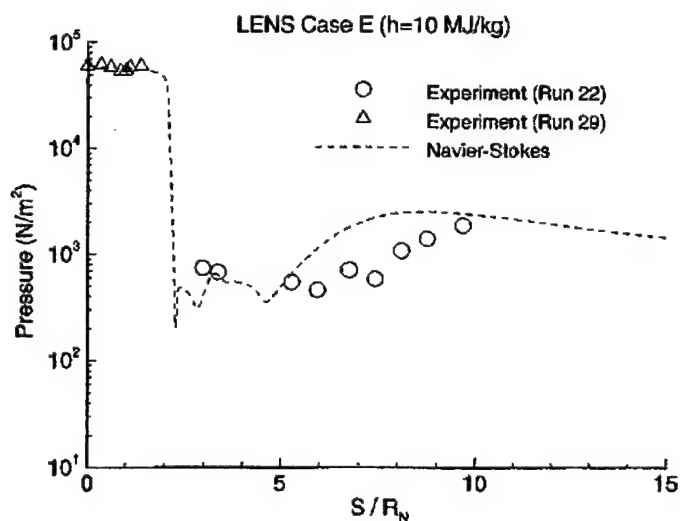
Figure 2-40   Comparison Between Calculations with the Cornell Navier-Stokes Code with Pressure Measurements made in LENS Facility in Runs 22 and 29 at "Match Point" Case E
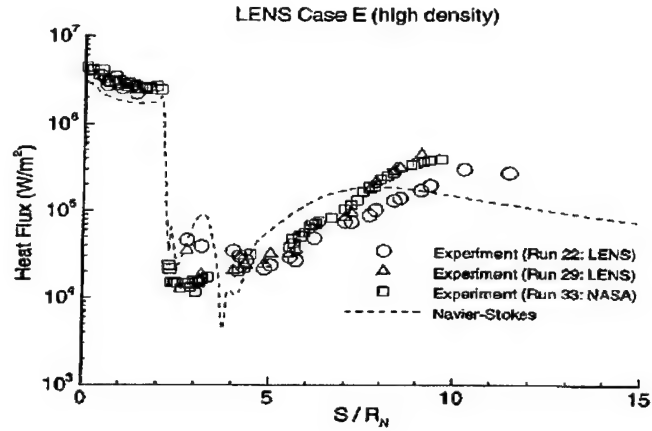
Figure 2-41 Comparison Between Calculations with the Cornell Navier-Stokes Code with Heat Transfer Measurements made in LENS Facility in Runs 22, 29 & 33 at "Match Point" Case E
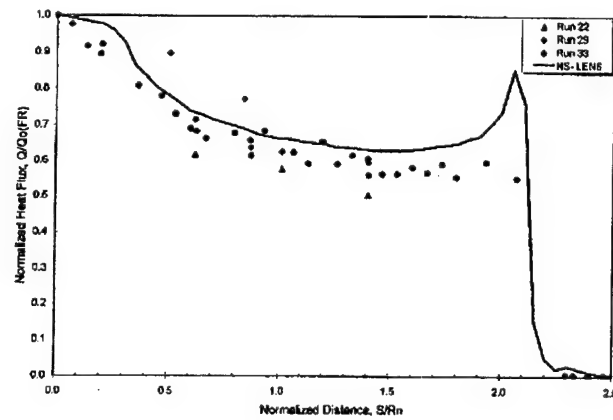
Figure 2-42 Comparison Between Calculations with Navier-Stokes Code by Gochberg with Normalized Heat Transfer Measurements made to the Front Face of the Planetary Probe in the LENS Facility in Runs 22, 29 & 33 at "Match Point" Case E
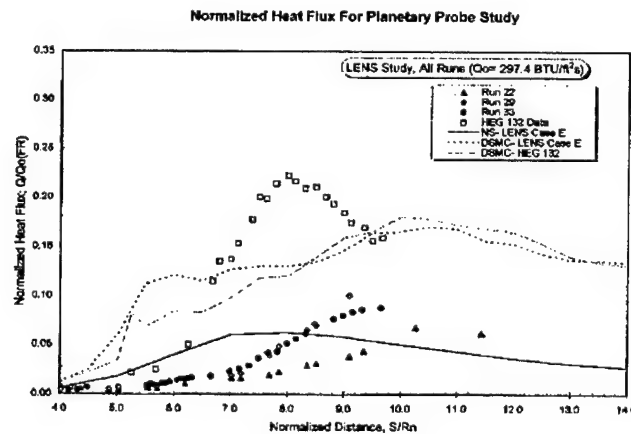
Figure 2-43 Comparison Between Calculations with Hybrid Navier-Stokes/DSMC Code by Gochberg with Normalized Heat Transfer Measurements made to the Rear Face and Sting of the Planetary Probe in the LENS Facility in Runs 22, 29 & 33 at "Match Point" Case E, including Measurements from HEG Run 132
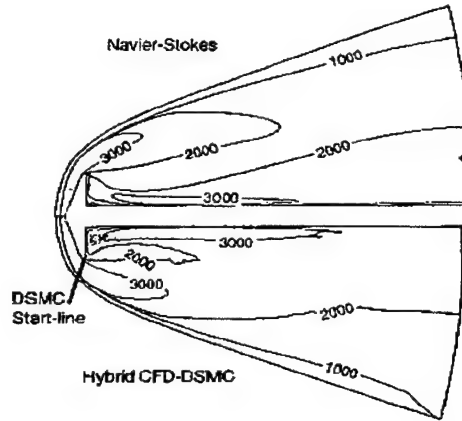
Figure 2-44 Flowfield Map Defining the Regions where Navier-Stokes and DSMC Calculations have been Overlapped for the Decoupled Navier-Stokes/ DSMC Computations Performed at Cornell
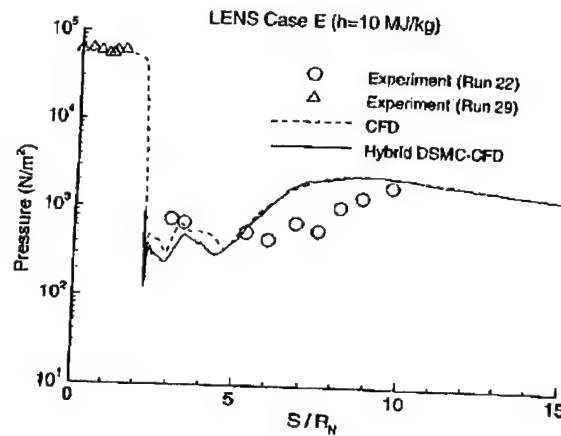
Figure 2-45 Comparison Between Pressure Measurements on Planetary Probe and Sting Configuration for LENS Case E and Calculations performed at Cornell Employing Decoupled Navier-Stokes/DSMC Calculations
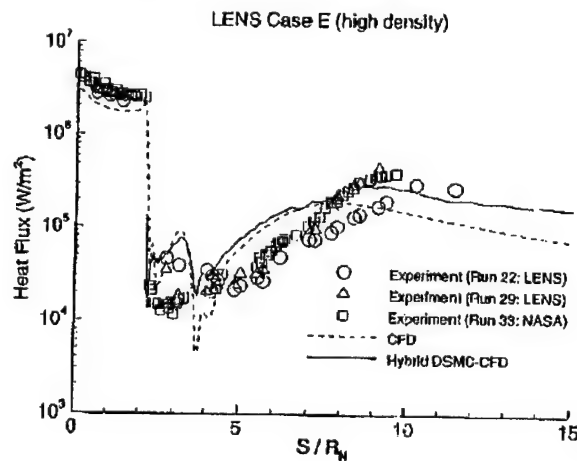
Figure 2-46 Comparison Between Heat Transfer Measurements on Planetary Probe and Sting Configuration for LENS Case E and Calculations Performed at Cornell Employing Decoupled Navier-Stokes/DSMC Calculations

3 EXPERIMENTAL STUDIES OF REAL GAS EFFECTS OVER A BLUNTED CONE/FLARE CONFIGURATION IN HYPERVELOCITY AIR FLOWS

SUMMARY
The experimental study presented in this chapter of the report was conducted to examine real gas effects in nonequilibrium flows developed in the contoured nozzle and over a spherically-blunted cone/flare configuration in the LENS hypervelocity shock tunnel. The research was conducted at velocities between 10,000 to 15,000 ft/sec for reservoir pressure conditions up to 700 bars. Both nitrogen and air used as the test gas provided the opportunity to examine the separate and combined effects of vibrational and chemical nonequilibrium. This experimental program was conducted in two phases. In Phase 1, which is reported later in Chapter 5, we examined the freestream flow close to the exit plane of the contoured nozzle employing the electron-beam technique coupled with spectrographic analysis of the flow using the OMA (Optical Multichannel Analyzer) and an infrared radiometer/spectrometer. Pitot pressure and stagnation point heating measurements were also made with survey rakes to examine the composition and spectral radiance of the freestream flow during the start-up, steady test time, and breakdown phases of the tunnel operation. Spectrographic data for N_2, NO and CO_2 were obtained to provide information on the vibrational temperature of the nitrogen and concentration of these species in the flow. Time-history records from photomultiplier measurements of the radiation from NO excited by an electron beam were compared with pressure records from pitot probes mounted in the flow to provide definitive information on the useable test time in the flow. The data was supported by similar radiometer measurements of data looking at CO_2 radiation. In Phase 2 of the study, described below, a large spherically blunted cone/flare configuration, which was highly instrumented with pressure and heat transfer gages, was tested in the LENS facility. The electron-beam apparatus was installed in the cone to obtain density and temperature measurements in the shock layer over the cone. Spectrographic measurements using the OMA were also made to examine the flowfield over the model. Measurements of the distribution of heat transfer and pressure over the model compared well with calculations made with a Navier-Stokes code incorporating models for vibrational and chemical nonequilibrium. Flowfield calculations were made to compare with measurements in the shock layer.

3.1 INTRODUCTION

Flight measurements of vehicle stability and heating levels on the Space Shuttle have demonstrated that real gas and viscous interaction effects can have a significant influence on vehicle performance; therefore, accurate prediction of such effects are very important. Experimental studies performed in ground-based facilities to provide detailed and accurate measurements of real gas effects with which to examine models of vibrational and nonequilibrium chemistry employed in the codes have proved difficult to perform because of stringent requirements to obtain chemically clean high temperature flows coupled with the sophisticated non-intrusive instrumentation required to measure gas chemistry in short duration flows.

Determining the properties of the freestream under high-enthalpy conditions, where chemical and vibrational nonequilibrium effects are important, represents a key part of the calibration of a hypervelocity facility. During the past four years, we have conducted a program of facility and instrumentation development designed to generate the environment and the measurement techniques to validate the real gas performance of the LENS

facility. A second major objective was to exploit the unique large scale, high-temperature and high-pressure capabilities of the LENS facility by performing studies where real gas effects coupled with complex viscous/inviscid interaction phenomena could be examined and compared with computational techniques which incorporate models with real gas effects. However, such an endeavor to obtain measurements with which to validate the models of vibrational and chemical nonequilibrium and dissociation employed in the numerical codes requires the development of sophisticated, accurate, and expensive non-intrusive diagnostic techniques.

A globally recognized problem exists in generating high temperature, chemically clean and well-defined, high-pressure hypervelocity flows at velocities above 4 km/sec in ground-based facilities. One approach for exploring this problem is to employ a standardized model with which to obtain comparative measurements in high-enthalpy facilities and compare this data with numerical simulations of the flow. For the past four years, a sting-mounted planetary probe configuration has been employed as such a standard and has been tested in the LENS shock tunnel and a number of other large hypervelocity test facilities. The measurements made in these studies have been compared with each other and with computations using state-of-the-art DSMC and Navier-Stokes methods. One such effort is reported in Reference 1.

The blunted cone/flare configuration designed for the program described in this report is a second generation model whose geometry and size provide a relatively simple flowfield environment. In the developed flow, we can examine the chemical and vibrational nonequilibrium of the gas in the shock layer as it expands around the spherical nose, relaxes along the 15 degree cone, and is recompressed over the flare, where a small separated region is formed. Here we describe: (1) the design of the two experimental studies; (2) the preparation of the experimental facility to obtain clean nonequilibrium flows; (3) the models and the instrumentation employed in each phase of the study; (4) the major diagnostic tools (e.g., electron-beam apparatus, the infrared spectrometers/radiometers, and the Optical Multichannel Analyzer (OMA); (5) measurements of the freestream properties in the exit plane of the nozzle, with particular emphasis on the measurement of run time; (6) the measurements of the distribution of heat transfer and pressure over the spherically-blunted cone/flare model and comparison with pretest predictions made with the nonequilibrium Navier-Stokes code; and (7) calculations of the distribution of properties in the shock layer over the body and comparison with the experimental measurements.

3.2   EXPERIMENTAL PROGRAM

3.2.1 Program Objectives and Design

The design of the blunted cone/flare model and the selection of test conditions for the experimental program were supported with detailed computations performed by Boyd and George using a Cornell Navier Stokes code (Reference 2) which incorporates vibrational nonequilibrium and flow chemistry. Selecting the size of the model represents a compromise between allowing time for the flow to chemically relax along the cone and

achieving a Reynolds so large that the boundary layer becomes transitional and, therefore, becomes unpredictable. Both the flat plate and cone flare models must also be large enough to incorporate the electron-beam apparatus. The program was designed to obtain measurements with both air and nitrogen as the test gas for freestream velocities between 10,000 and 15,000 ft/sec so that we could generate a range of levels of vibrational and chemical nonequilibrium in the freestream and shock layer over the model. In this program, we sought first to examine the flowfield characteristics and composition at the exit plane of the nozzle. Here, we employ the electron-beam technique coupled with spectrographic and radiometer measurements to identify the characteristics of the flows and the levels of vibrational and chemical nonequilibrium. Measurements were made for both nitrogen and air flows to examine the separate and combined effects of vibrational nonequilibrium, oxygen dissociation and chemical non-equilibrium of the flow. Flowfield surveys across the exit plane of the nozzle were made with pitot pressure stagnation point heat transfer gages and cone pressure probes.

The studies of the freestream characteristics were followed by the installation of the large blunted cone/flare model, which was highly instrumented with pressure and heat transfer gages. Measurements of the distribution of heat transfer and pressure over the model were made for a range of freestream test conditions in both nitrogen and air flows. The electron beam apparatus was then installed in the conical section of the cone/flare model and the chisel probe, containing a chain of photo multipliers focused at three stations across the shock layer, mounted on the side of the cone. The OMA, fitted in a vacuum-tight box, was re-deployed in the test section to obtain spectrographic data just upstream of the measurement stations for the electron beam.

3.2.2 Experimental Facilities

The experimental studies were conducted in the LENS facility which is described in subsection 2.2.2. The velocity/altitude performance of the LENS facility is shown in Figure 3-1, with annotations giving the points where the tunnel is calibrated for helium operation.

3.2.3 Models and Instrumentation

There were two basic models constructed for this study. The first was a flat plate model that housed the electron beam and probe assembly employed in the freestream diagnostic studies. The second, the spherically blunted cone/flare model, was used in the studies of nonequilibrium flow, evaluating the thermal and chemical models employed in the Navier-Stokes codes. Both of these studies were conducted with the contoured D nozzle (Reference 3).

3.2.3.1 Freestream Survey Model and Instrumentation

A photograph of the model housing the electron beam and supporting the photomultiplier diagnostic unit and the pitot pressure and total heat transfer probe assembly is shown installed in the test section of the LENS

42

shock tunnel in Figure 3-2. A schematic diagram showing how the 50 kV electron-beam apparatus is installed in the "ship model" is shown in Figure 3-3. Here it can be seen that a small double-wedge extension has been fitted onto the flat plate to bring the beam through the boundary layer. A single electromagnet system fitted above the cathode has been especially designed to focus the beam to a small diameter at the point where it enters the tunnel flow. The beam passes through a very small hole (~50μm diameter) in a graphite diaphragm which allows electrons to leave the gun but effectively isolates its interior from the flow in the test section. This minimized electron beam attenuation within the gun due to back-streaming of the test gas into its interior. Two turbo-molecular pumps are used to evacuate the gun and maintain a sufficiently good vacuum for a directly heated tungsten filament to be used as the cathode and survive even with pressures of some tens of Torr in the test flow. As shown in Figure 3-4, the Faraday cup is attached to a telescoping sting to capture the beam and record the current. The cup is retracted outside of the exit plane of the nozzle just prior to the run. Pitot pressure and total temperature probes are mounted downstream of the electron beam to record the conditions in the freestream.

"The spectrographic measurements made with the OMA (Optical Multichannel Analyzer) and the radiometer/spectrometer aero-optic instrumentation also formed key components of the non-intrusive diagnostics suite. The OMA is constructed from a moderate resolution spectrograph coupled to an intensified silicon diode array detector. The light integration time for the detectors is several milliseconds. The spectra from the vibrational bands can be fitted to obtain vibrational temperature in addition to providing a detailed knowledge of the chemical composition of the flow. A schematic diagram of the OMA is shown in Figure 3-5. A photograph of the OMA encased in a vacuum-tight housing is shown in Figure 3-4. The infrared radiometer/spectrometer apparatus is shown schematically in Figure 3-6. The InSb detector used in the radiometer has a 1 mm diameter sensing element with a 30-degree cold Field of View (FOV) aperture. The 60-degree off-axis parabolic mirror has a 152.4 mm focal length and is designed for operation with a 50 mm aperture. The spectrometer has a 32-element liquid nitrogen cooled InSb detector. The array can be spread across a 9 mm length. Each element has a dedicated amplifier so that all 32 channels can be recorded simultaneously.

3.2.3.2 Spherically Blunted Cone/Flare Model

The large spherically blunted cone/flare model used in Phase 2 of the real gas studies is shown installed in the LENS facility in Figure 3-7. The basic design of the large sphere/cone/flare configuration is shown in Figure 3-8. This configuration was selected by performing a series of calculations for a range of model geometries and freestream conditions to select a shape that would allow us to examine key nonequilibrium flow phenomena along the cone surface and in the recirculation region over the cone/flare junction. Shown in Figure 3-9 is the electron-beam apparatus installed just downstream of the spherical nosetip to provide measurements of the initial shock layer flow before it relaxes along the cone. Figure 3-10 shows the electron-beam positioned to obtain flowfield surveys in the separated region over the cone/flare junction. The photomultiplier detection system is contained in a chisel-ended

cylindrical support system which is mounted to the side of the cone, as shown in Figure 3-11. The system is fitted with three slits so that the image of the beam is focused by the lens at three points across the shock layer along the electron beam axis. The intensity of the radiation from each station is recorded on separate optical trains and photomultiplier tubes. Experimental studies were designed to obtain measurements over a range of freestream conditions at velocities of between 3 and 4.5 km/sec employing both air and nitrogen as the test gas. Numerical solutions to the Navier-Stokes equations were obtained prior to the test program by Srinivasan and Boyd (Reference 7) for the cases studied in the experimental program. The instrumentation and data recording and reduction are discussed in subsection 2.2.3.

3.3   RESULTS AND DISCUSSION

3.3.1   Introduction

The development, application and interpretation of the non-intrusive measurement techniques employed to measure the freestream and shock layer properties, represent important and difficult tasks. However, under the high-enthalpy test conditions employed in these studies, meaningful measurements can be made only when flow contamination has been nearly eliminated. This is achieved during extensive preparations for this and other programs by reducing particulate from the diaphragms, and the melting, ablation and erosion of the reservoir and throat region of the tunnel to an imperceptible amount. Success is manifested by the lack of dimensional change or appearance of the reservoir or throat region of the tunnel which, in turn, reduces the dust in the test section to a negligible amount. These improvements allow us to employ thin film gages in the stagnation region of the flow on models which would otherwise experience gage erosion and require the use of coaxial heat transfer instrumentation.

In the development programs leading up to these studies, infrared spectrometers and radiometers were employed to monitor the efforts to generate contamination-free flows. These investigations were followed by the development and use of electron beam and laser diagnostics to measure test time and real gas effects where the emphasis shifted to instrument calibration and interpretation of the time histories. While we employed a number of techniques to examine the characteristics of the freestream, the electron beam and OMA spectrometer were the only non-intrusive diagnostics employed in the studies with the spherically blunted cone/flare model.

3.3.2.   Measurements of the Freestream Characteristics for the Real Gas Studies

During preparations for the studies of real gas effects on the flowfield over hypervelocity vehicles, a number of non-intrusive diagnostics were employed, including infrared and visible spectrometry, infrared radiometry, laser diode, and electron-beam techniques. The measurements using the infrared spectrometer proved particularly useful in identifying some of the important constituents of the freestream during flow establishment, steady run time, and flow breakdown. The infrared spectrometer forms one of the components of the Aero-

Optics/Radiation Instrumentation Suite (Reference 4) and is shown in Figure 3-12 mounted on a small optical bench supported above the aero/optical instrumentation. The instrument is shown schematically in Figure 3-6. Figures 3-13, 3-14, and 3-15 show typical plots that were obtained of the time history of the intensity of the spectral radiance during the startup, steady run time, and flow breakdown as a function of wavelength. These measurements, as well as those from other optical diagnostics, show that the onset of flow in the test section is accompanied by a flash of broadband radiation. This flash, we believe, results from the initial high pressure ratio shock as it propagates into the low-pressure flow in the test section. Similar observations are found with high speed Schlieren, holography and imagery systems.

Following the flash is a period of steady radiation terminated by the arrival of the expansion fan from the driver, closely followed by the driver gas. A highly luminous flash is then observed by all the diagnostics which, we believe, is caused by the radiation due to the reflected shock region as the flow hits the back of the test section. This region of highly luminous gas, possibly comprised of burning residual dust particles swept from the sides of the tank, envelope the model well after the steady run. The variation of the spectral radiance with wavelength during the starting process, shown in Figure 3-16, suggests continuum short wavelength radiation, which could result from glowing particulate coupled with water at 2.7 μm and the CO_2 band at 4.3 μm. In contrast, the variation of spectral radiance from the freestream during the steady run (Figure 3-17) shows little radiation in the 3-4 μm band, but the persistence of radiation is probably from the 380 ppm levels of CO2, with which the synthetic air was seeded to simulate its normal concentration in air. The radiation at wavelengths of greater than 5 μm could result from NO emitting in its vibrational band. The variation of band radiance with time obtained by integrating the spectrometer data is compared with that obtained with the infrared radiometer in Figures 3-18 and 3-19. There is very good agreement between radiation intensity measurements from the two different instruments. Again the time history records are found to be in agreement with other tunnel diagnostics as shown in Figures 3-20 and 3-21, where we show the time history from the radiation of CO2 compared with a record of the pitot pressure measured in the test section. These measurements suggest that the end of the test gas occurs at a time very close to the arrival of the expansion fan from the back of the driver.

The electron beam and OMA were employed together to examine the density and temperature of the freestream, the rotational and vibrational temperature of nitrogen, and the spectra and concentration of NO. The OMA was also used to monitor the level and source of the background radiation, and we attempted to identify the end of the useful test time by identifying the appearance of the driver gas, helium, in the test section by exciting the gas with the electron beam. For the studies of freestream properties, one of the two optical trains in the chisel probe was focused on the electron beam while the second was focused on the flow ahead of the beam to measure the level of background radiation. Good quality spectra were obtained for both the N_2 (2+) band and NO showing the classical band structure. The relative intensities of the lines suggest temperatures very close to the computed value of 1,200 °R. We also observe that during the tests there is a relatively low level of background radiation.

45

Focusing the photomultiplier train on the NO band, we obtained the trace shown in Figure 3-22a which can be compared with pilot pressure measurements made at the same time in Figure 3-22b. While we are unable to explain the relatively slow rise in the concentration measurements, we did observe the rapid disappearance of NO when the pitot records indicate the run is ending. While the radiation levels from NO were well above those of the background, we did not experience a similar success with He. We were unsuccessful in detecting the arrival of the He driver gas with the electron beam apparatus. While calibrating the electron beam to obtain density measurements in N_2 is a relatively simple matter, calibration to determine NO concentration is not. Simply, the electron beam interacts with NO in a static calibration chamber dissociating it, hence changing the concentration of NO along the beam. The lesson learned is that, in future programs, we must calibrate the beam in rapidly flowing gas so that the reactants do not radiate in the volume focused on the photomultiplier.

3.3.3 Real gas Studies with the Large Sphere/Cone/Flare Configuration

3.3.3.1 Introduction

The studies with the large spherically-blunted cone/flare configuration were conducted in two phases. In Phase 1, we employed a model highly instrumented with heat transfer and pressure gages to obtain detailed surface distributions for a range of freestream conditions at velocities between 10,000 ft/sec and 15,000 ft/sec for both nitrogen and air flows. In Phase 2, non-intrusive measurements of the flow were made using optical techniques. The electron beam gun and its associated pumping and electrical apparatus, together with photomultiplier detection systems, were then installed into the model. The OMA was also reconfigured to obtain measurements at and just upstream of the electron beam station.

The spherically-blunted cone/flare configuration, shown in Figure 3-23, was fully instrumented with heat transfer and pressure gages. The positions are illustrated in Figure 3-24 and tabulated in Table 3-1. The instrumentation density in the region in the immediate vicinity of the cone/flare junction was increased to detect and quantify the presence of a laminar separated region. We also maintained a high instrumentation density along the flare to accurately quantify the reattachment compression region. The compression region acts like a recirculation region in that it probably is more sensitive to real gas effects.

Phase 2 of the study was dedicated to the electron-beam survey of the flowfield. Although we recorded the outputs from the surface instrumentation, the disturbances from the chisel photomultiplier unit (see Figure 3-11) could influence all but the data from the front of the model. For this phase, measurements were made with the electron beam positioned at the upstream station as shown in Figure 3-9.

46

3.3.3.2 Surface Heat Transfer and Pressure Measurements

Measurements of the distribution of heat transfer and pressure over the model were obtained for six test conditions. Total enthalpy conditions were 5 MJ/kg and 10 MJ/kg, with reservoir pressures of 270 and 500 bars, with both nitrogen and air used as the test gas. These conditions were selected to explore the effects of the Reynolds number, which influences the occurrence of transition and total temperature and pressure which, in turn, influences the flow chemistry. The test conditions for these studies are listed in Table 3-2. The measurements of the distribution of pressure and heat transfer on the model for each of the six test conditions are presented in Figures 3-25 through 3-30. Both the test conditions and the surface measurements are available from the first author in the CUBDAT database (Reference 7). Both the pressure and heat transfer measurements show that there is a small separated region at the cone/flare junction, which is laminar (the heat transfer decreases). From observations of the shape and magnitude of the heating distribution in the reattachment region, it is believed that the flow remains laminar in this region. Comparisons between the measurements of pressure and heat transfer at the 10 MJ/kg, 500 bar test condition with air and the Navier-Stokes calculations by Boyd and George are shown in Figures 3-3 1a and 3-3 1b. Here, we see that the calculations are in good agreement with pressure and heat transfer measurements on the sphere and cone. However, there is poor agreement, in particular with the heat transfer, in the separated region and on the flare. The grid resolution in this region is believed to be at least part of the problem and this will be examined further. Detailed calculations will also be made for both catalytic and non-catalytic wall conditions for each of the conditions studied.

3.3.3.3 Navier-Stokes Computations

In preparation for this experimental program, calculations (Reference 6) were made to select the test conditions for this study and the measurement stations for the surveys. Based on these studies, we selected a 10 MJ/kg and 500 bar pressure reservoir condition with air and nitrogen as the test gases. With nitrogen as the test gas, only vibrational nonequilibrium is of principal interest, whereas in air, oxygen dissociation and the shuttle reactions are of key interest. Calculations of the nonequilibrium flow over the spherically-capped cone/flare configuration were made at a 10MJ/kg and 500 bar test condition. Figure 3-32 shows a contour map of the flow over the sphere/cone section of the model illustrating the positions of the test stations to be employed in this experimental program. The magnitude of the vibrational nonequilibrium is shown in Figures 3-33 and 3-34 along the stagnation streamline and at Station 3. From these distributions, it is clear that Station 2 provides an opportunity to measure significant departures from the translational temperature. Predictions of the number density distributions along the stagnation streamline and across the shock layer at Station 2 are shown in Figures 3-35 and 3-36. Again at Station 2, there is a large variation in the levels of dissociated oxygen and NO which should provide a good environment for the experimental studies. Finally, Figures 3-37 and 3-38 show the variation of vibrational and translational temperature along the body, as well as the number density of the species in the shock layer close to

the body. Again, levels of non-equilibrium exhibited in these calculations should provide ample opportunity to examine the validity of the real gas effects in these flows.

3.3.3.4 Flowfield Pitot Pressure Measurements

The distribution of pitot pressure in and adjacent to the shock layer was determined with miniature six probe pitot pressure rake stations and at some downstream positions on the electron beam apparatus. The extreme heat loads developed on the small 0.063 diameter probes necessitated the development of heat shields which protect the gages from the thermal loads while allowing a frequency of close to 1 kHz. The response of the instrumentation mounted in the pitot pressure rake stationed in the freestream is shown in Figure 3-39, illustrating the start and finish of the run as the bow shock swept across the rake assembly. Of particular interest is the response of the probe stationed close to the position of the bow shock, which illustrates the adjustment in shock position towards the end of the 5 ms run.

The comparison between the measured and predicted distribution of pitot pressure across the shock layer is shown in Figure 3-40. This figure illustrates the good agreement consistent with the knowledge that the predicted shock shape is not a parameter which is sensitive to the models of real gas chemistry employed in contemporary Navier-Stokes codes.

3.3.3.5 Electron Beam Measurements of the Flow

The flow at Station 2 on the sphere/cone/flare model was investigated using the electron beam fluorescence technique. This station is at a plane axially 6.39 inches (0.162 m) from the nose of the model. Details of the 50 kV electron gun and its installation in the model have already been described in Sections 3.2.3.1 and 3.2.3.2. Optical measurements were made using a multi-channel radiometer and an OMA, from which the number densities of N_2 and NO and the rotational and vibrational temperatures of the flow in the shock layer were to be inferred. A series of supplementary experiments were also performed with this equipment to detect the time of arrival of the driver gas in the test region, and to ascertain the composition of any contaminants in the flow. The reduction and presentation of the results from this part of the study are quite lengthy, and Chapter 5 of this report is devoted to this area of study.

3.4 CONCLUSIONS

An experimental study was conducted to examine real gas effects in nonequilibrium flows developed in the contoured nozzle and over a spherically-blunted cone/flare configuration in the LENS hypervelocity shock tunnel. Tests were made at velocities from 10,000 to 15,000 ft/sec for reservoir pressure conditions up to 700 bars. Both nitrogen and air were used as the test gas, providing the opportunity to examine the separate and combined effects of vibrational and chemical nonequilibrium of nitrogen and air. This experimental program was conducted

in two phases. In Phase I of the study, we examined the freestream flow close to the exit plane of the contoured nozzle employing the electron-beam technique, coupled with spectrographic analysis of the flow using the OMA (Optical Multichannel Analyzer) and an infrared radiometer/spectrometer. Pitot pressure and stagnation point heating measurements were also made with survey rakes. The combination of these techniques enabled us to examine the composition and spectral radiance of the freestream flow during start-up, steady test time and breakdown phase of the tunnel operation. Spectrographic data for N_2 NO and CO_2, were obtained to provide information on the vibrational temperature of the nitrogen and concentration of these species in the flow. Time-history records from photomultiplier measurements of the radiation from NO excited by an electron beam were compared with pressure records from pitot probes mounted in the flow to provide definitive information on the useable test time in the flow. The data was supported by similar radiometer measurements of data looking at CO_2 radiation.

In Phase 2 of the study, a large spherically-blunted cone/flare configuration, which was highly instrumented with pressure and heat transfer gages, was tested in the LENS facility. The electron-beam apparatus was installed in the cone to obtain density and temperature measurements in the shock layer over the cone. Spectrographic measurements using the OMA were also made to examine the flowfield over the model. Measurements of the distribution of heat transfer and pressure over the model compared well with calculations made with a Navier-Stokes code incorporating models for vibrational and chemical nonequilibrium. Flowfield calculations were made to compare with measurements in the shock layer.

The measurements indicated that a small separated region is generated at the cone/flare junction and that, for most of the cases studied, the flow remained fully laminar along the flare. Navier-Stokes calculations of the distribution of pressure and heating along the model were in generally good agreement with the flow over the spherical nose and along the conical surface. However, these predictions did not resolve the measured heating levels in the separated region or the magnitude of the heating rise along the flare. Calculations are presented of the distribution of chemical species in the shock layer over the body for the high-enthalpy conditions at which these experimental studies were conducted. These calculations indicate a significant degree of vibrational and chemical nonequilibrium, which provide good resolution for the shock layer measurements.

3.5 REFERENCES

1. Holden, M. Harvey, J. Boyd, I., George, J., and Horvath T., "Experimental and Computational Studies of the Flow Over a
   Sting Mounted Planetary Probe Configuration," AIAA 97-0768, Reno, NV, January 6-10, 1997

2. Dietrich, S. and Boyd, I.D., "A Scalar Optimized Parallel Implementation of the DSMC Technique," *Journal of Computational Physics,* Vol. 126, 1996, pp. 328-342.

3.   Holden, M.S., "Large-Energy National Shock Tunnel (LENS) Description and Capabilities" Brochure, February 1991.

4.   Holden, M.S., Craig, J.E., Parker, R.A. and Kolly, J.M., "Studies of Nosetip and Seekerhead Performance at Velocities up to 5 km/sec at Duplicated Altitude Conditions," paper presented at the *6th DOD Electromagnetic Windows Symposium* at Redstone Arsenal, Alabama, October 17-19, 1995.

5.   Harvey J., Bergman, R.C. and Holden, M.S., "An Experimental Study of Hypersonic Turbulence on a Sharp Cone," AIAA-89-1866, Paper presented at the *AIAA 20th Fluid Dynamics, Plasma Dynamics and Lasers Conference*, Buffalo, New York, 12-14 June 1989.

6.   Srinivasan, A. and Boyd, I.D., "Design of Thermochemical Nonequilibrium Experiments for the LENS Hypersonic Facility, AIAA 95-2006, 29th *AIAA Thermophysics Conference*, San Diego, June 1995.

7.   Holden, M.S., Moselle, J.R., Sweet, S.J. and Martin, S.C., "A Database of Aerothermal Measurements in Hypersonic Flow for CFD Validation," AIAA Paper No. 96-4587, Norfolk, VA.

Velocity/Altitude Performance of LENS Facility
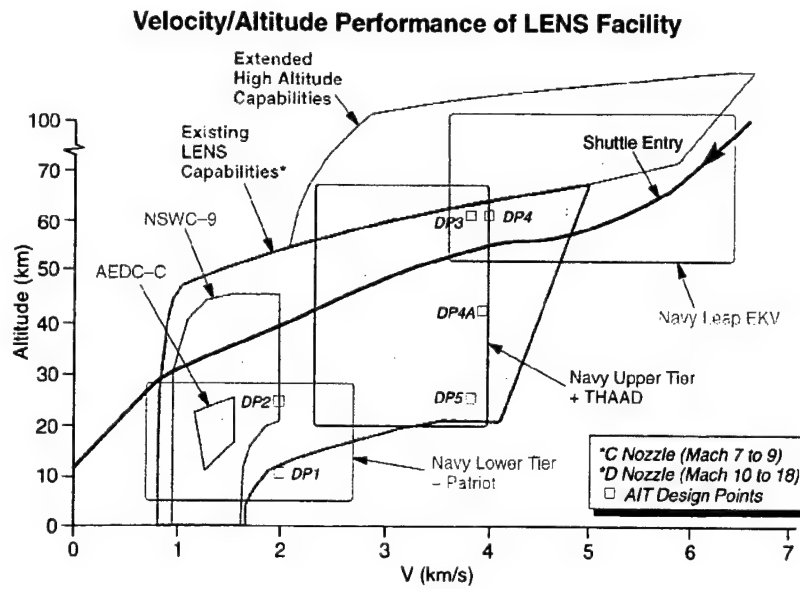
Figure 3-1 Velocity/Altitude Map for Upgraded LENS Facility
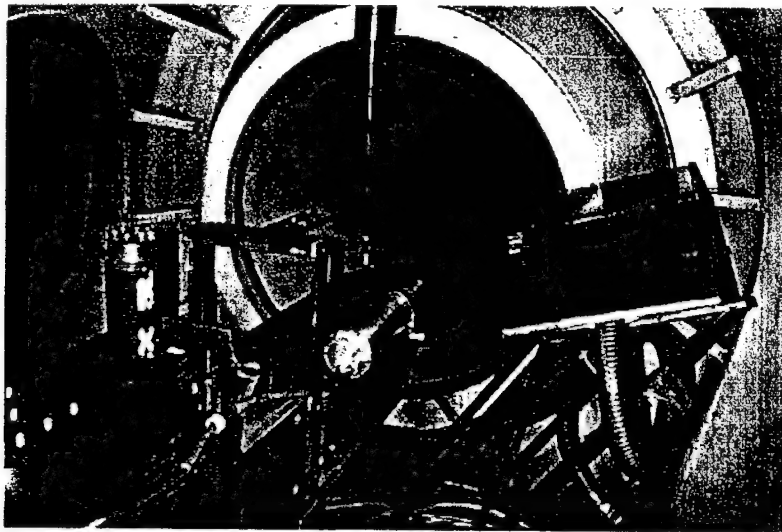
Figure 3-2 Photograph of Electron Beam Apparatus and Diagnostic Systems
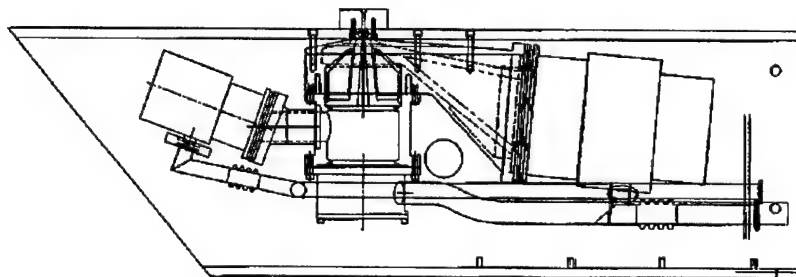
Figure 3-3 Electron-Beam Module Installed in the Flowfield Survey Apparatus

51
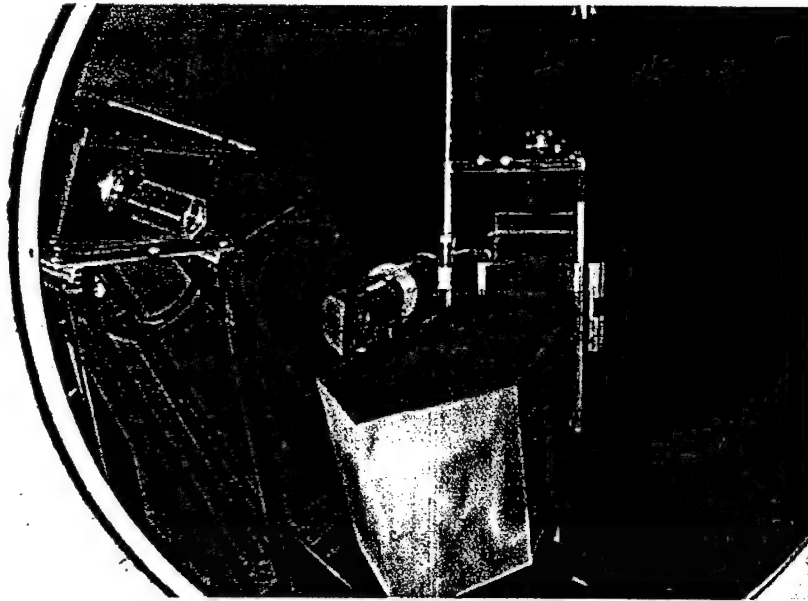
Figure 3-4 Electron-Beam and Spectrometer Flowfield Survey Apparatus Installed in the LENS Facility
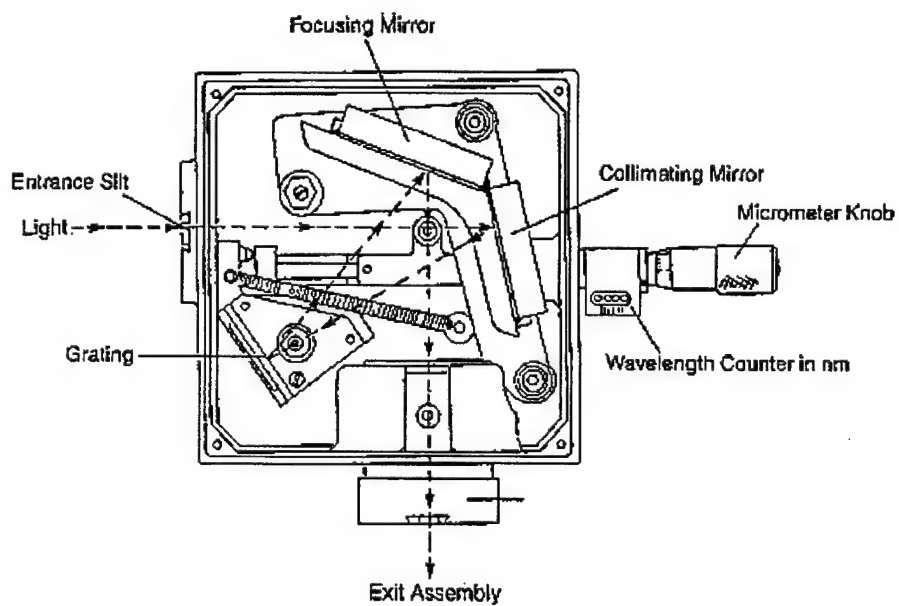
Figure 3-5 Schematic Diagram of the Optical Multichannel Analyzer (OMA)
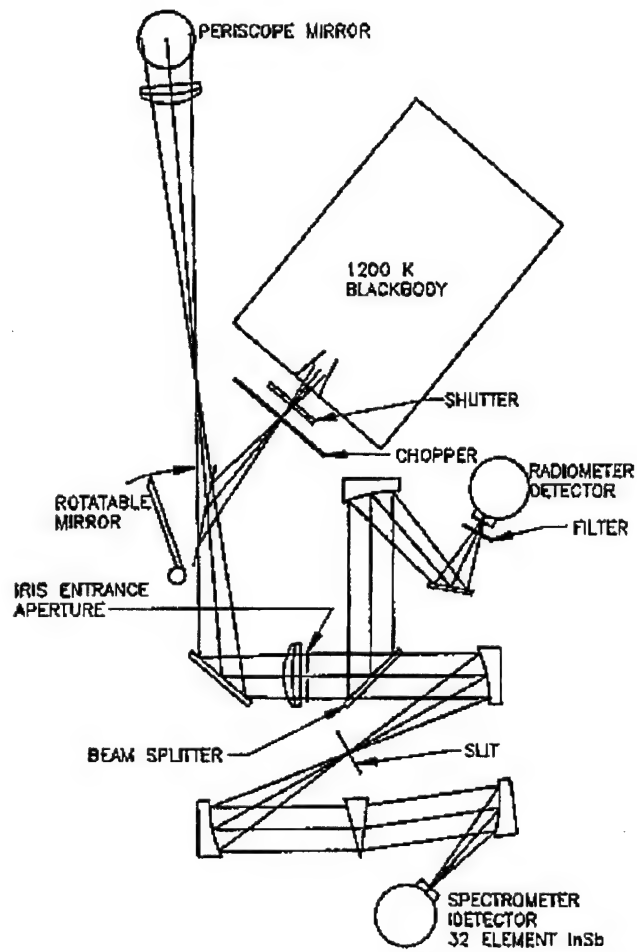
Figure 3-6 Major Elements and Layout of the Radiometer/Spectrometer System
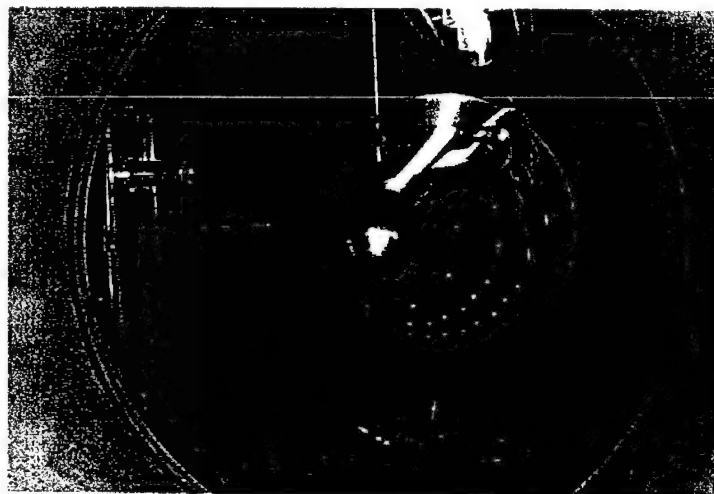
Figure 3-7 Cone/Flare Model in LENS Facility
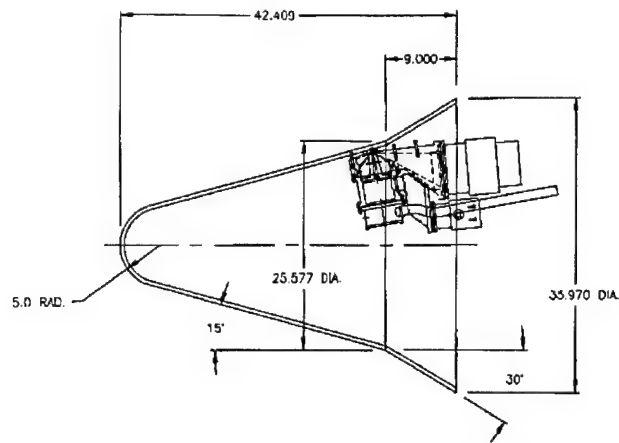
Figure 3-8 Schematic Diagram of Spherically-Capped Cone/Flare Configuration
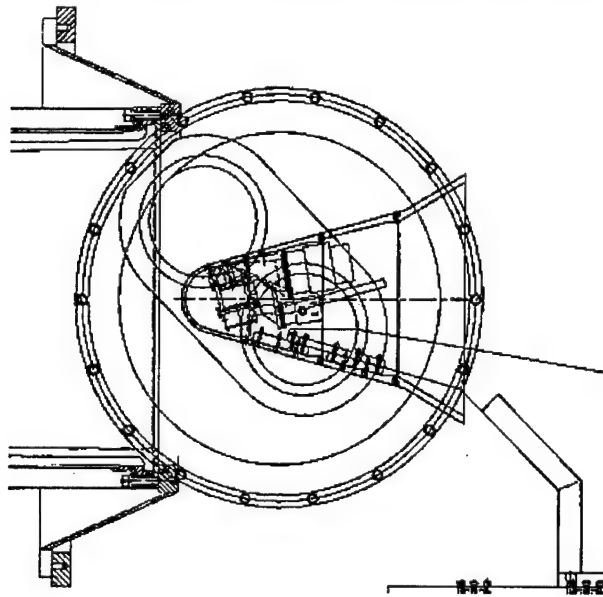
Figure 3-9 Electron-Beam Installed in Model at Station 2
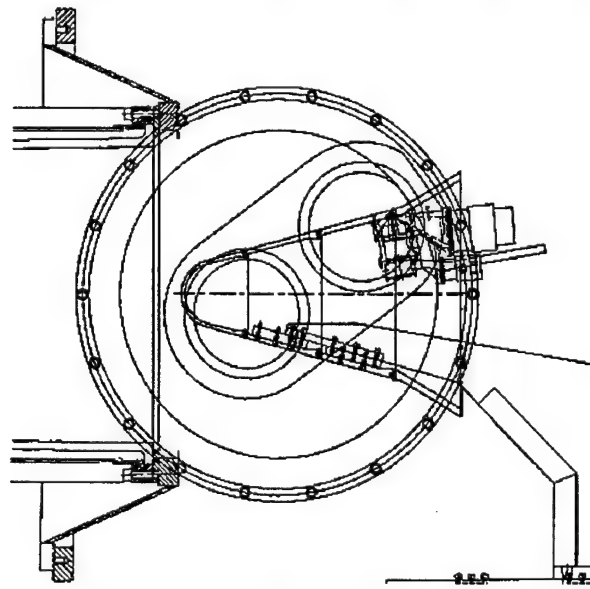
Figure 3-10 Electron-Beam Installed in Model at Station 3

54
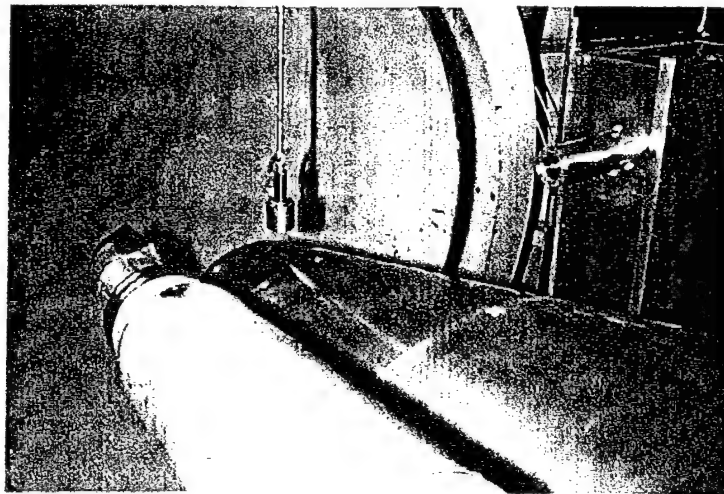
Figure 3-11 Chisel Probe Containing Photomultipler Diagnostics
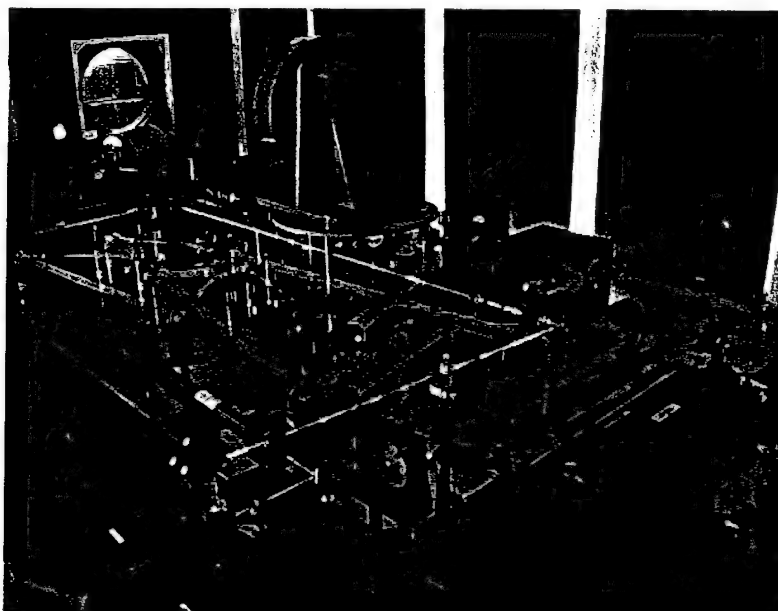
Figure 3-12 Aero-Optic/Radiation Instrumentation Suite
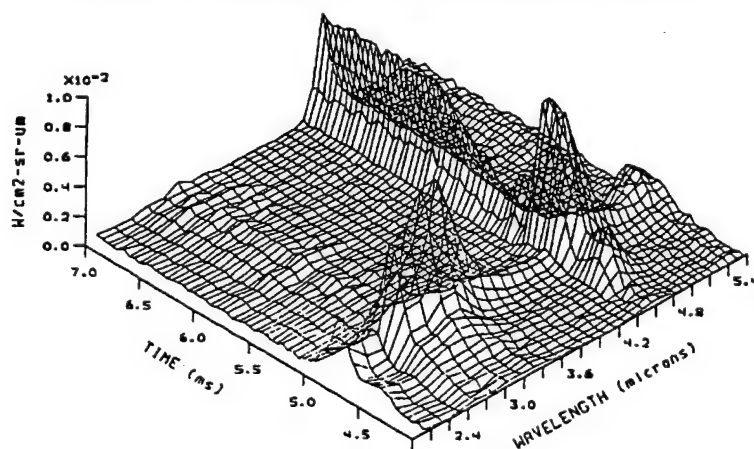
Figure 3-13 Spectral Radiance During Tunnel Starting

55
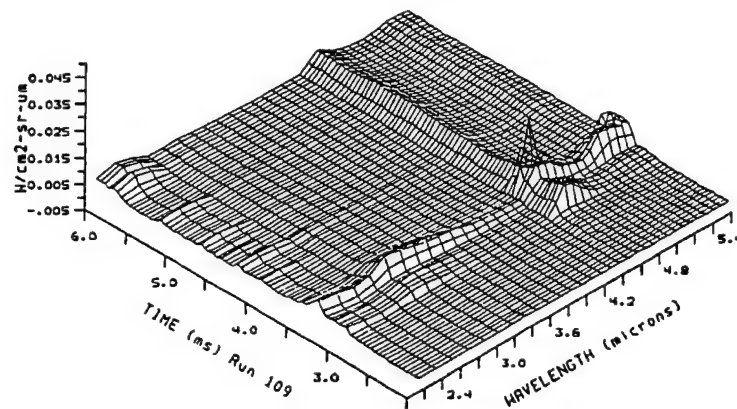
Figure 3-14 Spectral Radiance During Tunnel Run
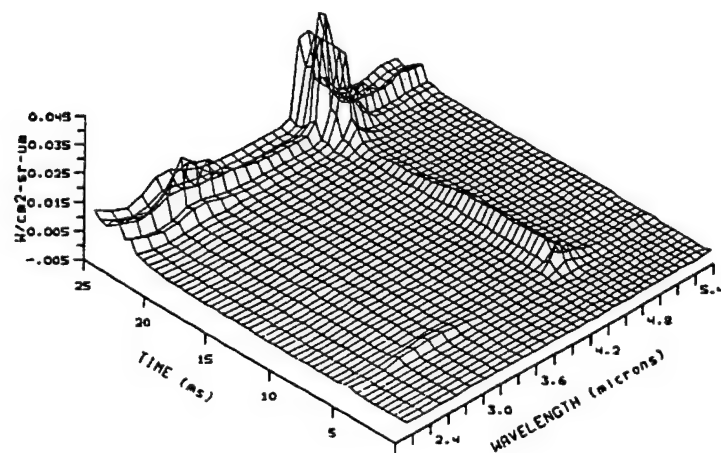
Figure 3-15 Spectral Radiance After Tunnel Run
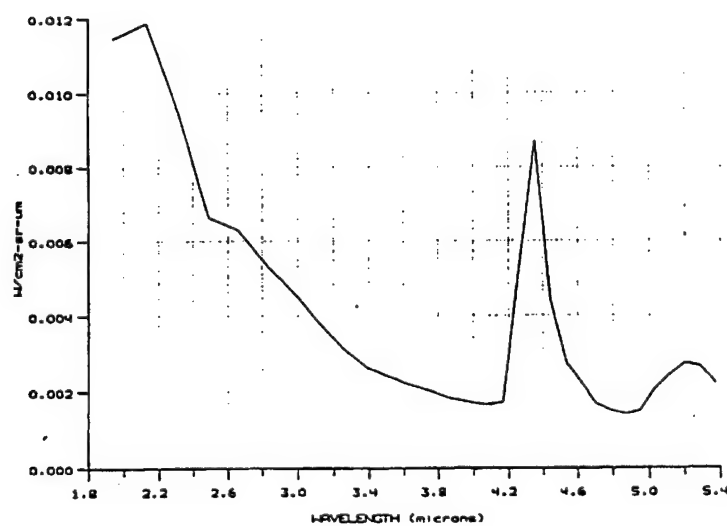
Figure 3-16 Spectral Radiance Measurement at Flow Start

56
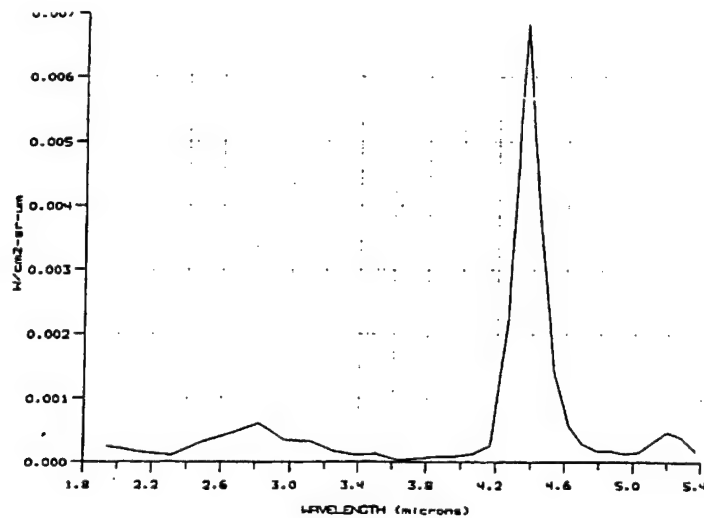
Figure 3-17 Spectral Radiance Measurement During Steady Test Time
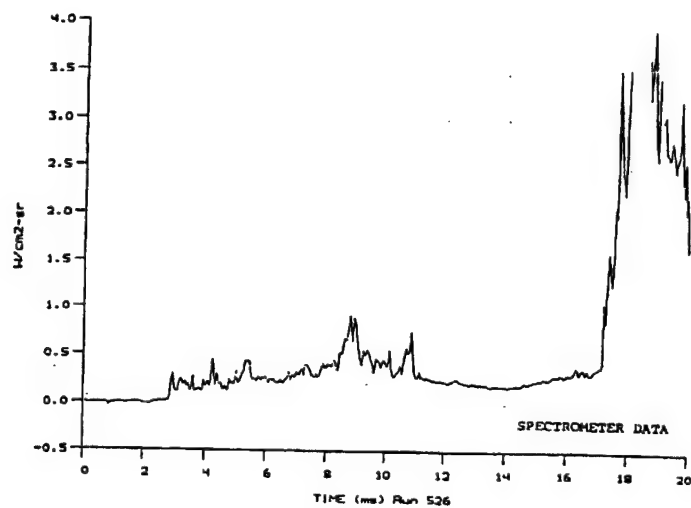
Figure 3-18 Time History of Integrated Band Radiance from Spectrometer
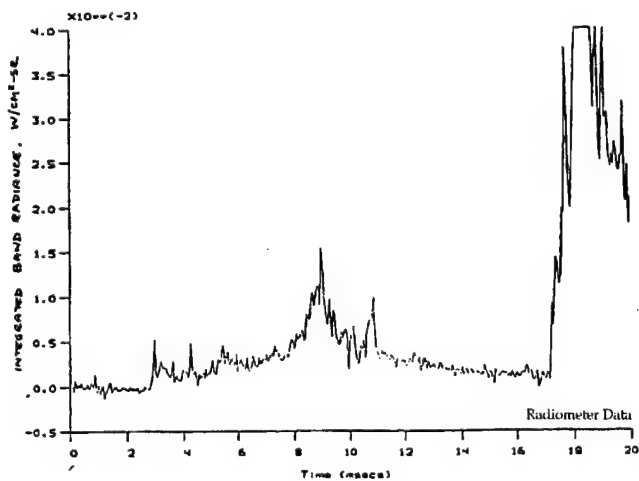
Figure 3-19 Time History of Integrated Band Radiance from Radiometer

57
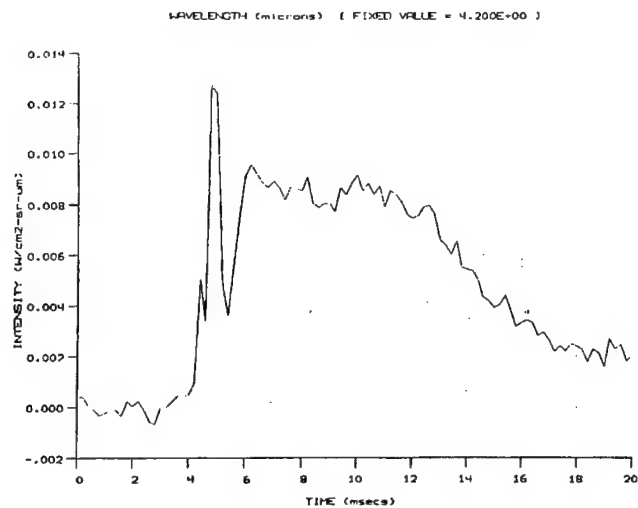
Figure 3-20 CO_2 Radiation Signal Time History
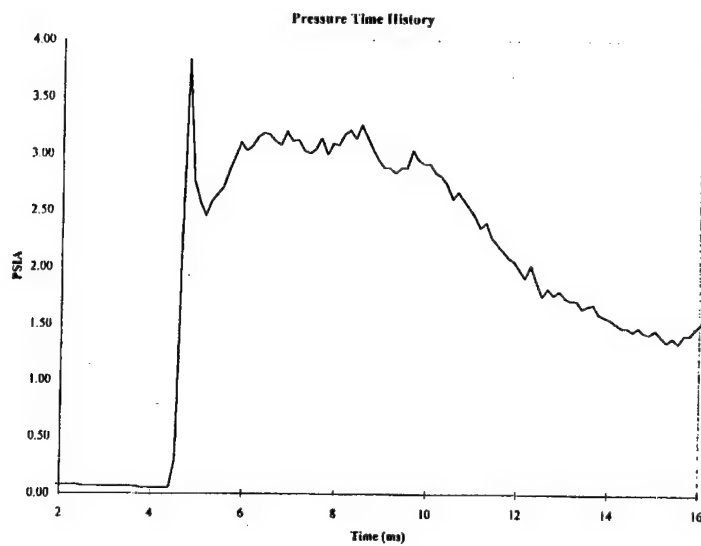
Figure 3-21 Pitot Pressure Measurement Time History
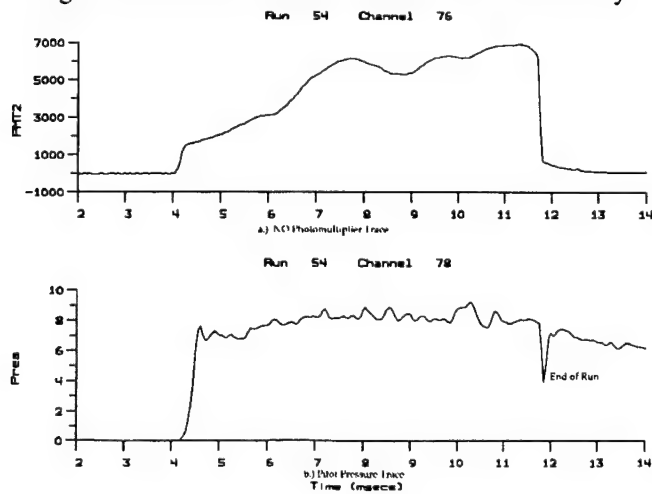
Figure 3-22 Photomultiplier Signals of NO Radiation

58

Model Configuration
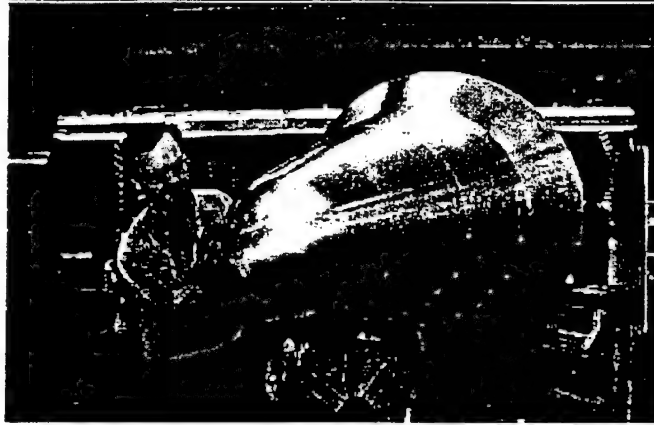
Figure 3-23 Large Sphere/Cone/Flare Configuration
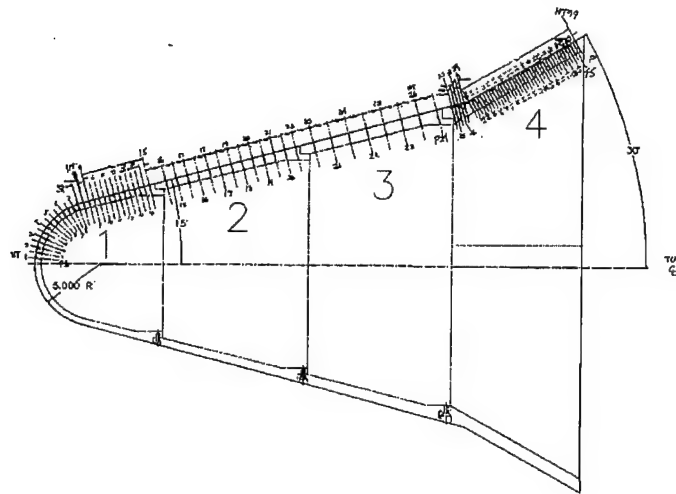
Figure 3-24 Locations of Pressure and Heat Transfer Instrumentation on Sphere Cone/Flare Model
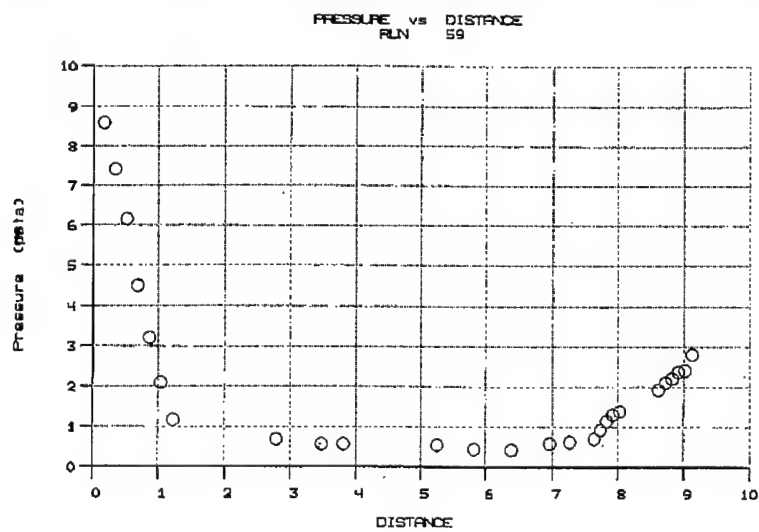
Figure 3-25a Distributions of Pressure (psia) Along Model for Run 59
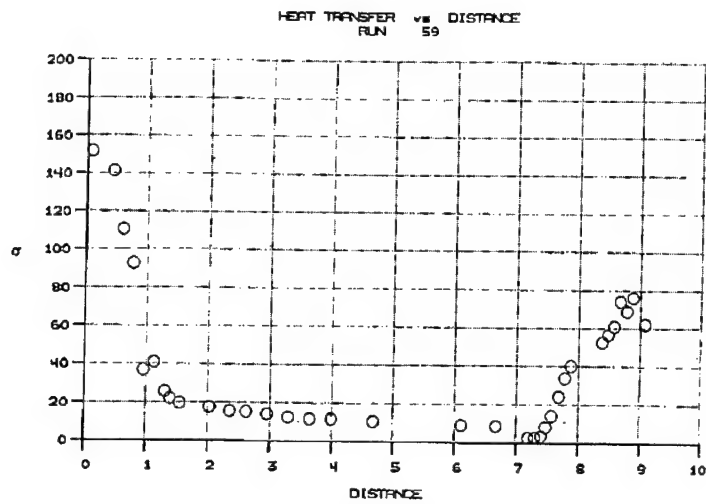
Figure 3-25b Distributions of Heat Transfer (BTU/ft²sec) Along Model for Run 59
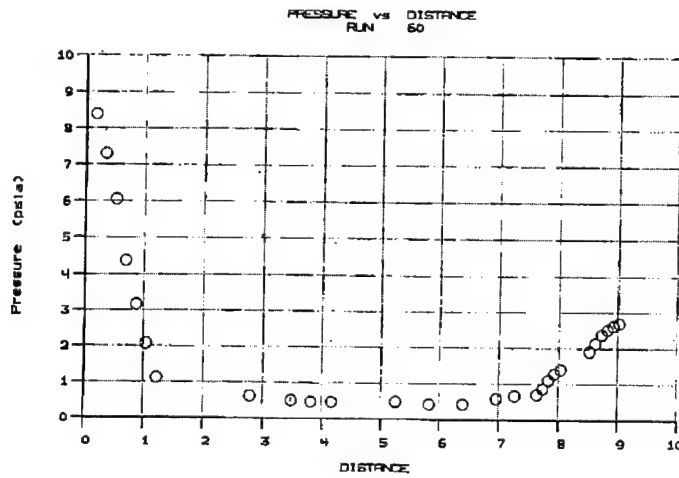
Figure 3-26a Distributions of Pressure (psia) Along Model for Run 60
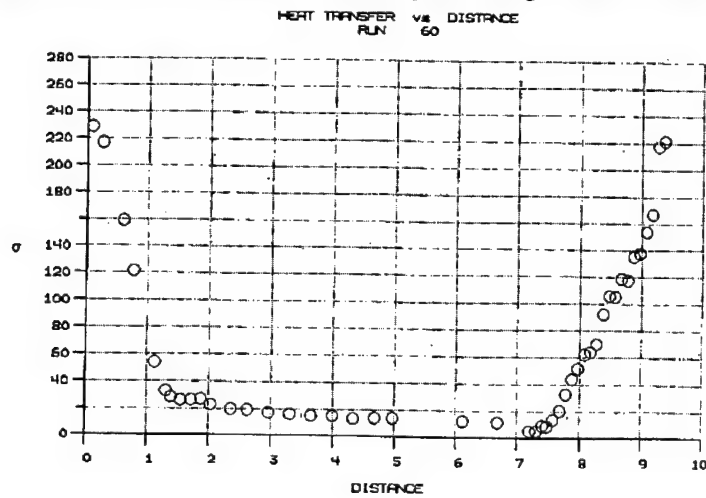
Figure 3-26b Distributions of Heat Transfer (BTU/ft²sec) Along Model for Run 60
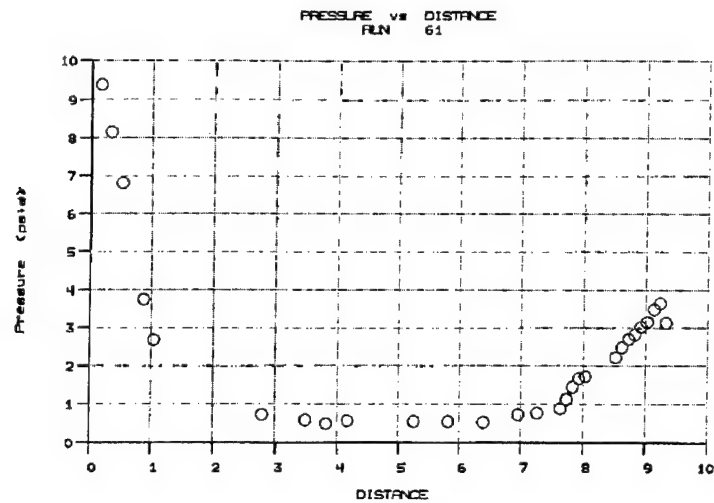
Figure 3-27a Distributions of Pressure (psia) Along Model for Run 61
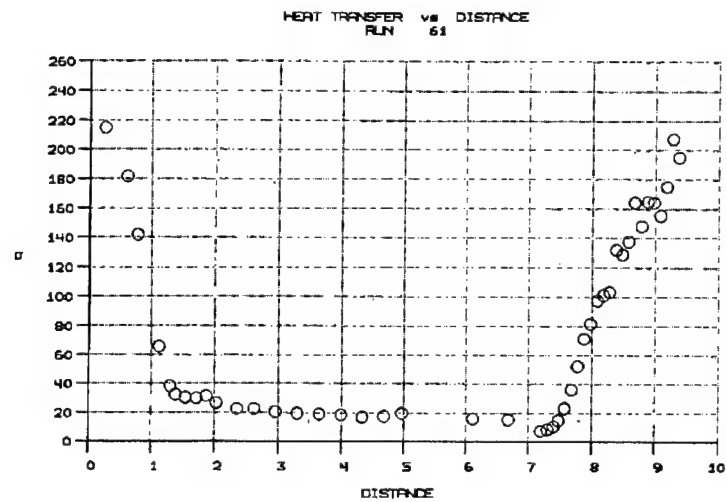
Figure 3-27b Distributions of Heat Transfer (BTU/ft^{2}sec) Along Model for Run 61
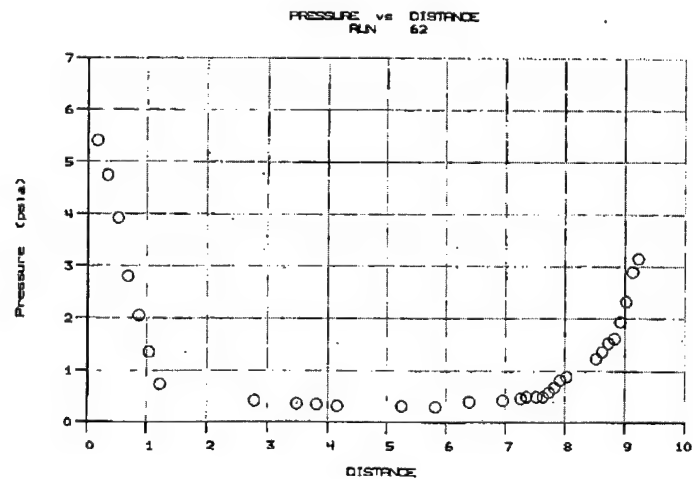
Figure 3-28a Distributions of Pressure (psia) Along Model for Run 62

61
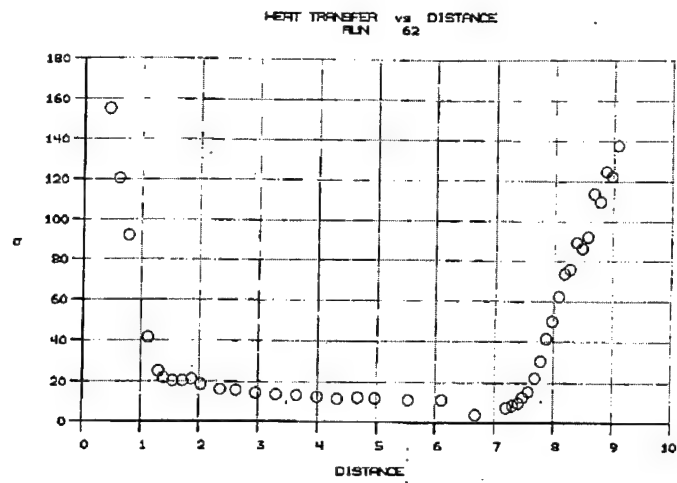
Figure 3-28b Distributions of Heat Transfer (BTU/ft²sec) Along Model for Run 62
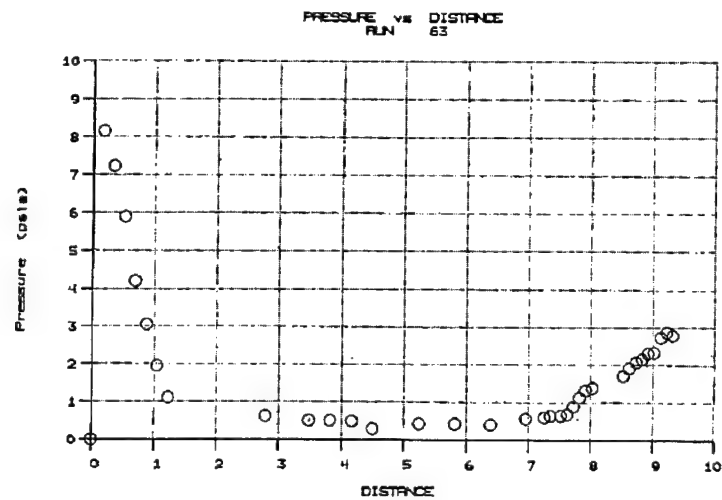
Figure 3-29a Distributions of Pressure (psia) Along Model for Run 63
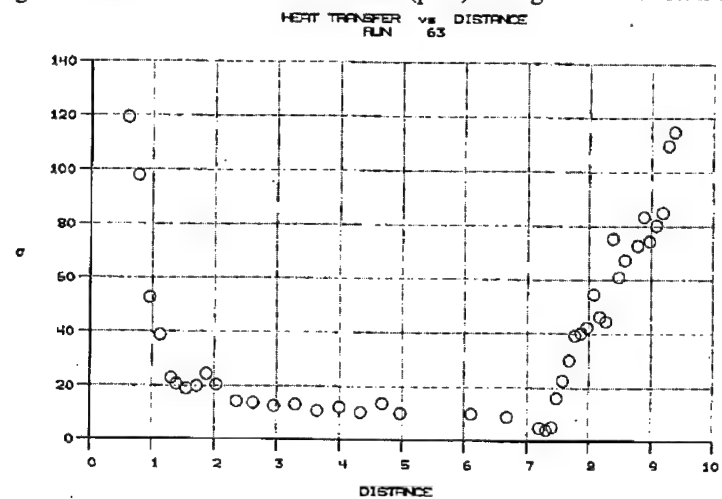
Figure 3-29b Distributions of Heat Transfer (BTU/ft²sec) Along Model for Run 63
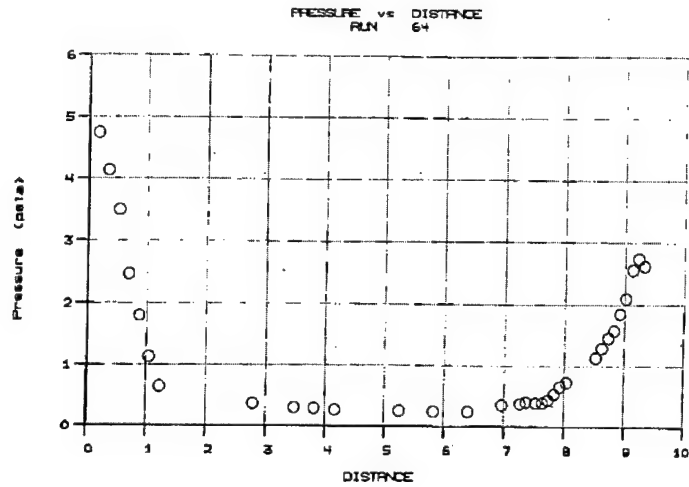
Figure 3-30a Distributions of Pressure (psia) Along Model for Run 64
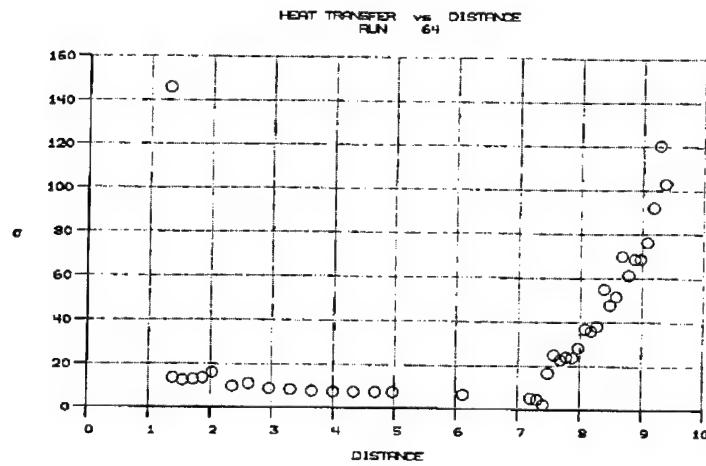
Figure 3-30b Distributions of Heat Transfer (BTU/ft²sec) Along Model for Run 64
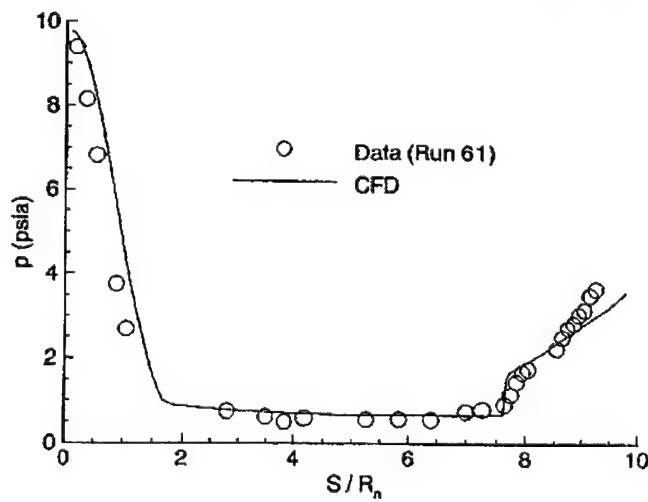
Figure 3-31a Comparison Between Navier-Stokes Code Calculations and Pressure Measurements for Run 61
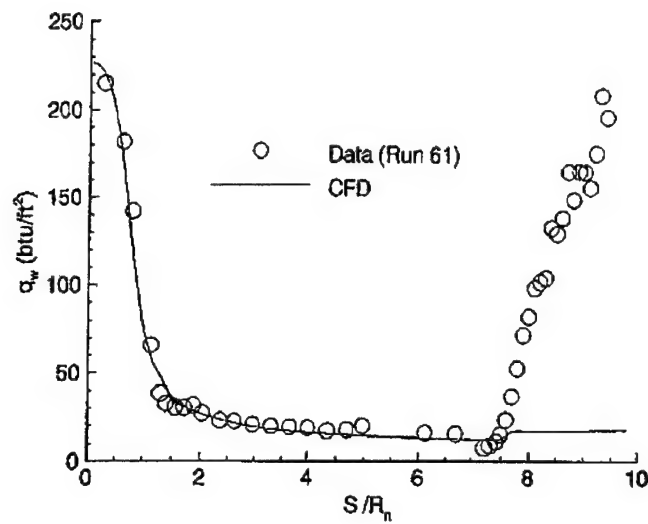
Figure 3-31b Comparison Between Navier-Stokes Code Calculations and Heat Transfer Measurements for Run 61
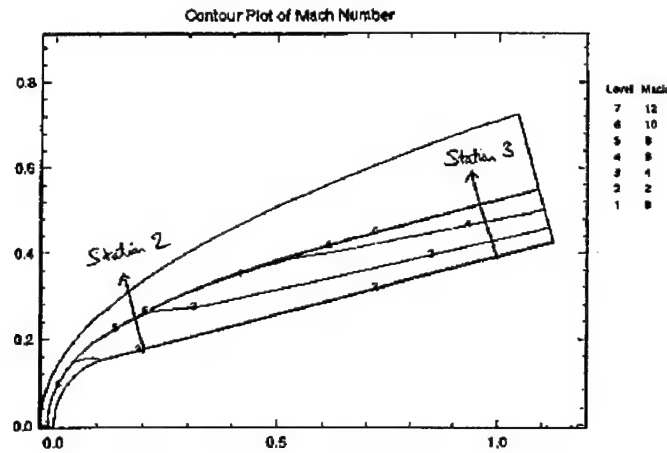
Figure 3-32 Mach Number Contours in Shock Layer and Measurement Stations on Model
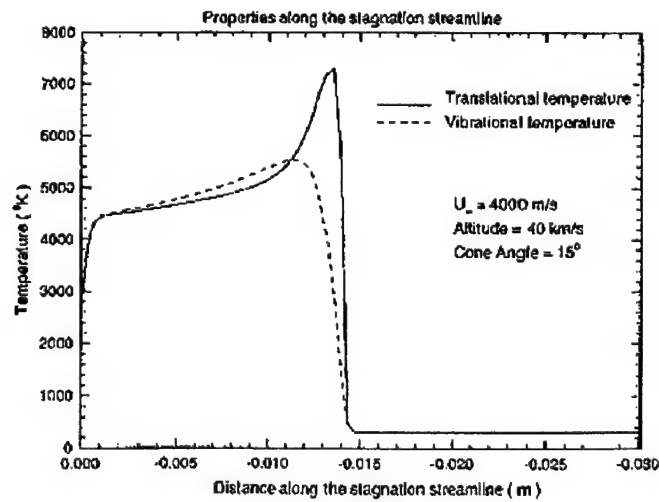
Figure 3-33 Temperature Distribution in Shock Layer Along Stagnation Streamline

64
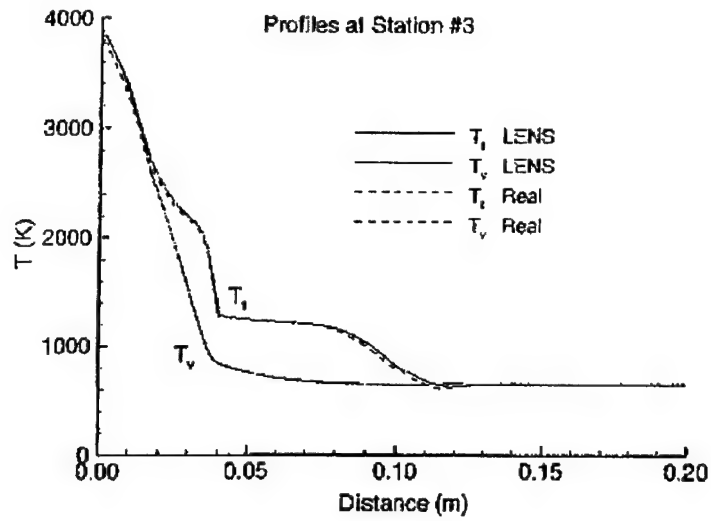
Figure 3-34 Temperature Distribution in Shock Layer Along Station 3
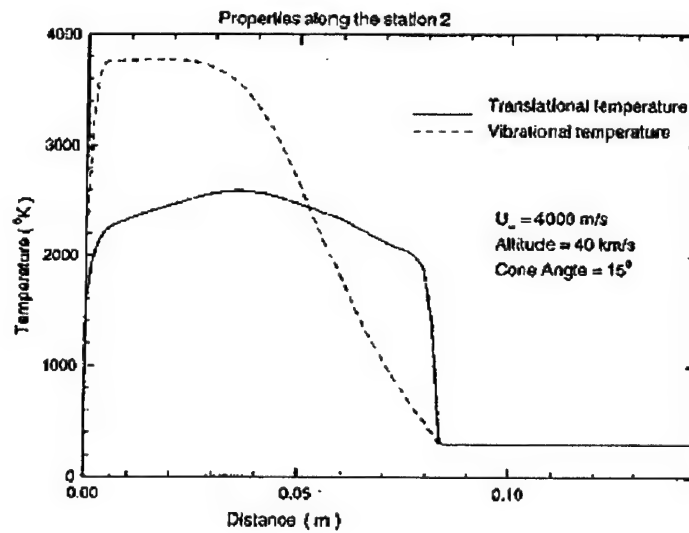
Figure 3-35 Temperature Distribution in Shock Layer Along Station 2
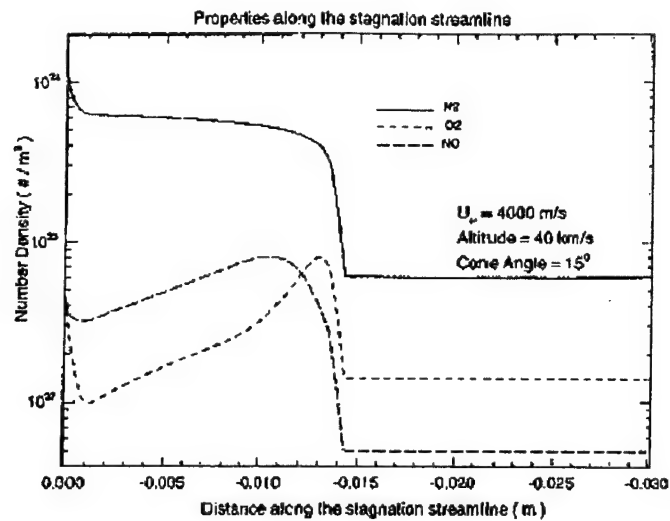
Figure 3-36 Distribution of Species Along Stagnation Streamline
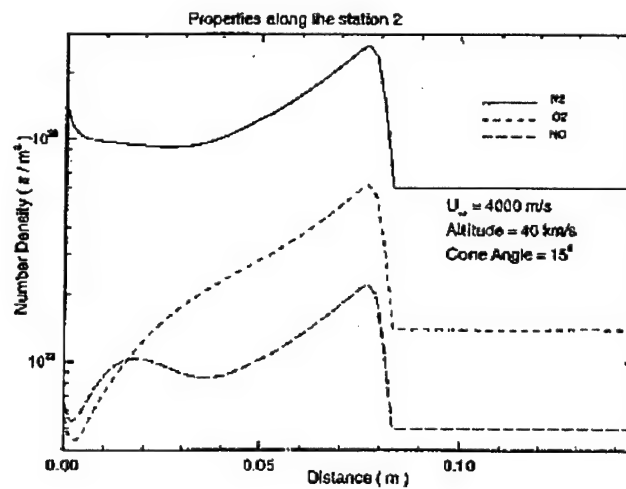
Figure 3-37 Distribution of Species Along Station 2
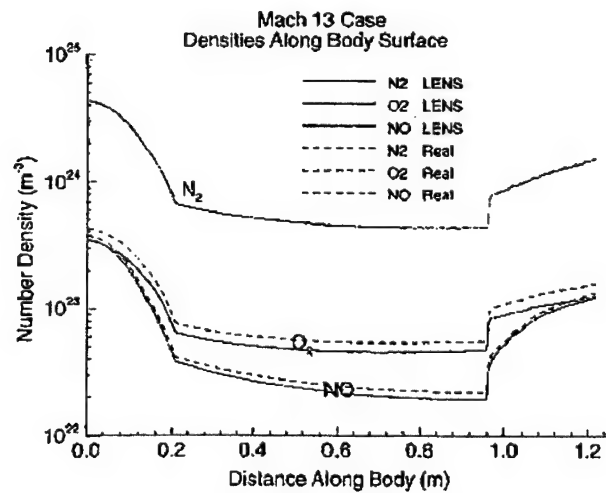
Figure 3-38 Distribution of Species Along Body Surface

66
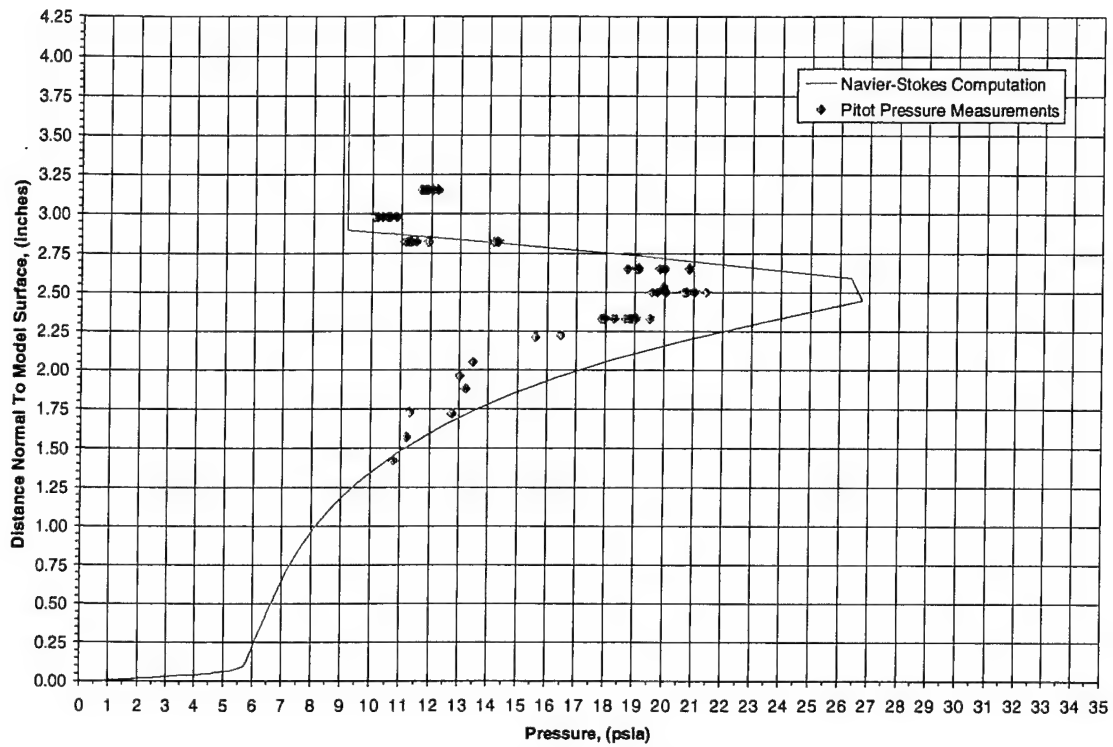
Figure 3-39 Comparison Between Measured Pitot Pressure and Computation Employing the Navier-Stokes Code
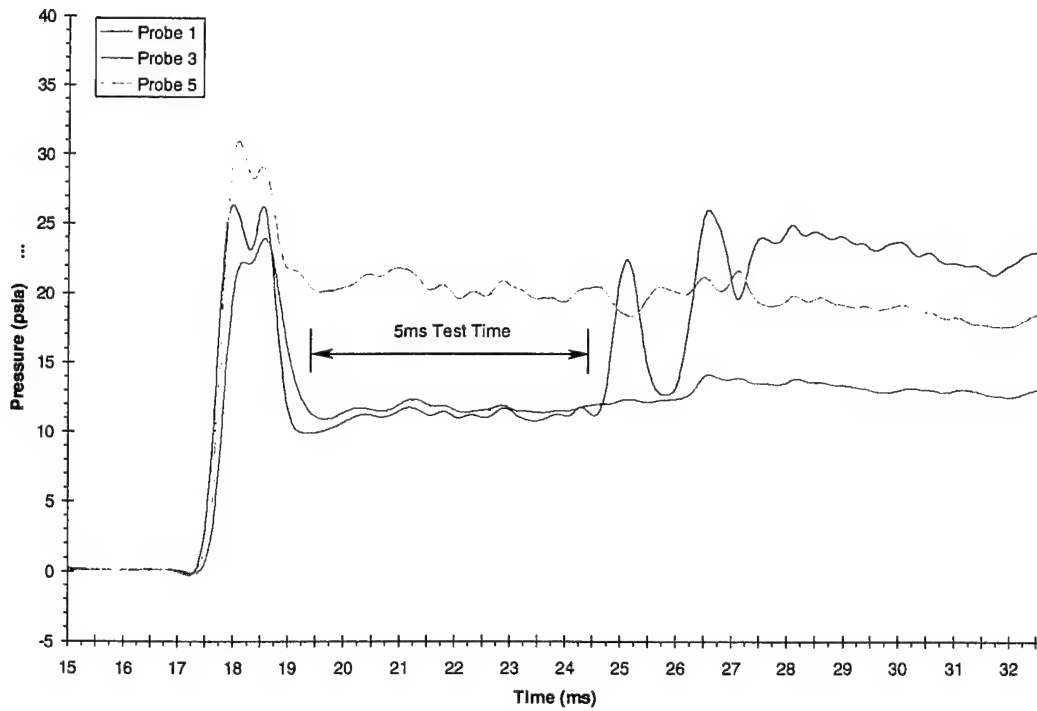
Figure 3-40 Time Histories of Pitot Pressure Instrumentation in Shock Layer Rake

67

Table 3-1
Gage Position of Spherically Blunted Cone/Flare
Configuration

Gage No.	S/Rn	Gage No.	S/Rn
P1	0	HT1	0.0873
P2	0.1745	HT2	0.2618
P3	0.3491	HT3	0.4363
P4	0.5236	HT4	0.6109
P5	0.6981	HT5	0.7854
P6	0.8727	HT6	0.9599
P7	1.0472	HT7	1.1345
P8	1.2217	HT8	1.3090
P9	1.4758	HT9	1.3958
P10	1.6358	HT10	1.5558
P11	1.7958	HT11	1.7158
P12	1.9558	HT12	1.8758
P13	2.1158	HT13	2.0358
P14	2.2758	HT14	2.1958
P15	2.7928	HT15	2.3558
P16	3.1372	HT16	2.6206
P17	3.4816	HT17	2.9650
P18	3.8260	HT18	3.3094
P19	4.1704	HT19	3.6538
P20	4.5148	HT20	3.9982
P21	5.2622	HT21	4.3426
P22	5.8302	HT22	4.6870
P23	6.3982	HT23	4.9782
P24	6.9662	HT24	5.5462
P25	7.2604	HT25	6.1142
P26	7.3604	HT26	6.6822
P27	7.5330	HT27	7.2104
P28	7.6330	HT28	7.3104
P29	7.7330	HT29	7.4104
P30	7.8330	HT30	7.4830
P31	7.9330	HT31	7.5830
P32	8.0330	HT32	7.6830
P33	8.1330	HT33	7.7830
P34	8.2330	HT34	7.8830
P35	8.3330	HT35	7.9830
P36	8.4330	HT36	8.0830
P37	8.5330	HT37	8.1830
P38	8.6330	HT38	8.2830
P39	8.7330	HT39	8.3830
P40	8.8330	HT40	8.4830
P41	8.9330	HT41	8.5830
P42	9.0330	HT42	8.6830
P43	9.1330	HT43	8.7830
P44	9.2330	HT44	8.8830
P45	9.3330	HT45	8.9830
		HT46	9.0830
		HT47	9.1830
		HT48	9.2830
		HT49	9.3830

Table 3-2
Test Conditions for Spherically Blunted Cone/Flare Studies

Run 59

Shock Mach Number	Mi	=	6.415
Reservoir Pressure	PO	=	7.541E+03 psia
Total Enthalpy	HO	=	6.1177+07 (ft/sec)**2
Stagnation Temperature	TO	=	8.2377E+03 degrees R
Freestream Mach No.	M	=	10.3836
Freestream Reynolds No.	Re	=	4.1219E+05 1/ft
Freestream Velocity	U	=	1.0812E+04 Ft/sec
Freestream Temperature	T	=	4.3636E+02 degrees R
Freestream Pressure	P	=	6.6858E-02 psia
Freestream Density	RHO =		1.2426E-05 slugs/ft/ft/ft
Pitot Pressure	Pitot =		9.2751E+00 psia
Wall Temperature	Twall =		5.318E+02 degrees R
Molecular Weight	MW =		28.0129
	N2 mole fraction = 9.999E-01		
	N mole fraction = .8.107E-05		

Run 60

Shock Mach Number	Mi	=	8.863
Reservoir Pressure	PO	=	7.322E+03 psia
Total Enthalpy	HO	=	1.1308E+08 (ft/sec)**2
Stagnation Temperature	TO	=	1.3103E+04 degrees R
Freestream Mach No.	M	=	9.2776
Freestream Reynolds No.	Re	=	1.5966E+05 1/ft
Freestream Velocity	U	=	1.4573E+04 Ft/sec
Freestream Temperature	T	=	1.0008E+03 degrees R
Freestream Pressure	P	=	8.1132E-02 psia
Freestream Density	RHO =		6.5634E-06 slugs/ft/ft/ft
Pitot Pressure	Pitot =		8.9296E+00 psia
Wall Temperature	Twall =		5.333E+02 degrees R
Molecular Weight	MW =		27.9641
	N2 mole fraction = 9.964E-01		
	N mole fraction = 3.561E-03		

Run 61

Shock Mach Number	Mi	=	9.23
Reservoir Pressure	PO	=	7.37E+03 psia
Total Enthalpy	HO	=	1.1807E+08 (ft/sec)**2
Stagnation Temperature	TO	=	1.1653E+04 degrees R
Freestream Mach No.	M	=	8.5298
Freestream Reynolds No.	Re	=	1.5051E+05 1/ft
Freestream Velocity	U	=	1.4503E+04 Ft/sec
Freestream Temperature	T	=	1.2062E+03 degrees R
Freestream Pressure	P	=	1.0292E-01 psia
Freestream Density	RHO =		7.0229E-06 slugs/ft/ft/ft
Pitot Pressure	Pitot =		9.5E+00 psia
Wall Temperature	Twall =		5.344E+02 degrees R
Molecular Weight	MW =		28.428
	N2 mole fraction = 7.361E-01		
	N mole fraction = 5.343E-11		
	O2 mole fraction = 1.572E-01		
	AR mole fraction = 9.152E-03		
	O mole fraction = 3.684E-02		
	NO mole fraction = 6.070E-02		

Run 62

Shock Mach Number	Mi	=	9.089
Reservoir Pressure	PO	=	4.121E+03 psia
Total Enthalpy	HO	=	1.1489E+08 (ft/sec)**2
Stagnation Temperature	TO	=	1.1174E+04 degrees R
Freestream Mach No.	M	=	8.6414
Freestream Reynolds No.	Re	=	9.4022E+04 1/ft
Freestream Velocity	U	=	1.4206E+04 Ft/sec
Freestream Temperature	T	=	1.1103E+03 degrees R
Freestream Pressure	P	=	5.7788E-02 psia
Freestream Density	RHO =		4.2454E-06 slugs/ft/ft/ft
Pitot Pressure	Pitot =		5.5E+00 psia
Wall Temperature	Twall =		5.376E+02 degrees R
Molecular Weight	MW =		28.1758
	N2 mole fraction = 7.299E-01		
	N mole fraction = 1.377E-10		
	O2 mole fraction = 1.471E-01		
	AR mole fraction = 9.071E-03		
	O mole fraction = 5.426E-02		
	NO mole fraction = 5.967E-02		

Run 63

Shock Mach Number	Mi	=	6.443
Reservoir Pressure	PO	=	7.411E+03 psia
Total Enthalpy	HO	=	5.7763E+07 (ft/sec)**2
Stagnation Temperature	TO	=	7.2363E+03 degrees R
Freestream Mach No.	M	=	10.3114
Freestream Reynolds No.	Re	=	4.5428E+05 1/ft
Freestream Velocity	U	=	1.0212E+04 Ft/sec
Freestream Temperature	T	=	4.076E+02 degrees R
Freestream Pressure	P	=	6.6676E-02 psia
Freestream Density	RHO =		1.3712E-05 slugs/ft/ft/ft
Pitot Pressure	Pitot =		9.1277E+00 psia
Wall Temperature	Twall =		5.323E+02 degrees R
Molecular Weight	MW =		28.9536
	N2 mole fraction = 7.337E-01		
	N mole fraction = 1.135E-40		
	O2 mole fraction = 1.625E-01		
	AR mole fraction = 9.321E-03		
	O mole fraction = 5.408E-04		
	NO mole fraction = 9.385E-02		

Run 64

Shock Mach Number	Mi	=	6.377
Reservoir Pressure	PO	=	3.983E+03 psia
Total Enthalpy	HO	=	5.6761E+07 (ft/sec)**2
Stagnation Temperature	TO	=	7.0783E+03 degrees R
Freestream Mach No.	M	=	10.2562
Freestream Reynolds No.	Re	=	2.5788E+05 1/ft
Freestream Velocity	U	=	1.011E+04 Ft/sec
Freestream Temperature	T	=	4.0373E+02 degrees R
Freestream Pressure	P	=	3.7581E-02 psia
Freestream Density	RHO =		7.8001E-06 slugs/ft/ft/ft
Pitot Pressure	Pitot =		5.0899E+00 psia
Wall Temperature	Twall =		5.342E+02 degrees R
Molecular Weight	MW =		28.9434
	N2 mole fraction = 7.337E-01		
	N mole fraction = 2.028E-40		
	O2 mole fraction = 1.624E-01		
	AR mole fraction = 9.318E-03		
	O mole fraction = 1.249E-03		
	NO mole fraction = 9.336E-02		

4 REAL GAS EFFECTS ON REGIONS OF VISCOUS-INVISCID INTERACTION IN HYPERVELOCITY FLOWS

SUMMARY

In this section of the report, we examine a number of hypervelocity flows where real gas effects can influence the flow structure and aerothermal loads developed in regions of viscous/inviscid interaction. A brief review is also presented of the phenomena associated with shock wave/turbulent boundary interaction in hypersonic flows and the problems that arise in modeling these flows. Real-gas effects can exert a significant influence on the aerothermal loads developed in hypervelocity flows where the gas is processed through a series of shocks or in a region of expanding flow. Such flows arise principally as a result of shock/shock or shock/ boundary layer interaction or in strongly expanding flows such as those developed at the trailing edge of the Space Shuttle in the base region of a planetary probe. The effects of flowfield chemistry on laminar interacting flows over compression and expansion surfaces are discussed with particular reference to the control surface problems associated with the American Space Shuttle. A similar set of flow phenomena were examined in a study of real gas flows over a large blunt cone flare configuration. Here the emphasis was on the expanding flow downstream of the spherical nose tip and the flow separation generated at the cone/flare junction. Measurements made in these studies were compared with computations with a Navier-Stokes code incorporating real gas effects. The near wake flow behind a planetary probe configuration can be influenced by real gas effects generated in the expansion region immediately behind the body and the reattachment compression process at the neck of the wake. We review measurements made in the base flow region of a sting-mounted planetary probe configuration conducted in air and nitrogen at velocities of 10,000 ft/sec and 14,000 ft/sec. Theoretical predictions of the aerothermal loads generated in regions of shock/shock interaction have suggested that real gas effects can significantly enhance the peak aerothermal loads; however, these conclusions are not totally supported by the results of recent experimental studies. We review the results of these studies for flows where a planar shock is incident on the stagnation region over a blunt cylinder, and on the shock/shock interaction region developed over an idealized indented nose tip. Finally, we present a brief summary of the problems in predicting characteristics of regions of shock wave-turbulent boundary interaction in hypersonic flow; and we review the basic characteristics of these flows, discuss important effects associated with boundary layer transition, low Reynolds number, and the compressibility effects, as well as the intrinsic unsteadiness of these flows.

4.1 INTRODUCTION

Currently, because of difficulties in generating hypervelocity flows above Mach 10 in large-scale ground test facilities, the performance calculations for vehicles designed to fly up to orbital velocities must rely heavily on predictions from computations incorporating real gas effects. Recent developments in high-speed computers coupled with the corresponding implementation of efficient numerical techniques to obtain solutions to the DSMC and Navier-Stokes equations have made it easy to predict nonequilibrium flows around nose tips and simple conical configuration. However, the models of vibrational nonequilibrium, dissociation and nonequilibrium flow, and chemistry employed in such codes have not been well validated. For flows more complex than those over a blunt nose tip, for example those of the Space Shuttle, the modeling of vibrational and chemical nonequilibrium, as well as the vibrational/dissociation coupling, is not well founded. These problems are exacerbated for the design of air breathing hypervelocity vehicles to reach orbital velocities, where we must understand and model regions of

three-dimensional transitional shock/shock and shock/turbulent boundary layer interaction together with turbulent mixing and combustion, including real gas chemistry.

Although the effects of real gas phenomena on shock shape and stand-off distance have been well known for many years, computing the aerothermal loads in these flows remains a challenging task. The pressure distribution on blunt bodies in hypersonic flow is controlled principally by "Newtonian-type" particle impact. Thus, because the same number of atoms impact the surface whether or not the flow is dissociated, forebody pressure is relatively insensitive to vibrational or chemical nonequilibrium. The thermal loads in such regions, however, are more sensitive to nonequilibrium in the shock layer because of catalytic wall effects. Since the beginnings of interest in real gas effects, it was recognized that the pressure distribution in a highly expanding flow should be sensitive to nonequilibrium effects in the inviscid flow, because of the sensitivity of Prandtl-Meyer type flows to the local value of γ. The interpretation of early experimental studies to quantify such effects on two-dimensional wedge/ afterbody configurations was significantly complicated by viscous interaction effects at the model junction. Here, the laminar boundary layer thickens dramatically through the expansion process, influencing through viscous interaction the pressure distribution through this region. These studies demonstrated that to accurately predict the characteristic expansion flows, it was necessary to develop computation schemes capable of handling the coupled effects of viscous interaction and flowfield chemistry.

Within the past 10 years, a number of new high enthalpy ground test facilities have been designed and constructed with one of the principal objectives to more accurately understand real gas effects on the control problems similar to those encountered on the first flight of the Space Shuttle. During this flight, much larger control surface deflections were required to stabilize the Space Shuttle than were originally predicted on the basis of a large database of measurements obtained almost exclusively in low enthalpy facilities. The control system of the Space Shuttle was configured from compilations of pitching moment data from a large number of force tests conducted in high Mach number, low enthalpy ground test facilities with essentially an ideal gas as a test medium. Force data were also obtained from a CF4 tunnel, where a heavy gas test medium was employed to obtain a flow with a γ close to 1.2, the average γ developed in the dissociated gas of the shock layer over the windward face of the Space Shuttle. Figure 4-1 shows the large flap angles required in flight to trim the vehicle compared with the compilation of the data from the ground test facilities (Reference 1). The flight data shows little sensitivity to freestream Mach number, while the tunnel measurements predict a relatively strong variation. Initially, the larger-than-predicted flap deflections needed to trim the flight vehicle were believed to be associated with the loss of control effectiveness resulting from real gas effects. However, detailed numerical solutions to the Navier-Stokes equations suggest that the laminar separated region over the flap decreased in size as a result of real gas effects. The result is an improved control effectiveness rather than one that is degraded by real gas effects. The "flap pitch trim anomaly" was also explained with detailed Navier-Stokes computations, which demonstrated that the dissociated shock layer flow, as it expanded over the curved section of the trailing edge of the Space Shuttle

71

produced lower pressures than for an ideal gas flow with a γ of 1.4, as illustrated in Figure 4-2. Thus, although the flap was predicted to be more effective than the measurements in low enthalpy facilities would suggest, the lower pressures resulting from real gas effects on the trailing edge of the flight vehicle necessitates larger flap angles to trim the vehicle.

The ground tests conducted in the CF4 tunnel were successful in simulating the decrease in pitching moment with γ (as shown in Figure 4-3) only because of the relatively simple nature of the real gas phenomena controlling the pressures on the windward side of the Space Shuttle. In the critical phase of reentry, the uniform level of dissociation throughout the shock layer was such that this region of the flow could be represented, with reasonable accuracy, by a gas with an average γ of close to 1.2. Thus, testing this aspect of the problem in a constant γ facility achieved the required result. Recently, tests in high-enthalpy facilities (see Reference 2) have also validated this "real gas" effect. However, because these high enthalpy studies were conducted at relatively low stagnation pressure conditions, there was a significant level of dissociation present in the freestream, bringing the average γ in the freestream below 1.4. In this situation, the flow was similar to the last γ studies conducted in heavy gas facilities. To more accurately simulate such effects, it is necessary to operate high enthalpy facilities at large reservoir pressures to reduce the level of dissociation in the freestream, so that the chemistry in the shock layer is negligibly different from that occurring in flight.

Recently, further studies have been conducted in a number of high enthalpy facilities to examine flows where real gas effects might be expected to exert a significant influence on the flow structure and aerothermal loads. Examples of flows where real gas effects can be important in controlling the inviscid and viscous structure are illustrated in Figure 4-4. Figure 4-4a shows the flow over the Space Shuttle where, because the flow in the shock layer on the windward side of the vehicle is highly dissociated, lower pressures are experienced in the expansion region than would be the case for an ideal gas flow, which results in a higher-than-predicted requirement for the flap angle. The flow in the expansion and recompression regions of a base flow, as illustrated in Figure 4-4b, can also give rise to significant nonequilibrium effects. Here, real gas effects in the expansion region, coupled with those in the nearly isentropic recompression process at the neck of the wake, may alter the base flow structure and the pressure levels developed in the base region. Real gas effects may be also expected to influence the aerothermal loading over a blunt cone flare configuration, where again we expect the flow in the expansion region to be controlled by combined viscous inviscid interaction and flow chemistry effects and the region of shock wave-boundary interaction at the cone flare junction to exhibit effects similar to that adjacent to the control surface on the Space Shuttle. Finally, we consider two flowfields involving regions of shock/shock interaction which have been found to be sensitive to real gas effects. The first is the flow over a cylindrical leading edge where an oblique two-dimensional shock is incident, and the second is the shock/shock interaction generated by the flow over an idealized indented nose tip as illustrated in Figures 4-4c and 4-4d, respectively.

In the following sections of this paper, we discuss measurements and computations of the high enthalpy flow in regions of shock wave/boundary layer interaction over a blunt cone flare model. We then discuss the results of measurements made in the high-enthalpy flow over planetary probe configurations and the computations made to predict these flows. We then describe experimental studies and computations to examine the real gas effects in regions of shock/shock interaction over cylindrical leading edges and on a highly indented nose shape. Finally, a brief review is presented of the characteristics of shock wave-turbulent boundary layer interaction in hypersonic flows and the current status of the prediction techniques available to describe them.

4.2 REAL GAS EFFECTS IN REGIONS OF SHOCK WAVE/BOUNDARY LAYER INTERACTION

4.2.1 Introduction

The relatively efficient compression processes through a series of shocks in the separation and reattachment regions of flows generated by shock wave/boundary layer interaction, coupled with the high temperature, slow mixing characteristics of a separated region, have lead researchers to suggest that the characteristics of such flows could be strongly influenced by real gas effects. The calculations by Furumoto, Zhong and Skiba (Reference 3) of the real gas effects on separated flows induced by shock wave/boundary layer interaction support such speculation. Figures 4-5a, -5b, and -5c show the pressure, heat transfer and skin friction distributions, respectively, through a large separated laminar flow induced by shock wave boundary layer interaction. As can be seen from the skin friction distribution shown in Figure 4-5c, the length of the separated region shrinks progressively as the effects of vibrational and chemical flow nonequilibrium are added. The greater pressure recovery in the real gas flows (shown in Figure 4-5a) leads to a slightly larger Stanton number (as shown Figure 4-5b). Such strong effects have yet to be validated in experimental studies. The modeling of not only the flow chemistry but also the vibrational/dissociation coupling remains a source of controversy which can only be resolved through comparisons between such computations and carefully conducted experimental studies.

4.2.2 Real-Gas Studies with the Large Sphere/Cone/Flare Configuration

4.2.2.1 *Measurements of the Heat Transfer and Pressure on the Spherically Capped Cone/Flare Model*

Two sets of studies were conducted with the large spherically-blunted cone/flare configuration shown in Figure 4-6. This model was highly instrumented with heat transfer and pressure gages to obtain detailed surface distributions for a range of freestream conditions at velocities between 10,000 ft/sec and 15,000 ft/sec for both nitrogen and air flows. The electron beam and the associated pneumatic and electrical apparatus, together with photomultiplier detection systems, were also installed into the model.

73

The instrumentation density in the region in the immediate vicinity of the cone/flare junction was increased to detect and quantify the presence of a laminar separated region. The flare region was densely instrumented to accurately quantify the reattachment compression region. Measurements of the distribution of heat transfer and pressure over the model were obtained for total enthalpy conditions of 5 MJ/kg and 10 MJ/kg, with reservoir pressures of 270 and 500 bars, with both nitrogen and air used as the test gas. These conditions were selected to explore the effects of the Reynolds number, which influences the occurrence of transition and total temperature and pressure and influences the flow chemistry. The test conditions for these studies are listed in Table 3-2. Measurements of the distribution of pressure and heat transfer on the model for nitrogen and air flows at the two total enthalpy conditions are presented in Figures 4-7 and 4-8. Both the pressure and heat transfer measurements show that there is a small separated region at the cone/flare junction which is laminar (the heat transfer decreases). Comparisons between the measurements of pressure and heat transfer at the 10 MJ/kg, 500 bar test condition with air and the Navier-Stokes calculations by Boyd and George (Reference 4) are shown in Figures 3-34a and 3-34b. While the calculations are in good agreement with pressure and heat transfer measurements on the sphere and cone, the size and characteristics of the separated regions are not well predicted.

4.2.2.2 *Flowfield Measurements over Spherically-Blunted Cone/Flare Model*

Calculations of the nonequilibrium flow over the spherically-capped cone/flare configuration were made at a 10MJ/kg and 500 bar test condition. Figure 3-35 shows a Mach number of the flow over the sphere/cone section of the model illustrating the positions of the test stations to be employed in this experimental program. The magnitude of the vibrational nonequilibrium is shown in Figures 3-36 and 3-39 along the stagnation streamline. Predictions of the number density distributions across the shock layer at Station 2 are shown in Figures 3-38 and 3-40. From these distributions, it is clear that Station 2 provides an opportunity to measure significant departures from the translation of temperature. Again at Station 2, there is a large variation in the levels of dissociated oxygen and NO which should provide a good environment for the experimental studies. Finally, Figure 3-41 shows the variation of vibrational and translational temperature along the body as well as the number density of the species in the shock layer close to the body. Again, levels of nonequilibrium exhibited in these calculations should provide ample opportunity to examine the validity of the real gas effects in these flows.

4.3 STUDIES OF REAL GAS EFFECTS IN HYPERVELOCITY NEAR WAKE FLOWS

4.3.1 Introduction

The sting-mounted planetary probe configuration has become a *de facto* standard for the comparison and calibration of high-enthalpy facilities and numerical codes incorporating Monte Carlo and Navier-Stokes solution techniques. The planetary probe model shown in Figure 2-5 is a sting-mounted, spherically blunted 70° cone with a flat base, which is attached to a long cylindrical sting. While the measurements on the front face provide a basis

for evaluating the properties of the freestream, the complex flow in the base region provides the basis for examining time establishment and the chemical nonequilibrium, and (unfortunately) the effects of shear-layer transition. Measurements have been made to examine the pressure and heat transfer distribution over the planetary probe configuration under high enthalpy conditions in the HEG, LENS and F4 hypervelocity facilities and in the low-enthalpy Mach 12 facility at NASA-Langley. To ensure that the measurements were not influenced by the instrumentation employed, measurements were made in each of the facilities with common model, instrumentation and data reduction techniques. In the studies conducted in the LENS facility, measurements were made with both air and nitrogen as the test gas. Computations for low density flows were made with the Monte Carlo technique while Navier-Stokes solutions were obtained under the highest Reynolds number conditions with continuum flow. A further set of calculations were made with a hybrid scheme to ensure that rarefaction effects which occur in the expansion fan did not introduce significant low density effects. The test conditions for the air and nitrogen flows are shown in Tables 2-1 through 2-6 and Table 3-2, respectively.

4.3.2 Comparisons Between Numerical Simulations and Experimental Measurements

Comparisons were made between Navier-Stokes solutions and the measurements obtained for LENS test cases E and F, which were at the 10 MJ/kg enthalpy and 500 bar reservoir conditions with air and nitrogen, respectively, as the test gas. LENS test case E was developed as a match point between the various hypervelocity facilities where the planetary probe has been tested. In particular, measurements have been obtained in the HEG and LENS shock tunnels, as well as the "hot shot" facility Tunnel F in France, at the nominal 10 MJ/kg and 500 bar test case conditions with air. Because of the high density levels at which these studies were conducted, the flow over the front face and in the majority of the wake can be considered as a fully continuum regime, and solutions based on the Navier-Stokes equations provide the only practical prediction technique. However, in the expansion region above the separated base flow, the densities may be low enough that the assumption in such computations is invalid and, in this regime, the DSMC code could be more accurate. Therefore, calculations employing the Navier-Stokes code to compute the forebody flow coupled with a DSMC method to compute the base region have been pursued. Comparisons between the calculations of heat transfer and pressure obtained by Muylaert et al. (Reference 5) using the TINA code were compared with measurements of heat transfer rate for Run Numbers 22, 29, and 33 and are shown in Figure 2-38. The computations are in excellent agreement with the experimental measurements on the front face of the probe, but fall slightly below the measurements downstream of the reattachment region on the sting. As discussed earlier, we believe that, for Run Numbers 29 and 33, the heating levels downstream of the reattachment region may be influenced by the beginning of a transition process. Finally, Figures 2-40 and 2-41 show the comparisons between the heat transfer and pressure measurements and computations performed at Cornell University using Navier-Stokes/DSMC computations. Again we see that, while predictions for the forebody are in good agreement with the measurements, the flow in the recompression region is not well predicted and the measurements are above the predictions downstream of the recompression region on the sting. Comparisons

between the measurements made at 5 MJ/kg for runs 15 and 16 and at 10 MJ/kg for Runs 33 and 34 (see Figures 4-9a and b and 4-10a and b) for air and nitrogen flows, respectively, and computations for these two cases suggest that in these particular flows, the size of the wake and the distributions of heat transfer and pressure to the downstream of the base region are not strongly influenced by real gas effects.

Although discrepancies may occur between individual computations due to incorrect implementation, the differences may also illustrate a general potential weakness of the continuum codes in handling flows where there are very rapid expansions such as those that occur around the rim of this configuration. In this instance, a failure to compute the localized flow in the region of the rim will set inappropriate upstream conditions for the wake and reattachment flow computations where the discrepancies may be amplified. To explore such effects, comparisons were made between the pressure and heat transfer measurements for the LENS Test Case E condition and computations employing the hybrid technique and the Navier-Stokes/DSMC computation for the boundaries illustrated in Figures 2-45 and 2-46. The two prediction techniques do not significantly differ, although the predictions at the end of the reattachment region employing the hybrid code are in better agreement with the experiment. Again, the pressure measurements have exhibited a slower return to the sting pressure than predicted by either the Navier-Stokes or hybrid codes.

4.4 REAL GAS EFFECTS IN REGIONS OF SHOCK/SHOCK INTERACTION

4.4.1   Introduction

The heating levels and gradients in regions of shock/shock interaction are among the most severe. Because they can be unsteady, and are invariably transitional, they are extremely difficult to predict accurately. The large heating and pressure loads developed in these regions result principally from an efficient recompression process where the gas in the stagnation region is processed through a series of oblique shocks. This applies particularly to the Type IV shock/shock interaction illustrated in Figure 4-11, where the flow is processed through a series of shocks terminating in a stagnation region preceded by a strong normal shock. It is the sensitivity of the shock patterns to the local γ which led Edney (Reference 6) to speculate that the heating rates developed in these flows would be more severe as a result of real gas effects. Similar but lesser effects might be expected for the Type III interaction region illustrated in Figure 4-12, where the real gas effects might be expected to influence the aerothermal loads in the reattachment region of the free shield layer.

4.4.2   Predictions of Real Gas Effects in Regions of Shock/Shock Interaction

Following the empirical relationships of Edney for real gas effects in regions of shock/shock interaction, a number of studies have attempted to quantify these effects. Recently detailed numerical solutions have been obtained using DSMC and Navier-Stokes codes to investigate how real gas effects influence the structure of nomi-

76

nally Type IV interaction regions in high-enthalpy flows in the laminar low-density and continuum regimes. Studies by Carlson and Wilmoth (Reference 7) using a Monte Carlo method have examined the effect of flowfield chemistry on a shock/shock interaction region in low density flows. They found that grid size and selection had a significant effect on the solution and that careful gridding at the base of the interaction region was of critical importance to an accurate prediction of the heating levels. Typical solutions for the heat transfer and pressure distribution generated in the region of shock/shock interaction over a cylindrical model for perfect gas and finite rate chemistry are shown in Figure 4-13. It can be seen from these predictions that real gas effects can result in almost doubling the peak pressure levels in the interaction, and the peak heating levels are increased by approximately 150 percent when real gas effects are present. A similar set of predictions were made by Furumoto and Zhong (Reference 3) for continuum real gas flows employing a Navier-Stokes computation. These calculations (shown in Figure 4-14) indicate that, while the real gas effects on pressure are relatively weak, enhancements to the heating levels are similar to those calculated by Carlson and Wilmoth (Reference 7). Again, it is noted that the solutions are extremely sensitive to grid selection.

4.4.3 Measurements of Real Gas Effects on Regions of Shock/Shock Interaction

Recently, three experimental studies have been conducted to investigate the influence of real gas effects on the structure and aerothermal load generated in regions of shock/shock interaction. Studies of shock/shock interaction resulting from the impingement of a planar shock in the stagnation region of a cylindrical leading edge were conducted in the HEG piston driven shock tunnel by Kortz et al. (Reference 8). In these studies, holographic interferometry was employed to record the interaction between the incident shock and the shock layer and heat transfer instrumentation employed to obtain distributions around the cylinder. A hologram of a Type IV interaction over the cylinder from the studies of Kortz, MacIntyre and Eitelberg (Reference 8) is shown in Figure 4-15, together with their reconstruction of the flowfield as shown in Figure 4-16. They conclude that the real gas effects' structure is significantly different from the character of the flow for an ideal gas. These experimental studies have suggested that for Types III and IV interactions, the peak heating and pressure levels are, in fact, lowered by real gas effects as a result of an increase in the scale in the interaction region (as discussed in Reference 9). Similar conclusions were reached by Sanderson (Reference 10) as a result of experimental studies conducted in the T5 piston driven shock tunnel. The computations and experimental measurements made in these studies again suggest that real gas effects cause an increase in the scale of the interaction region which results in a reduction in the peak heat transfer and pressure levels generated in these flows.

More recently, in studies conducted by Holden (Reference 11), measurements were made in regions of shock/shock interaction at enthalpy levels of 5 and 10 MJ/kg for both air and nitrogen flows. At the enthalpy level of 10 MJ/kg, the air is highly dissociated in the stagnation region of the cylinder, while the nitrogen behaves like an ideal gas flow. In these studies, the model was densely instrumented with high-frequency thin-film instrumen-

77

tation to achieve a level of spatial and temporal resolution which exceeded those of the earlier studies. The model employed in these studies is shown supported in the LENS Hypervelocity Shock Tunnel in Figure 4-17. Typical sets of measurements obtained for Type IV-like interactions in both air- and nitrogen-free streams are shown in Figures 4-18 and 4-19. The measurements indicate that, while real gases have a minor influence on pressure, the heat transfer rates are larger in the air flow. Calculations employing the DSMC and Navier-Stokes techniques are being made for comparison with the experimental measurements. The initial results of these calculations suggest that real gas effects should enhance the peak heating of these flows. The discrepancy between the theoretical predictions and the experimental results from different studies remain to be explained and further experimental data are needed over a range of freestream enthalpy conditions to provide an accurate data set with which to refine the thermal chemical models employed in the prediction schemes.

4.4.4 Studies of Real Gas Effects in Regions of Shock/Shock Interaction over Indented Nose Shapes

Earlier experimental studies on indented nose tips by Holden (Reference 12) and more recently computations by Candler (Reference 13) have suggested that the flow structure over, as well as the aerothermal loads generated on, a blunted cone/cone configuration similar to that of an idealized indented nose tip can be sensitive to real gas effects. Originally, indented nose shapes were studied because of an interest in the development of flows over ablated nose tips, similar to those generated with graphite nose tips during the ballistic reentry. Later Candler, in numerical studies designed to select configurations which were sensitive to real gas effects, suggested a cone/cone configuration similar to those studied earlier by Holden. The cone/cone configuration in our recent experimental studies was based on suggestions by Candler and is shown in Figure 4-20. This model was highly instrumented with high-frequency heat transfer and pressure gages to provide distribution of the surface properties as well as information on any high-frequency flow oscillations that may arise. Measurements were again made in air and nitrogen flows at enthalpies of 5 and 10 MJ/kg. Flow conditions for these studies are listed in Tables 2-5 and 2-6. Figures 4-21 and 4-22 show the distribution of heat transfer and pressure over cone/cone configuration for air and nitrogen flows, respectively, for a totally enthalpy of 10 MJ/kg. By comparing the measurements in these two figures, it can be seen that significantly larger peak heat transfer and pressure rates are generated in the air flow than in the flow with pure nitrogen. Thus, these measurements generally support the theoretical calculations which suggest that peak thermal loads in regions of shock/shock interaction are exacerbated by real gas effects. However, the measurements in the flow at the 5 MJ/kg total enthalpy condition shown in Figures 4-23 and 4-24 do not appear to generate as strong an interaction region and are less sensitive to real gas effects. Computations employing the Navier-Stokes code are being made to examine both these flow configurations.

4.5 FLOW PHENOMENA ASSOCIATED WITH SHOCK WAVE-TURBULENT BOUNDARY INTERACTION IN HYPERVELOCITY FLOWS

The large heat transfer and pressure gradients generated in regions of shock wave/turbulent boundary layer interaction at hypersonic speeds make it essential to develop prediction techniques to define the scale of these interaction regions and the aerothermal loads developed within them. While in the general regions of shock wave/boundary layer interaction are unsteady, their gross characteristics and mean properties of these regions can be defined with relative accuracy from correlations of experimental measurements. At hypersonic speeds, it is relatively difficult to separate a turbulent boundary layer, and compression angles of over 27 degrees are required before a region of incipient separation is generated. An intriguing aspect of small turbulent regions in hypersonic flow is that the recirculation region is formed first at the base of the turbulent flow as if the laminar sublayer were separating, as shown in Figure 4-25. Then, even for relatively large increases in flow deflection angle, the recirculation region remains embedded within the original boundary layer (see Figure 4-25).

Regions of shock wave/turbulent boundary layer interaction are characterized by severe normal and axial pressure gradients generated by unsteady shock systems which traverse the turbulent boundary layer; this viscous rotational flow presents the turbulence modelers with significant problems. The shock systems that are embedded within the turbulent flow are shown for an incident shock flow near incipient separation in Figure 4-26. High-frequency skin friction measurements at the base of a turbulent separated flow shown in Figure 4-27 illustrate the grossly unsteady nature of interacting flow in the region close to flow separation. The unsteady structure of a turbulent separated region over a compression ramp is further illustrated by the wavy shock structure in the holographic interferogram with a very short exposure in Figure 4-28. In spite of the complexity of these flows, correlations of the conditions required to induce incipient separation can be obtained with relative ease in terms of the basic model and freestream parameters for both incident shock and corner flows, as illustrated in Figures 4-29 and 4-30. For both wedge- and shock-induced well separated flows, the heat transfer and pressure in the plateau and peak loading region are available from simple correlations. However, a successful correlation has yet to be derived to define the length of the separated region in terms of simple flow and model parameters.

Currently, even the most sophisticated numerical codes employing the most advanced turbulent modeling techniques have been unable to accurately predict the detailed distribution of heat transfer and skin friction in high-speed regions of shock wave/boundary layer interaction from Mach 3 to Mach 15. In hypersonic flows, it is necessary to introduce and model effects associated with compressibility and low Reynolds number. As illustrated in calculations of a Mach 11 flow by Horstman shown in Figure 4-31, none of the current turbulence modeling techniques are capable of predicting the heat levels or the skin friction levels with even reasonable accuracy. Even for flows in the supersonic regime over adiabatic walls, a recent study by Knight and Degrez (Reference 14) found that, although the pressure distribution could be predicted with reasonable accuracy, the heat transfer and skin friction at the base of these interaction regions were poorly predicted.

To obtain predictions of the basic characteristics of regions of shock wave-turbulent boundary layer interaction, where separation takes place in the sublayer, it would seem prudent that, rather than employing sophisticated "global" turbulence modeling techniques (which remain incapable of capturing the complex flow physics), we return to employing relatively simple zone-specific turbulence models which characterize the basic flow phenomena in each region of the flow. We could expect such an approach to provide a relatively accurate solution for the pressure distribution. This solution could then be used with empirical correlation techniques to calculate the heating in regions of separated flow with an accuracy required for engineering predictions. Predicting the unsteady characteristics of these flows in the hypervelocity regime appears totally intractable at this time.

4.6   CONCLUSION

In this section we examined a number of hypervelocity flows where real gas effects can influence the flow structure and aerothermal loads developed in regions of viscous/inviscid interaction. A brief review is also presented of the key flow phenomena associated with shock wave/turbulent boundary layer interaction and the problems that arise in modeling these flows. Real gas effects can exert a significant influence on the aerothermal loads developed in hypersonic flows in situations where a gas is processed through a series of shocks or is rapidly expanded. Such flows arise principally in regions of shock/shock or shock/boundary layer interaction or in the base region of hypersonic vehicles. The effects of flowfield chemistry on the laminar interacting flows over compression and expansion surfaces have been discussed with reference to the control surface problems associated with the Space Shuttle. A similar set of flow phenomena were examined in an experimental study of the real gas flows over a large blunt cone/flare configuration. Measurements made in these studies were compared with Navier-Stokes solutions incorporating real gas effects. Measurements in highly expanded flows were obtained in the base region of a planetary probe configuration for both air and nitrogen flows at velocities of 10,000 ft/sec and 14,000 ft/sec. Comparisons between experiments and numerical computations suggested that real gas effects did not exert a significant effect on the characteristics of the flows that were studied. Experimental studies of real gas effects in regions of shock/shock interaction were made on a cylindrical leading edge and an axisymmetric indented nose shape. While theoretical predictions suggest that real gas effects can significantly enhance the aerothermal loads generated by these flows, the results from the experimental studies have not been as definitive.

A brief review of the status of the prediction techniques to describe regions of shock wave-turbulent boundary layer interaction in hypervelocity flow suggests that, while the gross features of these flows may be predicted with the current models of turbulent flow, the current computational techniques are incapable of predicting heat transfer and skin friction with any accuracy.

4.7   REFERENCES

1. Throckmorton, D.A., "Configuration Aerothermodynamics of Entry Vehicles," AGARD Aerothermodynamics and Propulsion Integration for Hypersonic Vehicles, AGARD Report 813, October 1996.

2. Rostand, P., "CFD to Support the Reduction of Uncertainties in Ground to Flight Extrapolation," AGARD FDP Workshop on Hypersonic Experimental and Computational Capability Improvement and Computational Capability Improvement and Validation, April 1997.

3. Furumoto, G.H. and Zhong, X., "Numerical Simulation of Viscous Unsteady Type IV Shock-Shock Interaction with Thermochemical Nonequilibrium," AIAA Paper 97-0982, Paper presented at 35th Aerospace Sciences Meeting and Exhibit, Reno, NV, January 1997.

4. Boyd, I. and George J., "Experimental and Computational Studies of the Flow Over a Sting Mounted Planetary Probe Configuration," AIAA Paper 97-0768.

5. Private Communication, November 1996.

6. Edney, .,, "Anomalous Heat Transfer and Pressure Distributions on Blunt Bodies at Hypersonic Speeds in the Presence of an Impinging Shock," FFA Report 115, Aeronautical Research Institute of Sweden, 1968.

7. Carlson, A.B. and Wilmoth, R.G., "Monte Carlo Simulation of a Near-Continuum Shock-Shock Interaction Problem," AIAA Paper 92-4532.

8. Kortz, S. Mcintyre, T.J., and Eitelberg, G., "Experimental Investigation of Shock-on-Shock Interactions in the High-Enthalpy Shock Tunnel Gottingen (HEG)," Shock Waves at Marseilles I., Hypersonics, Shock Tube and Shock Tunnel Flow, Proceeding Marseilles, France, 1993.

9. Sanderson, S.R. and Sturtevant, B., "Shock Wave Interactions in Hypervelocity Flow," Shock Waves at Marseilles I, Hypersonics, Shock Tube and Shock Tunnel Flow, Proceeding Marseilles, France, 1993.

10. Sanderson, S.R. and Sturtevant, B., "Shock Interference Heating in Hypervelocity Flow," Proceedings of the 20th International Symposium on Shock Waves, Volume I, World Scientific, Pasadena, CA, July 1995.

11. Holden, M.S., "A Review of Recent Development , Testing and Code Validation Studies in the LENS Facility," AIAA Paper 96-1598, 1996.

12. Holden, M.S., "Studies of the Heat-Transfer and Flow Characteristics of Rough and Smooth Indented Noseshapes," AIAA Paper 86-0384.

13. Private Communication, August 1996.

14. Knight and Degrez, AGARD FDP Workshop on Hypersonic Experimental and Computational Capability Improvement and Computational Capability Improvement and Validation, April 1997.

STS-1 Shuttle Hypersonic Pitch Trim Anomaly
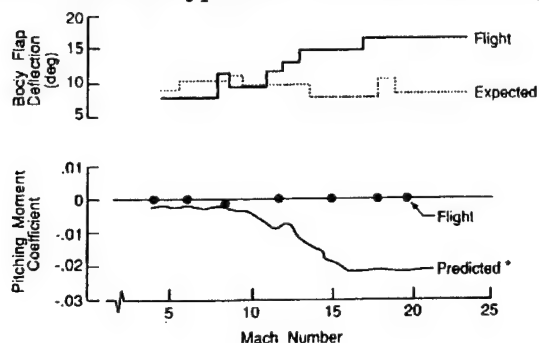
Figure 4-1 STS-1 Shuttle Hypersonic Pitch Trim Anomaly (Reference 1)

Orbiter Windward Centerline Pressures
(α = 40 deg, No Bodyflap)
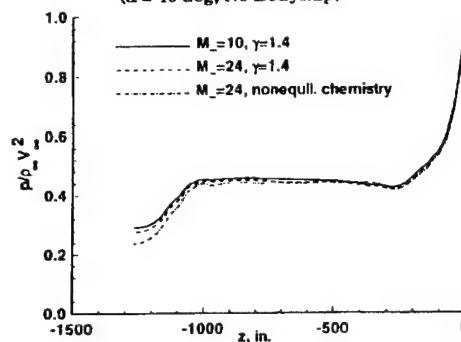
Figure 4-2   Orbiter Windward Centerline Pressures (Reference 1)
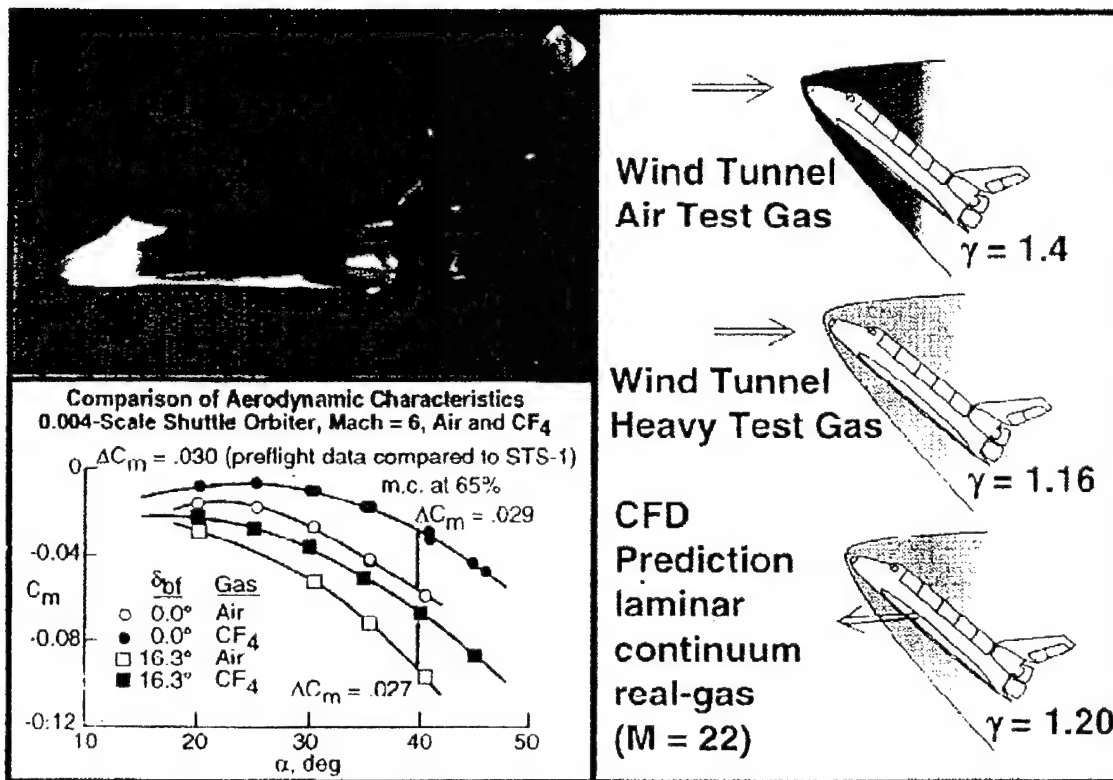
Figure 4-3 C_m Increments Assessed by Testing in CF4 (Reference 1)

82

- **Expansion Regions and Separated Flows**

Space Shuttle	Wake and Baseflows

a. Expansion Region R.G. Results in Lower Pressures. Dissociated Shock Layer ($\gamma = 1.2$). Separated Flow

b. Expansion Region. Recirculating Flow

- **Regions of Multi-Shock Recompression**

Shock/Shock Interaction	Indented Nose Configuration

c. Multiple Shocks

d. Multiple Shocks
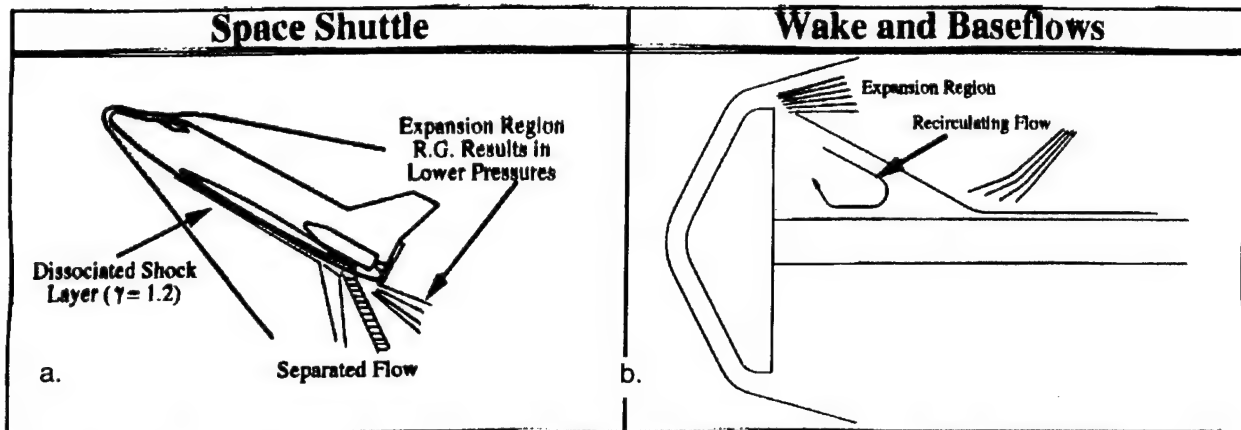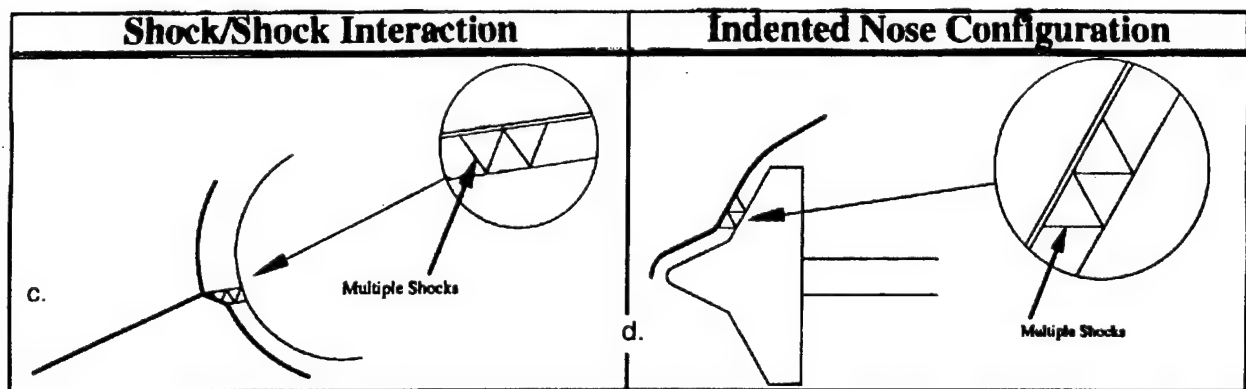
Figure 4-4   Real Gas Effects in Expansion Regions, in Separate Flows and Regions of Multi-Shock Recompression (Reference 1)
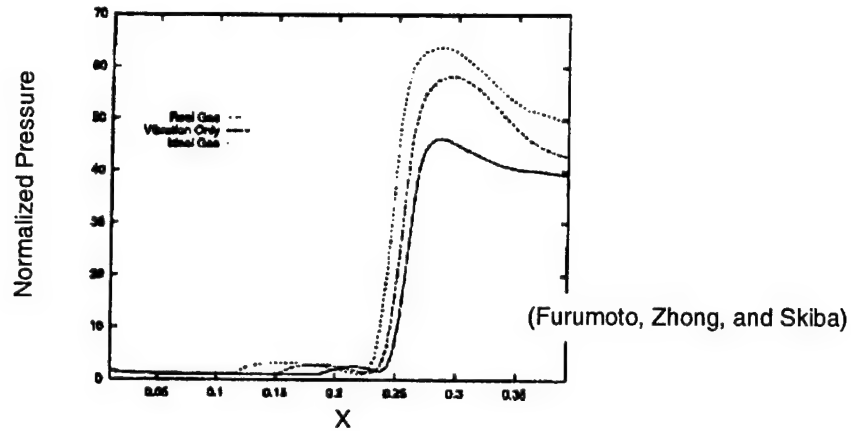
Pressure Distribution along the Flat Plate for Three Gas Models
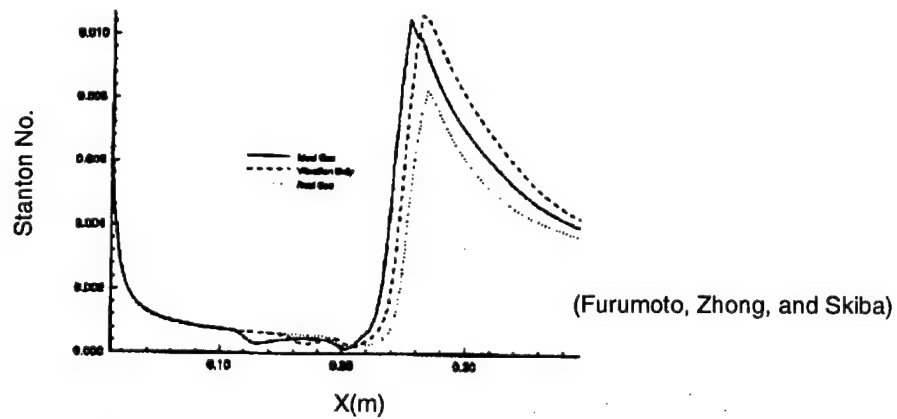
Heat Flux Distribution along the Flat Plate for Three Gas Models
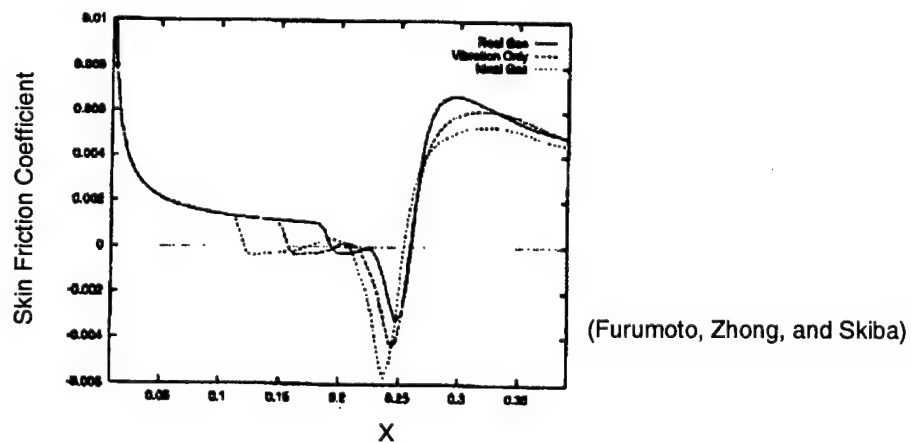
Skin Friction Coefficient Distribution along the Flat Plate for Three Gas Models

Figure 4-5 Real Gas Effect on Separated Flow Induced by Shock Wave-Boundary Layer Interaction
(Reference 3)
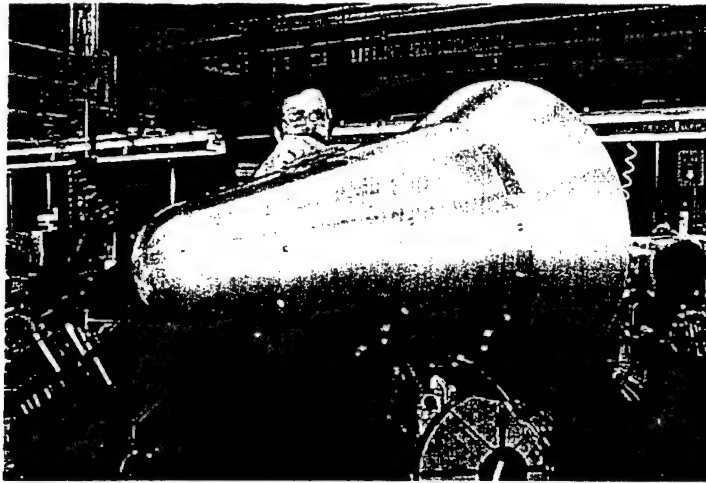
Figure 4-6   Real-Gas Effects in Regions of Multi-Shock Using Blunted Cone/Flare Configuration
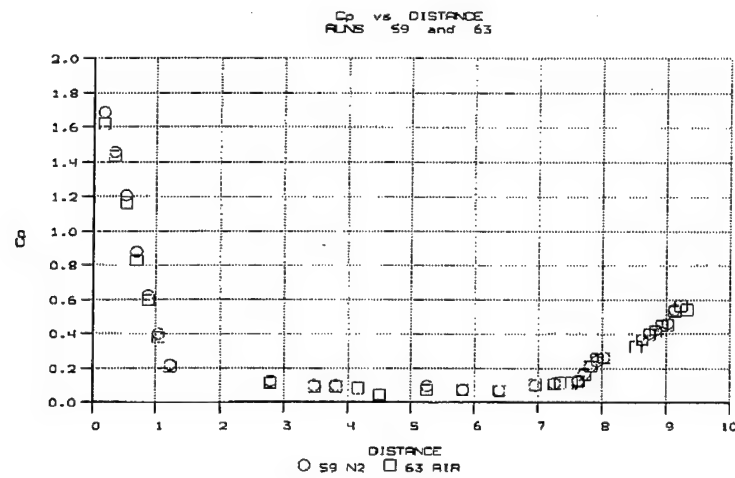
Figure 4-7a   Distribution of Pressure Coefficient for Air and Nitrogen Flows at 5MJ/kg
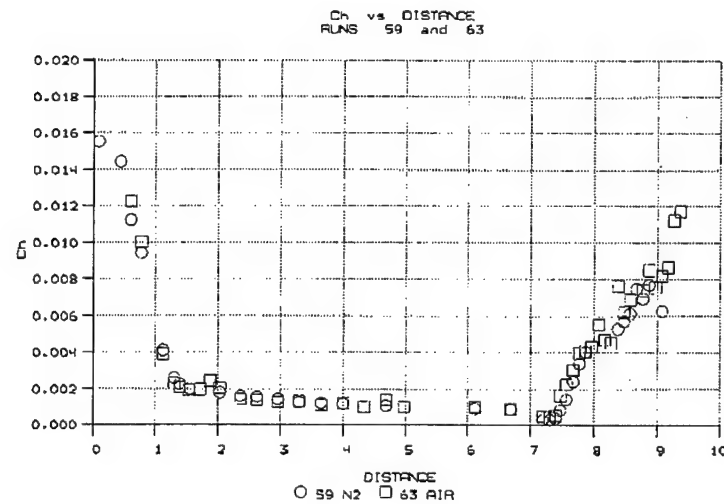
Figure 4-7b   Distribution of Heat Transfer Coefficient for Air and Nitrogen at 5MJ/kg
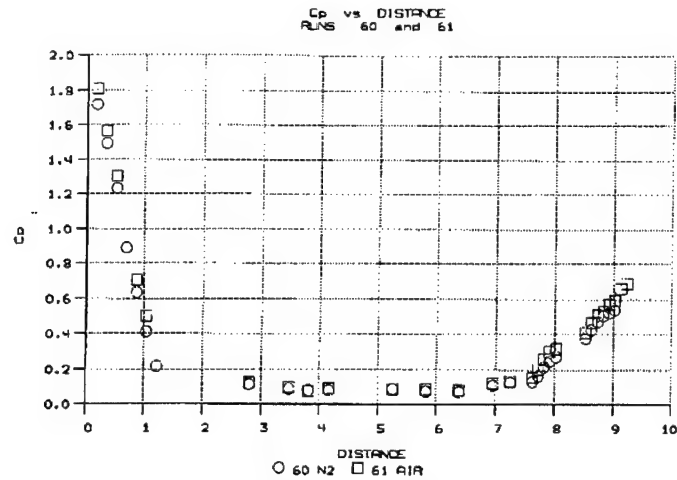
Figure 4-8a Distribution of Pressure Coefficient for Air and Nitrogen Flows at 10MJ/kg
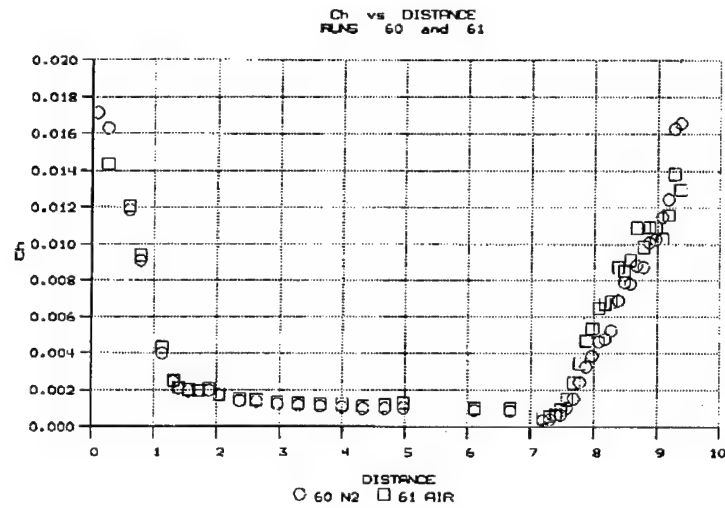
Figure 4-8b Distribution of Heat Transfer Coefficient for Air and Nitrogen at 10MJ/kg
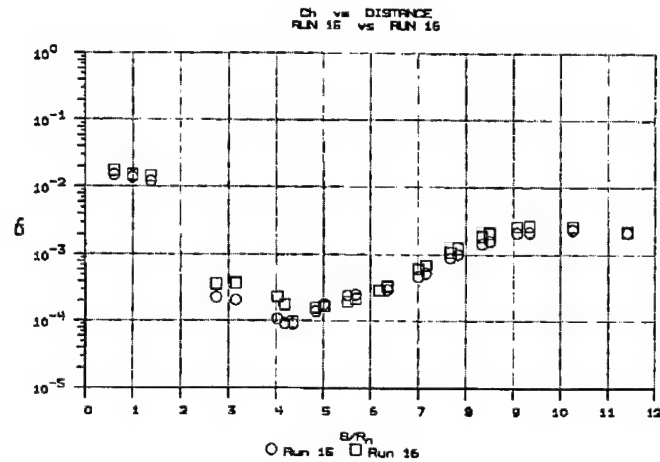
Figure 4-9a Comparison Between the Distribution of Heat Transfer Coefficient for Air and Nitrogen Flows for the 5MJ/kg, 500 Atmosphere Reservoir Condition

86
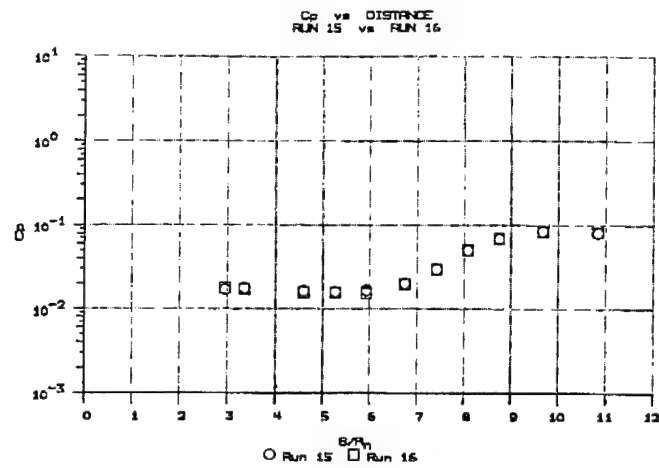
Figure 4-9b Comparison Between the Distribution of Pressure Coefficient for Air and Nitrogen Flows for the 5Mj/kg, 500 Atmosphere Reservoir Condition
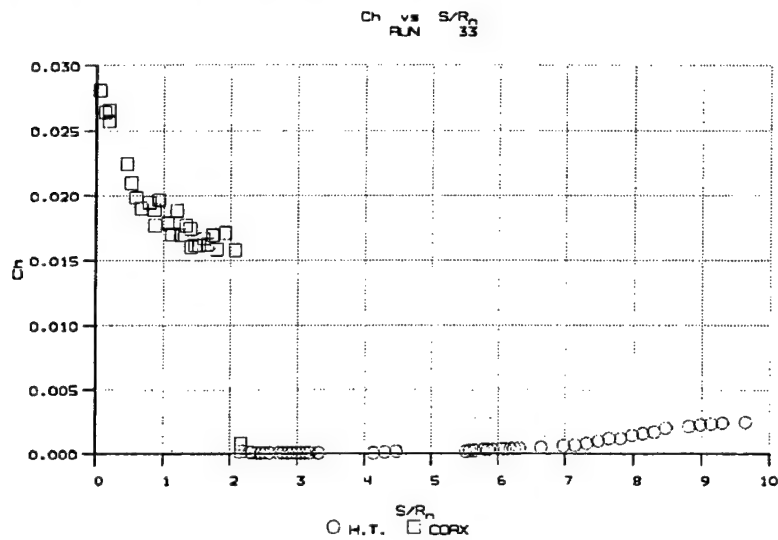
Figure 4-10a Distribution of Heat Transfer Coefficient for Air at 10MJ/kg
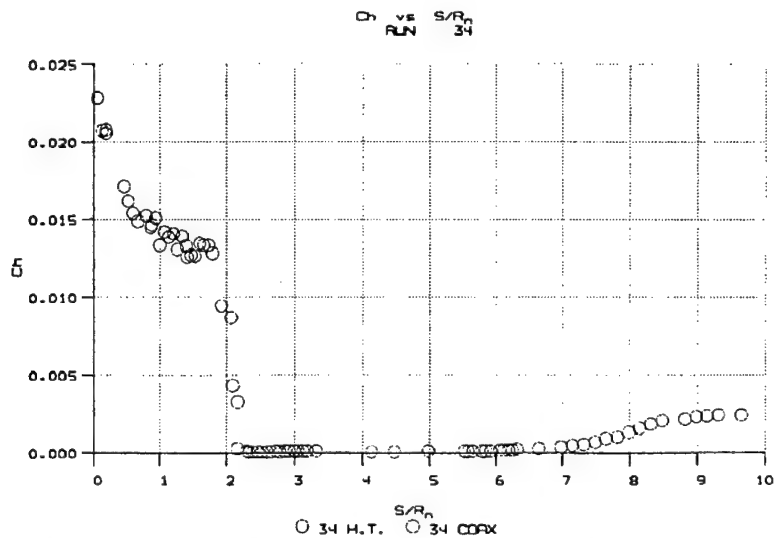
Figure 4-10b Distribution of Heat Transfer Coefficient for Nitrogen at 10 MJ/kg

87

$$\frac{q_{max}}{q_{stag}} = 1.03 \left(\frac{\frac{D}{2}}{\Delta l} \frac{P_{max}}{P_{stag}} \right)^{\frac{1}{2}} \ (Ref.\ 2)$$

CYLINDER

BOW SHOCK

$\frac{D}{2}$

M>1   M<1

JET BOW SHOCK

M<1

③

JET, M>1

⑦ ⑧

②

⑥

IMPINGING SHOCK

① ⑤

Δl

M>1

④

M<1

SHOCK WAVE

— · EXPANSION WAVE

--- SHEAR LAYER

BOW SHOCK
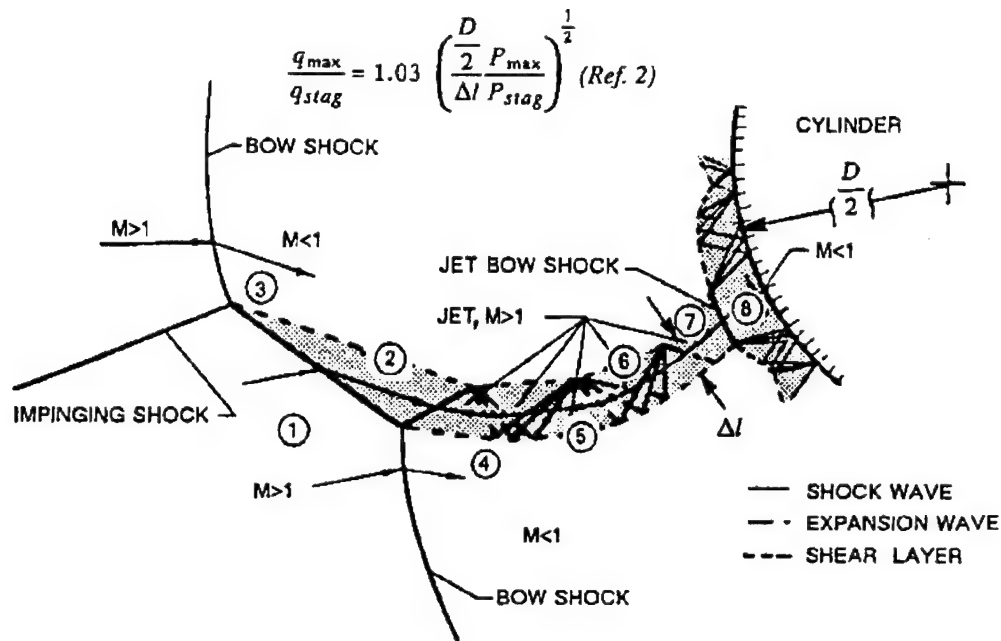
Figure 4-11 Schematic Diagram of a Type IV Interference Pattern Impinging on a Cylinder

$$\frac{q_{max}}{\varrho_{ws}U_s(H_{aw}-H_w)} \div$$

$$\text{LAMINAR} \rightarrow 0.19 \left[\frac{\varrho_{ws}U_s\delta_{SL}}{\mu_{ws}\sin a} \right]^{-0.5} where \ \delta_{SL} = 5 \left(\frac{\ell_{SL}\mu_2}{\varrho_2 U_2} \right)^{0.5}$$

$$\text{TRANSITIONAL} \rightarrow 0.021 \left[\frac{\varrho_{ws}U_s\delta_{SL}}{\mu_{ws}\sin a} \right]^{-0.2} where \ \delta_{SL} = 0.123 \ \ell_{SL}$$

BOW SHOCK

M<1

M>1

③

BODY

SHEAR LAYER

P

SL

α

IMPINGING SHOCK

②

R

M>1

M>1 ⑤

①

Q

④
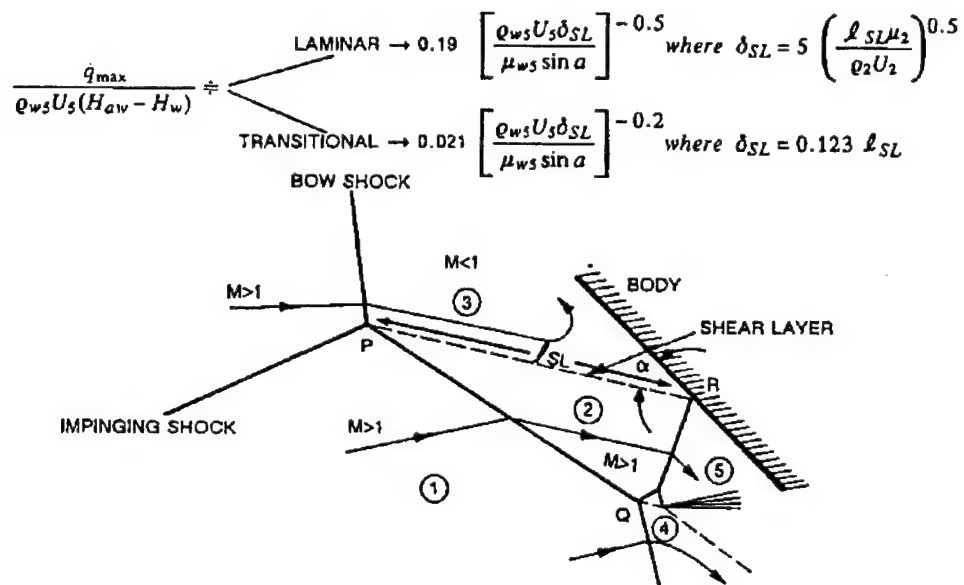
Figure 4-12 Schematic Diagram of Type III Interference

88
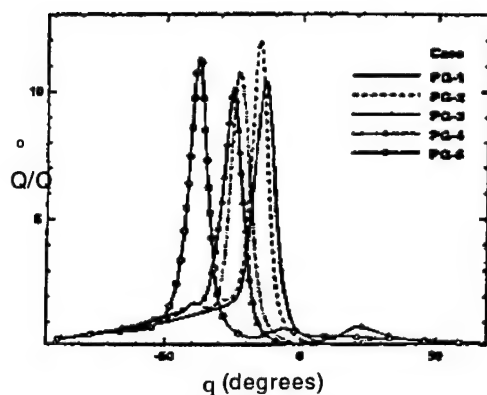
a. Perfect Gas Model Heat Transfer
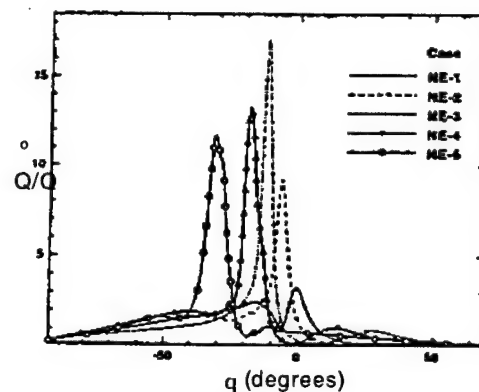
b. Nonequilibrium Model Surface Heat Transfer
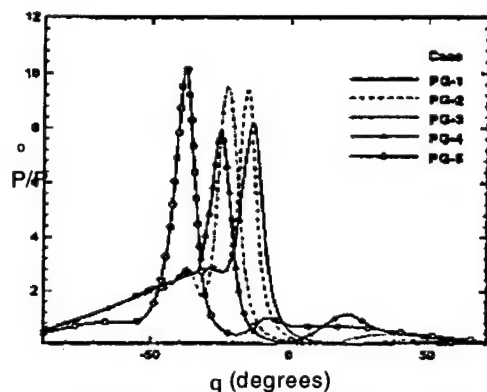
c. Perfect Gas Model Pressure Profiles
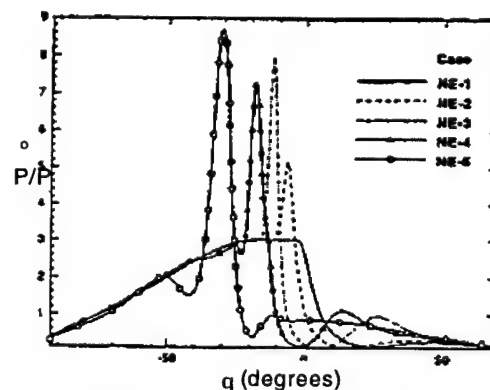
d. Nonequilibrium Model Surface Pressure Profiles

Figure 4-13   Navier Stokes Computations of Real Gas Effects on Aerothermal Loads Generated in Shock/Shock Interaction Regions by Furumoto and Zhong (Reference 3)
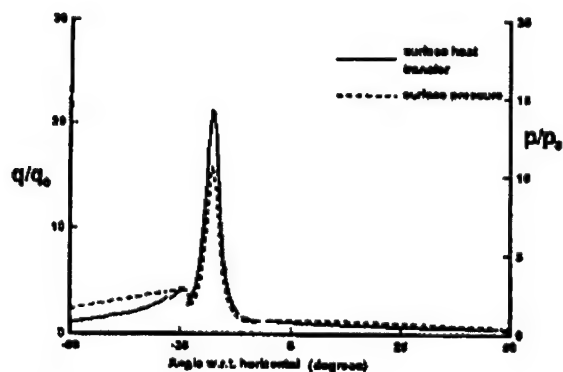
a. Surface Properties for Near Perfect Gas Case.

$q_o = 24 Mw / m^2, P_o = 1.9 \times 10^5 Pa$
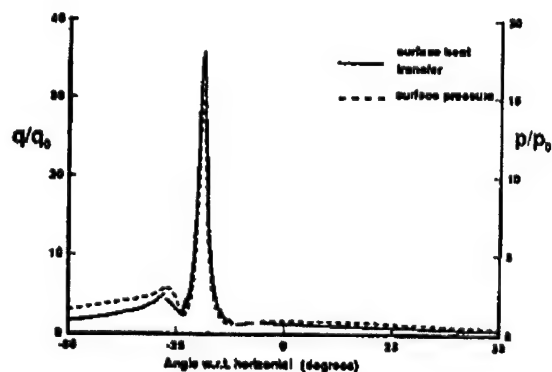
b. Surface Properties for Finite-Rate Chemistry Case.

$q_o = 15 Mw / m^2, P_o = 2.0 \times 10^5 Pa$

Figure 4-14   DSMC Computations of Real Gas Effects on Aerothermal Loads Generated in Shock/Shock Interaction Regions by Carlson and Wilmoth (Reference 7)

89
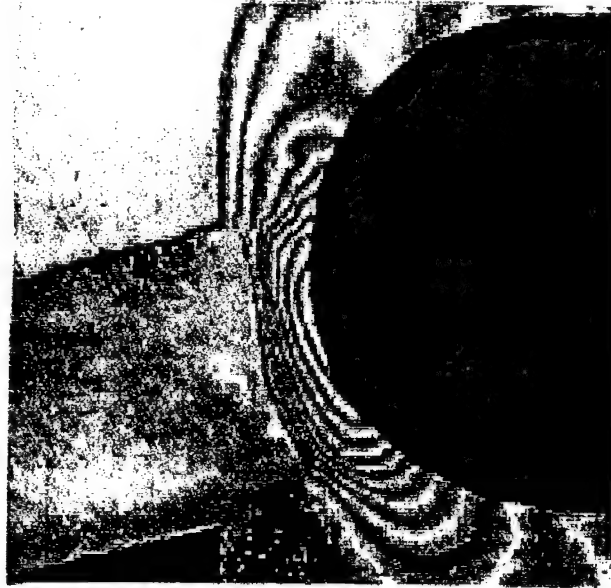
Figure 4-15   Interferogram for Type IV Shock/Shock Interaction (Reference 8)
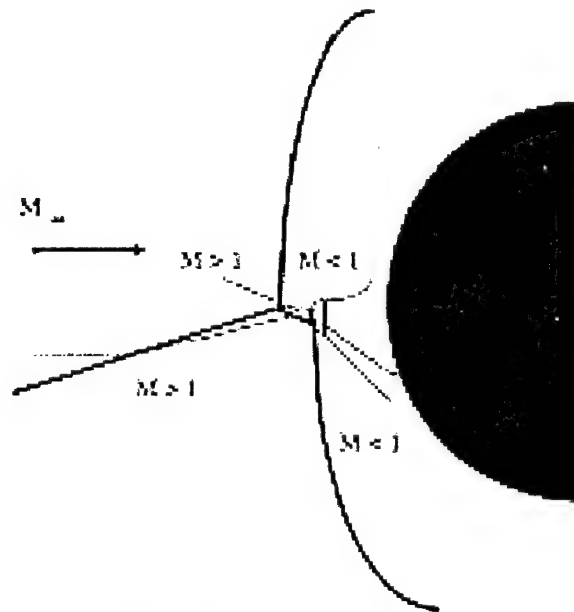
Figure 4-16   Diagram Illustrating Type IV Interaction for High Enthalpy Real Gas Flow (Reference 8)
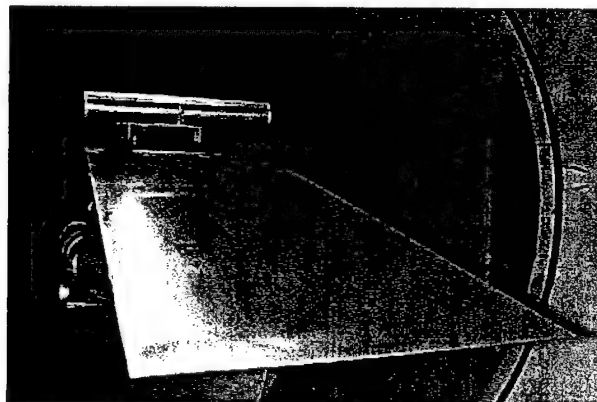
Figure 4-17   Shock/Shock Interaction Model Installed in the LENS Facility
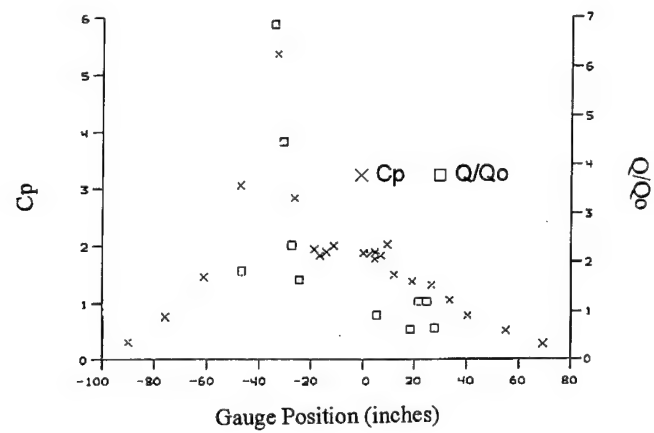
Figure 4-18 Pressure and Heat Transfer Distribution in Shock/Shock Interaction Region Over 3" Cylinder in Air At 10 MJ/kg
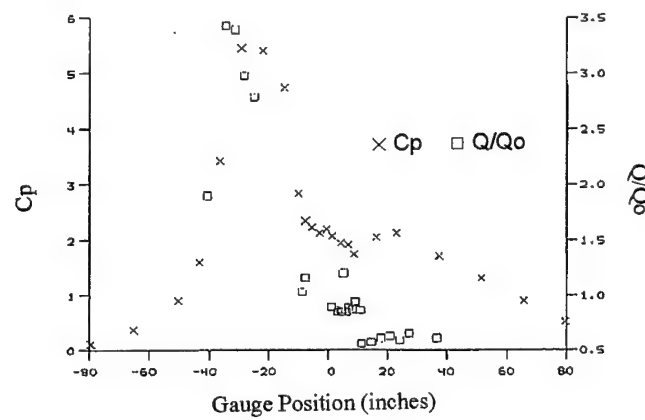
Figure 4-19 Pressure and Heat Transfer Distribution in Shock/Shock Interaction Region Over 3" Cylinder in Nitrogen At 10 MJ/kg
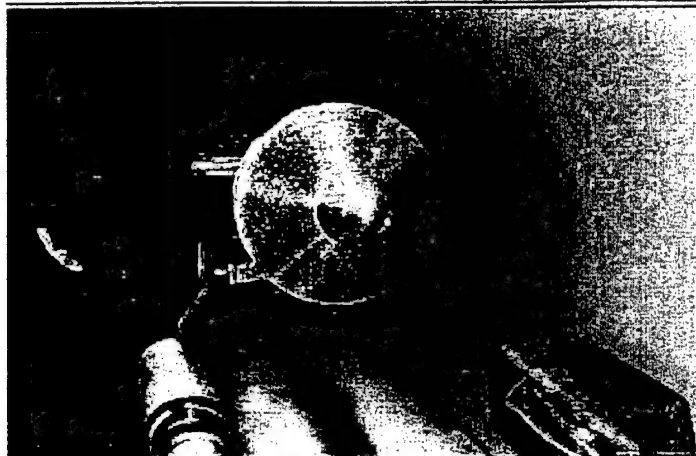
Figure 4-20 Real-Gas Effects in Regions of Multi-Shock Using Indented Nose Configuration

91
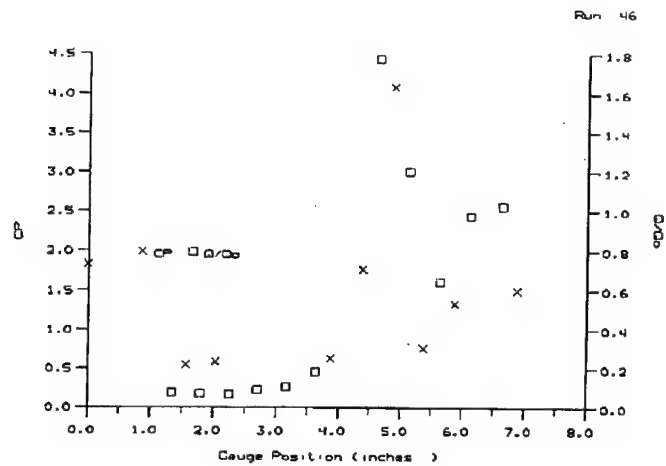
Figure 4-21 Pressure and Heat Transfer Distribution Over Blunted Cone/Cone Configuration in Air at 10MJ/kg
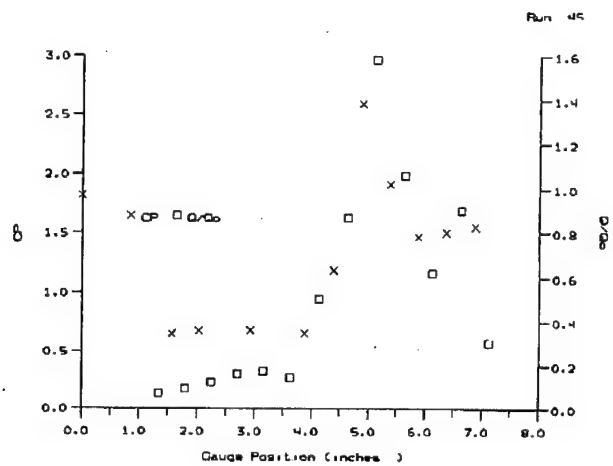
Figure 4-22 Pressure and Heat Transfer Distribution Over Blunted Cone/Cone Configuration in Nitrogen at 10MJ/kg
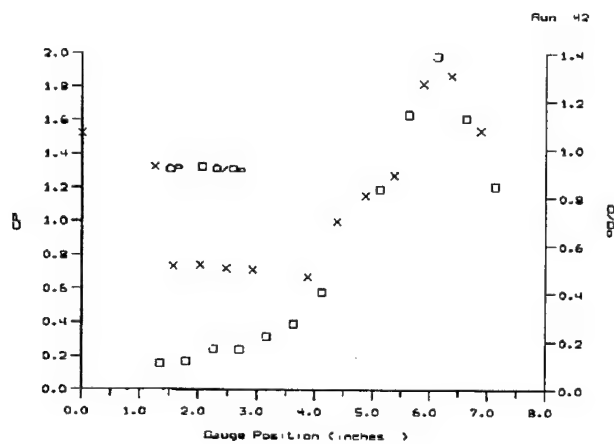
Figure 4-23 Pressure and Heat Transfer Distribution Over Blunted Cone/Cone Configuration in Air at 5MJ/kg
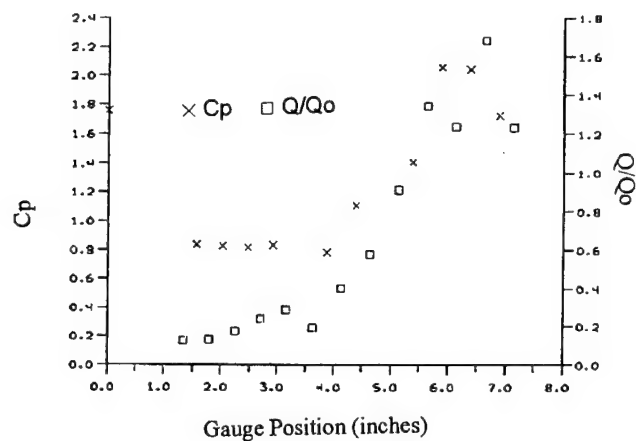
Figure 4-24 Pressure and Heat Transfer Distribution Over Blunted Cone/Cone Configuration in Nitrogen at 5MJ/kg

(a) Wedge angle 27°

(b) Wedge angle 30°

(c) Wedge angle 33°

(d) Wedge angle 45°
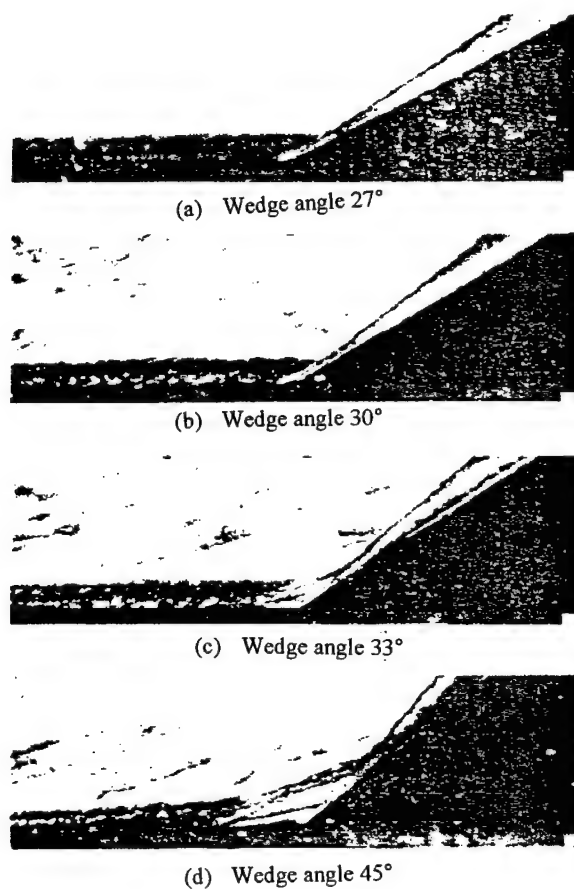
Figure 4-25 The Development of a Wedge-Induced Separated Region ($M_\infty = 8.6$ $Re_L = 22.5 \times 10^6$)

(a) SHOCK GENERATOR ANGLE = 12.5°

(b) SHOCK GENERATOR ANGLE = 15°

(c) SHOCK GENERATOR ANGLE = 17.5°

(d) SHOCK GENERATOR ANGLE = 19.8°
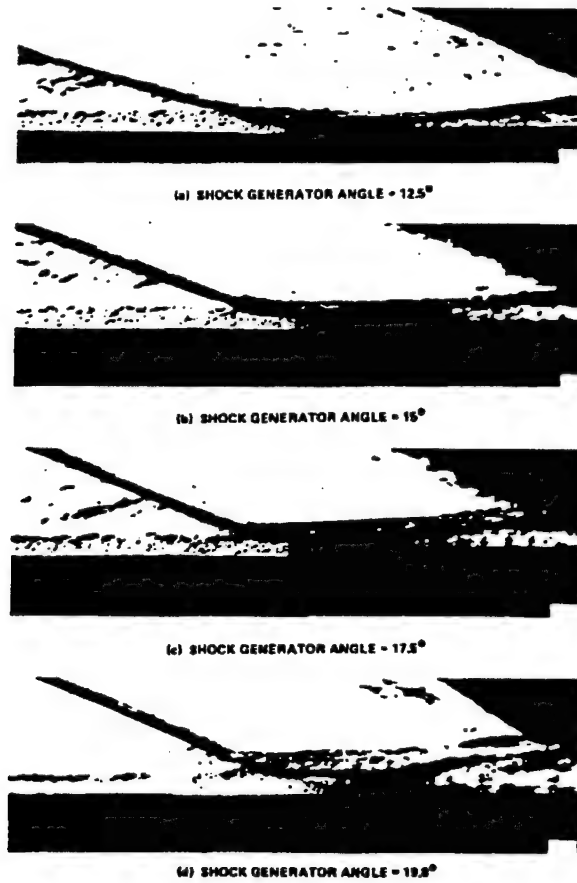
Figure 4-26 The Development of a Shock-Induced Separated Region ($M_\infty = 8.6$ $Re_L = 22.5 \times 10^6$)

UPSTREAM
OF
SEPARATION

DOWNSTREAM
OF
SEPARATION

Figure 4-28 Flow Structure in a Two-Dimensional
Corner Flow (M = 11 $Re_L = 30 \times 10^6$)
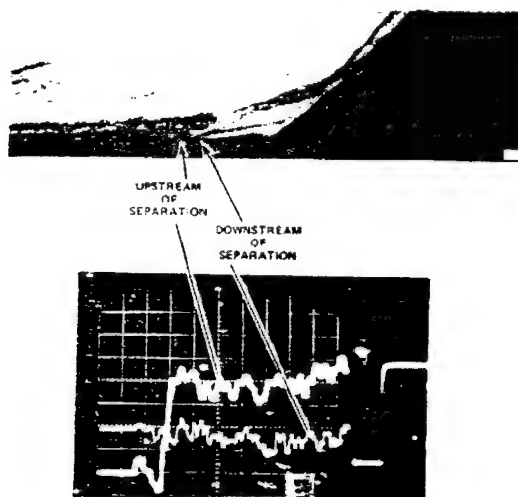
Figure 4-27 Output from Skin Friction Gages in the
Separation Region

94

Incipient Separation in Wedge-Induced Separated Flow (M∞ = 8.6, Re$_L$ = 22.5 x 10^6)
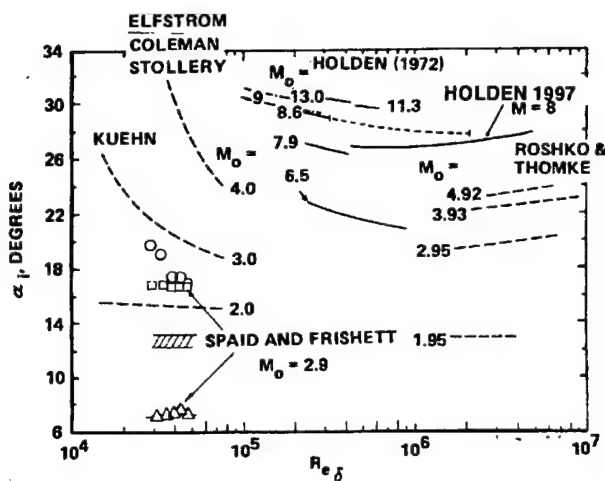
Figure 4-29a Wedge Angle to Induce Incipient Separation

Incident Shock-Induced Incipient Separation at Mach 6.5 and Re$_L$ = 27 x 10^6
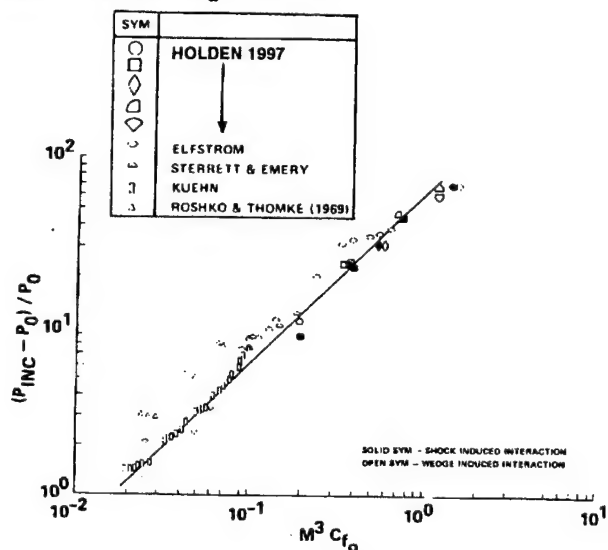
Figure 4-29b Correlation of Incipient Separation Conditions for Wedge- and Shock-Induced Turbulent Interaction Region
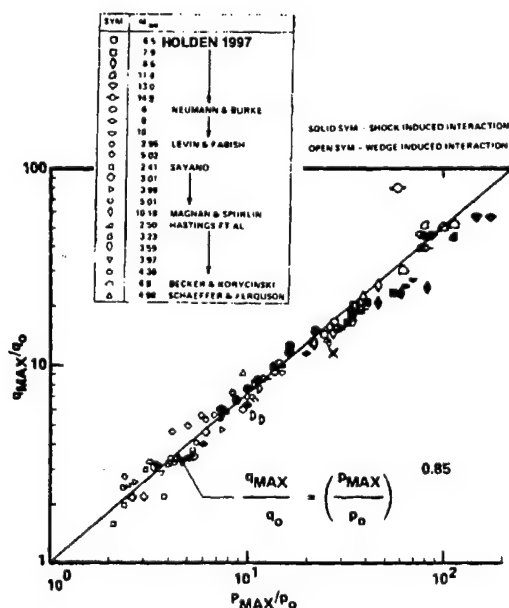
Figure 4-30a Maximum Heating Rate in Wedge- and Shock-Induced Turbulent Separated Flows
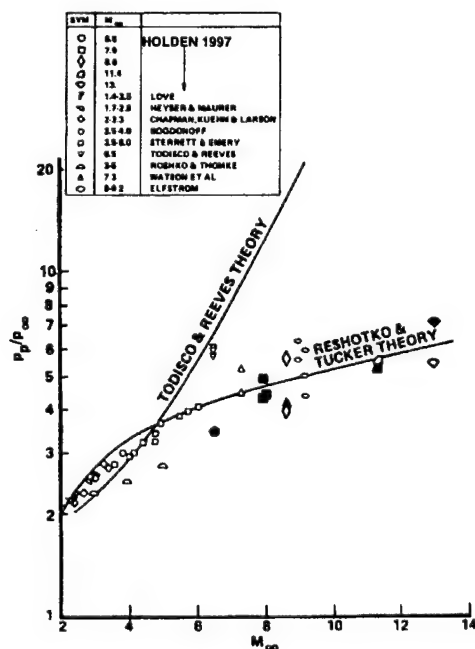
Figure 4-30b Plateau Pressure in Wedge- and Shock-Induced Turbulent Separated Regions

95
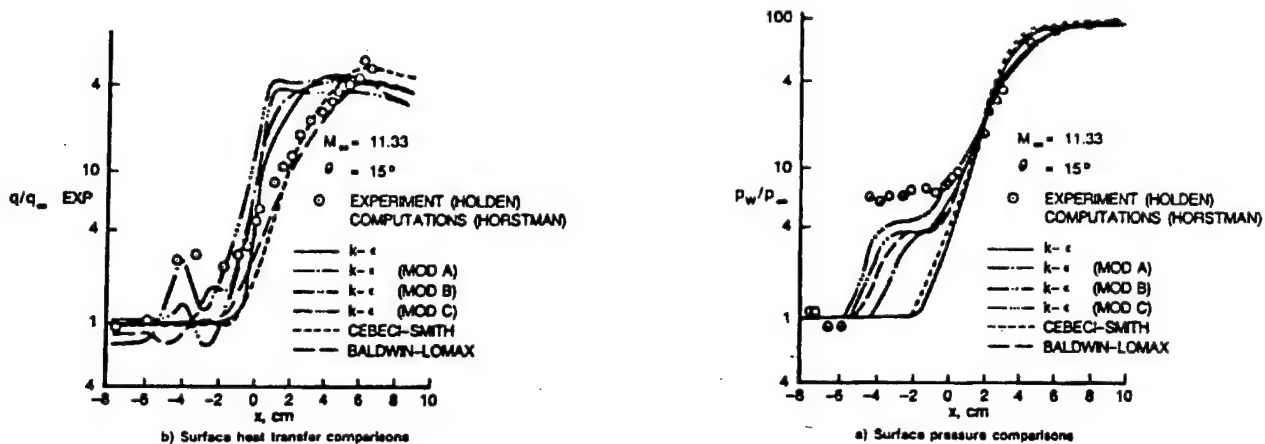
Figure 4-31 Comparison Between Navier-Stokes Solutions and Measurements in Shock-Induced Turbulent Separated Boundary at Mach 11

5 MEASUREMENTS OF FLOWFIELD CHEMICAL AND THERMODYNAMIC NONEQUILIBRIUM IN HYPERVELOCITY FLOWS

SUMMARY

In this section, we present details of the non-intrusive optical measurements that were made to investigate the characteristics of the flow in the free stream of the LENS shock tunnel, and in the shock layer of the sphere/cone/flare model. Two methods of interrogation of the flow were employed - direct flow radiance and electron beam excited fluorescence measurements. The aim of the tests was to obtain data on the species concentration and on rotational and vibrational temperatures. The latter proved to be more successful. Comparisons with Navier-Stokes computations show good agreement with both temperature components just outside the boundary layer, but measurements made in the center of the shock layer indicate a sizable overprediction in both cases. The species concentration measurements were not successful and quantitative comparisons with the numerical results could not be made. Supplementary tests to detect the arrival of the hydrogen or helium driver gas were also inconclusive. Detection of the former was based on sensing OH, which, it was assumed, would be indicative of hydrogen/air combustion. No sharp rise in OH concentration was found; instead the only evidence of this compound being present suggested that it was the product of the decomposition of trace hydrocarbon contaminants. Detection of the arrival of He proved also not to be possible because of continuum blackbody radiation in the visible wavelengths. This radiation could originate from the reservoir or throat region scattered into the detector field of view (FOV) or from minute traces of particulate in the test flow.

5.1 INTRODUCTION

This chapter describes the non-intrusive optical measurements that were made as part of the program of research to study real gas effects in nonequilibrium hypervelocity flows. Two types of diagnostic techniques were explored, namely electron beam induced fluorescence and direct radiance measurements. Both were used to study the undisturbed flow in the shock tunnel and to investigate the flow in a region between the bow shock wave and the surface of the sphere/cone/flare model.

Electron beam fluorescence measurements are made by firing a narrow pencil of high energy electrons into the test flow. Atoms and molecules within the path of the electrons become excited and then spontaneously relax to a lower energy state, usually emitting light as they do so. The wavelengths and intensity of this fluorescence are specific to the type and state of the particle from which they originate. Consequently, the technique, which is conceptually very similar to the laser induced fluorescence (LIF) method, can be used to make species specific measurements of concentration and temperature. The advantage of using a beam of electrons induce the fluorescence is that this only excites a narrow region of the flow, and thus very localized observations can be made. If appropriate optics are used to direct the light from the localized emission to the recording radiometer or the spectrometer, spatial resolution in all directions of better than 0.05 inches can be achieved. The disadvantage of both laser and electron induced fluorescence methods is that they require a detailed knowledge of the complex radiation and emission processes.

The second technique used, direct flow radiance measurements, requires the gas to be self-luminescent. For wind tunnel studies without combustion occurring in the flow, this restricts the investigations to high enthalpy test conditions where sufficient temperatures are generated for the gas spontaneously to emit thermally excited radiation. The present study, which was conducted at 5 and 10 MJ enthalpies, falls within that category. The technique has much in common with the electron beam induced fluorescence method. The same optical systems can be used, linked either to a radiometer or a spectrometer. Species specific data on the concentration and temperature components of the gas can be inferred. Since light from any point within the field of view of the optics is recorded, high spatial resolution cannot be achieved, but the method is relatively less complicated and is thus a strong contender for experiments in short duration test facilities where reliability and robustness are essential elements of any instrumentation set-up.

In the following sections of this chapter experiments will be described in which both techniques were used to make number density, rotational and vibrational temperature and shock tunnel end-of-runtime measurements.

5.2 ELECTRON-BEAM-INDUCED FLUORESCENCE MEASUREMENTS

In a series of LENS tests with the cone/sphere/flare model, electron-beam-induced fluorescence was utilized to probe the flowfield around the model. Information was sought on the gas species concentrations of NO and N_2, the rotational and vibrational temperatures of N_2 or other gas species, and the presence of contamination in the test gas.

5.2.1   Instrumentation

Figure 5-1 is a schematic of the model and the electron beam diagnostic. The electron beam gun is located inside the model. The electron beam exits the model through a graphite plug sanded smooth to the contour of the model surface and at an axial plane 6.39 inches (0.162 m) from the model nose. A radiometer is mounted on the model in such a way as to allow for its rotation and translation along the model. This movement allows initial alignment of the device and also redirection of the instrument fields-of-view (FOV). The Optical Multichannel Analyzer (OMA) is mounted inside a large aluminum box which is supported just clear of the flow so that only its "snout" containing optical elements protrudes into it.

The radiometer recorded time-resolved fluorescence intensity in a chosen wavelength region. Figure 5-2 shows the optical arrangement. An image of the gas which has been excited by the e-beam is formed on a plate with three slits machined into it, each slit is 0.012-inch wide, and the slits are separated by 0.25 inch. With a system magnification of approximately two, the three FOV's span a spatial extent of 1 inch, with each covering an ideal spatial height of 0.024 inches of the fluorescing flow.

Two 2-inch diameter CaF_2 lenses are used to form the image of the e-beam onto the slits. The use of paired lenses in this way minimizes spherical aberration and leads to improved spatial resolution. The CaF_2 lenses are UV grade to allow the use of the radiometer throughout the visible and UV wavelength regions. Since the bandpass of inteference filters is influenced by the angle at which the light passes through them, the nearly parallel light path between the lenses provides an ideal region in which to place these filters. Table 5-1 lists the filters that were used in this test series.

TABLE 5-1

RADIOMETER FILTERS

Filter Designation	Center Wavelength (nm)	Bandpass @ FWHM (nm)	Peak Transmission (%)
NO	240	21.20	19
N_2	337	2.63	27
OH	307	1.69	7
He	500	10.50	64

Coupled with Schott BG-24 Glass Filter for Blocking

In order to minimize the aerodynamic disturbance caused by the radiometer, it is aligned in the stream direction. The light from the electron beam has thus to be turned through a right angle which is done using a MgF_2 overcoated aluminum mirror. These optical components are positioned inside an aluminum housing with a chisel-shaped leading edge. This housing is closed to the flowfield by a UV-grade fused silica window. The instrument's sharp leading edge and orientation to the flow streamline direction minimize the establishment of radiating gas in front of the window.

Three Hammamatsu R292 photomultiplier tubes (PMT's) are positioned behind the slit plate as the radiation sensors. The centermost one receives the radiation directly, while the outer PMT's radiation is directed by two small MgF_2 overcoated aluminum mirrors positioned at the proper angles. The radiation spot size on the outer PMTs' faces is larger than on the center sensor, as can be inferred from Figure 5-2. A CaF_2 window (not shown in the figure) separates the PMT's from the rest of the optics, permitting their housing to be at atmospheric pressure.

In designing the radiometer, the distance between the fused silica window and the e-beam was to remain fixed at 5.750 inches. To maintain focus at the four wavelengths of interest, the lens pair had to be moved slightly, changing the magnification to the values shown in Table 5-2. Also, the radiometer was repositioned during the series of tests in order to investigate different areas of the flow. The positions were chosen so that each field of view at each location overlapped into its neighbor. For the position nearest to the model, the FOV of the lowest PMT was located 0.250 inches from the surface. Other positions are with the center PMT focused at 1.625 inches, 2.650 inches, and 3.500 inches above the model respectively.

TABLE 5-2
SLIT IMAGE MAGNIFICATION

Species	Wavelength	Magnification
NO	240 nm	2.19
N_2	337 nm	2.00
He	500 nm	1.81

Bench tests showed that the actual FOV (defined with edge intensities of 10 percent of maximum) had a height of 0.035 inches, slightly larger than the calculated product of the slit height times the magnification of 2.19 = 0.026 inches. There was also very little crosstalk between the three independent FOV's, thus yielding excellent spatial resolution.

Figure 5-3 is a schematic of the OMA configuration which was used to record the spectral content of the e-beam fluorescence over a specified period of time. This instrument was deployed directly opposite the radiometer, as shown in Figure 5-1. The detector/monochromator unit is mounted inside an aluminum box that is sealed, so that the OMA equipment remains at atmospheric pressure. A 1,200 g/mm, 300 nm blazed grating was used for all runs except He, when a 500 nm blazed grating was used. This grating allows the recording of a 130 nm spectral region, in which the center wavelength can be varied. Table 5-3 lists the center wavelengths used for each gas species.

TABLE 5-3
OMA CENTER WAVELENGTHS

Species	Center Wavelength
NO	265 nm
N_2	365 nm
OH	265 nm
He	485 nm

The e-beam fluorescence was imaged onto the slit of the monochromator by a single fused silica lens at a magnification of approximately 2. Since only a singlet lens was used, the spatial resolution of this instrument is less than that of the radiometer. Due to the nature of the OMA box mounting inside the tunnel and the changing volume of the radiating gas at various distances from the model, optically the detector area may be filled differently from run to run. This is not a problem, as the OMA is intended to compare relative spectral intensities, not absolute intensity from run to run. A fused silica window was mounted flush on the snout of the OMA box to insure that stagnating gas would not form and radiate into the optical train. Beginning with Run 10, a mechanical shutter was placed in front of the monochromator slit. The shutter was controlled to open just before the onset of flow and to close just after the data were recorded, a necessary precaution to ensure that strong radiation from post-test gas processes would not overwhelm the microchannel plate and contaminate the recorded data.

The electron beam gun, described in detail in Section 3.2.3.1, was operated with a nominal beam current of 1 ma with a 45kV accelerating potential. The e-beam current was measured by a graphite Faraday cup positioned near the model. Just before the run, this cup was repositioned out of the flowfield. The advantages of this particular design of e-beam source are its compactness and high-pressure operation. Its size allows deployment inside a model, as was utilized in this test series. Operationally the gun burns its own hole through the graphite plug separating the high vacuum filament region from the high pressure external flow. With a co-located turbo-molecular pump, the e-beam operates at tens of Torr of external pressure without significant internal attenuation of the beam due to test gas ingress.

5.2.2   Species Number Density Measurements

5.2.2.1 Nitric Oxide Radiometric Data

Nine runs were made in which air was used as the test gas and where the radiometer was equipped with the NO filter. With He as the driver gas, a freestream velocity of 3.1 km/sec was generated. Throughout these nine runs the radiometer was moved to the four positions previously detailed to obtain a profile of the NO number density from the freestream down to the model. The NO 240 nm filter used in these tests monitors the NO γ Band, 0-1 and 0-2 radiation.

Figure 5-4 shows the typical raw data traces for the three FOVs in the radiometer. The data is from Run 19. In general, all traces show a similar structure. There is a sharp start-up transient signal, followed by a relatively steady interval and flow breakdown occurring near 17 msec. In detail, traces show minor differences which give confidence that the three FOVs are indeed independent.

Figure 5-5 plots the unnormalized or raw PMT signal strength vs. the distance from the model surface for the nine NO runs. The data are averaged values from the 7 msec to 10 msec interval shown on Figure 5-4. Two runs

(3 and 16) are with the e-beam off during the run, in order to provide a measure of the background radiation contributing to the induced fluorescence signal. Run 3 contrasts to Runs 2 and 11, with a background of about 15% of the induced signal. Run 16 contrasts to Run 15. Here the background contributes less than 0.5%. A complete background check was not recorded for all of the tests, but these two yield the sense that the recorded signals are dominated by the e-beam induced signal. The differences in the two background measurements cannot be accounted for.

In Run 17, the e-beam was on, but a UV-blocking - visible transmitting filter was installed in the radiometer optical train. Since the signal level was unexpectedly high at this position, the UV blocking filter showed that the nitric oxide UV radiation, rather than any leaked visible radiation, was the dominant contributor to the recorded signal.

The remaining six runs in Figure 5-5 are intended to define the NO number density profile. Runs 2 and 11 and Runs 18 and 29 are repeats which show quite good tunnel repeatability. From pitot pressure rake data, described elsewhere in this report, the model bow shock at this e-beam axial position is determined to be located around the 2.6-inch distance from the model. Above 2.8 inches, the pressure data do not show a strong gradient since this is undisturbed freestream gas.

The results presented in Figure 5-5 are difficult to interpret. The PMT data acquisition system was not calibrated in-situ at the NO γ-band wavelengths, but the power supply voltage to each tube had been set such that each channel had very nearly the same sensitivity. The failure of the overlapping traces to join up smoothly is thus difficult to explain. Run-to-run variation in the beam current during the rest time is a possible, although unlikely, explanation. With the absence of a second radiometer monitoring the intensity of the emission at a fixed point along the beam axis, however, it is impossible to rule this explanation out as a cause of the anomoly. Adjusting the gain of each set of data to bring the overlapping traces onto the same level yields a very flat profile within the shock layer (distance < 2.6 inches), with a sharp fall in number density at the shock. Beyond the shock (distance > 2.6 inches), the number density is thus much lower than within the shock layer. Adopting this correction procedure involves making large adjustments, which is not considered reasonable. Furthermore, it produces an almost constant NO density distribution within the shock layer, which does not agree with the CFD-predicted profile. Alternative correction schemes have been tried, yielding equally uncertain results. Quantitative comparisons with the Navier-Stokes solutions of Boyd cannot be made.

The experiment has demonstrated that e-beam fluorescence intensity measurements in the UV range are feasible, but (a) the lack of comprehensive calibrations at the NO wavelength over a range of gas temperatures and (b) the failure to use a fixed point control radiometer to enable normalization of each reading to be done have resulted in a set of data that is impossible to interpret with any degree of certainty.

102

It should be noted that no attempts were made to correct the data theoretically for the effects of e-beam attentuation or of gas temperature on the fluorescence. The high levels of the uncorrected PMT output measured in the freestream, where the NO densities would be relatively low, may be due to a temperature dependence of the fluorescence, about which nothing is known.

Despite the calibration problems, it is concluded that these tests demonstrated that experiments can be conducted in a short-duration shock tunnel in which the intensity of the electron beam fluorescence is measured. The lessons learned from this series of tests suggest strongly that comprehensive bench calibrations on NO over as wide a temperature range as practical should first be performed before repeating these experiments. The uncertainties in making absolute intensity measurements can, and should be, avoided by using a fixed reference radiometer against which data can be compared and normalized.

5.2.2.2 N_2 Radiometric Data

Four runs were made in which the radiometer was equipped with the N_2 filter. Air or N_2 were used as the test gas, and, as with the NO tests, a freestream velocity of 3.1 km/sec was chosen, obtained using He as the driver. The 337 nm filter used in these tests monitored the N_2 Second Positive Band, 0-0 radiation.

Figure 5-6 plots the raw PMT signal strength versus the distance from the model surface for these N_2 runs. This series was not as extensive as the NO, and a full profile was not recorded. Runs 20 and 21 used air as the test gas, while Runs 22 and 23 used N_2 as the test gas. Run 23 is with the e-beam off as a background radiation check, and the background appears to be minimal. Run 21 (with air) has lower signals than Run 22 (with N_2). Partly this result is due to the approximate 20% decrease in N_2 number density in air, but also it gives some insight into the role of quenching in the flowfield. Results from a room-temperature calibration test demonstrating the quenching effect of oxygen on the emission from N_2 will be presented in Section 5.2.5.5. Anticipating these results, it was shown that the addition of 20% O_2 to N_2 results in about a 40% reduction in the signal. The reduction shown in Figure 5-6 is a little over 50%, which is consistent with these results if the decrease in N_2 number density in air is also taken into account.

The Navier-Stokes calculation for these test conditions shows the N_2 number density rising from the surface model towards the shock location, where it then sharply falls off to a steady value in the freestream. The steady rise appears to be consistent with the data shown in Figure 5-6, but the point outboard of the shock (which forms at about 2.6 inches) is anomolous and cannot be explained.

103

5.2.3 Vibrational and Rotational Temperature Measurements

5.2.3.1 Introduction

This chapter summarizes an analysis of electron beam excited spectrometric data acquired during a LENS shock tunnel program conducted in January and February of 1997. This program consisted of a set of 30 runs made with air or nitrogen as the test gas. Hydrogen or helium was used as the driver gas, producing free stream enthalpies of about 10 and 5 MJ, respectively. The principal observations made during this program were of the electron beam excited fluorescence of the test gas flow over a model. All of the tests were conducted at Station 2 on the sphere/cone/flare model at zero angle of attack. Detection was accomplished by use of an Optical Multichannel Analyzer (OMA). The OMA wavelength range was varied to observe the spectra from different species, as described below. All OMA data were acquired with the 1,200 lines/mm, 300 nm blaze grating with a 100 μm slit. Other supporting information acquired includes a set of data from radiometers with bandpass filters. Three OMA observation positions above the model surface were used. The furthest was 3-1/2 inches (90 mm) above the model, which was in the free stream flow. The closest position was at 1/4 inch (6.4 mm) above the model surface and was well within the shock layer. The middle position was made at a location either 1-5/8 inches or 1-7/8 inches (41.3 or 47.6 mm) above the model. These two middle positions also sample the shock layer at essentially equivalent locations.

The following section of the report is confined to an analysis of the rotational and vibrational temperature profiles in the high-velocity flow over the model and in the free stream. This analysis is based mainly upon the observed electron beam induced excitation spectra. For an initial inspection of the data, it was decided to concentrate on the analysis of the air data. Nitrogen runs showed generally complex spectra which interfered with the e-beam induced transitions useful for the temperature analysis. All air runs within the 30 run set were analyzed, including those runs which are essentially duplicates. All of the results presented are for the 5 MJ test case unless specifically stated otherwise.

5.2.3.2 Rotational Temperature Analysis

Rotational Models

The rotational temperature analysis of the e-beam induced OMA spectra was accomplished using two different models which had been developed prior to the present program. The first model was a dipole-dipole model of the N_2^+ (B-X) (0,0) vibronic band system ($N_2^+(1^-)$) based upon the work of Muntz (1962 and 1963). The second was an *ad hoc* model for the analysis of the N_2 (C-B) (0,0) vibronic band system ($Ni(2^+)$) based upon the assumption of the establishment of a Boltzmann rotational distribution in the emitting C state.

Muntz, in the above references, pioneered rotational temperature analysis of electron induced spectra of N_2. In $N_2^+(1^-)$ electron beam induced fluorescence, primary electrons simultaneously ionize and electronically excite the N_2 to produce the N_2^+ ion in its excited B state. This state emits radiation in a transition down to the ion's ground X state. The B v'=0 to X v"=0 band system shows P and an R branches. Muntz (1962) gives expressions for the R branch. The expressions for the P branch were derived. The relative intensity of the various transitions is, of course, a function of the rotational temperature. A FORTRAN program was written to use these expressions to calculate the transition intensities as a function of wavelength. In order to match the partially resolved band shape observed with the OMA, a variable Gaussian instrumental linewidth smearing function was used. This instrumental line width can be obtained from mercury calibration spectra of the OMA. The entire spectrum generation program was incorporated in a least squares fitting program, so the actual OMA spectrum could be directly fit. The parameters in the fitting program were: (1) a baseline offset to account for imperfect OMA baseline subtraction, (2) a wavelength offset to account for imperfect OMA wavelength calibration, (3) the spectrum intensity, and (4) the rotational temperature. Two different versions of the model were developed. The first had only the four parameters described above and required the input of the Gaussian instrument width obtained from a mercury lamp calibration spectrum. The second version added the Gaussian instrument width as the fifth parameter. Only the rotational temperature parameter affects the shape of the rotational envelope; therefore, the rotational temperature is very sensitive to the width of the observed OMA spectrum.

A second model was used to fit the $N_2(2^+)$ electron beam data. In contrast to the well-established and theoretically justified $N_2^+(1^-)$ model described above, no model has been established to describe the $N_2(2^+)$ e-beam induced spectrum. Hence, the assumption was made that the electron excitation, which is accomplished by secondary electrons, produces a Boltzmann rotational distribution in the N_2 C state. This assumption allows the calculation of the rotational lines as a function of rotational temperature. These expressions were incorporated into a FORTRAN fitting program very similar to the $N_2^+(1^-)$ program described above. The fitting parameters were the same as the other model. There were also two versions of the model having either five or four parameters, depending on whether the Gaussian instrumental function is fit or derived from a mercury calibration spectrum. The validity of this $N_2(2^+)$ temperature model can only be judged from its success or lack thereof in data fits where a direct comparison can be made to either the $N_2^+(1^-)$ model or in data fits at known conditions.

Rotational Temperature Fits

The $N_2^+(1^-)$ model has been applied to room temperature calibration data during the present program and on previous programs. The results have been consistent in indicating temperature slightly above room temperature. Typically, temperatures in the 350 to 400K range are obtained. This increase above room temperature could be explained by the slight heating of the near stagnant gas in the calibration chamber. For the present program, three 5 MJ air runs were analyzed with the $N_2^+(1^-)$ model. For Run 21, the observation position was 3-1/2 inches above the model surface, which implies free stream conditions. Figure 5-7 shows the data points (circles) and the model fit.

.

(line). The rotational temperature obtained in the fit is 158 (22) K, where the number in parenthesis is the standard deviation of the temperature parameter. This low rotational temperature was expected for the free stream. Runs 30 and 11 are at the 1-7/8 inch position which was within the shock layer. Table 5-4 shows a summary of the rotational temperature fits. Figures 5-8 and 5-9 show the data fits for Runs 30 and II. The $N_2^+(1^-)$ model shows values on the order of 2,000 K for this observation position, which is about 25% higher than Boyd's Navier-Stokes calculations. Unfortunately, the $N_2^+(1^-)$ band data at the 1/4-inch observation position are obscured in Runs 15 and 17 by the presence of other transitions, which precludes a $N_2^+(1^-)$ rotational temperature analysis.

TABLE 5-4
ROTATIONAL TEMPERATURE SUMMARY

Position (inches)	Run No.	$N_2^+(1^-)$ Temperature (K)	$N_2(2^+)$ Temperature (K)
3-1/2	21	158 (22)	–
1-7/8	30	2,316 (253)	2,232 (144)
1-7/8	11	1,944 (258)	2,080 (109)
1/4	15	–	1,905 (173)
1/4	17	–	1,845 (160)

To attempt to gain information about the rotational temperature in the 1/4-inch position, the $N_2(2^+)$ model was used. To establish the validity of the model, the $N_2(2^+)$ data from Runs 30 and 11 were fit. Figures 5-10 and 5-11 show these fits. The comparison of the rotational temperatures obtained using the two different models is shown in Table 5-4. In both cases, the rotational temperatures agree within 150 K, which is identical within statistical expectations. The empirical conclusion is that the $N_2(2^+)$ model seems to be satisfactory. With this success, the $N_2(2^+)$ model was applied to Runs 15 and 17 at the 1/4-inch position. The fits are shown in Figures 5-12 and 5-13. The rotational temperature is slightly lower at the 1/4-inch position than at the 1-7/8-inch position, as indicated in Table 5-4. The result at 1/4-inch agrees closely with Boyd's Navier-Stokes calculations described in Section 3.3.3.3 (see Figure 5-14), but the experiment yields substantially higher rotational temperatures than the predictions at 1-7/8 inches from the surface. The measurement at 3-1/2 inches agrees quite well with the expected value and confirms that the shock wave was nearer to the surface than this point.

5.2.3.3 Vibrational Temperature Analysis

Three different types of data were used to derive vibrational temperatures. The first was an e-beam excited $N_2(2^+)$ emission. The second was the thermal excitation of OH, which was observed in two runs. The third was

.

unexpectedly strong NO (A-X) emission, which is e-beam induced. The remainder of this section describes the models that were formulated and their application to a vibrational temperature analysis of the data.

$N_2(2^+)$ Emission Temperature Model and Analysis

$N_2(2^+)$ e-beam induced emission data were taken on the OMA over a wide spectral range from 300 to 430 nm, which included the following vibrational bands on the C-B system: 2,1; 1,0; 0,0; 1,2; 0,1; 1,3; and 0,2. Figures 5-15 and 5-16 show the observed data for Runs 11 and 21 at the 1-7/8 inch and 3-1/2 inch observation positions. A model was developed in which the initial excitation of the C state and the emission on the C-B electronic band system were accounted for by the standard treatment (Hertzberg (1950)):

$$I_{abs} \; \alpha \; N_{v''} \; \nu_{v'v''} \; q_{v'v''} \qquad (1)$$

$$I_{em} \; \alpha \; N_{v''} \; \nu_{v'v''} \; A_{v'v''} \qquad (2)$$

where I is the intensity of the observed absorption or emission transition, ν is the vibronic transition frequency, A is the Einstein A coefficient, q is the Franck-Condon factor, and the subscripts v' and v'' refer to the vibrational state of the upper and lower electronic states. The vibrational temperature dependence in the model enters through the value of $N_{v''}$. A literature search for the values of the constants required in Equations 1 and 2 for nitrogen was conducted. The values were taken from Forrest et al. (1992). A program was written to calculate the temperature dependence of all observed vibrational bands. The ratio of the intensity of (v', v''/0,0) is shown as a function of temperature for all observed vibrational bands in Figure 5-17. Due to an unfortunate coincidental similarity of some of the constants used in both Equations 1 and 2, the v'=0 and v'=1 sequences show very similar temperature dependencies. Therefore, as shown in Figure 5-16, the ratios of any two of the v'=0 and v'=1 bands are virtually independent of temperature. A fact confirmed experimentally by comparing Figure 5-15 (Run 11; 1-7/8-inch position in shock layer) and Figure 5-16 (Run 21; 3-1/2-inch position in free stream) which correspond to positions in the flow with grossly different vibrational temperatures. The relative peak heights of the various v'=0 and v'=1 bands can be seen to be quite similar. Only the 2,1 band shows any substantial temperature dependence. Figure 5-18 shows the ratio (2,1/1,0) as a function of temperature. Note the flat temperature dependence below 500 K. At these low temperatures, vibrational excitation is so minimal that it is irrelevant to the ratio. Only upon substantial vibrational excitation at temperatures above 500 K does the ratio show a measurable and useful temperature dependence.

Three test runs (11, 21, and 30) were completed before it was appreciated that deriving the vibrational temperature from the $N_2(2^+)$ spectra was to prove very difficult; the vibrational temperature could have been determined by choosing another band from the N_2 spectrum. The most obvious candidate, because of its brightness, would be the N_2^+ (1⁻) band. There is, however, a very rapid transfer of energy between the ionic and vibrational modes, there is a danger that the vibrational temperature of the excited molecules will be increased above its true value. The use of this band was, therefore, not entertained. Figure 5-15 (Run 11) shows a spectrum measured within

the shock layer where the temperature would have been above 500 K, and the (2,1/1,0) intensity ratio method should yield results. Unfortunately, two further problems are encountered in analyzing the data. The first is that, at this higher rotational temperature, the vibronic bands get much wider. This was used as the basis for obtaining rotational temperature, as described in the previous section. However, this broadening of the bands causes the 2,1 and 1,0 bands to overlap severely, which greatly complicates the vibrational analyses. The second problem is that, unfortunately, the OH (A-X) band system also overlaps into this spectral region. A considerable effort was made to subtract out the OH band and to fit the shape of the 2,1 and 1,0 spectral region. The results were not satisfactory. No credible vibrational temperature analysis of these two runs was possible. Attempts were not made to use the $N2^+$ spectra for the reasons given above.

A free stream $N_2(2^+)$ spectrum is presented in Figure 5-16 (Run 21), but as the flow temperature is below 500 K, a meaningful value of the vibrational components cannot be deduced from these data. All that can be concluded is that it is below 500 K.

OH Vibrational Temperature Analysis

Runs 4 and 9, with 1-5/8-inch observation positions within the shock layer, exhibited an OH (A-X) band system strong enough to see the 0,0 and 1,0 transitions. These data were analyzed assuming a thermal excitation model for the band emission. Using this model, the ratio of the (1,0/0,0) bands is determined by the Boltzmann population distribution and Equation 2. A literature search for the pertinent constants produced Richards et al (1987). The intensity ratio required to obtain the vibrational temperature was determined for each run by two different methods as a check. The first method was to ratio the peak heights and the second method was to ratio the peak areas. The data for Run 4 were obtained from early in a test run in which a helium driver was used. As shown in Table 5-5, the two methods produced OH vibrational temperatures slightly below 3,000 K. In Run 9, a hydrogen driver was used, producing a 10 MJ test flow, which presumably would yield a higher temperature than the helium driver if all other factors were constant. The vibrational temperature from the peak height ratio is 3,222 K. However, the peak area analysis yields a value below 3,000 K. The peak height analysis may be more reliable in this case, judging by the higher temperature obtained from the hydrogen run.

TABLE 5-5
OH VIBRATIONAL TEMPERATURE

Run	Enthalpy	Tvib Peak Area	Tvib Peak Height
early 4	5 MJ	2,970 K	2,950 K
9	10 MJ	2,803 K	3,222 K

NO Vibrational Temperature Model and Analysis

The NO (A-X) electron beam induced emission was surprisingly intense for such a minority species in the flow. These spectra also present a great challenge to make a valid vibrational temperature analysis. The NO data in Runs 20, 19 and 18 are shown in Figures 5-19, 5-20, and 5-21, respectively. The v'=0 sequence clearly is much more intense than the v'=1 sequence. The first model attempted was an excitation-emission model using Equations 1 and 2 similar to the $N_2(2^+)$ vibrational temperature model. The predictions of this model bore no resemblance to the data recorded in Runs 20, 19 and 18. The exact reason for this model failure is not understood at the present time. However, the energy levels of the two electronic systems are very different. The $N_2(2^+)$ system is a three-level system. Excitation goes from the N_2X^1 ground state to the extremely high energy C^3 state. The emission is on the C^3 to B^3 electronic transition. The molecule is left in an excited triplet state well above the ground singlet state. The NO(A-X) system has two-levels. The molecule starts in the X^2 ground state and makes an allowed transition to the lower energy A^2 state. Since this is a resonance transition it rapidly radiates right back down to the X^2 state. The high intensity of the NO emission compared to the $N_2(2^+)$ emission raises the possibility of an entirely different electron excitation mechanism being operative. Therefore, the failure of the excitation-emission model is disappointing, but not surprising.

A different model was adopted for the NO vibrational temperature analysis. The assumption was made that the vibrational levels of the NO A state were produced in a Boltzmann distribution. This assumption can only be justified based upon comparisons with data fits from other models, since there is no theoretical foundation. The emission then proceeds according to Equation 2. This model is similar to the model used for the OH vibrational temperature analysis. Once the expressions for the vibrational band intensities were written as a function of temperature, they were incorporated into a least squares fitting program. In this way, the relative peak intensities of all of the various v'=0 and v'=1 transitions can be used to fit the vibrational temperature. One further complication must be accounted for. The transitions which end in v"=0 will be strongly self-absorbed. This effect is obvious from an examination of the 1,0 and 0,0 bands in Runs 20, 19 and 18, shown in Figures 5-19, 5-20 and 5-21. The intensity of these bands is substantially smaller than would be predicted from their A coefficients due to radiation trapping. Furthermore, at large vibrational temperatures, the vibrational population in the v"=1 state is substantial enough that some self-absorption of the 0,1 transition occurs, although the effect is less pronounced than for the 1,0 and 0,0 self-absorption. The simplest solution to this problem is to eliminate the 1,0 and 0,0 bands from all of the vibrational temperature fits and the 0,1 band from the high-temperature shock layer fits.

Using this vibrational model, the shock layer (1/4-inch position) data from Run 18 was fit. The vibrational temperature obtained from the data fit was 3116 (535) K, which is shown in Figure 5-22 compared with Boyd's Navier-Stokes prediction. The spectrum in Run 19 was also obtained at the 1/4-inch position; however, it was taken very late in the test, essentially after the valid test time. A somewhat lower vibrational temperature, 2,355 (163) K, was obtained. This lower temperature reflects changes occurring right at flow breakdown and incidentally is

109

consistent with flow breakdown occuring when predicted. Figures 5-19 and 5-20 show the observed data (line) and calculated peak intensities from the model fit (bars).

Using the vibrational model, the free stream data from Run 20 were analyzed. Figure 5-19 shows the observed data and calculated peak intensities from the model fit. The determined vibrational temperature is 1,461 (282) K, which is significantly higher than the <500 K value for N_2 obtained from the $N_2(2^+)$ vibrational temperature analysis of the free stream. It is difficult to decide which is the better measurement. The N_2 model would seem to be on firmer theoretical grounds. However, the sensitivity of the (2,1/1,0) ratio to low vibrational temperatures is poor. An error of less than 20 percent in the measured ratio would be sufficient to bring the two temperatures into agreement at the higher value. A course of action that could help to resolve this problem would be to make an NO room temperature calibration and use the present model to see if the determined vibrational temperature was near room temperature.

5.2.3.4 Future Experiments and Lessons Learned

The present program was well executed in the sense that a good range of quality data was taken. The unfortunate and essentially accidental flat temperature dependence of the v'=1 and v'=0 $N_2(2^+)$ vibrational band intensities proved to be a major obstacle to obtaining a vibrational temperature profile from the N_2 spectra. The (2,1/1,0) ratio might still produce reliable vibrational temperature profiles if certain precautions are taken. The first measure would be to clean up the residual OH signal presumably originating from outgassed H_2O or, more likely, from other contaminants, such as hydrocarbons, which were present during most runs. While this signal was not very intense on Runs 11 and 30, it still was substantial enough to interfere with the accurate determination of the (2,1/1,0) ratio. The problem of overlap in the 2,1 and 1,0 vibrational bands may be ameliorated by obtaining high-resolution data in this spectral region.

Obtaining high-resolution data would also be a way of improving the NO vibrational data analysis. One possibility would be to accurately measure the (1,5/0,4) ratio near 270 nm.

Finally, one immediate experimental measurement which would help to resolve some of the vibrational temperature problems would be to make a room temperature calibration study of the NO e-beam induced spectrum. As discussed above, such a measurement would either provide some measure of confidence in the NO vibrational model or expose it as invalid. An investigation into the temperature dependence of the electron beam excited emission of NO would be worthwhile.

5.2.3.5 Summary

In summary, a rotational analysis of the e-beam data has been conducted using two different models for the two different types of N_2 vibronic spectra. The measured free stream rotational temperature agrees closely with

the expected value from the shock tunnel calibration. The 1-7/8-inch shock layer temperature from both the $N_2^+(1^-)$ and $N_2(2^+)$ models is on the order of 2,000 K, which exceeds Boyd's Navier-Stokes predictions (see Figure 5-14). However, the $N_2(2^+)$ model fit of the 1/4-inch position data shows a rotational temperature that agrees well with the prediction.

The vibrational analysis of the e-beam data was less successful in terms of number of data points. The free stream value obtained from the $N_2(2^+)$ model of <500 K is considerably lower than the NO free stream value of 1,461 K. The $N_2(2^+)$ vibrational analysis was unable to produce a vibrational temperature for the shock layer, largely due to interference from other bands and overlap of the bands being rationed. The OH vibrational analysis was consistent and produced a vibrational value of approximately 3,000 K for the I-7/8-inch shock layer, which again exceeded the Navier-Stokes prediction. However, data were not available at other positions. The NO 1/4-inch observation position data produced a vibrational temperature of 3,100 K, which agreed closely with the computed value. Note that both the rotational and vibrational temperatures at the 1/4-inch position is similar to those at the 1-7/8-inch position. However, the Navier-Stokes computations predict considerably lower temperatures for both the translation and vibration at the 1-7/8 inch position.

These experiments have shown that consistent and plausible rotational and vibrational temperature data can be obtained in high-enthalpy flows using electron beam excitation and spectroscopic techniques. Several schemes used to reduce the data proved to be unsuccessful for a variety of reasons. Thus, care has to be exercised in deciding on the method to be used in any future applications of these techniques.

5.2.4 OH Radiometric and Spectral Data

Several tests were completed with the radiometer configured with the OH filter described in Table 5-1. The e-beam was not used, and the radiation observed was the result of thermal excitation behind the bow shock of the cone/flare model. The presence of OH was initially thought to be indicative of H_2O in the flow, but may originate from other hydrocarbon sources.

Table 5-6 lists the OH radiometric data for the three FOVs with air and N_2 as the test gas. The sequence is divided into two main subgroups, regular procedure and vacuum pumped procedure. These categories refer to the preparation of the driven tube before loading the test gas. In the regular procedure, the driven tube is evacuated by a mechanical vacuum pump to less than 1 Torr of pressure and then filled with the test gas. This procedure is done three times before the test gas is left in the driven tube for the run. In the vacuum pumped procedure, the driven tube is evacuated for at least six hours by a liquid nitrogen trapped diffusion vacuum pump to the 10^{-4} Torr pressure range to eliminate adsorbed water.

111

TABLE 5-6
OH RADIOMETRIC DATA

Run	Test Gas	Driver	Procedure	FOV1	FOV2	FOV3	Average
5, 6, 7	N_2	He	Regular	1.69	4.56	2.36	2.87
28	N_2	He	Vacuum	0.29	0.70	0.36	0.45
3, 4, 10	Air	He	Regular	0.07	0.13	0.11	0.10
30	Air	He	Vacuum	0.11	0.23	0.11	0.15
9	Air	H_2	Regular	1.94	3.67	2.12	2.58

The signal levels reported are average values derived from the 7 msec to 10 msec time interval for the He driver and from the 4.75 msec to 6.75 msec time interval for the H_2 driver. These time intervals are representative of the steady-state test flow for each condition.

Figure 5-23 shows a typical radiometric trace for the He driver with air as the test gas. The start-up transient is seen, followed by a fairly level, but slowly decaying signal lasting well beyond the end of the steady flow test period. The form of the trace is not unlike that seen in the radiometric traces for NO or N_2 in air. Figure 5-24 shows a typical trace for the H_2 driver with air as the test gas. A form of the trace similar to that in Figure 5-23 is seen, but the signal level is significantly increased due to the higher enthalpy. There is no indication of a rise due to water coming from combustion occurring at the interface between the H_2 driver and air driven gases, which would be expected to occur a few milliseconds after the steady test period. The peak towards the end of the trace is known to be due to the flow impinging on the end wall of the test section, sending a reflected wave back towards the test area, causing residual particulates to light up brightly.

Figure 5-25 displays a sample steady-state spectrum typical of both the He and H_2 runs with air. The OH 307 band dominates the spectrum with two atomic Cu lines noted and some low-level signal in the region of the NO γ bands. Spectra recorded at times later than steady state show a weaker OH 307 band riding on top of continuum radiation. Thus, the steady-state radiometric values reported in Table 5-6 are indeed representative of

For the air runs, one concludes from the data in the table that the higher enthalpy run with the H_2 driver does indeed produce more OH. However, the level is higher earlier in the run, and there is no evidence of a sharp increase at the expected time if burning of the driver gas has taken place. Further, on the basis of one run, the overnight vacuum pumping of the driven tube does not appear to affect the OH signal level. A result which suggests that the observed OH is not a dissociated product of residual H_2O, but a product of residual hydrocarbon

Figure 5-26 shows a typical radiometric trace for the He driver with N_2 as the test gas. This trace has a character very different from that of air. The start-up transient is dwarfed by a much larger signal that decays during the steady run time. Similar traces are seen for the H_2 driver with N_2 as a test gas.

Figure 5-27 displays a typical recorded steady-state spectrum for N_2 as a test gas. The OH 307 band is not seen in the spectra. There are some atomic and molecular spectra evident, but they are superimposed on a large continuum. Spectra recorded at times earlier than the steady state are similar to those in Figure 5-27, but a moderate amount of OH is present along with the continuum. Thus, the steady-state N_2 radiometric values reported in Table 5-6 are not representative of OH radiation, but are continuum radiation. The early time OH radiation may be from the residual air or water vapor in the nozzle/test section volume being excited and passing by the observation FOV. The lack of OH radiation during steady-state may be attributed to the lack of O_2 present to react with residual hydrocarbons to form OH. Again, there is an indication that residual H_2O in the driven tube is not a major contributor to observed OH signals during steady-state, since the same level of H_2O should be present for both the air and N_2 runs.

Spectra obtained at other wavebands indicate the presence of Si and CN during the nitrogen tests. The former suggests that traces of contamination exist that probably originate from Si rubber components used as seals on the shock tunnel. Neither Si nor CN were formed when air was used as the test gas; it is likely that oxides were formed which were not detectable in the observed spectroscopic bands.

From Table 5-6 one sees that the continuum radiation detected in N_2 runs is larger than the OH radiation detected in air runs. Also, as would be expected, the higher enthalpy H_2 driver run produced greater continuum excitation. Finally, based on one run, the six-hour vacuum pumping of the driven tube appears to have some lowering effect on the continuum radiation.

One concludes from these tests that there is no indication of water being present when H_2 is used as a driver gas. Although OH is detected, the levels suggest that the primary source of OH is not residual adsorbed water but traces of hydrocarbon contaminants in the driven tube.

5.2.5   Driver Gas Detection

5.2.5.7 *Introduction*

The electron beam fluorescence method has been proposed as a means to detect the arrival of the driver gas in the test region. This section of the report summarizes an experimental and theoretical study that was done to assist the design of such a program. The main goal was to investigate the detection of helium driver gas in small concentrations in air flows for pressures ranging from 5 to 50 Torr. The use of alternative seeding gases which could be introduced in the plenum between the double diaphragms has also been investigated. As a consequence,

tests on the emission from Argon were undertaken. Finally, the detection of molecular nitrogen at high pressures in the presence of O_2 is examined briefly.

5.2.5.2 Experimental Setup

The Calspan electron gun was aimed into a small calibration chamber into which mixtures of gases could be introduced. The chamber was fitted with a circular quartz window, allowing the observation of the beam area from an OMA spectrometer. The voltage of the beam was kept constant at 50kV for all the measurements, while the Faraday current was kept almost constant at 0.5 mA for most of the He experiments and 0.2 mA for the Ar experiments. The experiments were conducted for total pressures ranging from 5 to 50 Torr, while the concentration of the detection species varied from 3 to 20%. All the experiments were conducted at room temperature, which was measured to be about 292 K. The facility used did not allow the variation of the gas temperature.

The radiation intensity was measured as "counts", or radiation events. The number of counts that one gets from a gas flow depends on:

a) the density of the flow, or the pressure for isothermal conditions.

b) the density of the electron beam (number of electrons per second entering the flow field)

c) the voltage of the electron beam (i.e. the energy of the electrons)

d) the fraction of radiating particles in the flow.

The gases that were used in this investigation were N_2, O_2, He, and Ar. Initially an 80% N_2 20% O_2 mixture was made, and then either He or Ar was gradually introduced in increasing fractions. The tests were conducted at total pressures ranging from 5 to 50 Torr.

5.2.5.3 The He Spectrum

There are three main lines in the He spectrum i.e., 4921.9 Å with spectroscopic code $4^1D_2 - 2^1P_1^0$, 5015.7 Å with spectroscopic code $3^1P_1^0$-2^1S_0, and 5047.7 Å with spectroscopic code 4^1S_0-$2P_1^0$. The lines at 4921.9 and 5015.7 are the brightest in the spectrum of He. The 5015.7 Å line band is excited by primary electrons, whereas excitation of the two others is mainly caused by secondary electrons.

From previous studies (Muntz (1968)) of the properties of He fluorescence induced by an electron beam, it has been concluded that the 5015.7 line band is the most suitable for the detection of He. Although this line is very bright, the excited particles can lose their energy relatively easily in collisions with atmospheric species, and the radiation is thus quenched. We will discuss this subject in more detail in the following paragraphs.

5.2.5.4 *Prominent Lines in the Same Area of the Spectrum*

To be able to detect a He line, one must make sure that there are no other significant lines or bands from other atmospheric species in the same area of the waveband. Since the "window width" of the spectrometer (OMA) in our investigation was 50 nm, we are interested in lines that are within ±25nm of the target wavelength. In the general area of the He spectrum, N_2 has no significant transitions. The most important line bands in this area are at 4709.2 and 4651.8 Å, the strengths of which are only a fraction of the He line in question. The O_2 lines in the same area are at 4649.14, 4641.81, and 4638.85 Å. Again, these transitions are less significant than the He line band. For this reason, the 5015.7 Å line band has almost exclusively been used for its detection. The excitation transition is an allowed one, ensuring short lifetimes; in addition, the excitation transition can only be initiated by incident electrons (excitation cross section peaks at around 400 eV).

5.2.5.5 *Quenching Characteristics*

As mentioned earlier, the radiation emitted from a gas is proportional to the density of this gas. On this basis, one would expect the radiation from an electron beam to increase linearly with the density of the flow. However, this is not always the case. Intermolecular collisions between particles electronically excited by the electron beam and other particles of the flow can, in some cases, be very efficient in de-exciting the electronic states of a particle before it emits radiation. This phenomenon is called quenching. Not all species present the same characteristics in terms of how easy it is to de-excite them. Quenching is an undesirable effect, since it can significantly reduce the signal output of an electron beam (especially from dense flows) and confuse any

The evaluation of quenching in a gas can be defined by calculating the gradient of the light intensity as a function of the pressure. It has been found that a linear relationship is generally valid for all gases of the form:

where p is the pressure of the gas and p' is a parameter. The p' for various gases and transitions of interest are given in Table 5-7.

TABLE 5-7
QUENCHING COEFFICIENTS

Gas Transition	p'
CO_2 (3600-3700)	1.1
He (5015.7)	1.7
N_2 (first negative)	1.9
N_2 (second positive)	35
N_2 (pure nitrogen gas)	3

CO_2 would be an attractive contender for the end-of-run time (ERT) detection, as it is a strong radiator. However, this table indicates that the CO_2 is the most easily quenched species, closely followed by the 5015.7 He line. The second positive system of nitrogen seems to be the most resistant, a fact that has been confirmed in experimental measurements as the most predominant emission in high densities.

Evidently He presents a very large quenching cross section, which makes its detection at higher pressures very difficult. One can expect that the concentration of He should reach significant levels before we are able to detect its presence safely.

5.2.5.6 *Experimental Investigation*

A spectrum for pure He obtained in the experiment is presented as Figure 5-28. Tests were conducted for He concentrations between 3% to 20% and pressures from 5 Torr to 50 Torr. The mixture in all cases was originally 80% N_2 and 20% O_2 that was gradually enriched with He and later Ar. The temperature and beam current were kept nominally constant throughout each test. These results are presented as Figure 5-29.

The results indicate that the detection of He is a possibility even at relatively high pressures. It can be detected in simulated air at 50 Torr pressure even at concentrations as low as 10%, provided that the electron current is in excess of 0.5 mA. At lower currents, no signal was recorded. Larger concentrations (15% to 20%) can more easily be detected. It should, however, be emphasized that the light levels observed were low and detection would thus be a demanding task in the shock tunnel environment, where extraneous sources of scattered light will exacerbate the difficulty in making the measurement. It is observed that the intensity is pressure-dependent and that it falls significantly at pressures above 10 Torr.

5.2.5.7 *The Use of Argon as an End of Run Time Detector.*

Non-metallic species of the periodic table, i.e., Ar, Kr, Xe, may offer a very good alternative to He for the determination of the end-of-run time (ERT). These gases could be introduced into the plenum between the double diaphragms; they would thus arrive in the test section before the driver gas. These species present very similar spectroscopic properties. One of them, Ar, a species that has been used in electron beam measurements extensively and whose properties are well known, can be used as guidance for our investigation.

Caution must be exercised at this point since the 4600 Å argon line is less bright than the 5015 Å line of He. The advantage of Ar and the higher molecular weight noble gases is that they cannot be as easily quenched. It has been observed that the emission of the 4600 Å line band is not quenched up to densities of 10^{22} particles/m^3 The spectra of Ar and N_2 are presented in Figures 5-30 and 5-31. The x-axis in both cases corresponds to the same wavelength width.

To verify this suggestion, a number of tests were conducted where He was replaced with Ar. The investigation of the He line bands indicated that the threshold could be expected somewhere between 15% and 10% for most cases. An improvement in the ability to detect the ERT would be to reduce this threshold between 5% and 10% by using Ar. In the investigation of the Ar lines therefore we limited ourselves to low Ar concentrations.

Tests were conducted for Ar concentrations between 3% and 20%. The results are presented in Figure 5-32. From these we can see that the intensity of the 4600 Å line band of Ar increases with its partial pressure. This is an indication of the quenching characteristics of the Argon 4600 Å line. It appears that Ar is extremely resistant to quenching compared to He, where the intensity decreased with increasing pressure. We conclude that Ar may be preferable at higher pressures as an ERT detector. At low pressures, however, He gives a stronger signal than Ar, which makes its use in the cases of low density flows preferable to Ar because its line is brighter. The measurements indicated that the 10 Torr pressure is a dividing line between the application regime of the two species. Below 10 Torr, He appears to be a better choice than Ar, which, in turn, appears to be a safer choice for higher pressures. In this series of tests on the Ar mixture, the current intensity was intentionally kept low (~0.18 ma). The intention was to identify the margins of the Ar usage in these flows.

Other noble gases could be used as an alternative to Ar. Their spectra are similar, and their higher molecular weight would reduce the possibility of quenching of the fluorescence. Xe would conceptually be a viable contender, but its high cost rules it out as a practical alternative.

5.2.5.8 Quenching of Nitrogen Due to Collisions with Oxygen Molecules.

The study of the quenching characteristics of the atmospheric species mentioned in the above paragraphs poses the question as to what degree does the chemical composition of the flow influence the signal output from the electron beam source, if used for flowfield diagnostics. For atmospheric flows one problem of particular interest is the quenching of nitrogen by other species in the flow.

We considered a nitrogen flow at a relatively high pressure of 15 Torr that was gradually enriched with oxygen molecules up to 25% maximum. The signals received were compared to those from a pure nitrogen flow, having the same total pressure as the partial pressure of nitrogen in the oxygen-nitrogen flows. The electron beam current was kept very nearly constant at around 0.65 mA. The experimental installation was the same as the one described above.

Figure 5-33 presents the results of this experiment. The bottom horizontal scale shows the partial pressure of nitrogen in the mixture, while the upper scale gives the corresponding oxygen concentration. The difference between the two curves gives an estimation of the quenching effects of the oxygen particles.

117

This experiment demonstrates the effects of quenching of "foreign" species on electron beam fluorescence measurements, a fact that has to be kept in mind before trying to interrogate multi-species flows with the aid of an electron beam. The radiation output may be significantly modified through the interaction of the various species, and extensive calibration with different mixtures at a range of pressures is essential. These results confirm the level of quenching seen in the wind tunnel experiment reported in Section 5.2.2.2.

5.2.5.9 Helium Driver Gas Detection

In the previous section, it was shown that the e-beam gun can produce detectable excitation of atomic helium. The brightest transition is designated $3^1P_1°-2^1S_0$ and radiates at 501.57 nm. Based on the results of this laboratory experiment, the radiometer was configured in the LENS facility to detect helium with a 500 nm interference filter described in Table 5-1. The temporal detection of helium would indicate when driver gas, helium in this case, had begun to flow over the model. This detection would aid in establishing a test time for the run.

The OMA was set up to record spectra from 410 nm to 545 nm to include the atomic helium transition. ACSO-53 Corning glass filter was placed behind the spectrometer's slit to prevent the ultraviolet radiation from appearing in second order in the spectra. Both the radiometer and OMA FOV's were centered 3.5 inches above the sphere/cone/flare model, in the free stream. The OMA's integration time was 3 msec, from 11 msec to 14 msec during the test. The integration was late in the run time, to ensure that He driver gas would be present.

A simple demonstration test was devised to confirm that He could be detected spectroscopically with the equipment being used. With a N_2 atmosphere in the test section at 1.1 Torr, He was bled into the OMA FOV, and the resulting spectrum is shown in Figure 5-34. A small peak is seen at 501 nm in addition to the N_2 2^+ and $N_2^+ 1^-$ bands at 427 and 470 nm respectively.

Figure 5-35 shows the He filtered radiometer signal for shock tunnel Run 25 from PMT 3, which is typical of the PMT's, with e-beam excitation on. The trace shows a strong signal during the start-up transient, a steady-state period (in this case between about 6 to 9.5 msec), and then a large signal again as the test is over. What is not typical is the small signal present in the 2.0 msec to 4.5 msec time period. Since gas flow has not reached the test section yet, this signal must represent radiation from the high-temperature reservoir behind the throat or from behind the nozzle startup shock wave, scattering into the radiometer. This scattering must be from surface reflections, since the test section is under a vacuum. As stated, the flow has not yet reached the radiometer FOV. This early signal was not seen with the radiometer configured to detect NO or N_2. These species were detected at UV wavelengths, whereas the helium is in the visible. The lower energy visible radiation may be more plentiful in the radiation source.

Figure 5-36 shows a pilot pressure trace from a probe at the same location as the e-beam. The jump at 9 msec can be interpreted to indicate when the helium driver gas is flowing over the model, since it occurs is at the same time as the sharp rise in intensity of fluorescence was seen in Figure 5-35. One obvious conclusion is that the radiometer confirms the arrival of the He driver interface. This interpretation may be premature, inspection of the OMA spectrum for the 11 msec to 14 msec time frame confirms (see Figure 5-37). This shows a very different form to that obtained for a static gas sample (Figure 5-34). The most obvious feature of the spectrum is that it conforms broadly to a blackbody radiation curve for about 2,800 K. The peaks for the N_2 spectrum are just discernable, but the He 501 nm line is totally swamped by the continuum radiation.

The source of the continuum radiation is unclear, but at the low levels of light being recorded, it could originate from a very small concentration of hot particulate in the instrument FOV, from stagnated test gas in the instrument line-of-sight, or from light scattered into the instrument. At this time during the test, a strong radiation source still exists in the reservoir behind the throat, and also at the end wall of the test chamber, where the test gas is now stagnated. Scattering could again occur off surfaces or from cold particulates in the instrument line-of-sight. The high temperature inferred from treating the source as a blackbody is consistent with any of the above mechanisms. These tests are thus unable to confirm directly the arrival of the He driver gas.

The radiation recorded in the trace shown in Figure 5-35 may be dominated by continuum radiation, although the OMA integration was later in time than the initial rise in signal at 9.5 msec in the radiometer trace of Fig. 5-35. The OMA result was confirmed by repeating the experiment without e-beam excitation and very little change in the curve was seen.

5.3 CONCLUSIONS

The development and application of two non-intrusive optical diagnostic techniques that are used in this study of hypervelocity, non-equilibrium flows are described in this section of the report. Both methods are based on recording the intensity and spectral content of the light emitted by the gas to infer its properties.

In the first method the direct radiance of the flow is observed. For this technique a prerequisite is that the gas be sufficiently hot for self-induced thermal radiation to occur. Although simple to implement, high spatial resolution cannot be achieved with this method because extensive volumes of the flow are likely to radiate, and thus information relating to specific points within the field of view of the optics cannot be discriminated. In the second method these limitations are avoided. Fluorescence in the gas is induced by a narrow beam of high energy electrons, which not only extends the range of observations to gases that are insufficiently hot to radiate themselves but also, at the same time, improves the spatial resolution to a level comparable with physical probes.

In this study both of these techniques were employed to investigate the free stream of the LENS shock tunnel and the region between the bow shock wave and the surface of a sphere/cone/flare model. Additional tests

were also conducted in an attempt to determine the time of arrival of the shock tunnel driver gas and to identify trace impurities in the flow.

Before the electron beam fluorescence measurements could be made, a suitable electron gun had to be developed. The dynamically pumped gun system was constructed in a compact form so that it could be installed within the test model. A novel electromagnet configuration was chosen which allows it to be run with external pressures of several tens of torr. The gun operated satisfactorily throughout the tests.

The most successful of the non-intrusive optical tests were the temperature measurements made with electron beam fluorescence. Conceptually all of the gas' temperatures (i.e., translational, rotational and vibrational) can be inferred from the spectra. In practice, the translational temperature is exceptionally difficult to measure even in the most favorable situations. The demanding circumstances of testing in a short duration facility such as the LENS shock tunnel preclude even contemplating measuring this component. However, obtaining the other two components is a practical proposition, as the results reported prove. A variety of spectral techniques were tried - mostly with success - to obtain these temperatures for the 5 MJ test condition only. Rotational temperatures at points within the shock layer and in the free stream were deduced from two separate bands in the N_2 spectrum, which agree well with each other. Good agreement was also obtained between vibrational temperatures derived independently from OH and NO spectra. Unfortunately, even though good quality $N_2(2+)$ spectra were recorded, it proved to be inherently impossible to infer vibrational temperatures from the $N_2(2+)$ below about 1,500K, thus, a free stream value was not obtained.

Because only a single temperature point could be measured in each test, the volume of data is, needless to say, sparse. Even so, comparisons are possible with the Navier Stokes computations prepared by Professor I Boyd for the sphere/cone/flare body at the same test condition. From profiles of the rotational and vibrational temperatures (Figures 5-22 and 14, respectively) for a point near the beginning of the conical section of the body it can be seen that the values for both temperature components measured on the edge of the boundary layer (at ¼ - inch from the surface) agree quite closely with the computation. In the middle of the shock layer the agreement is significantly worse, with the measured values being about 26% and 38% higher, respectively. Since the measurement of the free stream rotational temperature also agrees quite well with the predicted value, the experiment suggests that Navier Stokes code is under-predicting the temperatures in the center of the shock layer.

Radiometer studies were made with electron beam induced fluorescence in an attempt to measure the number density of NO and N_2 in the shock layer. Despite an extensive series of tests, the data are unsatisfactory, and direct quantitative comparisons with the Navier Stokes results cannot be made. It is thought that there are two main reasons for the failure: (a) a lack of comprehensive bench calibration work on NO in isolation and in the presence of other gases covering a range of temperatures; and (b) the omission of a second radiometer measuring

the intensity of the fluorescence at a fixed point, for example, in the free stream, which could have been used as a control against which the data for each test could be normalized.

Two series of experiments were performed to detect the arrival of the driver gas; neither was conclusive, although other useful information about the flow was obtained. The first set was based on the detection of OH, which, it was thought, would be indicative of the arrival of the interface between the H_2 driver and the air driven gas. For OH to be present combustion would have to occur. The tests revealed that traces of OH were present during all of the tests with air. However, tests with N_2 showed no OH during steady-state, where clearly no reaction producing water could occur. There was the possibility that the signal arose from water that had been adsorbed into the walls of the driven tube and nozzle prior to the test, but tests in which this source was eliminated did not change the OH emission. It was concluded that the source was likely the decomposition of small quantities of hydrocarbon contaminants. No discernible rise in OH occurred at the time when the interface should arrive. In any event, it is unlikely that combustion would occur between the driven and driver gases because an extensive buffer region of He, which originates in the double diaphragm section of the tunnel, is used to eliminate the contact between the driver and driven gases. Direct spectrometric detection of H_2O would seem a more appropriate experiment to perform. Traces of Si, CN and Cu were also detected in the flows with N_2.

The second set of tests was intended to detect directly the arrival of He when it was used as the driver gas. Bench calibrations had shown that it is possible to observe the He 501 nm line in the electron-beam excited fluorescence in a mixture of He and N_2. A radiometer set to observe this wavelength showed a large signal throughout the entire shock tunnel test period, with absolutely no indication of the arrival of the driver interface. Measurements of the spectrum of this radiation revealed that all of it, except for the brightest N_2 lines, was completely swamped by a continuum blackbody radiation corresponding to about 2,800K. Since 2,800K is in the range of the reservoir temperature, it is assumed that the radiation comes from the scattering of light originating in the reservoir or from other stagnation regions, or from minute hot particulates passing through the test region. The radiation made measurements in the visible spectral range very difficult. It should, however, be born in mind when interpreting the results of these experiments that The levels of light intensity that were being detected were very low and the amount of contamination needed to produce these effects is minimal.

5.4 REFERENCES

E.P. Muntz, *Physics of Fluids,* 5, 80, (1962).

E.P. Muntz, The Electron Beam Fluorescence Technique, AGARDograph 132, December (1968).

G. Hertzberg. Spectra of Diatomic Molecules, Van Nostrand-Reinhold, New York (1950).

Forrest R. Gilmore, Russ R. Laher, and Patrick J. Espy, *J. Phys. Chem. Ref. Data,* 21, 1005. (1992).

Richard A. Copeland, J.B. Jeffries, and David Crosley, *Chem. Phys. Lett.,* 138, 425 (1987).

RADIOMETER

ELECTRON BEAM

OPTICAL
MULTICHANNEL
ANALYZER

OMA

ELECTRON BEAM GUN

MODEL

SECTION A-A

A

A
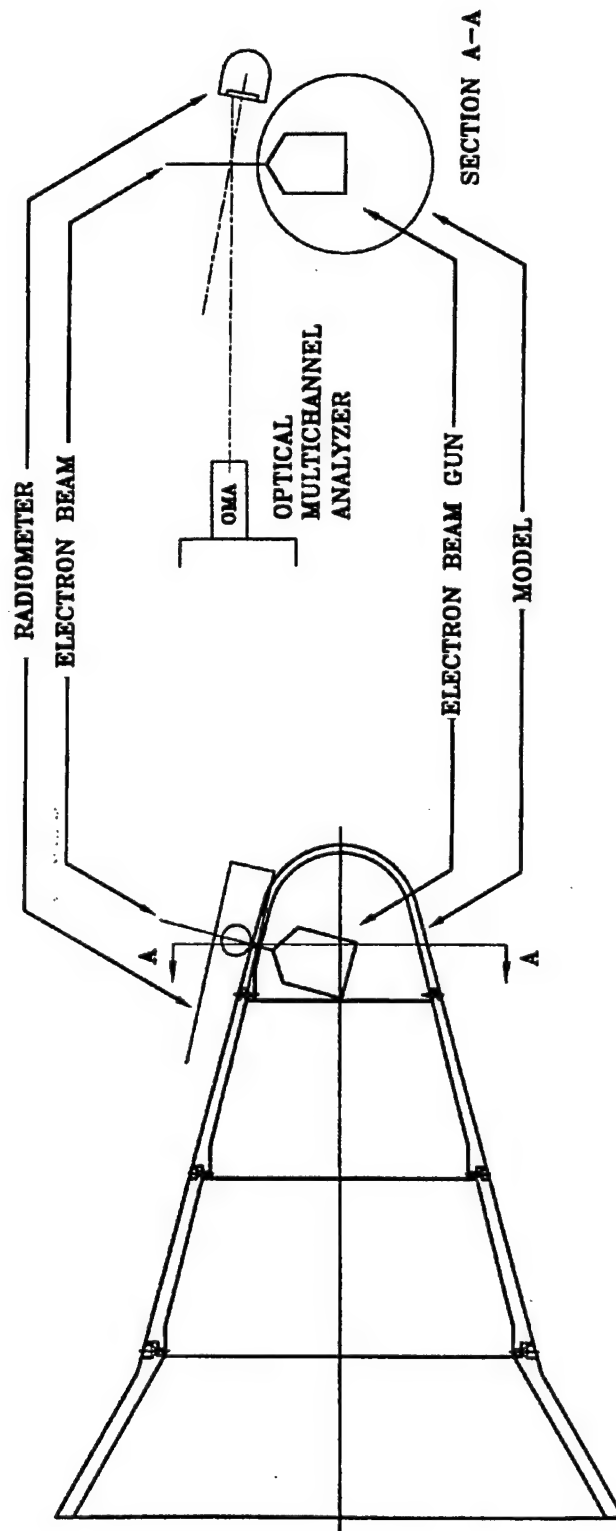
Figure 5-1. Schematic of Model and Electron Beam Diagnostics

Figure 5-2. Radiometer Optical Arrangement

PMT assembly rotated 90°

Electron Beam

Fused Silica Window

MgF$_2$ Coated Mirror

CaF$_2$ Lenses

Baffle

Filter

Slit Assembly

Hamamatsu R292 PMT

123

Fused Silica window
2 in. dia., 0.375 in thick

Fused Silica lens 2 in dia. 6 in f.l.

Shutter

Jarrell Ash Monospec 18
Monochromator

Princeton Applied Research
Model 1421 gated detector
array

Aluminum box at
atmospheric pressure
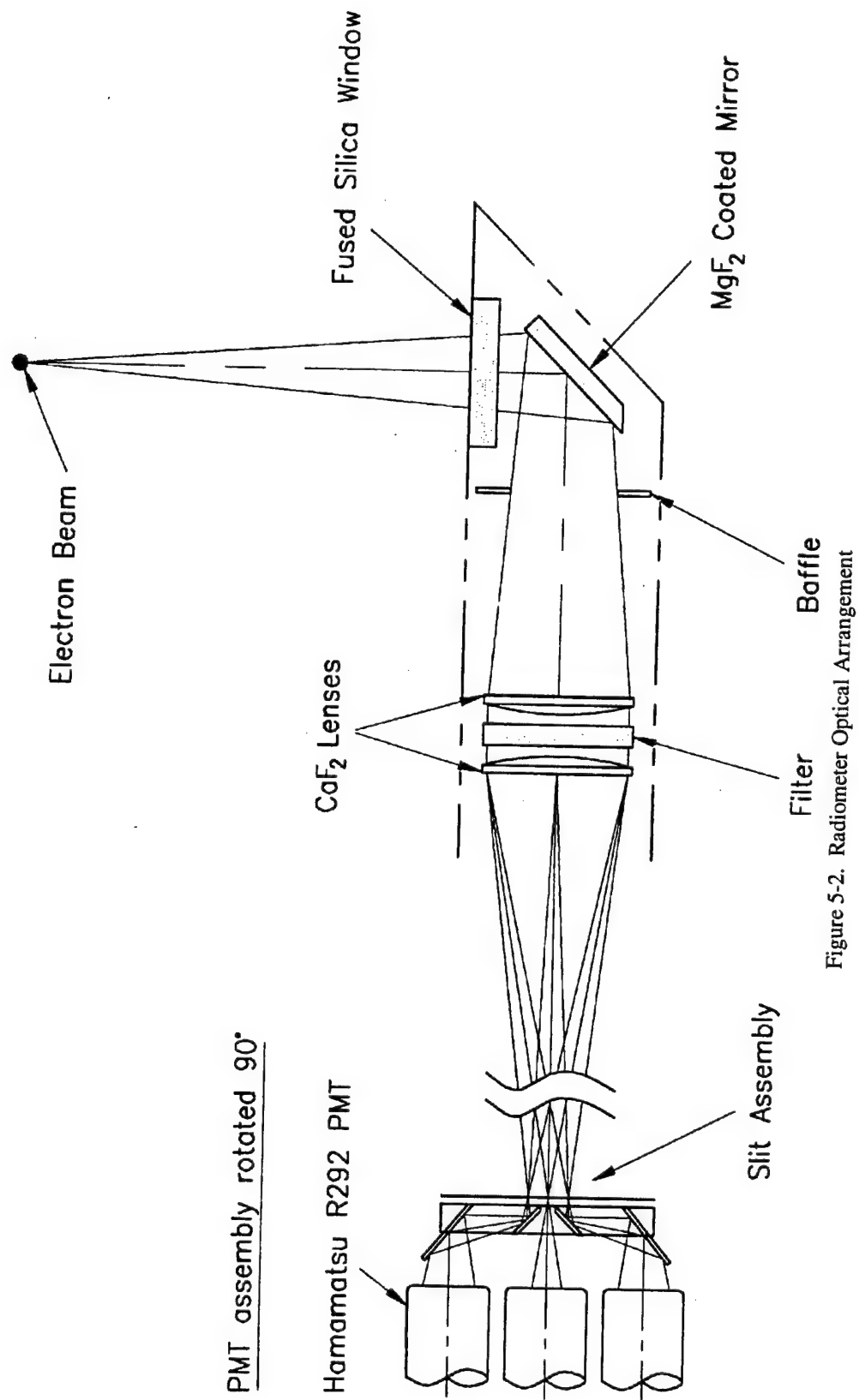
To OMA controller
and PC

e-beam

17'

9'

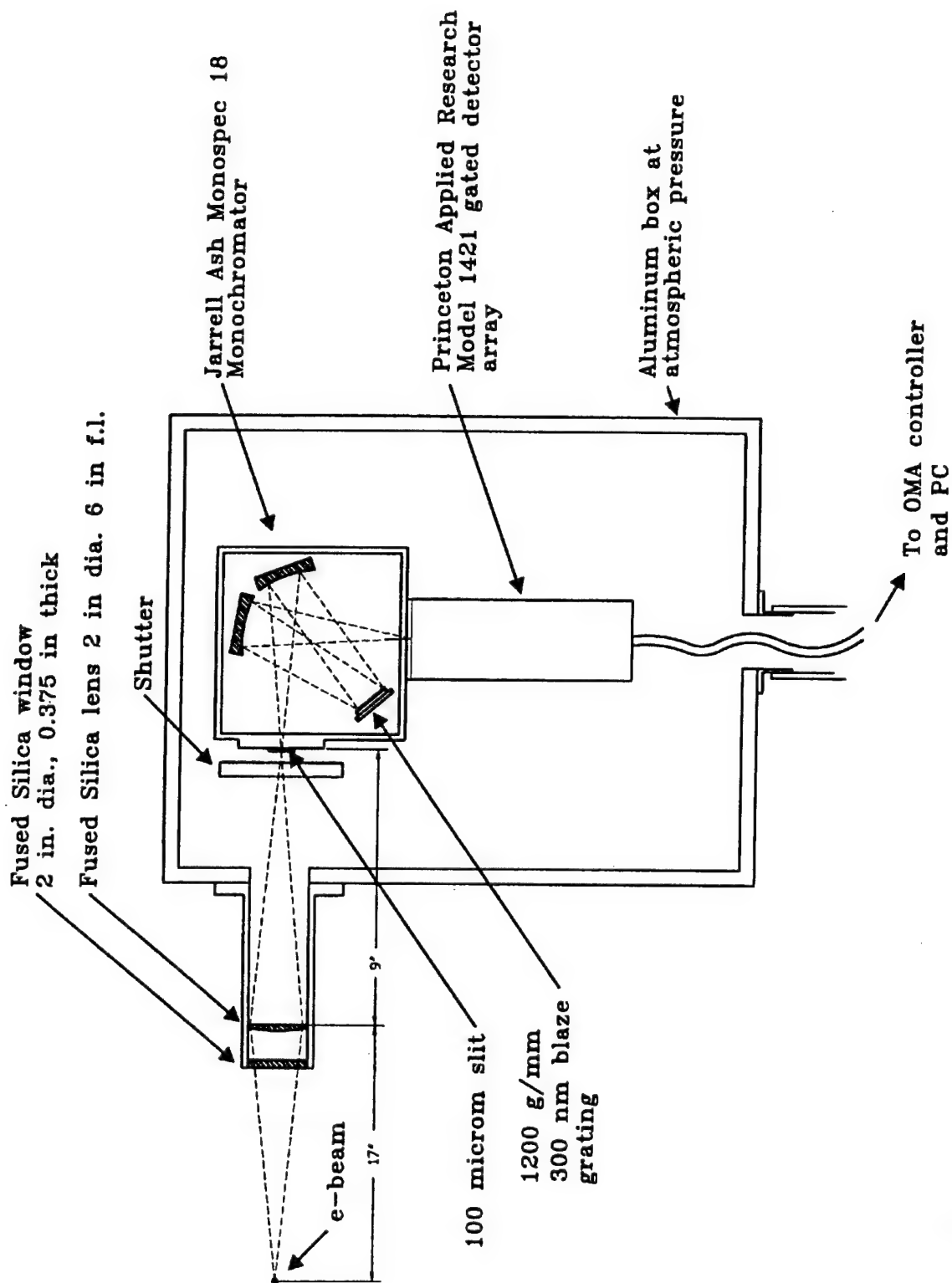100 micron slit

1200 g/mm
300 nm blaze
grating

Figure 5-3.   Optical Multichannel Analyzer (OMA) Detector and Monochromator Arrangement for Spectral Data Collection
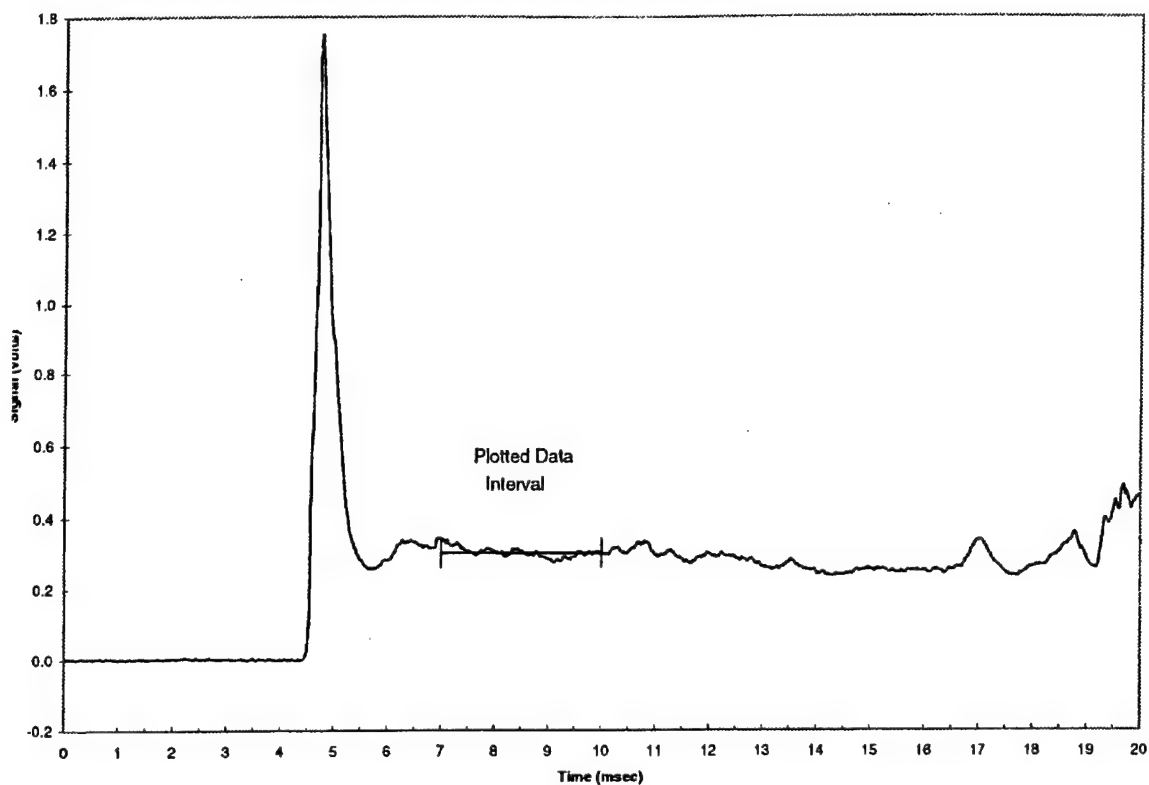
Figure 5-4. A Typical Radiometric Record (taken from Run 19; FOV1)
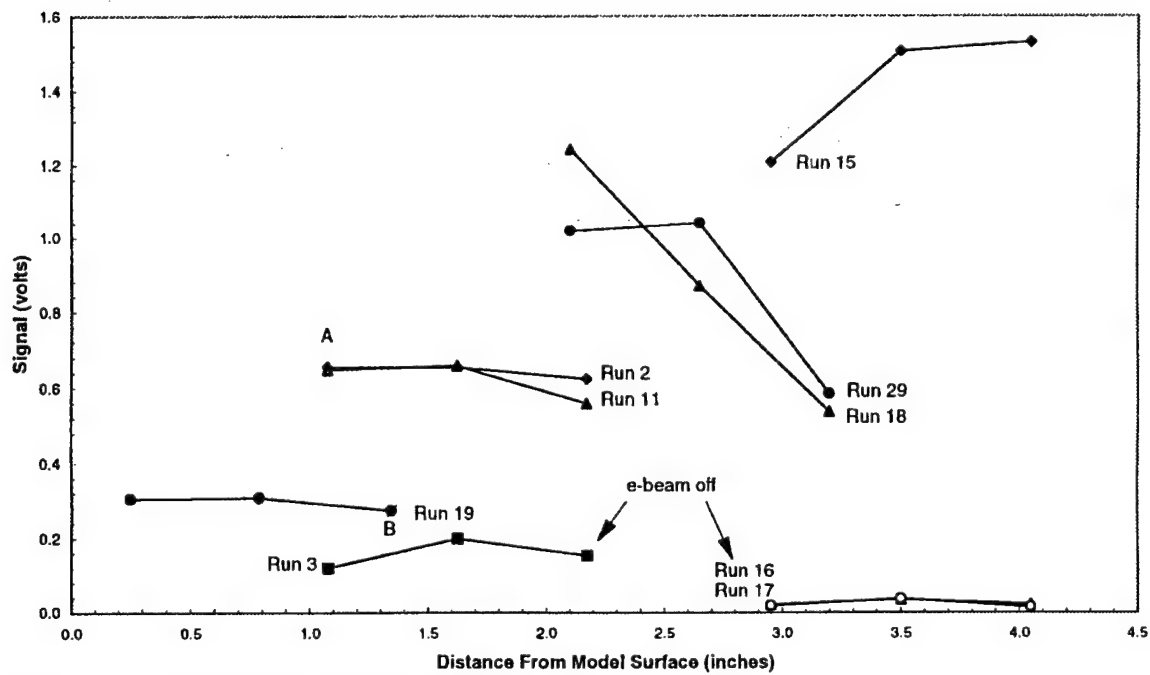
Figure 5-5. Unnormalized NO Radiometric Data
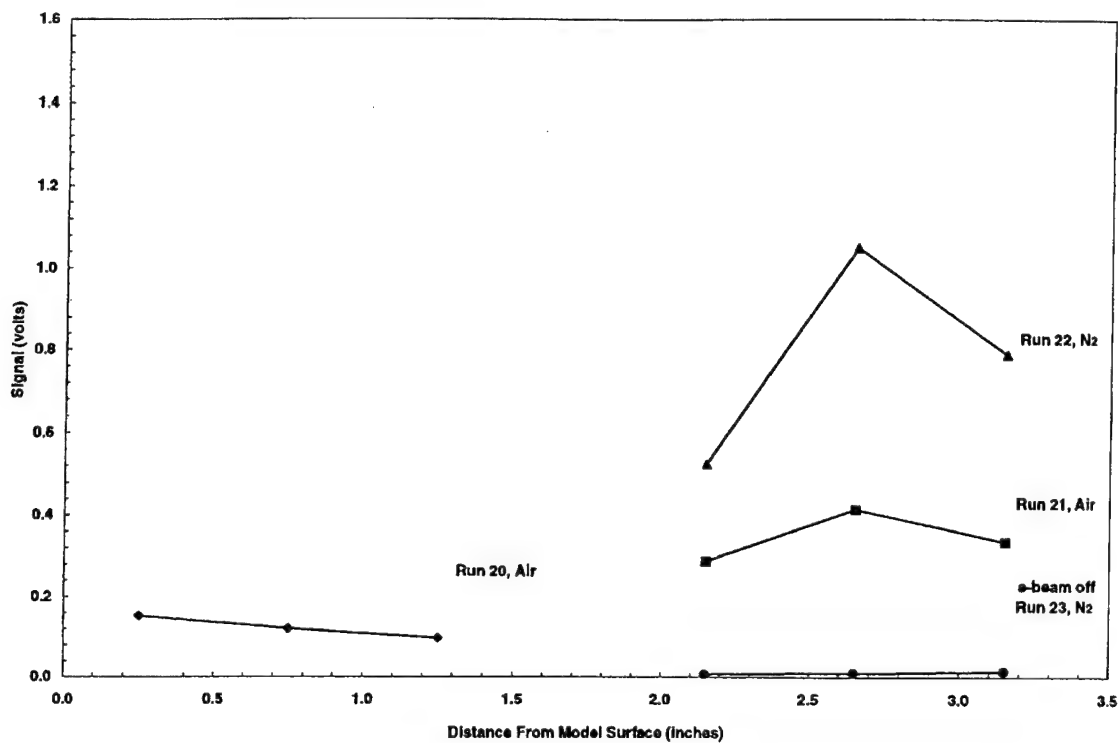
Figure 5-6. Unnormalized N_2 Radiometric Data
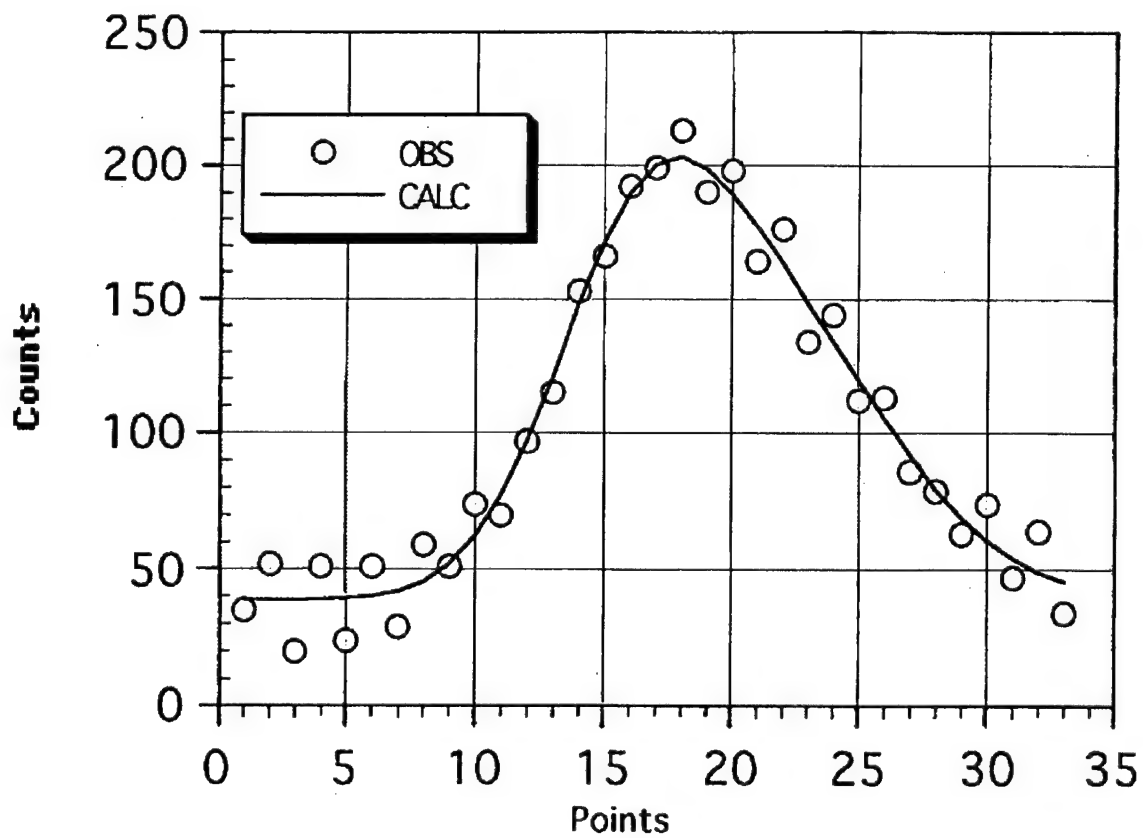
Figure 5-7. Run 21 Rotational Fit of $N_2^+(1^-)$

126
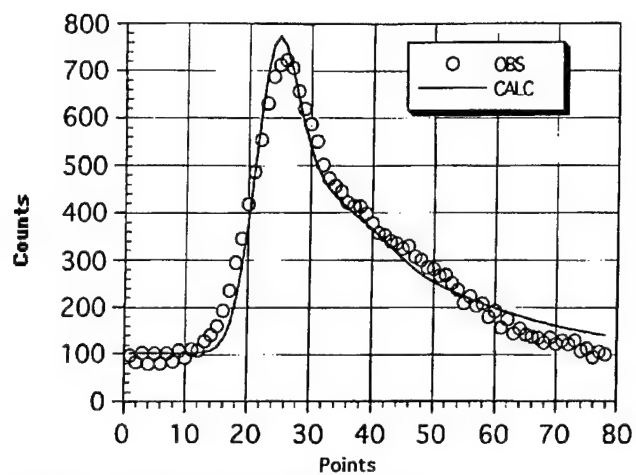
Figure 5-8. Run 30 Rotational Fit of N_2^+ (1^-)
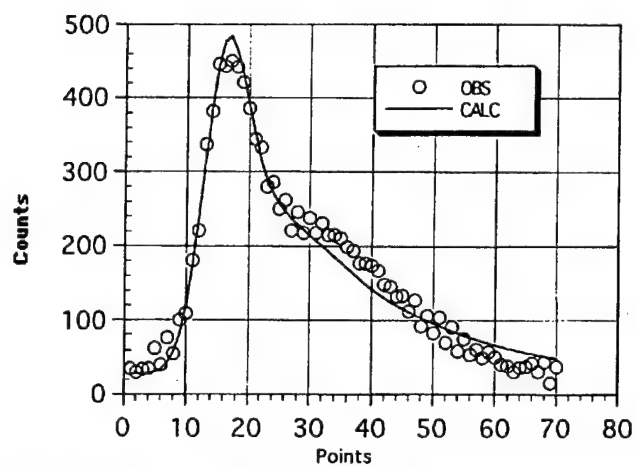
Figure 5-9. Run 11 Rotational Fit of $N_2^+(1^-)$
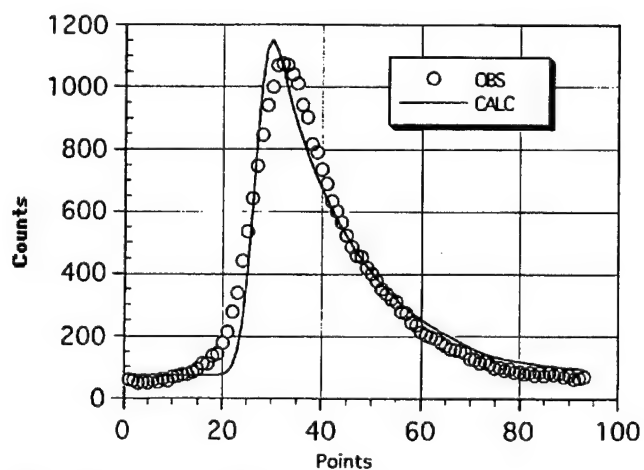
Figure 5-10. Run 30 Rotational Fit of N_2 (2^+)

127
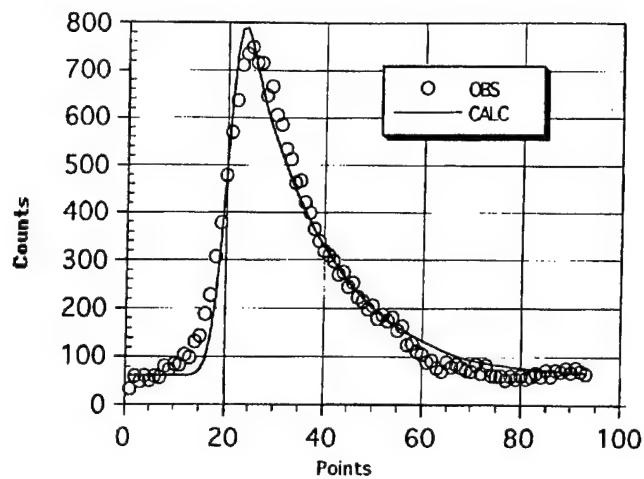
Figure 5-11. Run 11 Rotational Fit of N_2 (2^+)
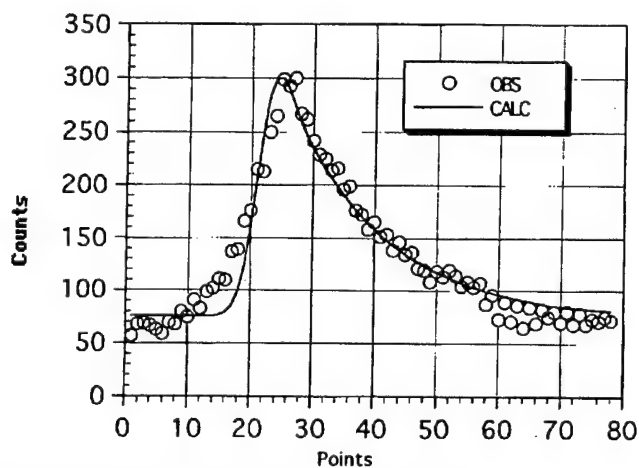
Figure 5-12. Run 15 Rotational Fit of N_2 (2^+)
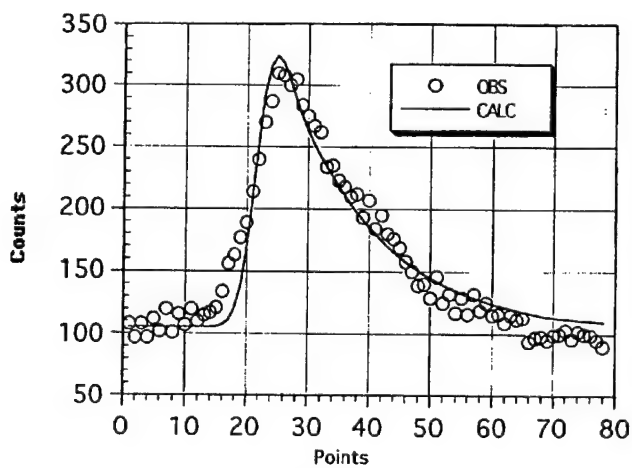
Figure 5-13. Run 17 Rotational Fit of N_2 (2^+)

128
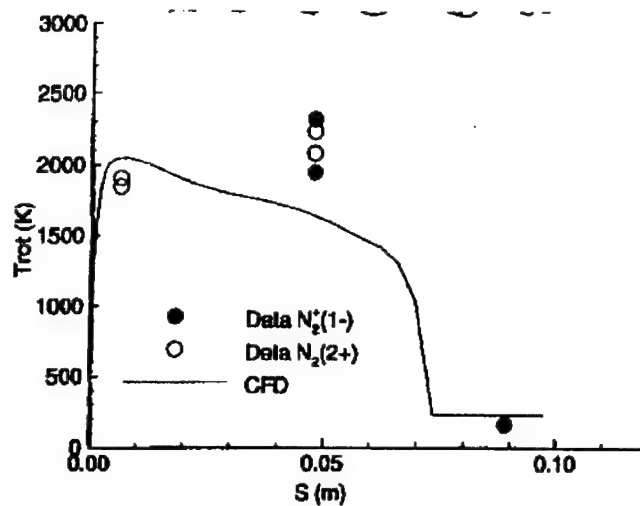
Figure 5-14.   Measured and Computed Rotational
                Temperature Profile at Station 2
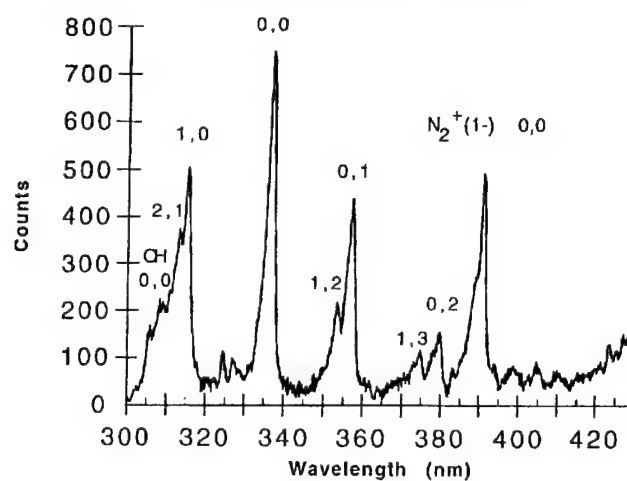
Figure 5-15. Run 11 N_2 (2^+) Vibrational Spectrum
            (Other Transitions as Noted).
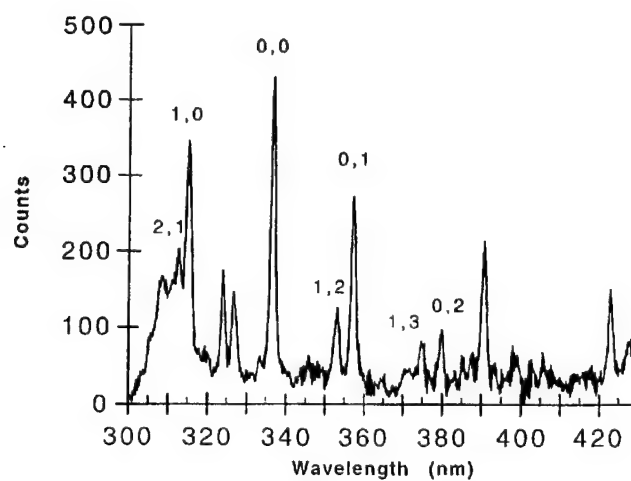
Figure 5-16. Run 21 N_2 (2^+) Vibrational Spectrum
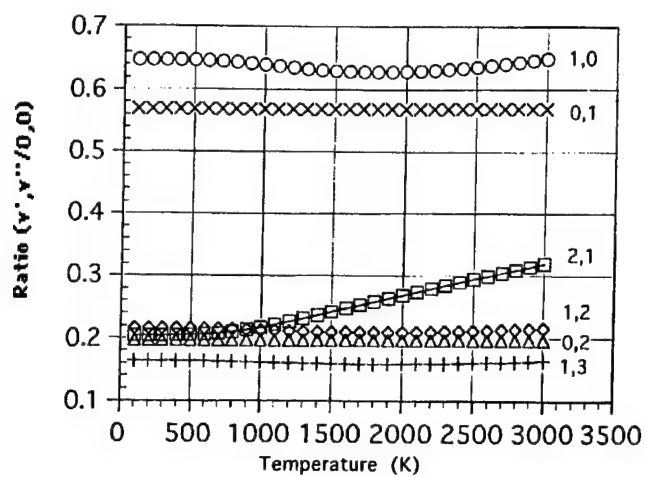
Figure 5-17. Temperature Dependence of N_2 (2^+)
Vibrational Bands
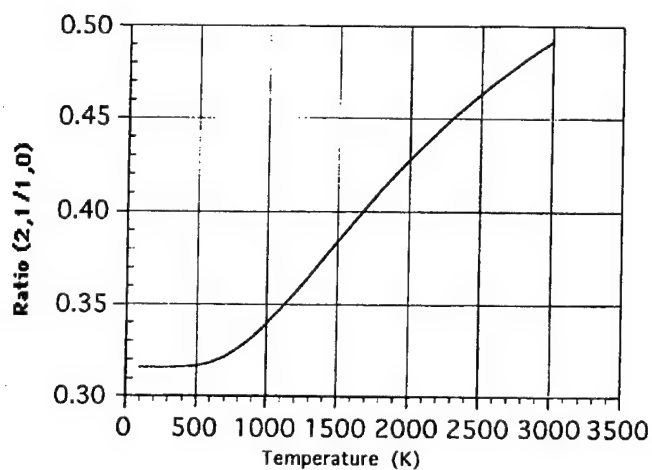
Figure 5-18. Temperature Dependence of the N_2 (2^+)
(2,1/1,0) Ratio
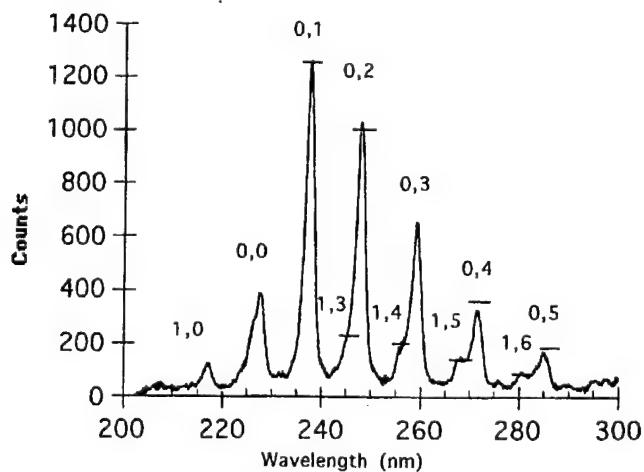
Figure 5-19. Run 20 NO Vibrational Spectrum

130
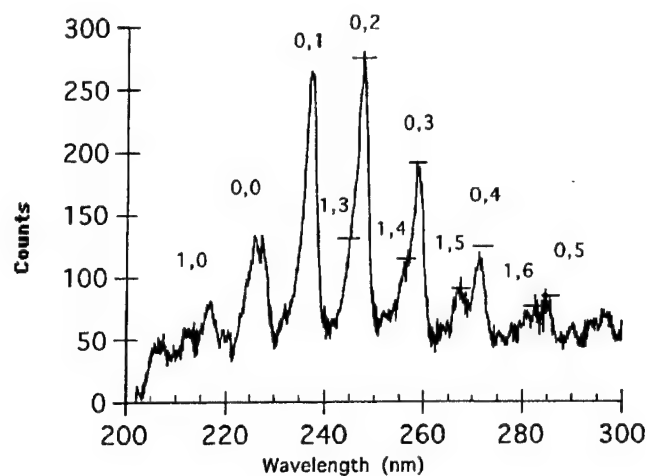
Figure 5-20. Run 19 NO Vibrational Spectrum
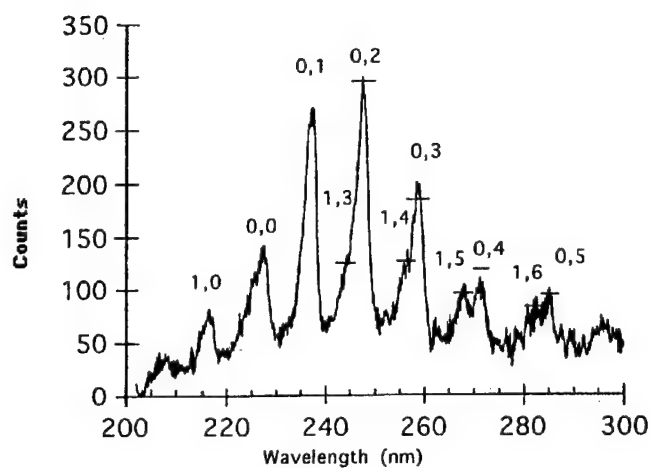
Figure 5-21. Run 18 NO Vibrational Spectrum
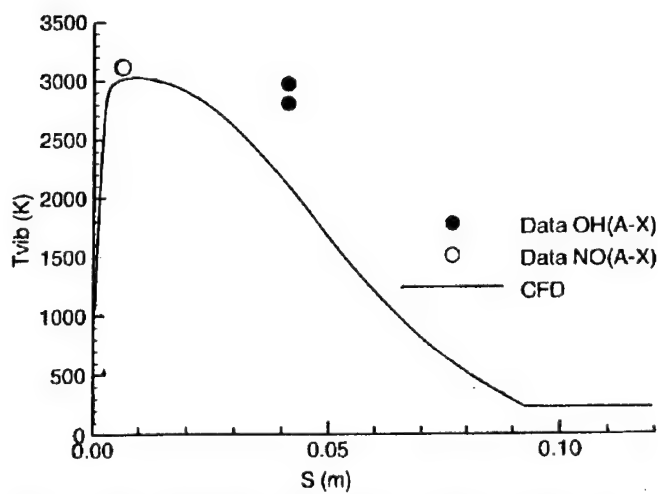
Figure 5-22. Vibrational Temperature Profile at Station 2

131

msec
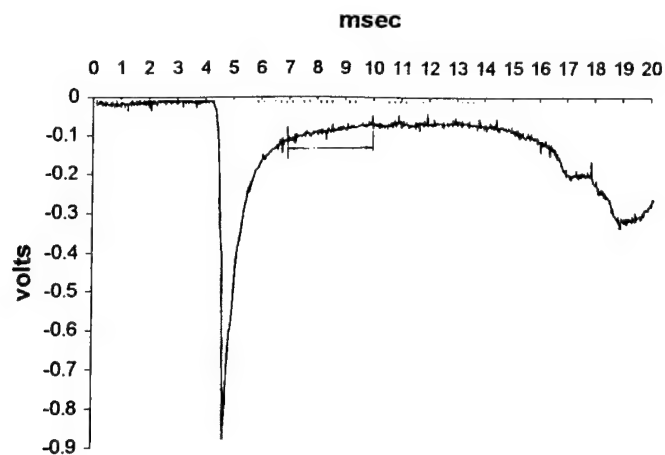
Figure 5-23 OH Radiance for a 5 MJ Test with Helium Driving Air as the Test Gas. (Note: Intensity is plotted increasing downwards; steady flow time is indicated)

msec
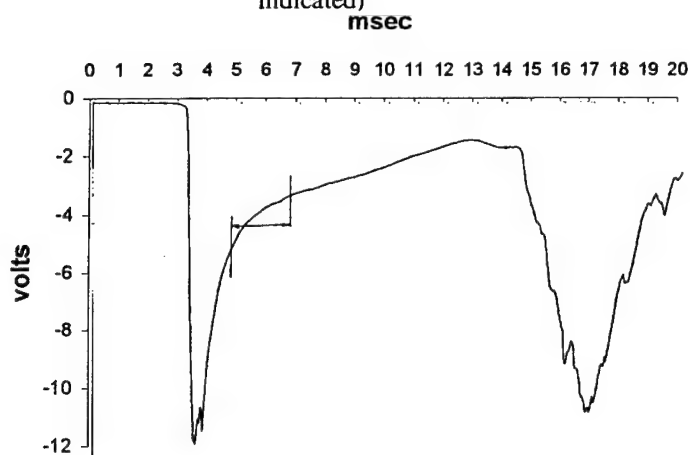
Figure 5-24. OH Radiance for 10 MJ test with Hydrogen Driving Air as the Test Gas (Steady flow time is indicated)
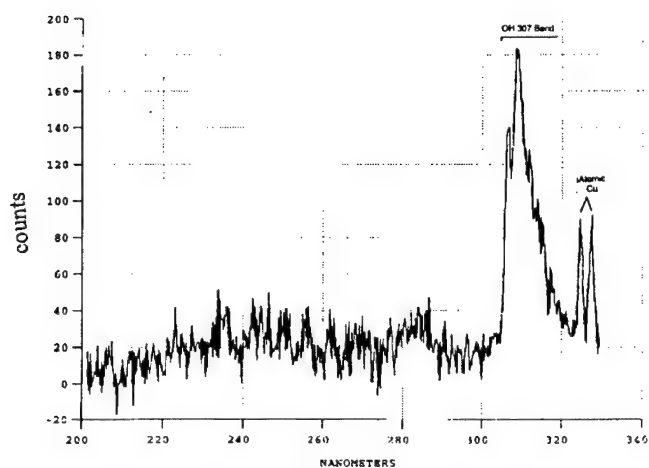
Figure 5-25. Spectrum With Air as the Test Gas

132
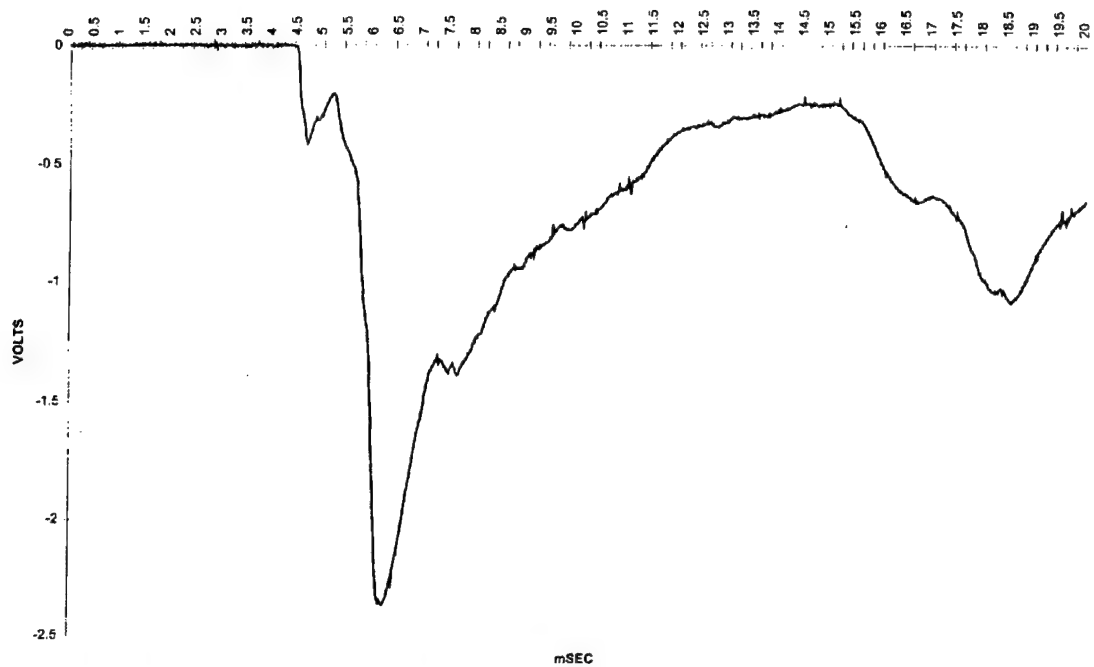
Figure 5-26. Radiometric Trace with He driving N_2
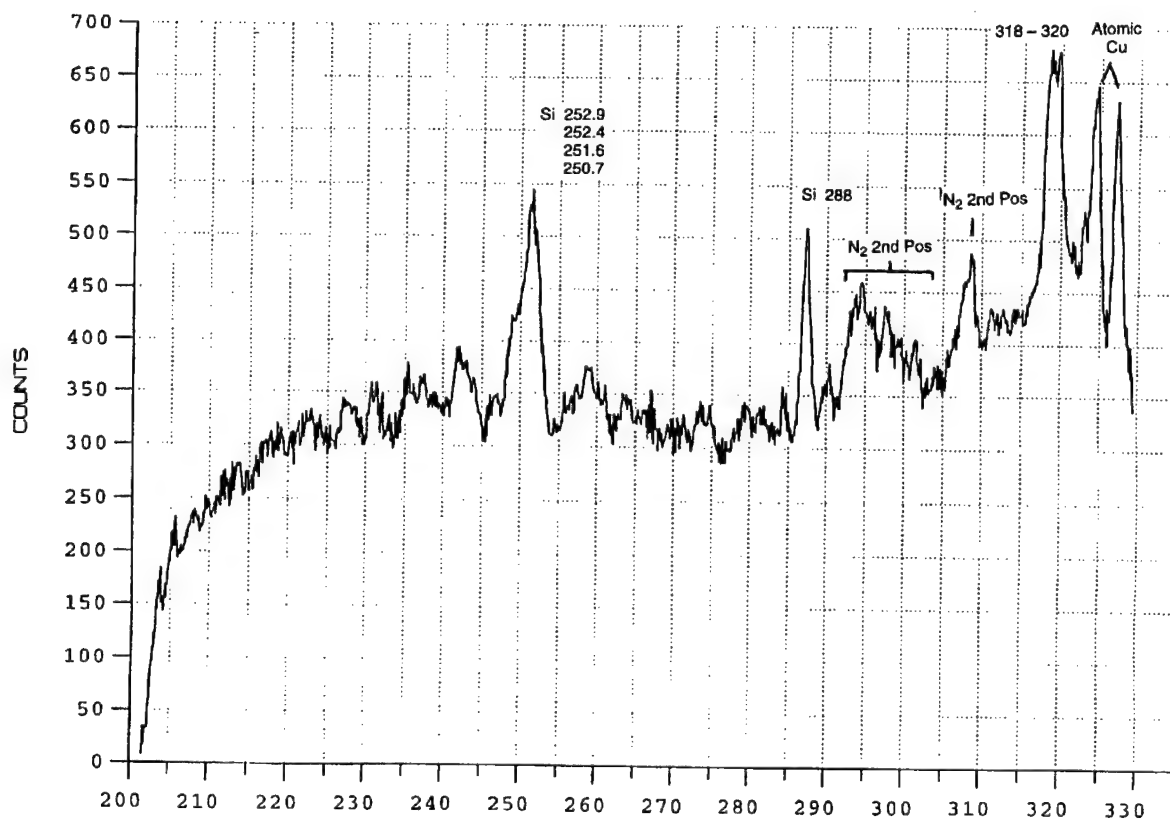
Figure 5-27 Typical Spectrum for Nitrogen as the Test Gas
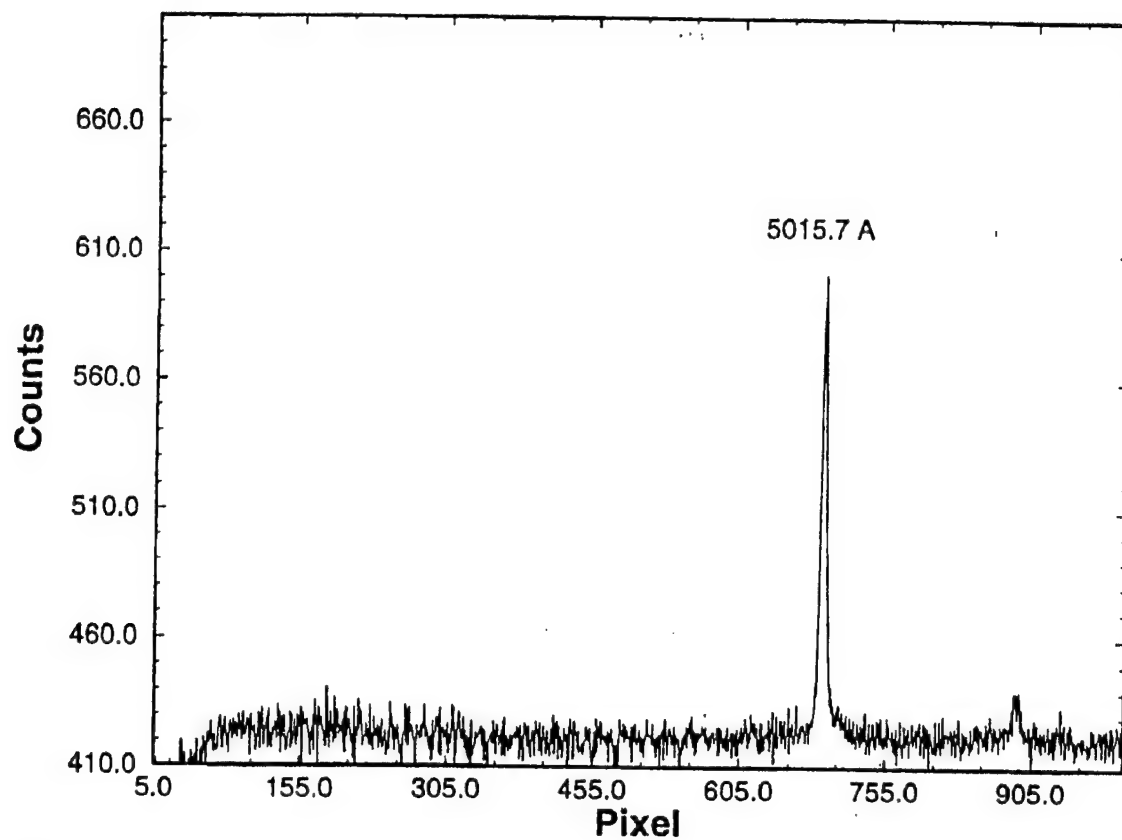
Figure 5-28. He Spectrum
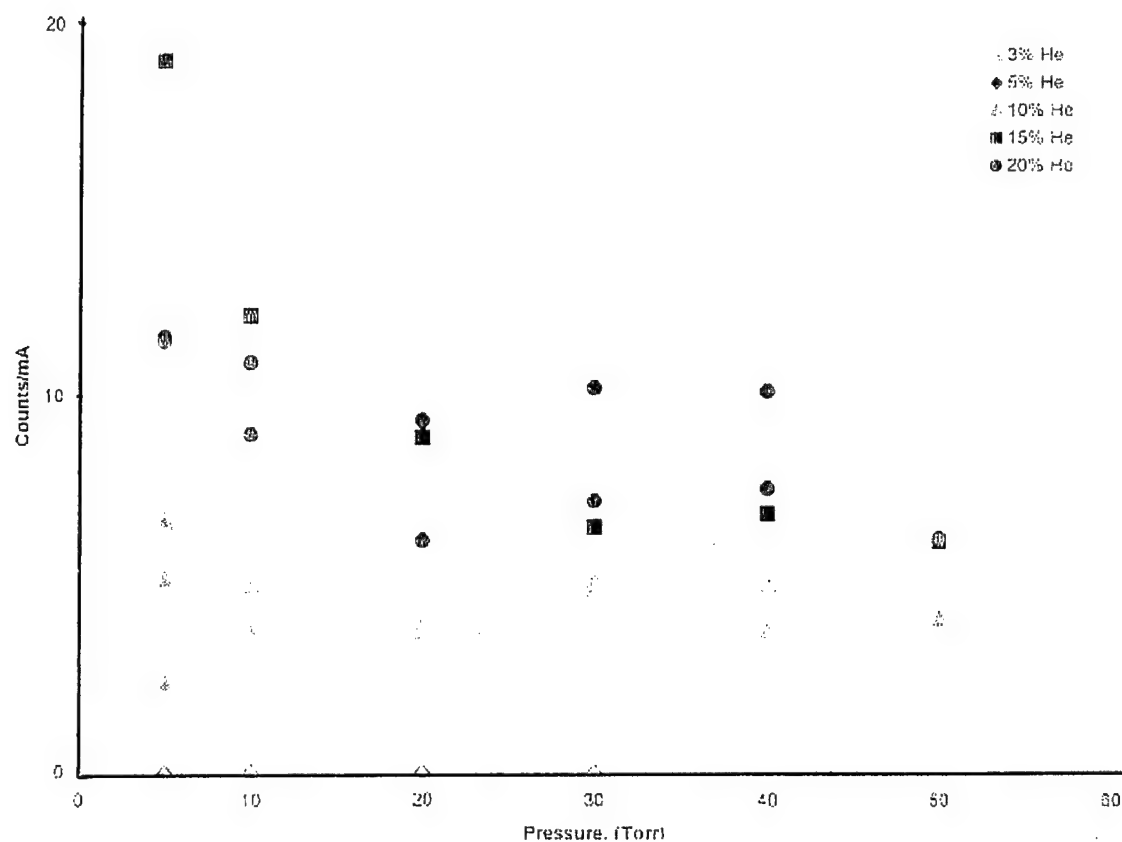
Figure 5-29. The Effect of Pressures on the Intensity of He Radiation at Various Concentrations in Air

134
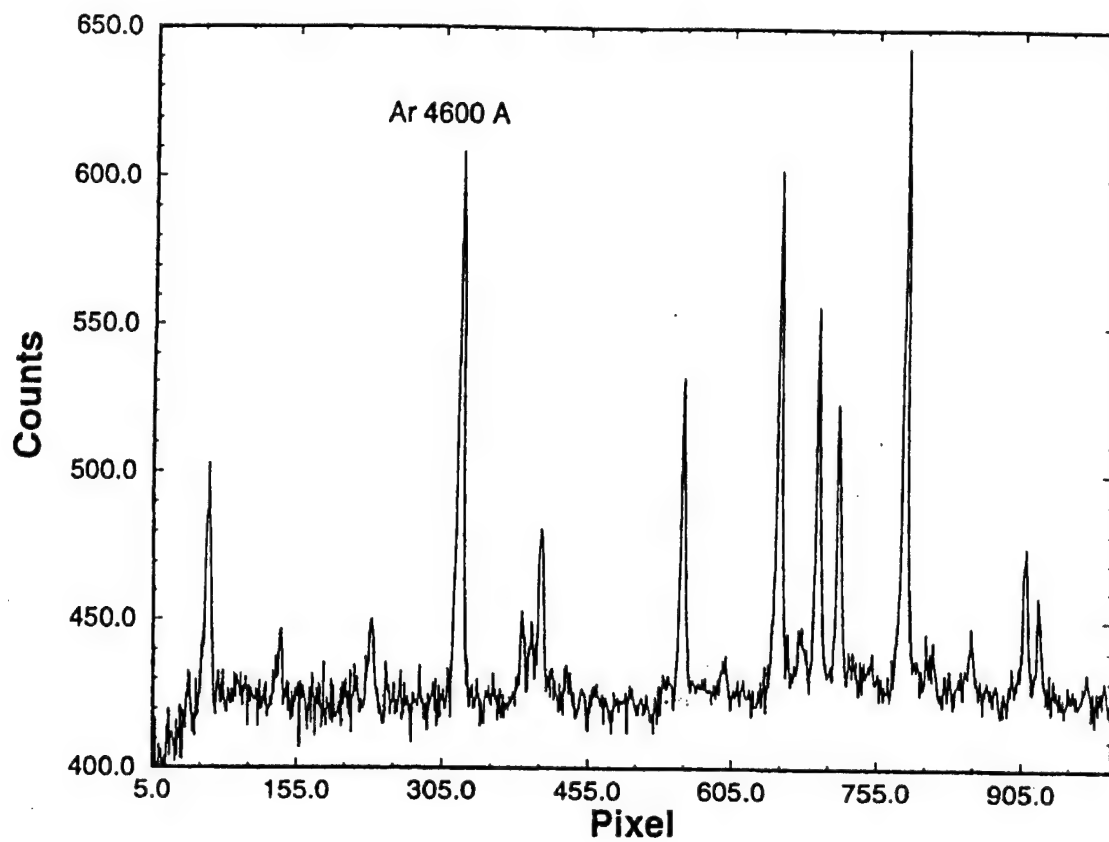
Figure 5-30. Ar Spectrum
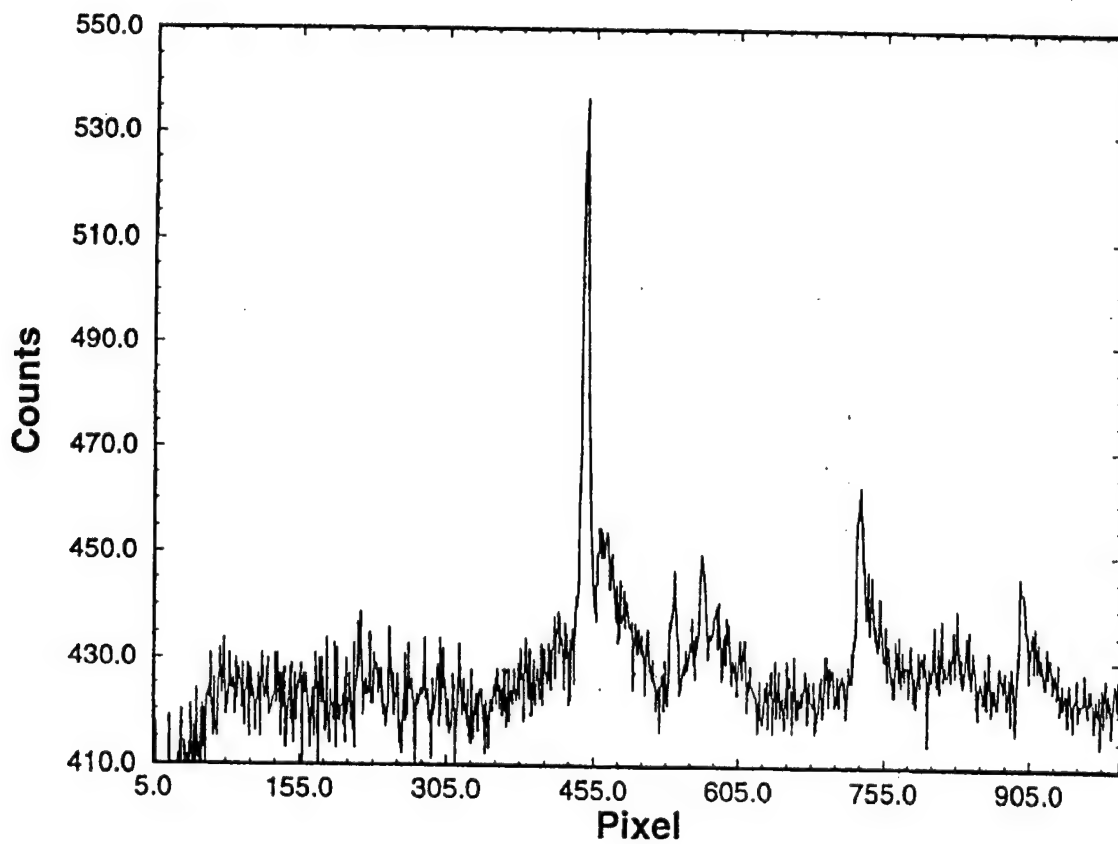
Figure 5-31. N₂ Spectrum

135
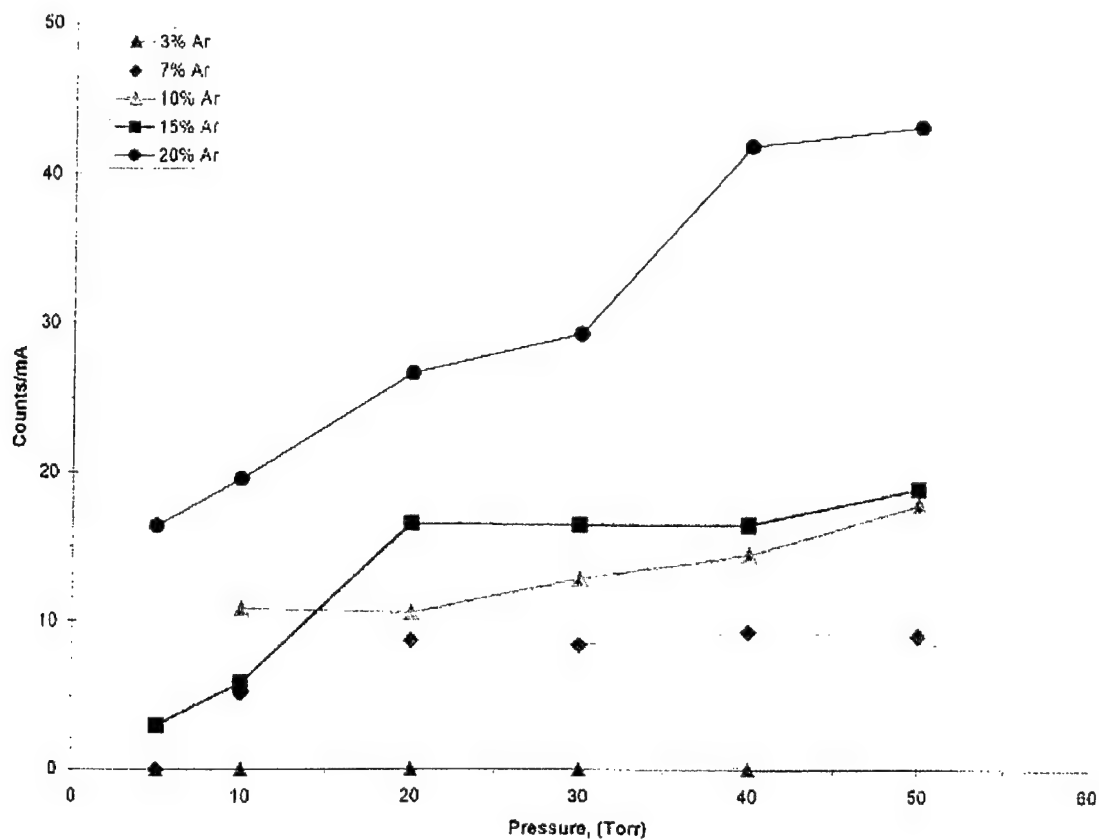
Figure 5-32. The Effect of Pressure on the Intensity of Ar Radiation at Various Concentrations in Air
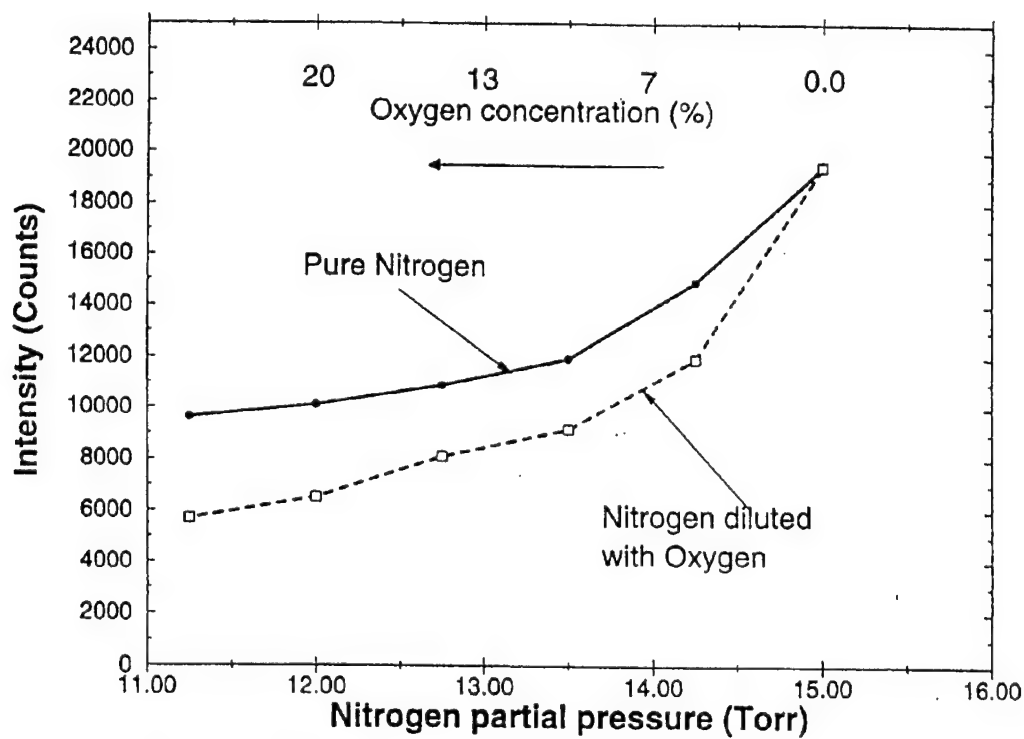
Figure 5-33. Quenching Effects on Nitrogen

136
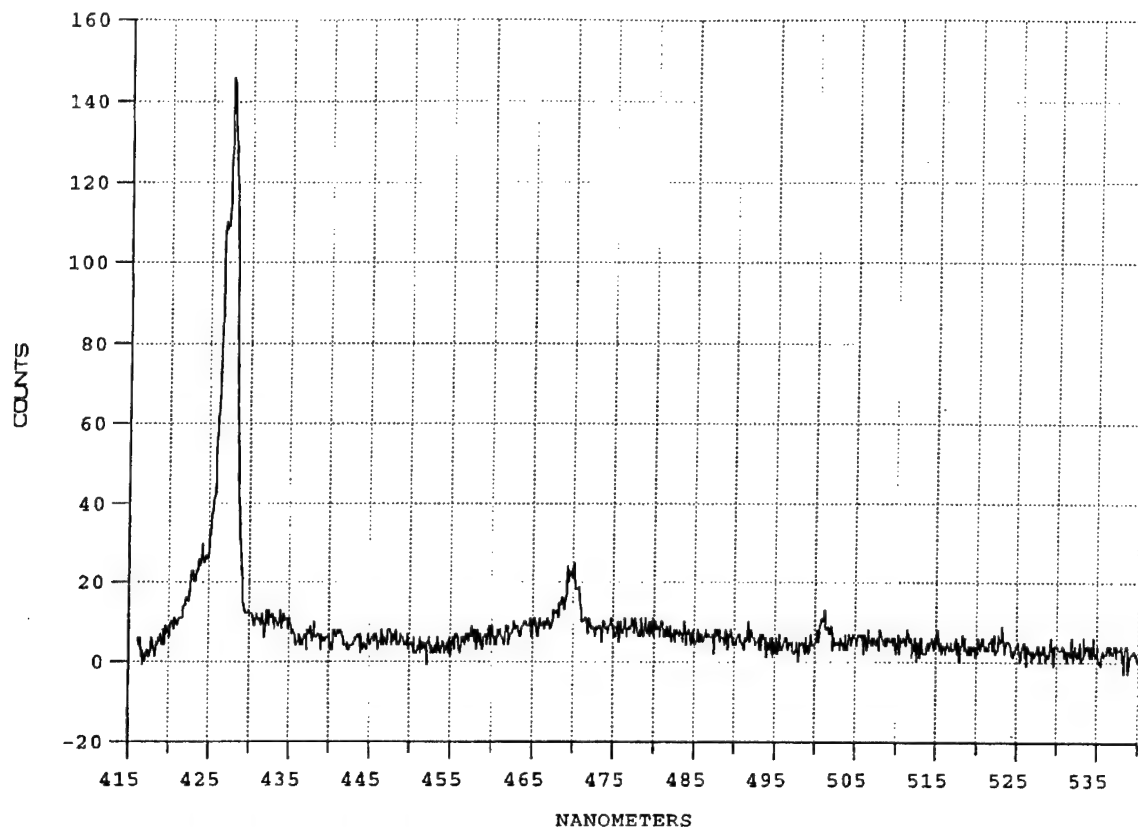
Figure 5-34. Nitrogen Spectrum with He Present in a Static Gas Sample
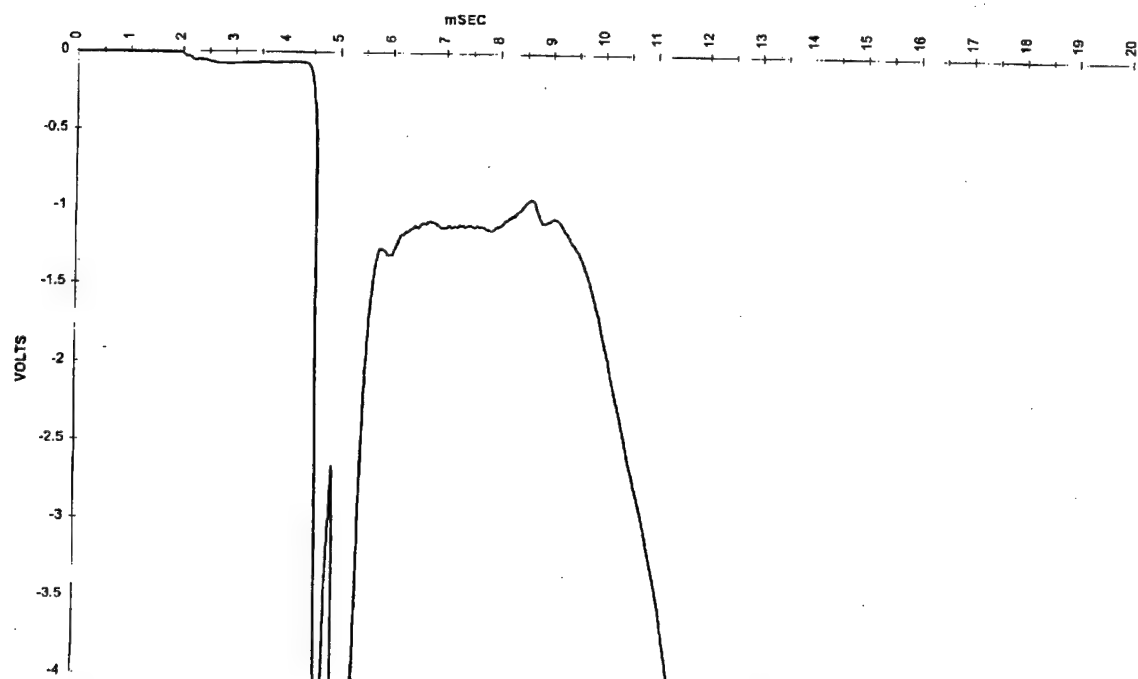
Figure 5-35. Radiometer Trace with E-Beam on and He 501 nm filter installed. (Run 25; Intensity Increasing Downwards on Plot)

137
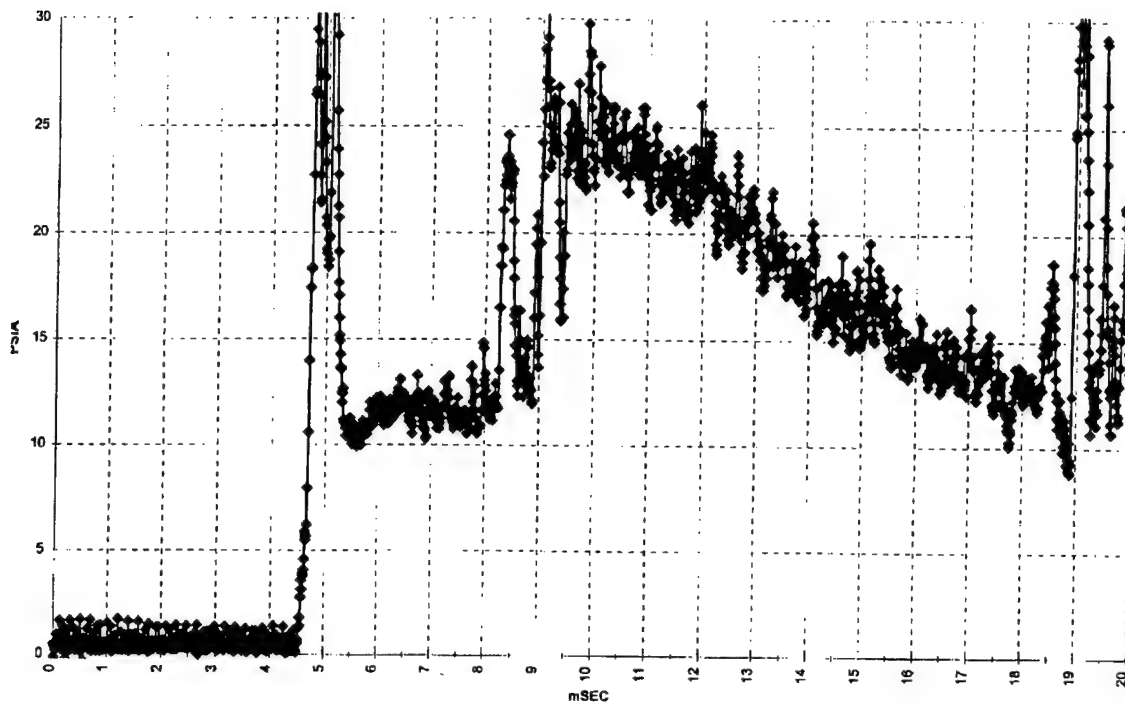
Figure 5-36. Pitot Pressure Record

Black Body Radiation Curves

3200 K

2800 K

2400 K
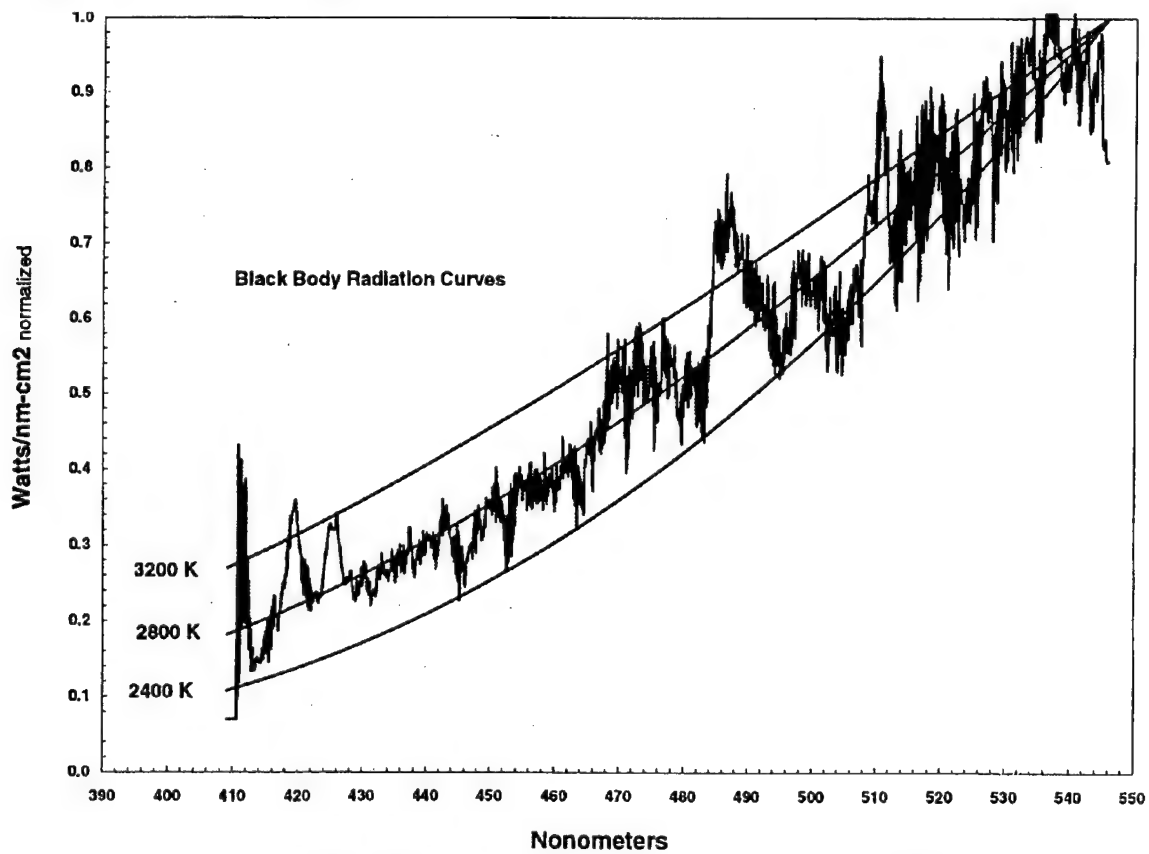
Figure 5-37. Spectrum Recorded Between 11 msec and 14 msec with E-Beam Excitation

138

6 MACH 12 HYDROGEN COMBUSTION STUDIES IN LENS FACILITY

SUMMARY

In this chapter we review the results of studies of mixing and combustion made to examine the key problems associated with the design of air breathing hypervelocity vehicles designed to operate up to Mach 12. Measurements of the distributions of heat transfer and pressure over a flat plate/expansion configuration are presented for a series of mixing and combusting flows generated by the burning of a vectored hydrogen jet with the 12,000 ft/sec high-pressure air flow. These studies demonstrated that it is possible to efficiently mix and combust hydrogen in high-velocity flows to generate pressure rises large enough to make scramjet propulsion at such velocities a potentially viable approach. Measurements made in these studies also demonstrated that the LENS test facility is capable of generating 5 to 6 msec of high-quality airflow at velocities of 12,000 ft/sec and from 3 to 4 msec at velocities approaching 15,000 ft/sec.

6.1 INTRODUCTION

To develop the scramjet propulsion systems necessary to power hypersonic vehicles to velocities up to 15,000 ft/sec will require detailed fundamental and configuration studies in ground-based hypervelocity facilities. To generate the turbulent mixing which would occur in the combustor of a hypervelocity scramjet engine, it is of key importance to develop reservoir pressure conditions of above 1,500 atmospheres. Such large reservoir pressures are required not only to replicate the turbulent characteristics of the flow, but also to obtain meaningful measurement sets in flows with significant vibrational and chemical non-equilibrium and combustion effects. Only by obtaining measurements in flows in which the velocity, pressure, and mixing characteristics are duplicated, is it possible to provide accurate data with which to assess combustor performance and provide information with which to examine and improve the modeling of turbulence, real gas effects and combustion that is employed in advanced Navier-Stokes computations. In fully turbulent hypervelocity flows, compressibility, turbulent mixing, combustion, flow separation, and non-equilibrium real gas chemistry are phenomena of key importance which must be understood and modeled. In order to obtain such measurements, it is vital to develop advanced hypervelocity testing facilities which can operate at extremely high energy levels and pressures, and generate high-quality, well-defined and clean free stream conditions.

6.2 EXPERIMENTAL PROGRAM

6.2.1 Objectives and Test Conditions

A series of experimental studies was conducted in the LENS facility to examine the mechanisms associated with hydrogen combustion in hypervelocity flow and examine the performance of a scramjet engine configuration at velocities of 12,000 ft/sec (3.6 km/sec) and a dynamic pressure of 1,000 psf (50 kPa). To obtain these conditions, the LENS facility was run at a total enthalpy of 7.5 MJ/kg and a reservoir pressure of 1,325 atmospheres. The studies were conducted with the contoured D-nozzle with throat configurations selected to

generate a free stream Mach number of 8 at a Reynolds number of 2.0 (10^6) per foot. Navier-Stokes calculations with the GASP code (Ref. I) were performed to establish the properties and size of the test core, as well as the initial free stream conditions. Figures 6-la through 6-1f show the nozzle exit Mach number, velocity, pressure, and density contours.

6.3   MODEL AND INSTRUMENTATION

The model used in these studies was a flat plate with an expansion surface designed and fabricated to examine basic mixing and combustion problems associated with hypervelocity flight up to 15,000 ft/sec (4.6 km/sec). These measurements follow a study with a NASP combustor model (Reference 2) tested under similar velocity and pressure conditions. Figure 6-2 shows this model installed in the test chamber of the LENS facility. The instrumentation layout is shown in Figure 6-3. To achieve the appropriate conditions on the flat plate to simulate a Mach 12 flight test, the flat plate is inclined to the free stream, as shown in Figure 6-4. The combination of Po, To, and d* (see figure 6-4 for definition of symbols), with the proper combustor ramp angle results in the proper pressure, temperature, and Mach number at the combustor inlet.

The instrumentation employed to evaluate the performance of scramjet engines in hypervelocity flow is basically a refined subset of the instrumentation for flowfield calibration and aerothermal measurements. In general, the overall performance of the scramjet can be evaluated on the basis of: (1) detailed surface measurements of heat transfer, pressure and skin friction or (2) detailed flowfield surveys which include information to deduce combustion efficiency. The accuracy of the drag and thrust measurements deduced from the surface measurements can be greatly enhanced by the direct measurement of force, particularly in the combustion chamber and nozzle sections of the engine. To accurately determine the performance of the engine from flowfield surveys, it is imperative that direct measurements be made to determine the water vapor content in the exit plane of the combustor.

The harsh aerothermal environment generated in the combustor of a scramjet engine by hydrogen combustion coupled with the high-pressure, high-enthalpy entrance conditions mandate the use of robust pressure, heat transfer and skin friction instrumentation. To measure the heat transfer rates in this flow, we generally employ a mix of thin-film heat transfer instrumentation and coaxial heat transfer gages. Because we consider thin-film instrumentation the most accurate, but fragile, way of measuring heat transfer, in the initial phases of the experimental program, we employ measurements from the thin-film gages to validate the outputs from the more rugged, but less accurate, coaxial thermocouple instrumentation. The thin-film heat transfer gages are coated with a thin insulating layer to prevent the output of the gage being influenced by electrons generated in the flowfield. Again, because of the high aerothermal loads generated in the combustor section, all pressure transducers are fitted with heat shields to prevent the sensors from experiencing a temperature rise during the steady-state run time of the tunnel (approximately 10 milliseconds). The measurement of skin friction provides key data to determine the drag of the engine. Two types of skin friction instrumentation are being employed to measure the skin friction at the

140

walls of the combustor and nozzle section of the engine. The Calspan acceleration-compensated piezoelectric gage (Reference 3), has been extensively modified to improve its thermal performance as well as to achieve a more accurate compensation of the gage. The Schetz oil-filled skin friction gage which employs strain gage sensors (Reference 4) is being employed in a form similar to that used in shock tunnel studies in the AMES facility (Reference 4). For both transducers, the key consideration to constructing the gage to provide a good thermal barrier in order to prevent temperature changes from influencing the piezoelectric or strain gage sensing mechanisms.

The measurement of the drag of the combustor and the nozzle section of the engine would provide the most direct measurements of engine performance. Making accurate force measurements in such an environment presents significant problems; however, acceleration-compensated force balances have been employed successfully to measure the thrust of the engines in flows with test times as short as one millisecond. It is conceivable that a full scale section of the combustor and nozzle downstream of the injection stations could be constructed to provide direct measurements of thrust in the 4 to 12 milliseconds run times generated in the LENS facility at velocities from 15,000 ft/sec to 8,000 ft/sec, respectively.

Indirect measurements of combustor performance can be obtained by employing picot pressure surveys coupled with a mapping of the water vapor content in the exit plane of the combustor. Again, a key problem in the pitot pressure measurements is to isolate the sensors from the very large aerothermal loads. Generally, the isolation is done by placing a heat-shielded transducer at the end of a long pitot tube, which is positioned outside the walls of the combustor. As discussed earlier, laser-diode technology has been employed (Reference 5) to directly determine both water vapor content and velocity. This latter technique is also to be used in defining the length of the steady flow time in the LENS facility driven by hydrogen gas. The development of intrusive and non-intrusive instrumentation to evaluate scramjet performance represents a key ongoing effort in the capability of the LENS facility to perform ground testing of full-size scramjet engines at Mach numbers from 6 to 15.

6.4   RESULTS AND DISCUSSION

Representative results are presented here from three test runs with air as the test gas for a reference and two hydrogen fueled runs. (Runs 13, 14 and 15). Figure 6-5a through 6-5d show some typical time history traces measured during these tests. These traces are non-dimensionalized by an appropriate reference quantity. Figure 6-5a and 6-5b show heat transfer history, and Figure 6-5c and 6-5d show pressure history as measured from a thin film heat transfer gauge. From these traces, it is evident that approximately two milliseconds are required to reach steady flow, after which a period of five milliseconds is obtained at near steady conditions. This duration of available steady flow is a significant increase over that obtained in other facilities at similar conditions. In addition, results from numerous hypersonic tests completed prior to these tests in the LENS facility and other Calspan facilities indicate that this amount of test time is required to fully establish the flowfield in this large combustor model.

141

Figures 6-6 and 6-7 show the time-averaged heat transfer and pressure results obtained from three test runs. These data were averaged over the period of steady flow conditions. The filled symbols in the figures indicate the data obtained along the centerline. Normalized data are presented from the fuel injector station downstream to the end of the expansion surface. Figures 6-3 and 6-4 shwo the sketch of the model and the instrumentation schematic for reference. The two fueled tests (Runs 14 and 15) indicate higher pressure and heat transfer levels by approximately 15% over that of the tare test (Run 13). These levels ultimately produced higher heat transfer and pressure on the expansion surface, as illustrated in Fugures 6-8 and 6-9, which are expanded views of Figures 6-6 and 6-7.

6.5   CONCLUSIONS

It has been demonstrated that the LENS facility is capable of generating the test times required to fully establish the flow through a large scramjet combustor at velocities of up to 12,000 ft/sec for reservoir conditions of over 1,500 atmospheres. Furthermore, the LENS facility is capable of generating 5-6 milliseconds of high-quality air flows at velocities of 12,000 ft/sec or from 3-4 milliseconds at velocities approaching 15,000 ft/sec.

6.6   REFERENCES

1.   McGrory, W.D., Slack, D.C., Applebaum, M.P., and Walters, R.W., "GASP Version 2.2 User's Guide," AeroSoft, Inc., Blacksburg, VA, 1992.

2.   Albrechcinski, T., Boyer, D., and Wehe, S., "The NASP 5th Entry Scramjet Combustor Measurements Program Performed in Calspan's Upgraded 96" Hypersonic Shock Tunnel," Calspan Report No. 7924-A, December 1993.

3.   Holden, M.S., Calspan Corporation, "A Study of Flow Separation in Regions of Shock Wave-Boundary Layer Interaction in Hypersonic Flow," AIAA-78-1169, Presented at the 11th Fluid and Plasma Dynamics Conference, July 10-12, 1978, Seattle, WA.

4.   Bowersox, R., Schetz, J., Chadwick, K., and Deiwert, G., "Direct Measurements of Skin Friction in Hypersonic High Enthalpy Impulsive Scramjet Experiments," AIAA-94-0585, 32nd AIAA Aerospace Sciences Meeting & Exhibit, January 10-13, 1994, Reno, NV.

5.   Hanson, R.K., "Laser-Based Diagnostics for Hypersonic Flows," Published in *New Trends in Instrumentation for Hypersonic Research*, Series E: Applied Sciences, Vol. 224, 1995.

APPENDIX I

LIST OF PUBLICATIONS ASSOCIATED WITH
THE CURRENT CUBRC STUDIES
CONDUCTED UNDER THE URI CONTRACT

Holden, M.S., "Recent Advances in Hypersonic Test Facilities and Experimental Research," AIAA 93-5005, Presented at the AIAA/DGLR 5th International Aerospace Planes and Hypersonics Technologies Conference, 30 November - 3 December 1993, Munich, Germany.

Boyd, I.D., Srinivasan, A., Muntz, E.P., Hanson, R.K., and Holden, M.S., "Thermochemical Nonequilibrium Design Calculations for Detailed Hypervelocity Experiments in the LENS Facility," AIAA-94-2097, Paper presented at the 6th AIAA/ASME Jiont Thermophysics and Heat Transfer Conference, Colorado Springs, CO, June 20-23, 1994.

Holden, M.S., "Development and Code Evaluation Studies in Hypervelocity Flows in the LENS Facility," Paper presented at the Second European Symposium on Aerothermodynamics for Space Vehicles and Fourth European High-Velocity Database Workshop, ESTEC, Noordwijk, The Netherlands, November 21-25 1994.

Holden, M.S., Kolly, J.M. and Chadwick, K.M., "Calibration, Validation and Evaluation Studies in the LENS Facility," AIAA 95-0291, paper presented at the 33rd Aerospace Sciences Meeting and Exhibit in Reno, NV, January 9-12, 1995.

Holden, M.S., Chadwick, K.M. and Kolly, J.M., "Hypervelocity Vehicle and Combustion Studies in the LENS Facility," AIAA 95-2523, paper presented at the 31st AIAA/ASME/SAE/ASEE Joint Propulsion Conference and Exhibit in San Diego, CA, July 10-12, 1995.

Holden, M.S., Craig, J.E. and Kolly, J.M., "Instrumentation for Flow Calibration and Vehicle Measurements in Hypervelocity Flows in the LENS Facility," paper presented at the 16th International Congress on Instrumentation in Aerospace Simulation Facilities at Wright-Patterson Air Force Base, OH, July 18-21, 1995.

Holden, M.S., Chadwick, K.M., Gallis, M.A. and Harvey, J.K., "Comparison Between Shock Tunnel Measurements on a Planetary Probe Configuration and DSMC Predictions," paper presented at the 20th International Symposium on Shock Waves at California Institute of Technology, Pasadena, July 23-28, 1995.

Holden, M.S. and Chadwick, K.M., "Hypervelocity Combustion Studies in the LENS Facility," paper presented at the 1995 JANNAF Combustion Subcommittee Meeting, NASA Marshall Space Flight Center, Huntsville, AL, October 23-27, 1995.

Holden, M.S., "Viscous/Inviscid and Real-Gas Effects Associated With Hypersonic Vehicles," paper presented at the AGARD-FDP-VKI Special Course, Brussels, Belgium, April 15-19, 1996

Holden, M.S., Moselle, J.R., Sweet, S.J., and Martin, S.C., "A Database of Aerothermal Measurements in Hypersonic Flow for CFD Validation," AIAA 96-4597, presented at the 7th International Space Planes and Hypersonic Systems and Technologies Conference, Norfolk, VA, November 18-22, 1996.

Holden, M.S. and Walker, B.J., "A Review of Recent Development, Testing and Code Validation Studies in the LENS Facility," AIAA 96-4598, presented at the 7th International Space Planes and Hypersonic Systems and Technologies Conference, Norfolk, VA, November 18-22, 1996.

Holden, M.S., Bergman, R.C., Harvey, J.K., Boyd, I.D. and George, J., "Experimental Studies of Real-Gas Effects Over a Blunted Cone/Flare Configuration in Hypervelocity Airflows," AIAA 97-0855, presented at the 35th Aerospace Sciences Meeting and Exhibit, Reno, NV, January 6-10, 1997.

APPENDIX I

Holden, M.S., Harvey, J.K., Boyd, I.D., George, J. and Horvath, T.J., "Experimental and Computational Studies of the Flow Over a Sting-Mounted Planetary Probe Configuration," AIAA 97-0768, presented at the 35th Aerospace Sciences Meeting and Exhibit, Reno, NV, January 6-10, 1997.

Holden, M.S., "Thermal Loads and Protection Systems for Transitional and Shock Interaction Regions in Hypersonic Vehicle Design," presented at the AGARD Conference on Future Aerospace Technology in the Service of the Alliance, Palaiseau, France, April 14-16, 1997.

Holden, M.S., "Aerothermal Characteristics of Shock/Shock Interaction Regions in Hypersonic Flows," presented at the AGARD Conference on Future Aerospace Technology in the Service of the Alliance, Palaiseau, France, April 14-16, 1997.

Holden, M.S., "Real-Gas Effects on Regions of Viscous-Inviscid Interaction in Hypersonic Flows," AIAA 97-2056, presented at the 28th AIAA Fluid Dynamics Conference, 4th AIAA Shear Flow Control Conference, Snowmass Village, CO, June 29-July 2, 1997.

(a) D-Nozzle Exit Mach Number

(b) D-Nozzle Exit Velocity

(c) D-Nozzle Cross Velocity

(d) D-Nozzle Exit Pressure

(e) D-Nozzle Exit Temperature

(f) D-Nozzle Exit Density
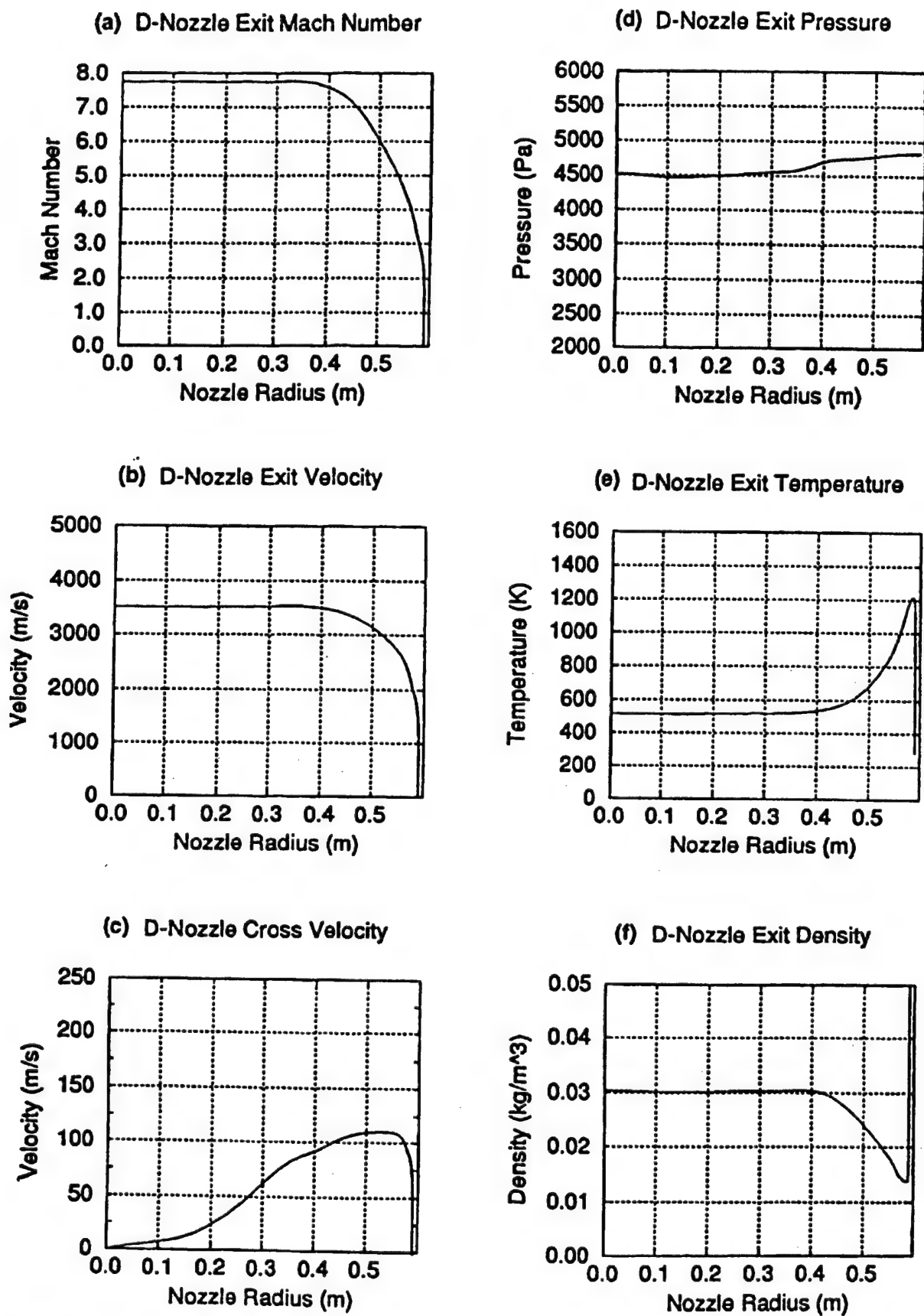
Figure 6-1   Nominal Freestream Conditions for the Mach 12 Combustor Tests

143
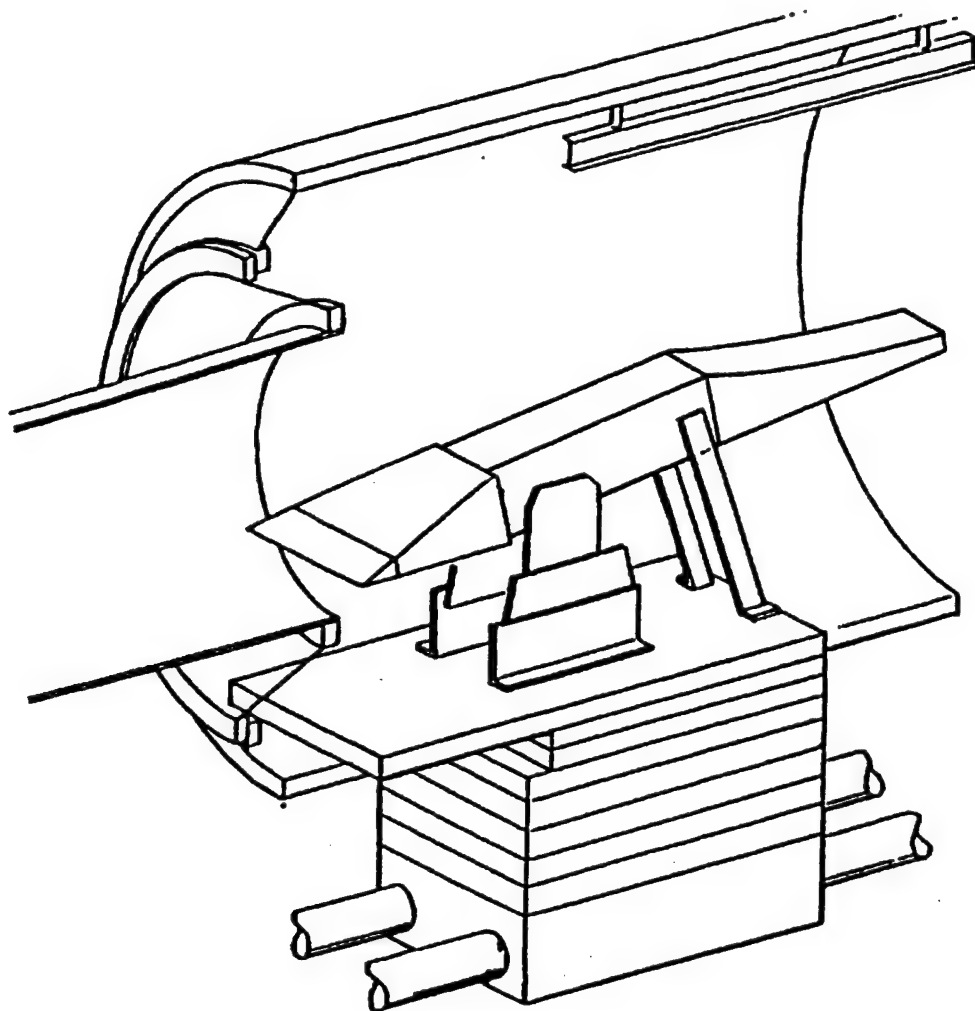
Figure 6-2 Schematic of the Combustor Model Mounted in the LENS Facility

144
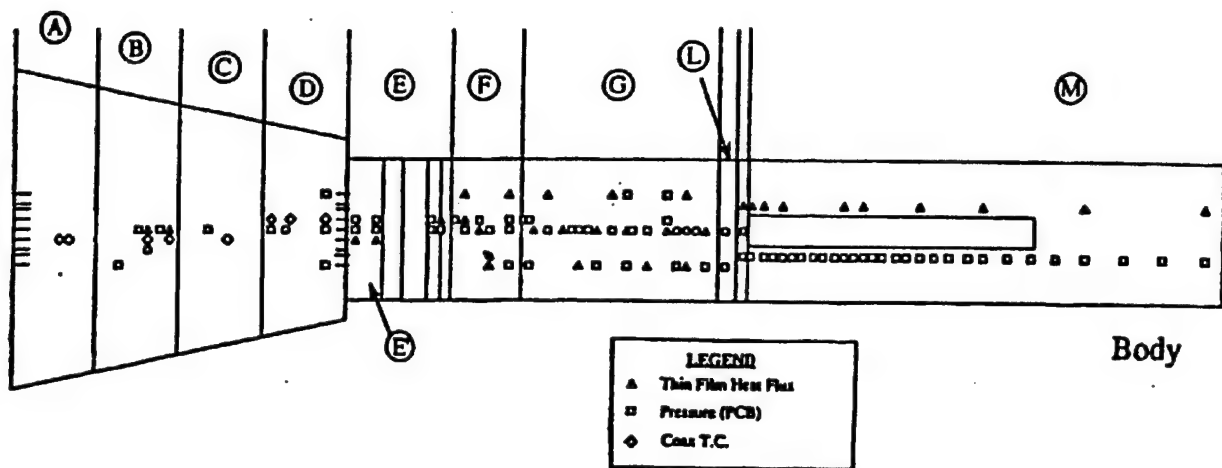
Figure 6-3 Combustor Instrumentation Configuration
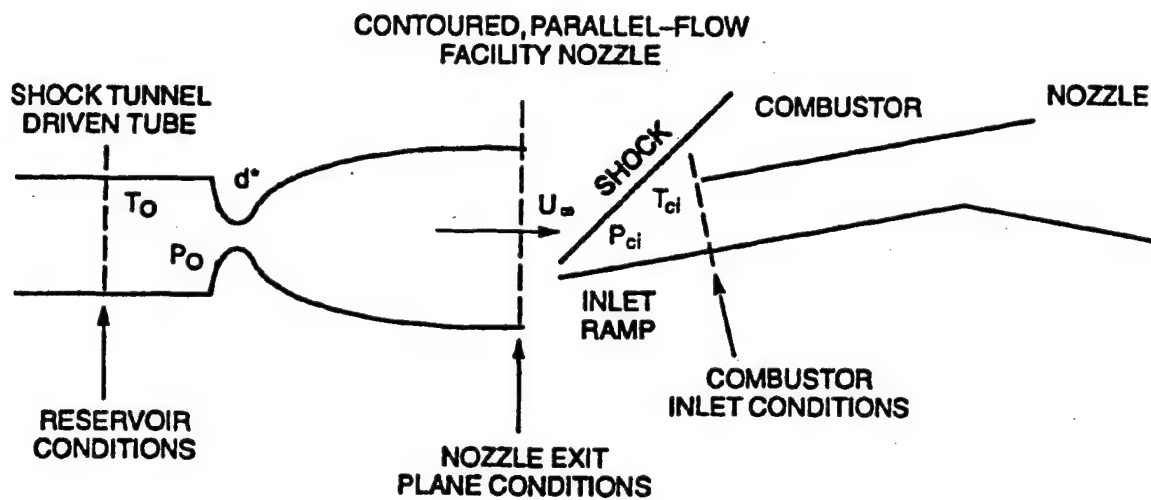
Figure 6-4 Schematic of Nozzle/Combustor Configuration
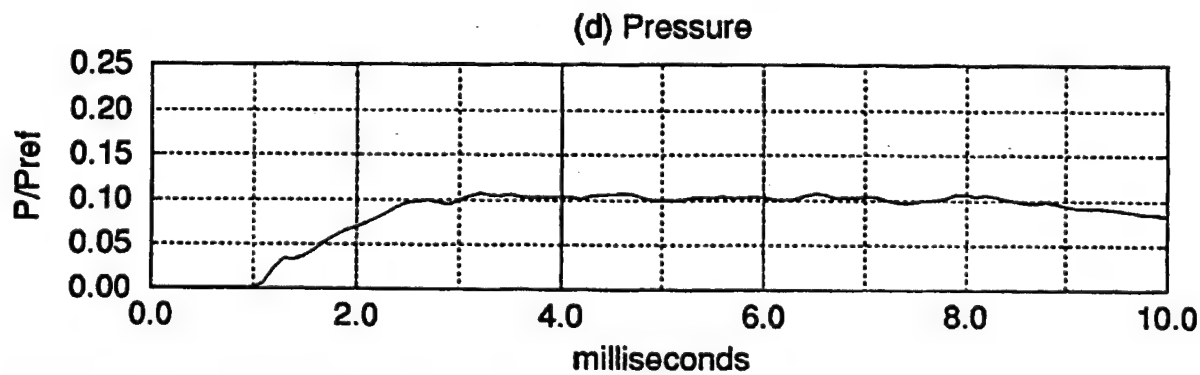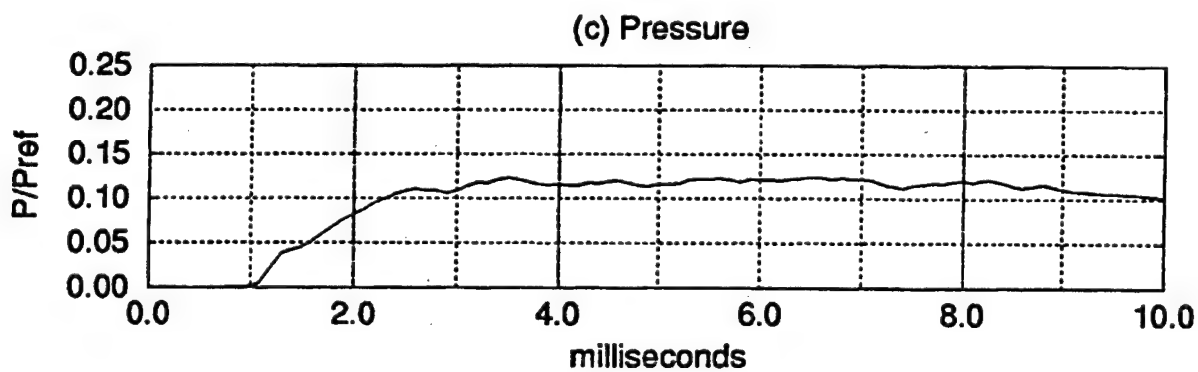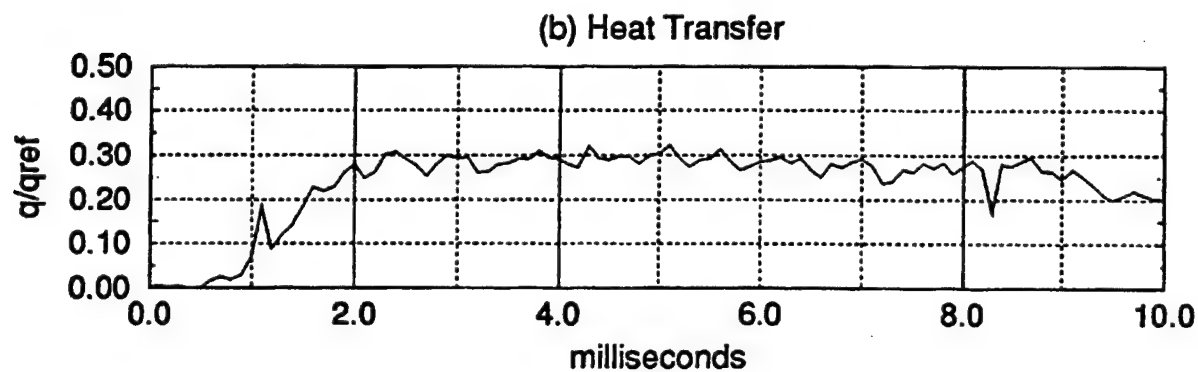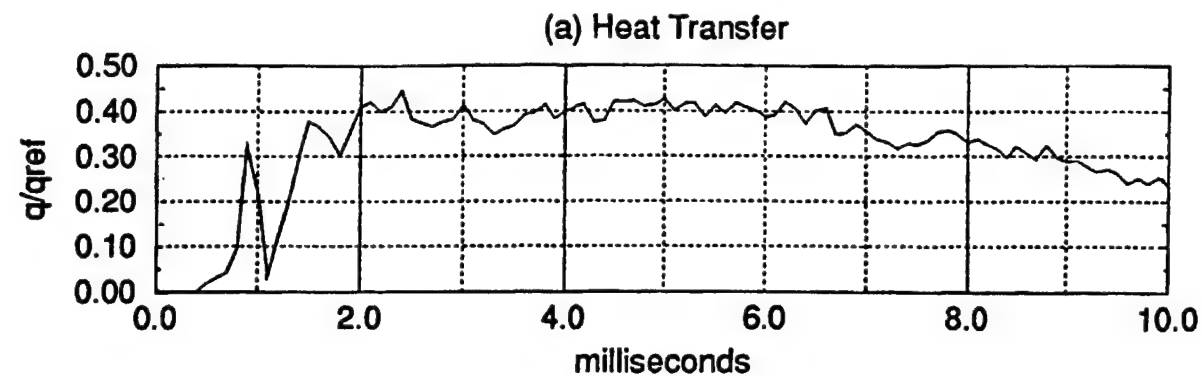
Figure 6-5 Typical Time Histories of Heat Transfer and Pressure for the Mach 12 Combustor Tests

146
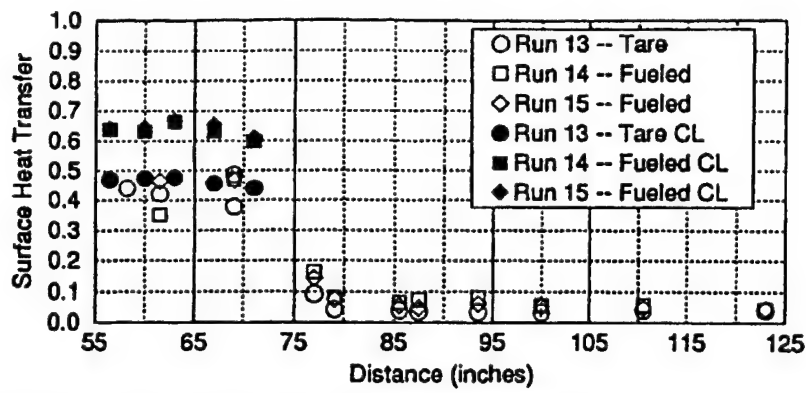
Figure 6-6 Heat Transfer Along the Flat Plate Combustor
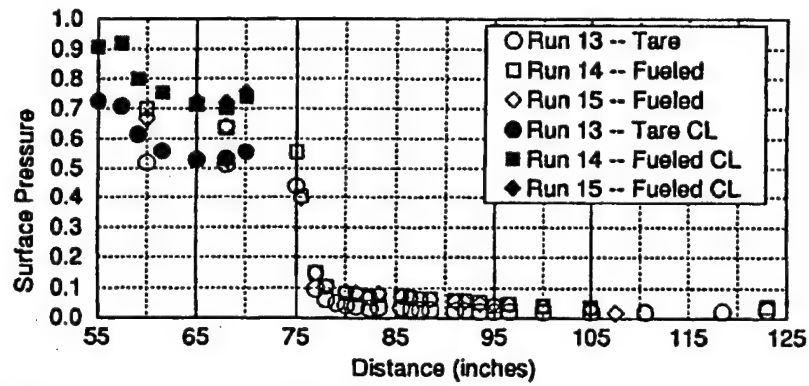
Figure 6-7 Pressure Along the Flat Plate Combustor
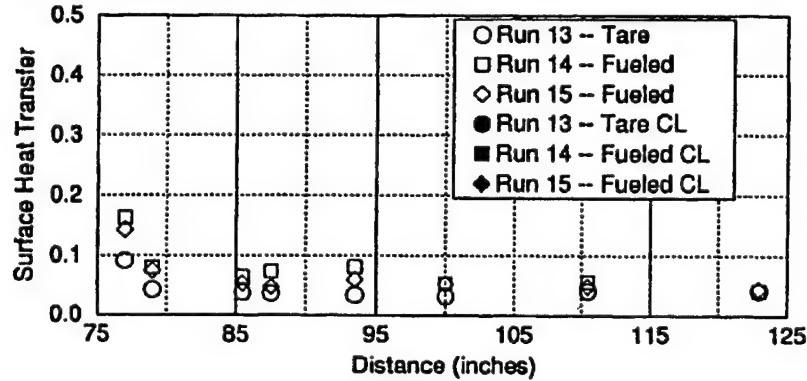
Figure 6-8 Heat Transfer Along the Expansion Surface
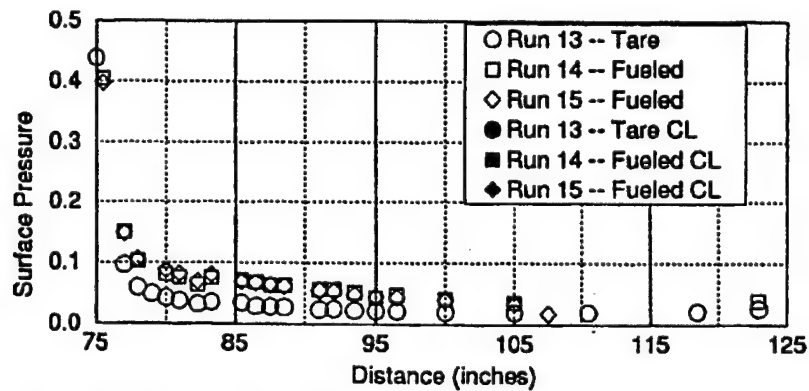
Figure 6-9 Pressure Along the Expansion Surface

147

SECTION II

INSTRUMENTATION DEVELOPMENT

This section authored by

R.K. Hanson, E.P. Muntz, S. Wehe, and F. Lutfy

II. I. Laser Diagnostics

Introduction

The component of the University Research Initiative undertaken by Stanford University was the development of laser-based, hypersonic flow diagnostics. The goal was to then apply these diagnostics to characterize the gasdynamic conditions in hypersonic flow facilities, as well as to measure important quantities (e.g., rotational and vibrational temperature, species concentration, and velocity) in specific hypersonic flowfields of interest. Target configurations included hypersonic air flow over a blunt cone and reacting flow of hydrogen injected into a supersonic air stream, as might be found in a scramjet engine configuration.

Both imaging and point diagnostics were developed. Planar laser-induced fluorescence (PLIF) imaging diagnostics with both OH and NO tracers were shown to be useful sources of quantitative, spatially- and temporally-resolved information in hypersonic flows. Experiments at Stanford validated PLIF techniques for hypersonic applications, while experiments at the Calspan and CUBRC facilities in Buffalo, New York focused on resolving issues associated with applications in the extreme environments of industrial test facilities.

Over the course of the URI program, a tunable diode laser (TDL) absorption diagnostic for hypersonic flows emerged as being of great utility and became an important part of the Stanford effort. Following validation of the technique at Stanford, application of the TDL diagnostic in the LENS facility provided detailed composition, temperature, and velocity information in the freestream of the shock tunnel flow. To our knowledge, these measurements are the first of their kind in this type of high-enthalpy, hypersonic flow regime. The measurements hold promise for extending the range of experimental data that can be collected in state-of-the-art facilities such as the LENS tunnel and for improving the accuracy and reliability of this data.

Stanford Development of PLIF for Hypersonic Flows

Planar laser-induced fluorescence (PLIF) is a powerful non-intrusive diagnostic technique which enables instantaneous, spatially-resolved measurement of flowfield properties. In essence, the diagnostic involves two key elements: a pulsed laser beam formed into a sheet to illuminate a plane in the flow field of interest and a time-gated intensified CCD camera which monitors the fluorescence induced by the laser pulse. The laser is tuned so as to excite a specific quantum state of the species being probed. Through knowledge of how the resulting fluorescence depends on fluid quantities of interest for a given tracer and excitation scheme, PLIF strategies can be developed to extract data on species concentration, temperature, pressure or density, and even velocity.

Development in these areas occurred primarily on the Stanford University Expansion Tube, which is shown in Figure 1. Unlike reflected-type shock tunnels such as the LENS facility, which expand gases in a high-enthalpy reflected-shock region through a nozzle, expansion tubes generate high velocity flows through an unsteady expansion. Despite this difference in operation from the LENS tunnel, the expansion tube provides an impulse facility capable of generating reacting or non-reacting hypersonic flows and is therefore suitable as a test bed with which to address the challenges of hypervelocity PLIF studies.

149
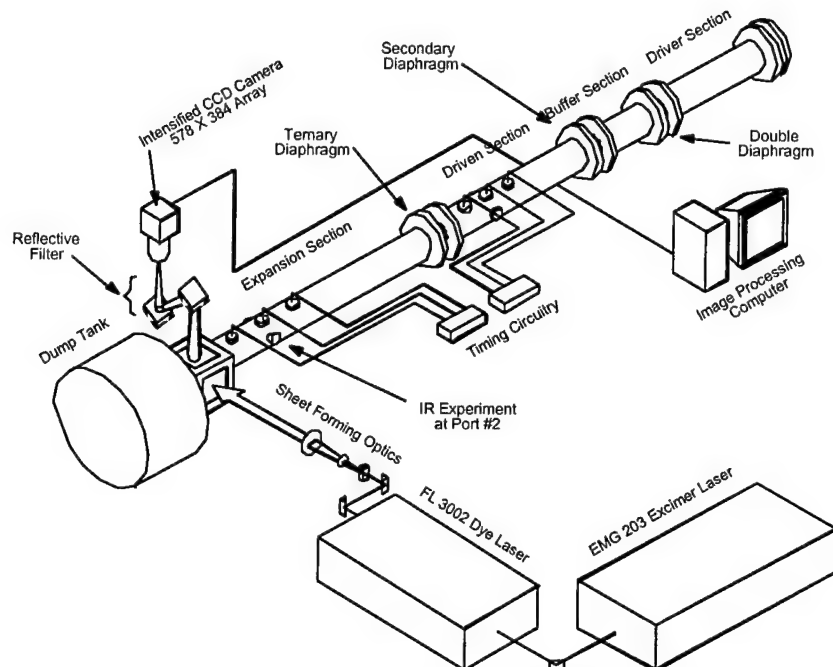
Figure 1. A schematic of the Stanford University Expansion Tube Test Facility. High enthalpy flow is generated along an unsteady expansion that occurs in the expansion section. A fast gated (5 ns) intensified CCD camera, with reflective filters mounted in front of it, collects the fluorescence emanating from the test section.

PLIF with an OH Tracer (Reacting Flow)

Initial expansion tube studies were aimed at demonstrating the ability of OH PLIF to mark combustion zones in supersonic and hypersonic flows. These experiments rely on linear laser excitation of tracer molecules (OH) in the flow followed by broadband collection of the fluorescence from the radiative decay of these excited molecules. Based on considerations of separation from neighboring lines and measurement sensitivity at the temperatures in question, the $Q_1(7)$ transition of the $A^2\Sigma \leftarrow X^2\Pi$ (1,0) band of OH, located at 283.31 nm, was selected for laser excitation.

For the expansion tube conditions considered, fluorescence signal changes most significantly with variations in local OH number density, allowing the images to be treated as rough maps of OH concentration suitable for identifying regions of combustion. Figure 2, for example, contrasts a weaker combustion case (top half of image) with a stronger combustion case (bottom half of image) in high-speed flow of a stoichiometric methane-air mixture over a cylinder. Freestream Mach number for the top half of the image is 4.5, compared to 6.2 for the bottom half. Top half freestream conditions are T = 480 K and P = 42 Torr; bottom half freestream conditions are T = 440 K and P = 67 Torr.

← Increasing OH Signal
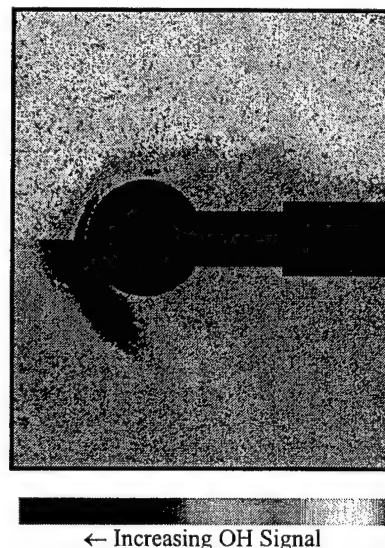
Figure 2. This composite PLIF image contrasts the weaker combustion conditions of the top half with the stronger combustion conditions of the lower half in high-speed flow of a stoichiometric methane-air mixture over a cylinder.[1]

150

PLIF with an NO Tracer (Non-Reacting Flow)

To demonstrate the viability of PLIF with a nitric oxide (NO) tracer as a diagnostic tool in hypersonic environments, a series of non-reacting flow studies was initiated in the expansion tube. Initial studies at Stanford with NO PLIF in supersonic and hypersonic flows have provided quantitative temperature images and images marking important flow features, such as shocks and expansions. Conveniently, NO often occurs naturally in the freestream of high-enthalpy shock tunnels, as it is chemically frozen out in the nozzle expansion process. Furthermore, NO is generated in the high-temperature stagnation regions and shock layer flows about aerodynamic models. Finally, propulsion systems generate NO as a byproduct of high temperature combustion.

In a sample application, NO PLIF images proved useful in determining the Mach number of a flow about a cylinder.[3] Figure 3 shows a NO PLIF image of a cylinder transverse to a nominally Mach 6 flow. A cut across the image 45 pixels above the shoulder of the cylinder reveals the sharp increase in PLIF signal across the shock. The increase in signal is primarily associated with the increase in NO number density. The shape of the bow shock can be determined from the discontinuity in the PLIF signal across the shock. The experimentally determined shape was compared to CFD calculations of the flowfield over a range of Mach numbers. The best-fit computed shock shape is shown in Figure 4. Calculations based on the PLIF result indicate that the flow Mach number is 6.0 ± 0.5.
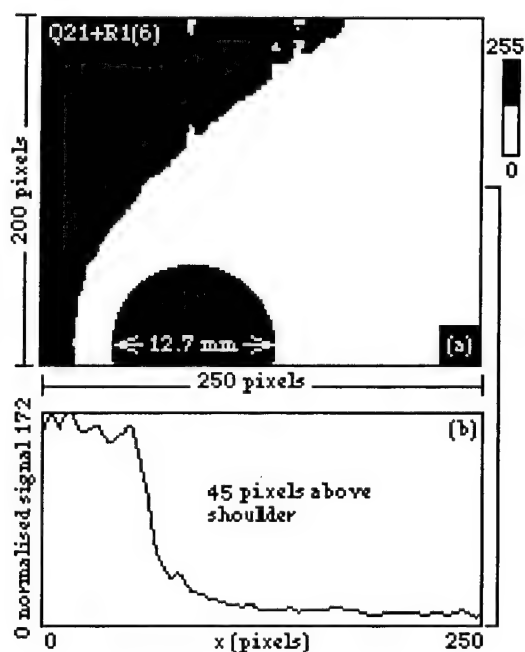
Figure 3. (a) NO PLIF image for nominal Mach 6 flow of air over a cylinder; (b) Profile of normalized fluorescence intensity for a horizontal cut 45 pixels (6.3 mm) above top of cylinder.
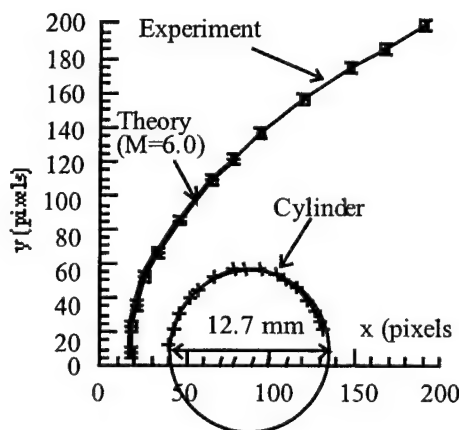
Figure 4. Shock shape from theoretical and experimental results.

In addition, demonstrations of two-line NO PLIF thermometry were performed for hypervelocity air flows.[2] The two-line technique involves sequential excitation of transitions with different initial quantum states, so that the local rotational or vibrational temperature may be determined from the ratio of the fluorescence signals. Many of the uncertain quantities affecting the fluorescence signal are eliminated in this ratio process, resulting in a quantity that depends on temperature in a known fashion.

151
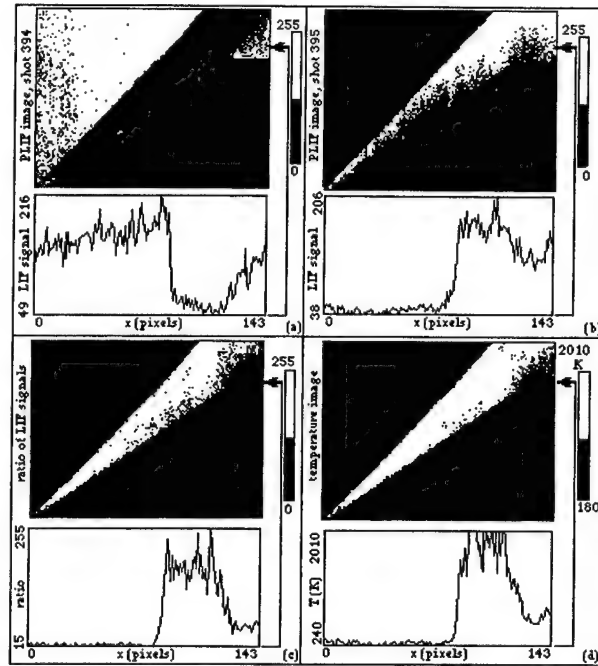
Figure 5. Images and profiles: (a) Fluorescence from excitation of the R2(15) line of NO; (b) fluorescence from excitation of the R2(15) line of NO; (c) ratio of fluorescence intensities from these respective images; (d) inferred temperature. The wedge angle is 35∞, the distance from the base of the image to the shoulder of the wedge is 12.7 mm, and the profiles are taken along a horizontal line 8 pixels (1.3 mm) above the shoulder.

Figure 5(a) and (b) display PLIF images resulting from single-shot excitation of the $R_2(15)$ line and $Q_1+P_{21}(25)$ line, respectively, of the $A^2\Sigma \leftarrow \Sigma^2\Pi^+(0,0)$ electronic transition of NO. Figure 5(c) displays an image of the ratio (rab) of these images. The significant variation in the value of rab throughout the flow indicates the strong temperature sensitivity of the selected line pair. In Figure 5(d), this ratio has been converted to a quantitative image of temperature. This figure exhibits the expected features. The temperature is seen to rise across the shock, maintain a reasonably constant value in the post-shock region, and then decrease in the Prandtl-Meyer expansion fan at the shoulder of the wedge. These kinds of successful demonstrations of qualitative and quantitative imaging in the Stanford hypersonic facilities validated the principles of PLIF application in hypervelocity flows.

Development of PLIF System for LENS Facility

Extending the success of hypervelocity PLIF imaging at Stanford to a high-enthalpy industrial test facility such as the LENS tunnel involved many additional challenges. Efforts at the Calspan-University of Buffalo Research Center (CUBRC), where the LENS facility is located, were aimed at identifying, analyzing, and addressing these challenges. Unfortunately, actual PLIF experiments in the LENS tunnel were pre-empted by a BMDO project that rendered the facility inaccessible. However, Calspan Corporation allowed preliminary diagnostic development experiments to be undertaken by Stanford in a smaller facility, the Calspan 48" Hypersonic Shock Tunnel. A PLIF imaging system suitable for high-enthalpy environments was designed and put into place in this facility. Work that was performed in this facility will likely contribute to the success of future PLIF experiments in large ground-test facilities.

Design of the Calspan PLIF system and design of the projected LENS PLIF system had to take into account a variety of difficulties unique to high-enthalpy impulse facilities. One significant challenge is the massive natural emission of light over many spectral bands. A scheme had to be devised for reducing the collection of the background light relative to the fluorescence signal. The approach developed involved discriminating the desired fluorescence both temporally and spectrally from the background emission.

Acquisition of a fast-gated (5 ns), UV-enhanced, intensified CCD camera (576 x 384 pixel) permitted the best possible temporal discrimination of the fluorescence by allowing gate widths on the order of the laser pulse width (~15 ns). An additional benefit of this short gate capability was the ability to "freeze" the flowfield in time and

152

space. Even at the highest expected velocity of 4.5 km/s, the fastest molecules would have traveled a distance of only 23 μm over the duration of the gate, less than the dimension of a individual pixel even for 1:1 imaging.
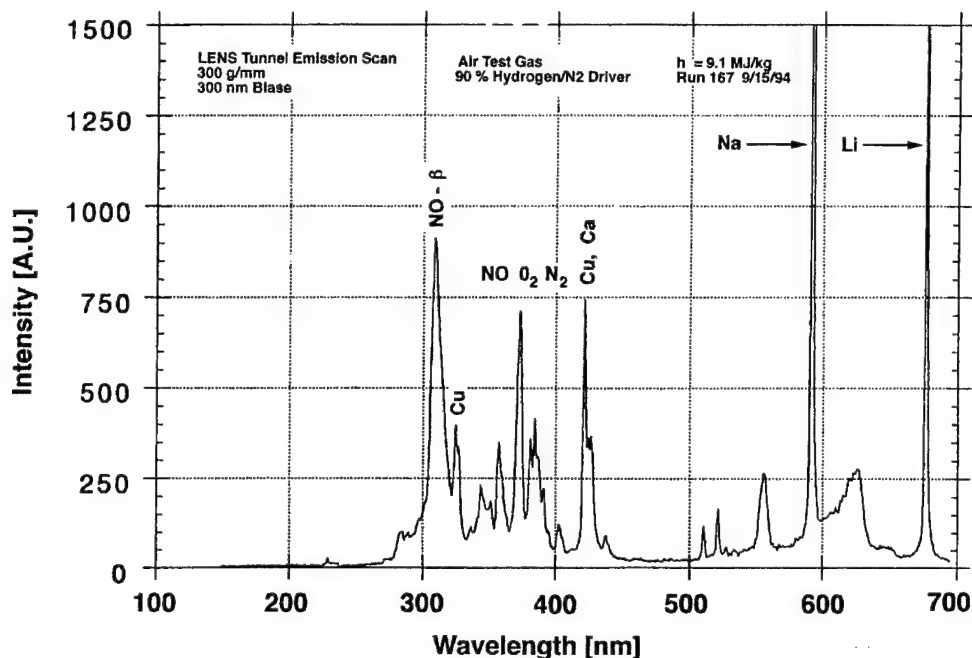
Figure 6. The natural emission radiation collected from a stagnation region in the LENS Tunnel using an optical multichannel analyzer (OMA). The signal below 280 nm is attenuated by the natural cut-off associated with the quartz fiber optic coupling.

A special arrangement for spectral filtering was also required. During the test time, light is emitted over a broad spectral range from a number of sources, both species present in the test gas mixtures (e.g., O_2) and flow contaminants (e.g., copper, beryllium, molybdenum, and tungsten) from the inner surfaces of the test facility. In order to design a spectral filtering scheme, it was necessary to first understand the spectral characteristics of the interfering light. During the first on-site visit to CUBRC by Stanford students (September 1994), a study was conducted in the LENS tunnel in which light was collected from the stagnation region of a planetary probe model using a fiber-coupled optical multichannel analyzer (OMA). Figure 6 shows a sample scan from a 9.1 MJ/kg air test in the LENS facility with a 90% H_2/N_2 driver gas, with a few of the more prominent features identified. It is clearly important to attenuate the significant natural emission of NO, O_2, N_2, and Cu in the 300 to 400 nm region when collecting the laser-induced fluorescence of NO, which is centered near 250 nm.

In environments with less interference, UG-5 optical glass is effective at attenuating elastically-scattered laser light at 226 nm while permitting sufficient transmission of the NO fluorescence. However, this simple filtering strategy has several inadequacies when faced with the more serious signal discrimination issues of the LENS tunnel environment. First, the maximum transmission of the UG-5 glass is only 81%. Second, its cutoff is insufficiently sharp, resulting in attenuation of the strongest NO band, whose fluorescence peaks near 236 nm. Third, the UG-5 filter continues to transmit out to 360 nm, allowing many of the interferences shown in Figure 6 to be collected by the camera.

A reflective filter system was designed that provides significant improvements over the simple UG-5 filter. In Figure 7, the performance of this system is compared with that of the UG-5 glass. The start of band-pass was selected to remove the signal resulting from elastic laser scattering at 226 nm. The filter cuts off near 300 nm to minimize interference from the O_2 Schumann-Runge bands.[3] Though the O_2 signal overlaps the NO fluorescence throughout the NO collection band, 300 nm is the wavelength at which fluorescence from NO and O_2 fluorescence is nominally equal. Above 300 nm there is no additional signal-to-noise benefit from filter transmission.
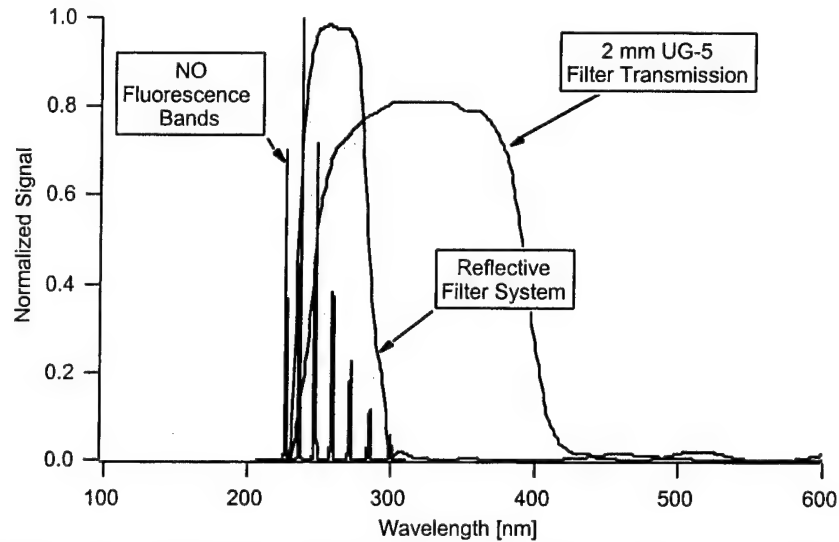
Figure 7. Comparison of the NO fluorescence signal from the $A(v'=0) \rightarrow X(v'')$ transitions, the spectral band pass of a 2 mm thick UG-5 filter, and the spectral band pass of a compound reflective filter.

Following the design of a PLIF system capable of performing well in the extreme conditions of high-enthalpy hypersonic tests, the necessary components were assembled at Calspan. Support structures and optical interfaces to the tunnel were constructed. Figures 8 and 9 show the final design of the PLIF system for the Calspan 48" shock tunnel. A Lambda Physik EMG 203 excimer laser, operating with a XeCl mixture, pumps a dye laser (Lambda Physik EMG FL3002), which is frequency-doubled to generate a 226 nm beam. Sheet optics bring the laser sheet through quartz windows into the tunnel test section. The ICCD camera is mounted on a stage on top of the test section, so as to collect the resulting images of NO fluorescence.
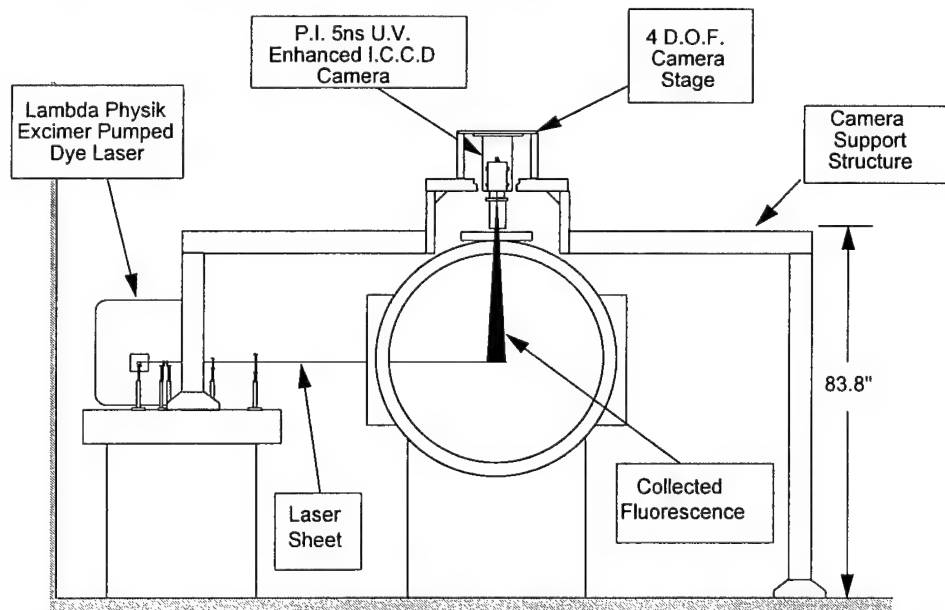
Figure 8. A view looking downstream into the Calspan 48" test section. The excimer pumped, dye laser system and sheet forming optics are shown to the left. A camera and arbor structure are shown above the facility including a special 4 degree of freedom stage affixed to the arbor.

154
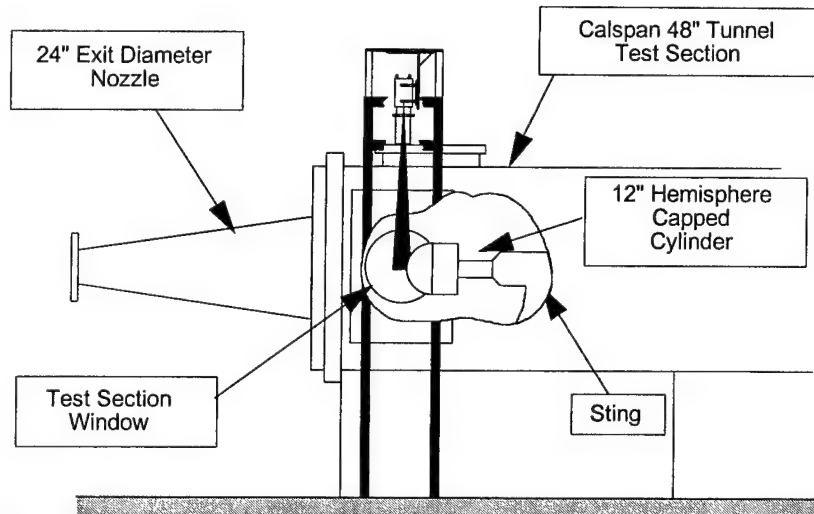
Figure 9. A side view of the Calspan 48" test section configured with a 24" exit-diameter nozzle. A cut-out in the test section illustrates the 12" hemisphere capped cylinder which served as the flow field model.

Figures 10 and 11 are photographs of the actual experimental configuration put in place on the Calspan 48" HST facility. Planned tests dictated by a Calspan contract were to involve 1.5 MJ/kg air flows at Mach 5. Ultimately, no PLIF data was collected due to delays in these air flow tests. However, the PLIF development work at Calspan and CUBRC did yield dividends in increased understanding and ability to overcome technical challenges associated with PLIF imaging in high-enthalpy impulse facilities.

Figure 10. Photo illustrating the excimer laser system installed in the Calspan 48" test laboratory.
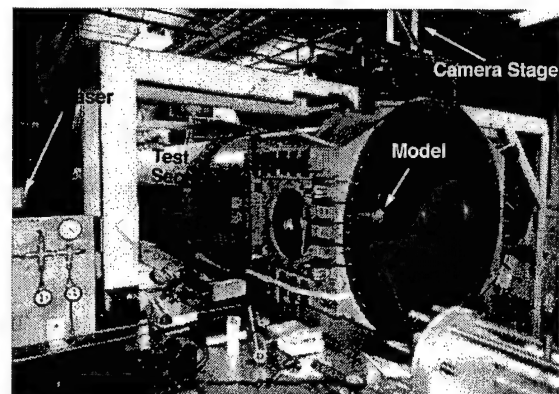
Figure 11. A photo of the Calspan 48 HST test section shown without the facility nozzle. The arbor structure is shown surrounding the test section with the laser systems and sheet optics to the left. The camera stage is shown on top.

Tunable Diode Laser Absorption Diagnostic For Hypersonic Flows

A convergence of the needs of Calspan/CUBRC with Stanford's experience in laser-based diagnostics drove development of an additional hypersonic flow diagnostic. A long unresolved question in high-enthalpy reflected-type shock tunnels has been when in a run the test gas first becomes contaminated with driver gas. Interaction between a hydrogen driver gas and air test gas would produce water vapor, which could be precisely detected by a tunable diode laser (TDL) absorption diagnostic. Development and implementation of this diagnostic would, therefore, provide useful information for Calspan and CUBRC. At the same time, it became apparent that, by enabling temporally-resolved, line-of-sight measurement of species concentration, temperature, and velocity in the LENS or Calspan tunnel test sections, the TDL diagnostic would significantly further the objectives of the URI program. Indeed, the TDL diagnostic became a major contribution of the Stanford program to the URI work,

155

yielding detailed data (species concentration, temperature, and velocity) characterizing shock tunnel conditions, the first measurements of their kind in this environment. Such measurements have the potential to further improve the data that can be collected from such state-of-the-art ground test facilities as the LENS tunnel.

TDL Absorption Theory

The principle behind the laser based technique is Beer's law, which states that the ratio of transmitted laser intensity, $I(v)$, to incident laser intensity $I_0(v)$, through a gas containing an absorbing species is governed by:

$$\frac{I(v)}{I_0(v)} = \exp\left(-S(T)\, \Phi(v-v_0)\, P_i\, L\right)$$

where v is the laser wavenumber [cm^{-1}, proportional to frequency], $S(T)$ [cm^{-2}/atm] is the line strength of the species' resonance transition being probed with the laser, P_i [atm] is the partial pressure of the absorbing species, L [cm] is the measurement path length containing the species of interest, and $\Phi(v)$ is a line shape parameter that incorporates various mechanisms which broaden the spectral region of absorption. S and Φ are defined such that the integral over the line shape parameter is

$$\int_{-\infty}^{\infty} \Phi(v-v_0)\, dv = 1$$

The negative of the natural log of the laser intensity ratio is commonly referred to as the absorbance and is shown below:

$$-\ln\frac{I(v)}{I_0(v)} = S(T)\, \Phi(v-v_0)\, P_i\, L$$

The theoretical basis for determining gas temperature and species concentration from measured absorption spectra has been described previously.[4-6] In brief, the rotational gas temperature is determined from the ratio of measured H_2O absorbances obtained by tuning the narrow-bandwidth diode lasers across H_2O transitions originating from differing rotational levels in the same vibrational ground state. The partial pressure of the probed species is determined from the measured absorbance from one of the transitions using the known absorption line strength at the measured temperature. The translational temperature is determined directly from the width (FWHM) Δv_D (cm^{-1}) of the Doppler-broadened H_2O lineshapes given by

$$\Delta v_D = 7.162 \times 10^{-7}\, v_0\, \sqrt{(T_{tran}/M)}$$

where T_{tran} is the translational temperature, v_0 is the transition wavelength [cm^{-1}], and M is the molecular weight [amu] of the absorbing species.

Gas velocity was determined from the measured Doppler-shifted absorption obtained by directing a beam at an angle with respect to the bulk gas velocity. The relative shift of the absorption signal, Δv, at frequency v as seen by the gas moving at velocity V_{Gas} [m/s] is given by the relation

$$\frac{\Delta v}{v} = V_{Gas}\, \frac{\cos\theta}{c}$$

where c is the speed of light [m/s] and θ is the angle between the beam and the bulk gas velocity. A reference (unshifted) absorption signal was recorded in stationary gas using a static cell located in the control room.

Initial TDL Experiments (Calspan 96" Hypersonic Shock Tunnel)

Because of BMDO testing in the LENS facility that preempted initial diagnostic implementation, the first experiments to detect water vapor were performed in a Calspan facility, the 96" Hypersonic Shock Tunnel. This facility is a high-enthalpy impulse facility much like the LENS and capable of reaching similar enthalpies. The operational details and capabilities of the Calspan shock tunnel have been published previously.[10] Figure 12 shows how the diagnostic interfaces with the tunnel. An important advantage of the TDL technique is the fact that fiber optics can be used to locate the laser system remotely from the test facility. As a result, the operator can make

156

adjustments to the laser system as necessary even during the period before the test run when personnel are barred for safety reasons from being in the Facility Test Area.
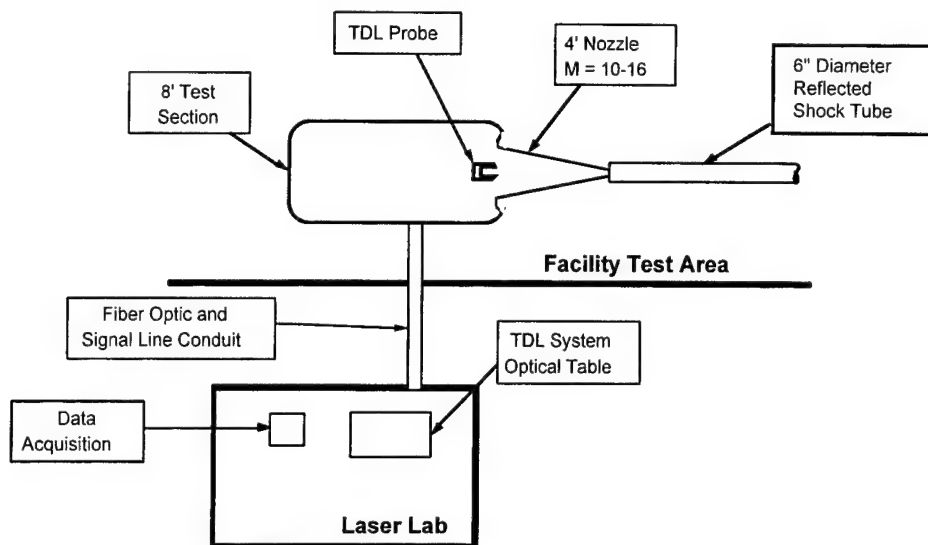
Figure 12. A plan view of the Calspan 96" HST laboratory area. The laser beams were fiber coupled to the probe located in the test section from a remote location.
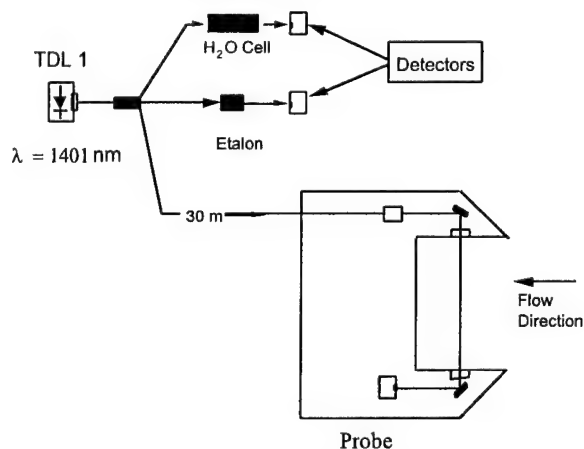
Figure 13. A schematic of the first generation water vapor probe to sense the presence of water vapor in the Calspan 96" HST freestream.
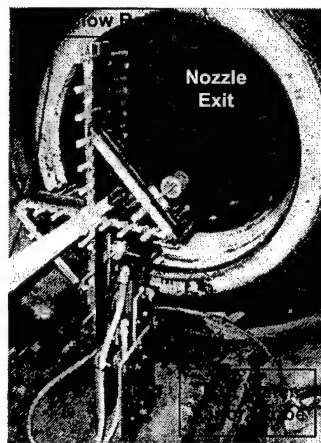
Figure 14. An aft view (looking upstream) of the TDL water vapor probe installed in the test section of the Calspan 96" HST. An airflow calibration rake was in place alongside the probe during these experiments.

As shown in Figure 13, "pitch" and "catch" electro-optics to send the measurement laser across the flow are located in a hardened structure that is then mounted in the tunnel test section (Figure 14). The distance between the two arms of the probe is 18 cm, and the overall length is 25 cm. For comparison, the nozzle exit diameter is 121 cm. The probe casing was fabricated from 0.3 cm thick, 6.3 cm wide structural steel square tubing. The fiber-coupled beam was split into three legs (10:10:80) using a 1×3 splitter. One 10% leg was passed through a solid-etalon interferometer (2.001 GHz spectral range) to measure frequency as the laser was tuned across the water absorption feature. The other 10% leg was directed through a low-pressure cell filled with water vapor for tuning purposes. The test beam (80%) was directed from one arm of the probe across the flow to the other through 3∞ wedged windows to avoid etalon effects.

The time resolved TDL absorption measurements show the evolution of water vapor mole fraction with time during the 96" tunnel test (Figure 15). The test gas was hydrocarbon-free air, and the driver gas was hydrogen. The error

157

bars on each point reflect uncertainties in the freestream pressure, temperature, and line strength, as well as random uncertainty in the measurement and inaccuracies in baseline subtraction. In these first experiments no spectral filtering of the background tunnel emission was in place, causing uncertainty in baseline determination to be a significant contribution to error. In one check on the validity of the measurement, nitrogen was used as the test gas in a shock tunnel run, and, as expected, no water vapor was observed. The results in Figure 15 for the air test gas indicate the presence of water vapor earlier than expected in the shock tunnel test time.
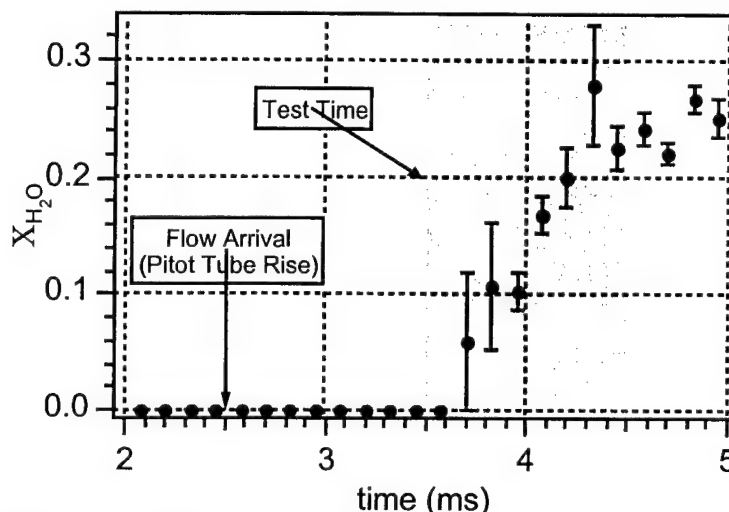
Figure 15. A time history of the estimated water vapor mole fraction for a 10.0 MJ/kg test point in the Calspan 96" Shock Tunnel.

TDL Absorption Measurements of Concentration, Temperature, and Velocity (LENS Facility)

Following the initial success of TDL absorption measurements in the Calspan facility, a concerted effort was mounted to measure time-resolved concentration, temperature, and velocity in the LENS facility. During the year following initial TDL application, refinements were made in laser line selection, detector frequency response, and optical configuration. In addition, the probe hardware was upgraded to include a second laser channel and a multi-pass beam. With the addition of the second, angled laser, the second-generation probe was capable of simultaneously measuring multiple freestream properties, including water vapor concentration, rotational and vibrational temperature, and velocity, all as functions of time (8 kHz repetition rate).[11]

H_2O transitions were selected to yield the optimum temperature sensitivity and absorption detectability for the probed flowfields using available semiconductor diode lasers. The spectroscopic parameters of the transitions probed are listed in Table 1.

| Line | λ_0 | ν_0 | S_0 | $E"$ |
	nm	cm^{-1}	cm^{-1}/atm	cm^{-1}
1	1400.74	7139.10	0.232	325.35
2	1395.69	7164.90	0.00330	1394.81

Table 1. Parameters (T = 296 K) for the H_2O lines probed in the present work.[12]

158
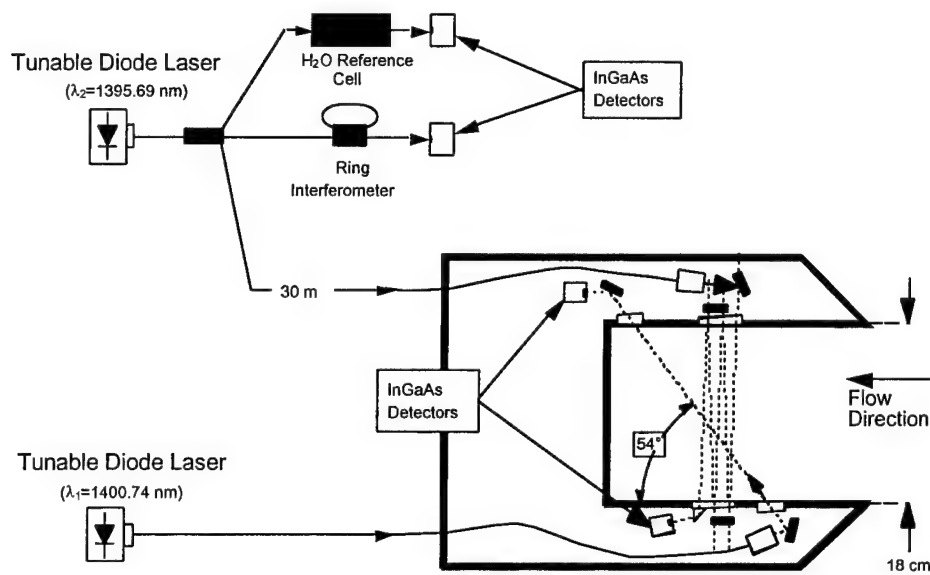
Figure 16. A schematic diagram of the set up used to record diode-laser absorption measurements in the LENS high-enthalpy pulsed facility.

Figure 16 illustrates schematically the layout of the electronics and optical components within the probe and the remote laser control systems. The distance between the two arms of the probe is 18 cm and the overall length is 40 cm. For comparison, the nozzle exit diameter is 121 cm. The probe casing is fabricated from 0.32-cm thick, 6.3-cm wide structural-steel square tubing with ports available for internal adjustment of the optics.
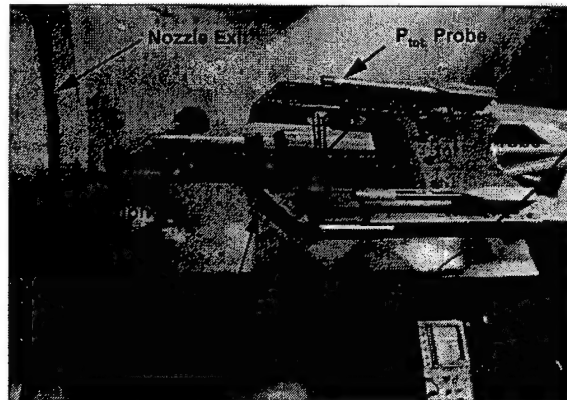
Figure 17. A Photo of the water vapor probe installed in the LENS facility.

The beam was directed from one arm of the probe to the other through (3°) wedged windows to effectively avoid etalon (interference) effects. The 1400-nm beam (λ_1) was directed at a 54° angle with respect to the bulk gas velocity. The 1396-nm beam (λ_2) was directed through the test gas 5 times in a multi-pass arrangement using a pair of high-reflectivity gold-coated mirrors to increase the path length, and thus the signal-to-noise ratio. The laser transmission intensities were monitored with InGaAs photodetectors (2.6-MHz bandwidth) mounted inside the probe. In addition, an iris was affixed in front of each detector to minimize the collection of shock-induced emission. Ports on the top of the probe provided access to the mirror and detector mounts for optical alignment.

The fiber-coupled beams were divided into three legs (10:10:80 split) using a 1×3 splitter. For each laser, one 10% leg was passed through a ring interferometer (0.835-GHz free spectral range). The transmission signal through the interferometer was recorded with a 10-MHz detector and used to convert the transmission trace from the time domain to the laser-frequency domain. The other 10% leg was directed through a low-pressure cell filled with water vapor to yield a reference (unshifted) absorption trace. All of the data signals where acquired at a 5-MHz sampling rate with 12-bit resolution to yield 625 points per scan.

159
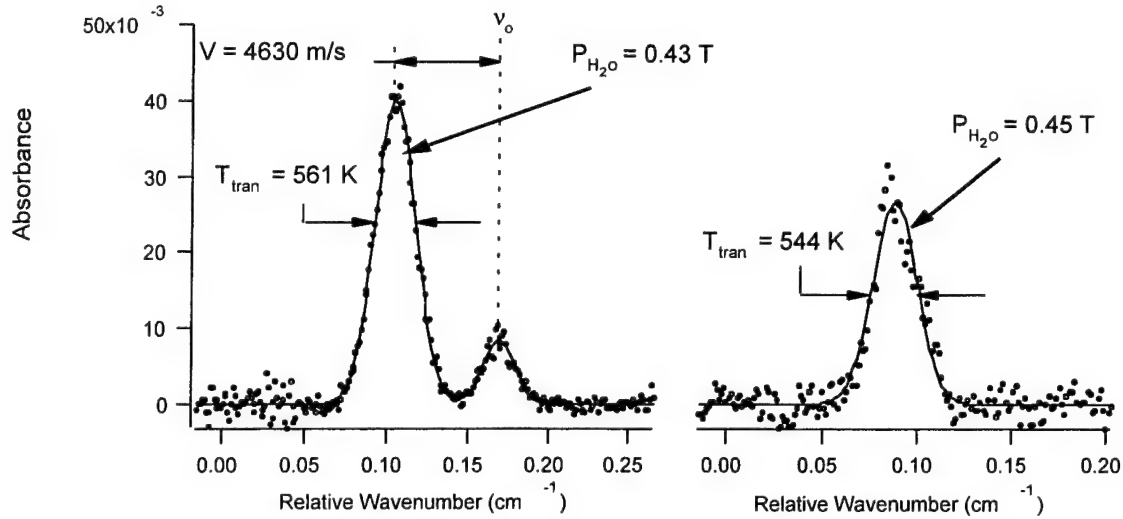
Figure 18. Reduced absorption profiles obtained from a single laser scan near 1400 nm and 1396 nm in a test with air seeded with 6% water vapor. The rotational temperature, obtained from the absorbance ratios of λ_1 and λ_2, is 560 ± 13 K.

Rapid scans of the absorption lineshapes of the two transitions can be analyzed to yield the desired fluid quantities. Figure 18 presents measured Doppler-shifted (left λ_1) and unshifted (right λ_2) absorption lineshapes recorded from a single scan at t=3.6 ms in a 10-MJ/kg-enthalpy hypersonic air flowfield seeded with 6% water vapor. Seeding the test gas with water at the room-temperature saturation pressure prior to firing the tunnel increased the SNR of the absorption signal. Since the freestream pressure during the test was less than 8 Torr, collisional broadening was negligible and the measured absorption lineshapes were essentially Gaussian. In the left hand side of Figure 18, the smaller amplitude (unshifted λ_1) absorption is due to absorption by static gas contained within the probe. The larger amplitude (Doppler-shifted λ_1) absorption is by the test gas, which has a velocity component in the direction of beam propagation.

The observed Doppler shift corresponds to a freestream velocity of 4630 m/s, which is reasonably close to the value of 4500 m/s predicted by CFD modeling of the facility nozzle. (Note that this modeling did not include the effect of water seeded into the test gas.) Translational temperatures determined from the width of each Doppler-broadened lineshape [T_{trans} = 561 K (λ_1), 544 K (λ_2)] are in excellent agreement with the rotational temperatures determined from the two-line ratio of absorbances (T_{rot} = 560 K). The temperature predicted by CFD is 650 K. Finally, the integrated areas of the absorptions can be reduced to yield partial pressure of H_2O: 0.43 Torr according to λ_1 and 0.45 Torr according to λ_2.

The estimated total measurement uncertainties ($\Delta v = \pm 50$ m/s; $\Delta P_{H_2O} = \pm 0.03$ Torr (λ_1), ± 0.06 Torr (λ_2); $\Delta T_{trans} = \pm 15K$ (λ_1), $\pm 35K$ (λ_2); $\Delta T_{rot} = \pm 13K$) are due to the uncertainties in the spectroscopic parameters (line strengths), probed path lengths, and measured beam propagation angles, as well as in the determination of the absorption baseline. A statistical approach was used to determine the contribution of the baseline calculation to the experimental error.

The ability to record time histories of the above parameters is a significant advantage of the TDL absorption sensor. Figures 19 and 20 present time histories of water vapor partial pressure, temperature, and velocity acquired at an 8 kHz rate with the new sensor system. The signal from a pitot probe, indicating total pressure, shows the facility timing and is traditionally used to determine the steady total pressure test time interval, which runs from 3 to 9 ms in this case. The three ordinate axes indicating H_2O partial pressure, gas temperature, and gas velocity share the same time axis (abscissa). The first data points plotted correspond to the first laser transmission traces that could be reliably interpreted after the intense flash of broadband emission following facility start-up.

160
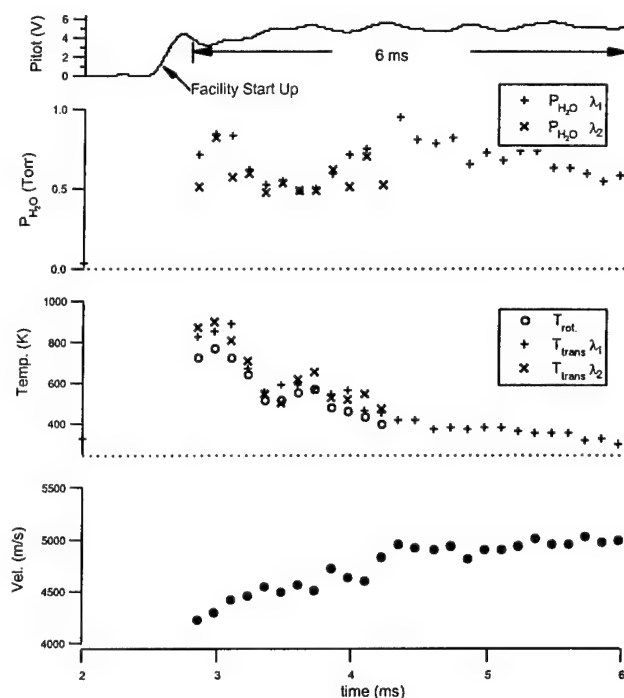
Figure 19. presents measured time histories of the total pressure (measured with a Pitot probe), H_2O partial pressure, gas temperature, and gas velocity in the LENS tunnel with air seeded with 6% water vapor as the test gas at a test condition of 10 MJ/kg.
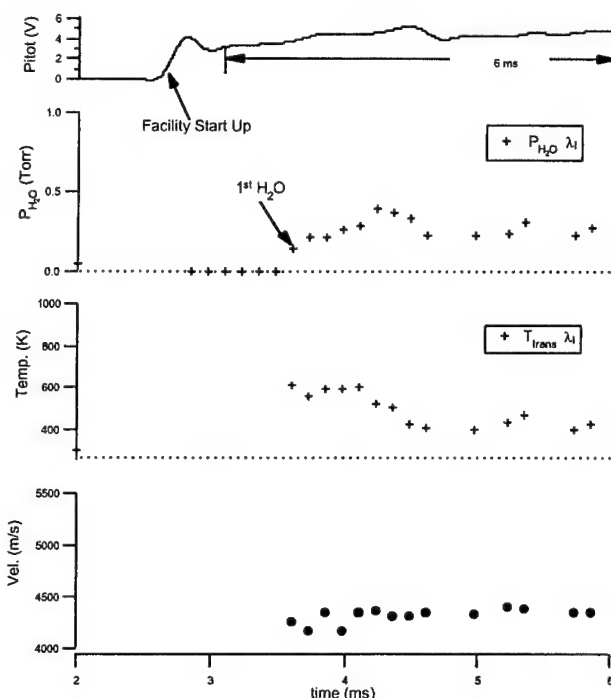
Figure 20. presents measured time histories of the total pressure (measured with a Pitot probe), H_2O partial pressure, gas temperature, and gas velocity in the LENS tunnel with a pure hydrocarbon free air test gas at a test condition of 10 MJ/kg.

Data from Figure 19 reveal the starting process of the nozzle. Initial measured temperatures ($t < 3$ ms) indicate the presence of hot H_2O (near 900 K) vapor behind the initial shock wave. The fluctuations in the temperature and pressure measurements prior to the test time indicate rapid temporal changes in the flowfield during the tunnel start up. The measured velocities exhibit a relatively gradual increase to the calculated steady-state value of 4500 m/s.

The measurements reach relatively constant values between $t = 3.2$ ms and $t = 4.2$ ms and are consistent with free-stream conditions ($T_\infty = 650$ K, $V_\infty = 4500$ m/s) estimated by CFD calculations. During the initial start-up and test-time interval the rotational and translational temperatures are in excellent agreement. As the temperature decreases below 420 K, the SNR of the absorption measurement near 1396 nm decreases substantially, and the accuracy of rotational temperature measurements decreases significantly. The measurement strategy may be easily modified enable accurate rotational temperature measurements at temperatures below 420 K by probing appropriate H_2O transitions with lower lower-state energy levels. Interestingly, the measured velocity continues to increase and eventually exceeds (by about 500 m/s) the calculated steady state value of 4500 m/s even as the temperature decreases. The increase in the measured gas velocity as the temperature decreases may be due to an increase in the atomic hydrogen concentration, which thus decreases the average molecular weight and increases the ratio of specific heats.

Figure 20 presents measurements from a 10-MJ/kg enthalpy run with a hydrogen driver and air test gas. Due to the relatively low H_2O concentrations present, only the results from the stronger (i.e., 1400-nm) H_2O absorption line are meaningful. Measurable values of H_2O partial pressures were detected as early as $t = 3.6$ ms, about 500 µs after the steady interval (i.e., test time) begins. These results are consistent with measurements recorded using the first-generation probe, which detected H_2O in the Calspan 96-inch Hypersonic Shock Tunnel. In similar enthalpy runs using nitrogen as the test gas, no H_2O was detected in the flow field for either facility.

In summary, gas temperature, velocity, and H_2O partial pressure have been measured with good accuracy and temporal resolution from Doppler-broadened H_2O absorption lineshapes near 1400 nm and 1396 nm. Measured translational temperatures were in excellent agreement with rotational temperatures for the entire temperature range

161

of 400-900 K. The measured values of temperature and velocity were consistent with calculated steady-state values (650 K and 4500 m/s, respectively) based on CFD models. The results obtained demonstrate the applicability of diode-laser absorption diagnostics for; direct multi-parameter gas measurements in hypervelocity flowfields, improved characterization of high-enthalpy facilities, and for experimental validation of CFD models.

The successful implementation of the TDL absorption measurements has stimulated interest in extending the diagnostic technique to other naturally-occurring or seeded species in the flowfield. Recent efforts have extended the diagnostic to potassium, an alkali metal which is naturally present in the flows of interest.[13] An attractive feature of potassium is that it is spectrally isolated from transitions in other species. Despite the small amounts present (on the order of 200 parts per billion were measured in the Calspan 96" shock tunnel), potassium's large line strength allows for a small physical probe size (5 cm by 1.25 cm in cross section). This reduced size, approximately 1/3 that of the second-generation probe described above, enables measurements in smaller-scale facilities or measurements close to test models. In addition, the smaller scale provides better spatial resolution in the measurement.

Conclusion

In pursuit the objectives of the URI initiative, Stanford University made contributions to the state of the art in laser-based diagnostics for hypersonic flows. Initial focus was on imaging diagnostics. Planar laser-induced fluorescence (PLIF) proved quite successful in university hypersonic facilities for quantitatively imaging species concentration and temperature, as well as for investigating combustion using OH as a combustion marker. Some practical difficulties in the application of a PLIF system in a large-scale industrial testbed were resolved, and a system was put in place on the Calspan 48" shock tunnel. While complications involving test schedules limited the PLIF results that could be obtained on Calspan and CUBRC facilities, many of the technical obstacles to such application appear to have been overcome.

A very successful outgrowth of the program has been the development of a TDL absorption sensor that is well-suited to the extreme environment of test facilities like the LENS tunnel. Rugged and reliable, the TDL probe was shown to yield accurate, time-resolved measurements of concentration, temperature, and velocity in the LENS facility and the Calspan 96" shock tunnel. This technique has the potential to become an important tool in the characterization of large, ground-based hypersonic test facilities, as well as in the collection of experimental test data.

References

1   Kamel, M.R., et al., "New Expansion Tube Facility for the Investigation of Hypersonic Reactive Flow", *33rd Aerospace Sciences Meeting*, Reno NV, AIAA-95-0233

2   Houwing, A.F.P., et al., "PLIF Imaging and Thermometry of NO/N2 Shock Layer Flows in an Expansion Tube", *34th Aerospace Sciences Meeting*, Reno NV, AIAA-96-0537.

3   Di Rosa, M.D., Klavauhn, K.G., and Hanson, R.K., "PLIF Imaging of NO and O2 in High-Pressure Flames", *Proceedings of SPIE - The International Society for Optical Engineering*, Vol. 2546, pp 509-518, 1995.

4   Arroyo, M.P. and Hanson, R.K., "Absorption measurements of water-vapor concentration, temperature, and line-shape parameters using a tunable InGaAsP diode laser", *Applied Optics*, Vol. 32, No. 30, 1993

5   Arroyo, M.P., Langlois, S., and Hanson, R.K., "Diode-Laser Absorption Technique for Simultaneous Measurements of Multiple Gasdynamic Parameters in High-Speed Flows Containing Water Vapor", *Applied Optics*, Vol.33, No. 15, 1994

6.   Baer, D.S. et al., "Scanned- and Fixed-Wavelength Absorption Diagnostics for Combustion Measurements Using Multiplexed Diode Lasers", *AIAA Journal*, Vol. 34, No. 3, March 1996.

10. Albrechcinski, T.A., et al., "Calspan's Upgraded 96 inch Hypersonic Shock tunnel: Its Development and Application in the Performance of Research & Testing at Higher Enthalpies", *33rd Aerospace Sciences Meeting*, Reno NV, AIAA-95-0236

11   Wehe, S.D., Baer, D.S., and Hanson, R.K., "Tunable Diode-Laser Absorption Measurements of Temperature, Velocity, and H_2O in Hypersonic Flows.", *35th AIAA Joint Propulsion Conference*, Seattle WA, AIAA-97-3267.

12. Toth, R.A., "Extensive Measurements of $H_2^{16}O$ Line Frequencies and Strengths: 5750 to 7965 cm^{-1}", *Applied Optics*, Vol. 33, No. 21, July 1994

13. Wehe, S.D., Baer, D.S., and Hanson, R.K., "Measurements of Bas Temperature and Velocity in Hypervelocity Flows Using a Diode-Laser Absorption Sensor.", *20th AIAA Advanced Measurement and Ground Testing Technology Conference*, Albuquerque NM, AIAA 98-2699.

163

II. II. Electron-Beam Diagnostics

This report outlines the results of the University Research Initiative effort at USC, which consisted of developing the pulsed-electron-beam fluorescence (PEBF) technique for nonequilibrium, chemically reacting hypersonic flows.

The electron-beam fluorescence (EBF) diagnostic effort at USC proceeded on two fronts. First, the development of the PEBF technique continued. Second, it was necessary to characterize the freestream conditions in the LENS facility using a continuous-wave (CW) electron-gun. The effectiveness of CW EBF in enthalpy regimes of 5 and 10MJ/kg was investigated, and a diagnosis of freestream conditions was performed. The parameters targeted were nitrogen number density, rotational and vibrational population distributions, flow contaminants, and test time. Using the data obtained in the LENS tests, it is now possible to better understand some of the limitations of CW EBF compared to PEBF and the need for an operational pulsed electron gun (PEG). The following is a discussion of the development milestones of the PEG and diagnostic limitations of CW EBF as compared to PEBF based on the results obtained in the summer/fall of 1996 during the LENS tests.

Nomenclature

$A_{B \to X}$	spontaneous transition probability
$A_{k,l}$	total spontaneous transition probability to lower state l
$B_{v_1''=0}$	rotational constant of zeroth vibrational level of the N_2 $X^1 \Sigma_g^+$ state
c	speed of light
C	mean molecular speed
e	electric charge
h	Planck's constant
I_P	P branch intensity
I_R	R branch intensity
k	Boltzmann's constant
K	rotational quantum number without electron spin
m_e	electron mass
n_e	number density of electrons
n_g	test gas number density
$n_k(t_b)$	excited state population
$n_{rate,0,k}$	excitation rate per unit volume to the excited state k from initial state 0
$N_{rate}(v',t')$	number of excitations to v' per unit time
$n(v',k',t')$	excited state population for times after the current pulse
$N(v',K')_0$	initial number of molecules in the excited state
$(n_{K'-1}'')_{v_1''=0}$	number density in the (K' - 1) rotational level
$(n_{K'+1}'')_{v_1''=0}$	number density in the (K' + 1) rotational level
P_{k,t_b}	emitted power observed at time t_b
$P(K',K_2'')$	rotational transition probability for a given K'
P_P	P branch rotational transition probability
P_R	R branch rotational transition probability
$Q_r(T_r)_{v_1''=0}$	rotational state sum
$q(v',v_2'')$	Franck-Condon factor for transition between v' and v_2''
R	radius of electron beam propagation chamber
r_b	electron beam radius
t	time after attainment of $N(v',K')_0$
t_b	time of an assumed uniform beam pulse

T_r	rotational temperature
$V_e(t')$	speed of electrons for during time t'
v_b	speed of beam electrons
v'	vibrational quantum number of $N_2^+ \, B^2 \, \Sigma_u^-$ state
v_1''	vibrational quantum number of $N_2 \, X^1 \, \Sigma_g^+$ state
v_2''	vibrational quantum number of $N_2^+ \, X^2 \, \Sigma_g^+$ state
χ_4	constant
β	v_b/c
μ_0	permeability of free space
σ	plasma conductivity
$v_{k,l}$	wavenumber of the transition
μ_0	permeability constant
γ	$(1-\beta^2)^{-0.5}$
τ	inverse of the spontaneous transition probability for the v' state
τ_{QC}	characteristic quenching time
$\Omega_e(v')$	excitation cross section for a vibrational level in the v' state
$\Omega_{Q,k}$	quenching cross section of the state k
$2\tau b$	full width at half maximum of current pulse

CW EBF Background

CW Electron-beam fluorescence is a well established and mature diagnostic technique for obtaining density, temperature, internal state population distributions and velocity measurements at points in low enthalpy gas flows [Muntz, 1968 and Gochberg, 1994]. The fluorescent intensity observed from a volume of gas excited by an electron beam can have a linear relationship (depending on gas composition and temperature) up to gas density below approximately 10^{17} cm^{-3} (~3 Torr at 300K)[Gadamer & Schumaker, 1958 and Gadamer, 1962]. At greater densities, collisional quenching causes a worsening nonlinearity between intensity and density, with measurement accuracies becoming increasingly uncertain as the density rises [Muntz, 1968]. Since nonequilibrium reacting flow studies must be conducted to quite high densities ($\approx 3 \times 10^{18}$ cm^{-3} for an equivalent altitude of 20 km)[Muntz et al, 1987] in the presence of uncertain quantities of quenching species, an alternative to CW EBF has been proposed, pulsed electron beam fluorescence (PEBF)[Muntz et al, 1987, Schilling et al, 1993 and Muntz & Erwin, 1993].

PEBF retains the advantage of CW EBF, which is the simultaneous broad band excitation sampling of vibrational and rotational internal energy states of most molecular test species, while making it possible to ameliorate quenching up to number densies of about 10^{18} cm^{-3} [Muntz & Erwin, 1993]. In addition, background light levels that are the bane of high enthalpy diagnostics are not as problematic, since the signal integration time is small.

PEG THEORY
Pulsed Electron Beam Generation

A new research field was established when the pseudospark was introduced to the world in 1979 by Christiansen and Schultheiss. It has attracted much attention from scientists interested in high-power switching applications [Frank & Christiansen, 1989; Lin & Chow, 1995]. The development of pseudospark discharge switches has also provided a simple and compact means of generating electron beams with desirable rise times and beam currents at high electron energies (Fig. 1).

PEGs are able to generate high-current transient electron-beams by utilizing the physics associated with the Paschen curve. The gas breakdown processes of PEGs stems from an avalanche initiated by the ionization of atoms and molecules after undergoing inelastic collisions with electrons moving in an intense electric field. The number of collisions an electron undergoes over a path length d is a function of the gas density present. Since the density is proportional to the gas pressure p, the number of collisions is considered to be a function of the product pd. It is now understood to be an experimental fact, known as *Paschen's law*, that the breakdown voltage between two parallel plates is a function of the aforementioned product pd.

165

Departures from Paschen's law have been reported [Liu & Rhee, 1995; Guseva, 1964] and are attributable to nonuniform field distributions.

The PEG operates on the left side of the Paschen curve, which plots breakdown potential versus the product of gas pressure and discharge path length. During commutation, which is initiated by a surface discharge trigger electrode, electrons are forced to follow field lines that take the longer path between electrodes. By placing small orifices (5mm diameter) at the centers of the PEG's electrodes, an axial discharge generating energetic electrons is produced. As the electrons are accelerated along the field lines, they acquire enough ballistic energy to detach from the field at the exit plane of the gun (Fig. 1). Factors such as distance between electrodes, triggering system, materials, gun chamber gas and operating potential all impact the specific operating conditions of pulsed electron guns [Benker & Christiansen et al, 1989, Frank & Christiansen, 1989].

An important issue associated with the operation of the PEG is electromagnetic interference (EM). Instantaneous beam power levels exceeding 10^9 W are commonly realized. The high beam power and short times imply large variations in dI/dt, which can induce currents in a variety of supporting equipment. Even the commonly reliable RG-58 BNC cable has showed weaknesses when used in proximity of the PEG. Consequently, the implementation of semi-rigid SMA cables and proper grounding techniques was necessary and has solved most EM noise issues.

Propagation of High-Current Beams Through a Neutral Gas
Assuming for the moment that no beam instabilities appear, a pulsed-electron beam will attenuate due to collisional scattering (typical in higher gas densities) and space-charge repulsion of beam electrons (significant for high-current densities and lower electron energies). However, the beam causes ionization of the background gas, which creates a potential well which helps to minimize beam divergence. Unfortunately, the propagation of intense electron beams involve many issues which do not lend themselves to simple quantitative analysis.

When an intense electron beam is injected into a neutral gas, the beam transport can be characterized as either transport through plasma or unneutralized beam propagation. The applicable situation depends on the speed with which the electron beam can ionize the gas, thereby creating a space-charge and/or current-neutralizing background. Current neutralization can occur when a high current electron beam generates a plasma which, in turn, induces free electron currents so as to cancel or minimize the self-magnetic field of the primary beam.

Generally speaking, it is helpful to characterize the neutral gas transport in terms of the ratio of the beam current to the space charge limit; I_b/I_{sc}, and the ratio of the beam current to the Alfven limit; I_b/I_A. I_{sc} and I_A can be defined by the following equations:

$$I_A \approx \frac{4\pi mc\beta\gamma}{\mu_0 e} = 1.7x10^4 \beta\gamma$$

$$I_{sc} = 38.5x10^{-6} V^{3/2}\left(\frac{D}{L}\right)^2 \qquad \text{(Amps)} \qquad (1)$$

For a 40keV electron beam, the corresponding I_A is equal to 7.3kA and I_{sc} is, for expected geometries, roughly 80A. Since typical primary beam current values range between 500-1400A, the condition $I_b < I_{sc} < I_A$ exists. Generally speaking, if the beam current I_b exceeds I_A, propagation is only possible when there are both charge and magnetic neutralization; if $I_b < I_{sc}$ propagation is always possible; and finally if $I_{sc} < I_b < I_A$ current neutralization is not necessary for propagation.

The effects of background gas pressure can be organized in three general ranges; (1) the low-pressure regime for which the charge neutralization time is of the order of, or greater than, the beam pulse duration ($\sim < 0.05$ Torr); (2) an intermediate-pressure which allows rapid electron avalanching and plasma conductivity (i.e. the charge neutralization time is of the order of the beam rise time or less)(~ 0.05-10

Torr); (3) a high-pressure regime where the neutral-gas-molecule-plasma-electron collision frequency substantially decreases the plasma conductivity ($\sim > 10$Torr). Since the densities of interest for high-enthalpy hypersonic flows lie between 10^{16} - 10^{18} cm^{-3} and the beam penetration depths required for successful diagnostics are on the order of a few centimeters, the potential applicability of PEBF becomes evident.

Space-Charge Neutralization

It is interesting to obtain a first-order approximation of the degree of space-charge neutralization within the electron beam. A positive ion density within the beam path which is comparable to the electron density will assist in counteracting the effects of electrostatic repulsion of beam electrons. From laboratory experiments, the beam diameter is typically 1mm with energy of 40keV and an average current of 1000A. The beam rise time is typically 10nsec, and these values correspond to a number of primary beam electrons totaling 6.24×10^{13}. Electrons with an energy of 40keV travel at 1.18×10^8 m/sec and will borough through a cylinder of volume $0.93cm^3$. The average electron density generated by the multi-electrode PEG at USC is 6.71×10^{13} cm^{-3}. The excitation rate due to primary beam electrons is given by the following [Muntz, 1968]:

$$\varphi = n_e \, v_e \, Q_{ij} \, (v_e) \, n_g \tag{2}$$

The value of the excitation cross section Q_{ij} (v_e) for the First Negative System (0,0) band of Nitrogen $(N_2^+[B^2\Sigma_u^+ \rightarrow X^2\Sigma_g^+]$ is roughly 0.5×10^{-18} cm^2. Therefore, assuming a 10nsec pulse, the expected nitrogen molecular ion density for neutral gas densities of 10^{16} and 10^{18} cm^{-3} is 4×10^{13} and 4×10^{15} cm^{-3} respectively. Based on this calculation, it is expected that the electron beam will be characterized as being close to space-charge neutralized at the lower densities and exhibit self-pinch behavior at the densities expected within the stagnation region of a flowfield. The self-pinching may not be critical for the stagnation region since a penetration depth of a couple of centimeters is needed to effectively probe the volume of interest.

Beam Instabilities

It is important to note that it is significantly easier to treat plasma waves when it is assumed that perfect thermodynamic equilibrium is all encompassing. Velocities could be defined as having a Maxwellian distribution; densities and magnetic fields would be totally uniform. In this kind of state of maximum entropy, there is no available energy to excite instabilities. Unfortunately, states that come about in any physical system are not in perfect thermodynamic equilibrium. The free energy that is available can cause waves to be self-excited, so that any equilibrium is tenuous. Instabilities always generate an action that decreases the free energy and brings the plasma closer to thermodynamic equilibrium. The classification of instabilities is typically ordered by the type of free energy that drives them. *Streaming instabilities* stem from either a beam of high-energy particles which travels through a plasma, or by a current which is driven through a plasma so that various species exhibit drift relative to each other. *Rayleigh-Taylor* instabilities occur when the plasma has density gradients or sharp boundaries, so that it is not uniform. In addition, an external force is applied to the plasma (typically hydrodynamic but not electromagnetic). Even in the absence of electric or gravitational fields, u*niversal instabilities* originate, since plasmas that are somehow confined are not in perfect thermodynamic equilibrium as the plasma pressure tends to cause an expansion, and this energy can result in driving an instability. *Kinetic instabilities* are caused by a deviation from the Maxwellian velocity distribution, where the instability is driven by the anisotropy of the velocity distribution. Although there is no shortage of specific instability modes that can be discussed which are catalogued within the four general types, there are a few which have been identified as common in the propagation of intense electron beams through a medium.
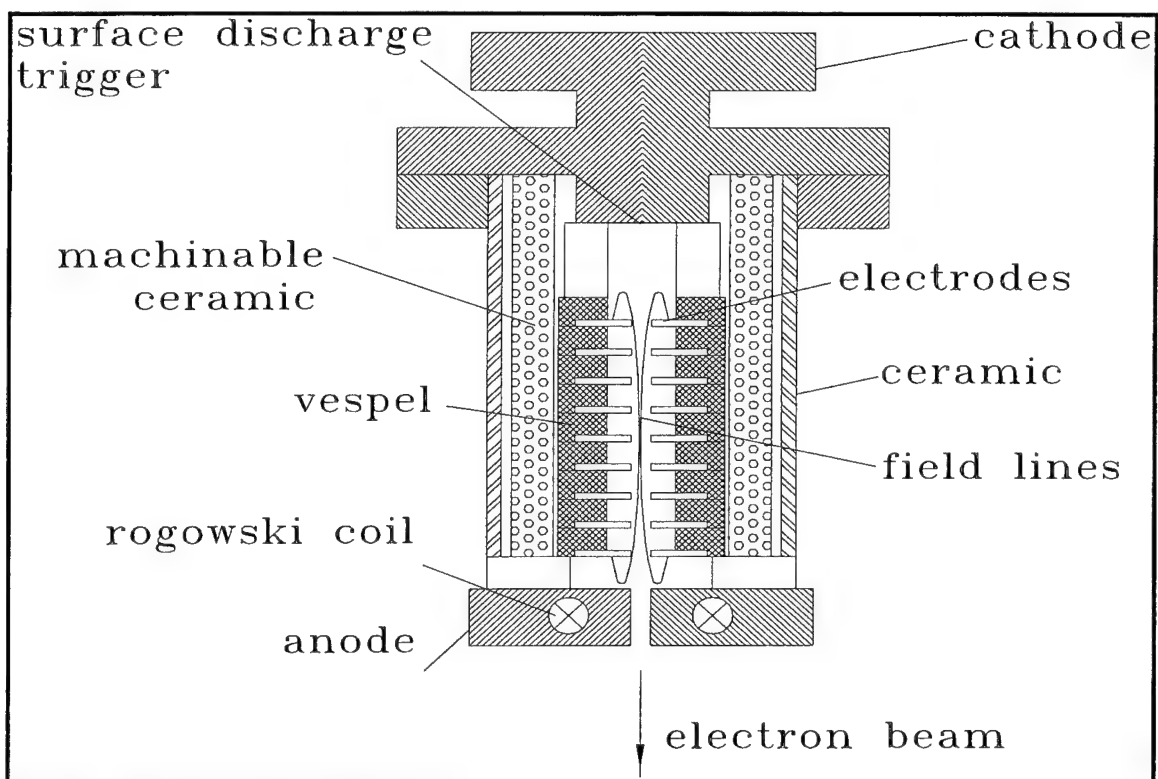
Figure 1: Second generation PEG design.

Labels in figure: surface discharge trigger, cathode, machinable ceramic, electrodes, vespel, ceramic, field lines, rogowski coil, anode, electron beam
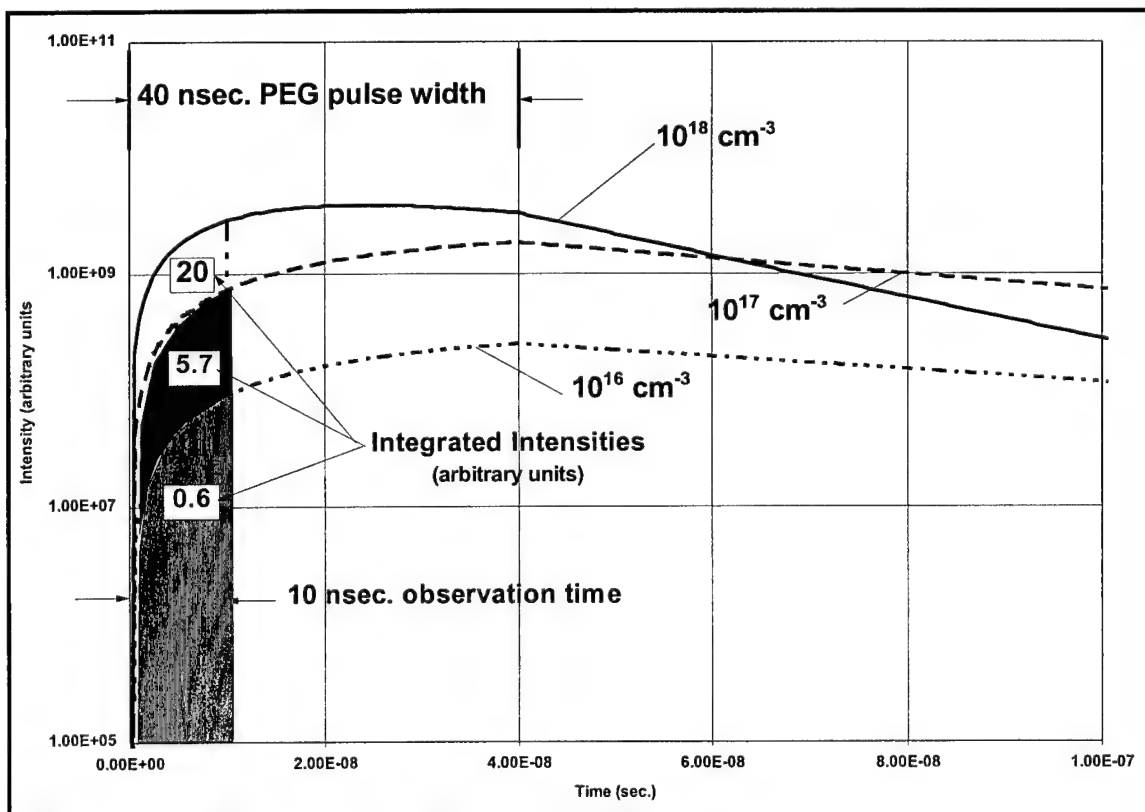
Figure 2: Quenching curves for nitrogen gas at 5000K

Labels in figure: 40 nsec. PEG pulse width, 10^{18} cm^{-3}, 10^{17} cm^{-3}, 10^{16} cm^{-3}, Integrated Intensities (arbitrary units), 10 nsec. observation time, 20, 5.7, 0.6, Intensity (arbitrary units), Time (sec.)

When an intense electron beam propagates through a plasma, it can be susceptible to transverse perturbations because of finite plasma conductivity [Miller]. The resistive hose instability is thus generated. If the beam axis undergoes a minute displacement, the magnetic field axis lags behind for timescales approaching the magnetic diffusion time, defined by the following expression:

$$\tau_b \cong 4\pi\sigma r_b^2 / c^2 \tag{3}$$

The interaction between the longitudinal beam current and the perpendicular component of the residual magnetic field will provide a restoring force, which tends to correct this situation. Under collisionless conditions the plasma can be regarded as being a perfect conductor and the beam displacement would only result in oscillations. However, if the plasma conductivity is finite, the beam displacement and the resulting restoring force are out of phase, and the instability grows.

The growth of the sausage instability is generated when radially symmetric perturbations of the beam are destabilized by the finite conductivity of the background plasma. In this instance, it is the plasma response to the beam envelope deviation from equilibrium which is of interest. As in the hose instability, the finite plasma conductivity is the root of the sausage instability, since any return current responding to the density perturbations of the beam cannot respond fast enough and lags behind on the order of τ_b . Consequently, the induced variations in the current density of the beam can become phased so as to exert forces on the beam which caus the initial disturbance to grow.

Since the ion densities within the plasma can be much greater than the beam electron density, the beam itself can represent a perturbation which can excite natural plasma oscillations. It is expected that the specifics of these oscillations will be primarily governed by the plasma parameters. The instabilities generated by this condition include the two-stream and cyclotron instabilities.

It is interesting to note that the observed beams of the PEG utilized in this research consistently propagated 7.5 - 8.0 cm downstream of the exit plane of the PEG. When this distance is exceeded, the positional variations of the beam ranged from slight to extreme, and little consistency was observed. The resulting departures can be attributed to some of the aforementioned instabilities. However, it is important to note that an effective penetration distance of only 5 cm would be considered adequate for any flowfield or freestream surveys and would allow effective calibrations to be performed.

PEBF THEORY
Quenching Analysis
An abbreviated quenching analysis is in order. Assume the pulsed electron beam current is I_B, n_g is the test gas number density under observation, $\Omega_{0,k}$ is the cross section for excitation. Assuming a beam cross section of A_B, the excitation rate per unit volume is

$$n_{rate,0,k} = 6.25 \times 10^{18}(I_B \, \Omega_{0,k} \, n_g \, /A_B) \tag{4}$$

Considering spontaneous emissions and quenching collisions, the time history of the excited state number density becomes

$$n_k(t) = \frac{n_{rate,0,k}}{A_{k,l}+C\Omega_{q,k}n_q}\left[1-\exp\left(-\left(A_{k,l}+C\Omega_{q,k}n_q\right)t_b\right)\right] \tag{5}$$

where $A_{k,l}$ is the transition probability, C is the mean molecular speed, $\Omega_{q,k}$ is the quenching cross section of the state k (1.5×10^{-16} cm^{-2} for N_2 C$^3\Pi$,$v'=0$), and t_b is the beam pulse width. Figure 2 highlights the emission intensities for densities of interest. The curves reflect the conditions of nitrogen gas at 5000K. For a given integrated beam current, intensity scales linearly with number density [Muntz et al, 1987, Schilling et al, 1993, Muntz 1993] (Fig. 2). For number densities around 10^{18} cm^{-3} and above, collisional quenching becomes progressively more dominant. The intensity curves in Fig. 2 were generated by introducing a simulated beam, whose FWHM of 40nsec was assumed to be a step function, into 3 different number densities. The calculations take into account excitation, spontaneous emission and collisional

quenching. The integrated intensity values are shown for an observation gate time of 10nsec. Taking full advantage of the quick rise times associated with PEG beams, the careful gating of optical diagnostics equipment within a narrow time frame (i.e. 10 nsec) allows quenching difficulties to be effectively delayed to higher densities ($\sim 10^{18}$ cm^{-3}). Using the PEG would effectively allow the direct measurement of number densities of various species in the stagnation region of flowfields within a single test run.

Rotational Temperature Determination

The rotational temperature is an important parameter to be measured. The bulk of the research done with CW EBF targeted nitrogen for two main reasons. First, nitrogen is the major constituent gas in the flows of interest. Second, nitrogen's First Negative ($N_2^+[B^2\Sigma_u^+ \rightarrow X^2\Sigma_g^+]$) and Second Positive Systems ($N_2[C^3\Pi_u \rightarrow B^3\Pi_g]$) are readily excited by primary and secondary beam electrons, respectively, and generate intense fluorescent signals. The First Negative System (0,0) band has traditionally been used for the determination of rotational temperature, since the structure is easily interpreted and the signal strength is high. The methodology used for CW EBF is applicable to PEBF studies [Lutfy & Muntz, 1995].

The rotational fine structure of the (0,0) band of nitrogen's First Negative System is characterized by a $\Sigma \rightarrow \Sigma$ transition. Consequently, only P and R branches are considered, which ameliorates interpretation difficulties. The following relations are taken from Muntz & Abel, [1964]. The intensity of specific rotational lines for the R-branch can be determined by using the following:

$$\left(I_{K_1' K_2''}\right)_{V_1' V_2''} = 2K'\chi_4[G]\exp\left(\frac{-B_{V''}K'(K'+1)hc}{kT_r}\right) \tag{6}$$

where [G] is defined by;

$$[G] = \frac{(K'+1)\exp\left(\dfrac{-2B_{V_1'}(K'+1)hc}{kT_r}\right) + K'\exp\left(\dfrac{2B_{V_1'}K'hc}{kT_r}\right)}{(2K'+1)} \tag{7}$$

Similarly the P-branch line intensities can be derived by applying the following:

$$\left(I_{K_1' K_2''}\right)_{V_1' V_2''} = 2\chi_4[G]\exp\left(\frac{-B_{V''}K'(K'+1)hc}{kT_r}\right) \tag{8}$$

where [G] is now defined by;

$$[G] = \frac{(K'+1)\exp\left(\dfrac{-2B_{V_1'}(K'+1)hc}{kT_r}\right) + K'\exp\left(\dfrac{2B_{V_1'}K'hc}{kT_r}\right)}{\left(\dfrac{2K'+1}{K'+1}\right)} \tag{9}$$

In addition, a correction is needed since in the $N_2X^1\Sigma$ state, the nuclear spin of the molecule causes the odd numbered rotational levels to have exactly half the population levels of the even numbered ones [Herzberg, 1950].

The experimental approach used in determining rotational temperature involves obtaining the ratio of the integration of the tail of the R-branch signal to that of the entire P-branch side. The targeting of the tail of the R-branch distribution allows greater temperature sensitivity. However, during actual test tunnel runs, the temperature is expected to exceed 5000K. Therefore, many rotational levels will be populated, which will extend the fine structure over a 300-400Å range. The extended fine structure will cause complications

due to overlap with other species and systems; for rotational temperature measurements a slope matching approach was used.

The relations 6 - 9 are only applicable to the First Negative System of nitrogen. The rotational structures of various species can be more involved; such as the introduction of a Q branch. Each system must be individually evaluated for such measurements.

Vibrational Population Distribution
By definition, it is expected that the vibrational and rotational temperatures will be decoupled in nonequilibrium flows. Consequently, there is also a need to assess the vibrational excitation levels in a non-intrusive manner. Again, the techniques used for CW EBF are applicable to PEBF work [Lutfy & Muntz, 1996]. The following relation can be used to determine the intensity of a particular vibrational transition [Muntz, 1968];

$$I_{V'V_2''} = \frac{\chi v_{V'V_2''}^4 \; q(V',V_2'') \sum\limits_{V_1''} \left[n_{V_1'} q(V',V_1'') \right]}{\sum\limits_{V_2''} \left[\left[v_{V'V_2'}^3 q(V',V_2'') \right] \right]} \tag{10}$$

It is interesting to note that equation 10 can be used for any diatomic molecule, as long as the relevant spectroscopic values (i.e. energy of level, term values for anharmonic oscillators, etc.) can be found and applied so as to determine the state sum. There is a substantial listing in Herzberg [1950]. It is anticipated that some inconsistencies will arise during actual test runs, since the spectroscopic values were largely determined at temperatures far less than those which will be encountered at hypervelocity flow facilities.

PEG Development
Overview
There has been an evolution in PEG design since PEBF research was initiated at USC. The first generation PEG incorporated a single electrode pair. The initial design proved that PEBF was feasible, but the beam produced by this device was inconsistent and was not suitable for diagnostics in shock tunnel facilities [Lutfy & Muntz, 1995]. A more consistent multi-electrode PEG was designed and built. The beam produced by the second generation PEG has 5 - 20 times the current of its predecessor, with significantly improved collimation. The 30 - 40keV electrons penetrate 5 - 8cm downstream of the anode exit without a significantly altered spatial distribution (+/- 1mm) [Lutfy & Muntz, 1996]. The beam is frequently observed to have more pronounced positional variations and sometimes quite dramatic directional changes at greater penetration depths, likely due to some of the instabilities discussed previously. The last major challenge remaining before PEGs can become fully operational is the issue of beam introduction to the test volume. The PEG operates on the left side of the Paschen minimum (i.e. 7×10^{14} cm^{-3}), since the beam must propagate through number densities of 10^{16} - 10^{18} cm^{-3} during shock tunnel runs a technique must be devised to effectively isolate the PEG chamber from the test section without significant beam attenuation. The PEG produces beams that are roughly 2mm in diameter, which governs the minimum orifice size (3mm diameter) that will safely allow the beam to propagate out of the PEG and into the diagnostic test volume without intolerable losses. Finally, the PEG's electrodes require varying degrees of conditioning (10 - 100 firings) to ensure consistent beam production. Hence, some form of environmental isolation for the PEG is mandatory. Several single event and continuous strategies in the form of valves and barriers have been considered and attempted and are described in more detail in Muntz & Lutfy [1996]. Presently, a fast acting rotary valve apparatus is being implemented to address this issue.

First Generation PEG
The first generation PEG consisted of a single electrode pair that had center orifice diameters of 5mm. The electron avalanche was initiated by using a tungsten wire, which acted as a trigger electrode (Fig. 3). The calibration facility consisted of a vacuum chamber that was mated to the exit aperture of the PEG. The PEG chamber was purged with hydrogen or helium gas and evacuated through the PEG's exit aperture.

171

The pumping was performed on the vacuum chamber side of the PEG, thus the test chamber pressure was always kept lower than the critical pressure level needed to operate the PEG (Fig. 3). There was a modest amount of robustness inherent to the first generation PEG, which allowed pressures of 2 – 165mTorr to be explored in the test cell. The test gas (mainly nitrogen) was introduced directly into the test cell by using a ring jet device.

The purpose of the experiment described above was to study PEBF and to gain some understanding of operational issues associated with PEGs. A schematic of the first generation PEG experiment is shown in Fig. 4. The optics focused the electron beam fluorescence within a field of view of about 2 cm at the center of the test chamber. The light was gathered by a collimating lens, reflected from a mirror and focused at the entrance slit of a SPEX 1404 spectrometer, such that the electron beam's image was perpendicular to the entrance slit. The spectrometer had a grating blazed at 500 nm, and f 6.9 optics and was operated at an entrance slit setting of 0.4 mm (corresponding to a resolution of 0.12 nm). The exit slit was replaced by an adapter, which was fabricated to block off 1.2 nm of wavelength space but allowed 1.7nm to pass on either side of the center mask. By carefully adjusting the spectrometer's settings (i.e. centered at 390.57 nm), it was possible to pass the P branch while cutting off the aforementioned portions of the R branch. Two 45° prisms directed the P and R branch light which diverged from the double exit slit to their respective photomultiplier tubes (PMTs), which have rise times of 2.5 nsec (Fig. 4). The wavelength calibration of the initial setup was performed using a helium-neon laser and a krypton discharge tube. Since the wavelengths of interest lay between 380.9 nm and 391.4 nm, it was necessary to ascertain the linear dispersion of the spectrometer at various wavelengths. The dispersion was verified to be constant between 632.8 nm (helium-neon laser), 557.028 nm (krypton discharge tube) and a 388.865 nm (helium discharge tube). A scaling factor of 2.0 was determined to exist in the PMT signals between the R and P branch channels by viewing the 388.865 nm line of the helium discharge tube. The current measurement was made using a Rogowski coil with a rise time of 20 nsec. This coil was placed reasonably close ($\approx$2 cm) to the test chamber viewing area to provide an accurate beam current measurement for the emission volume. Nitrogen was bled through a needle valve and channeled to a ring jet to provide an even gas distribution in the test chamber. The PEG operated in a low pressure hydrogen environment; the hydrogen was introduced directly into the gun and allowed to escape through the gun orifice and into the vacuum chamber. The pressure was measured using a McLeod gauge and a thermocouple gauge, both located close to the optical port. The signals from both PMTs and the Rogowski coil were processed by a Tektronics TDS-644A digitizer. The pulse generator was a Stanford Research model DG-535. The range of potentials that produced adequate PEG operation lay between 10 - 33 keV, with typical FWHM current pulse values of 50 nsec, at hydrogen pressures of 100 mTorr. Although the repetition rate of the PEG can be as high as 1.5 Hz, it was consistently operated at 0.2 Hz to prolong the useful life of the trigger electrode. Because the system had no differential pumping ability between the test chamber and PEG, the upper density range of nitrogen that could be explored before contaminating the PEG chamber was 5.3 x 10^{15} cm^{-3}. The PEG was operated at 33 keV for the experiments described in this section. A total of 64 runs were made at pressures varying between 5 and 150 mTorr.

First Generation PEG Calibration Results and Discussion
Because the available first generation PEG model had only two electrodes and exhibited somewhat erratic triggering, its electron beam was not very consistent nor very well collimated. Specifically, the beam's apparent diameter and direction of propagation varied significantly. From shot to shot the beam certainly did not occupy a constant volume within the test chamber, but wandered within and at the edges of the field
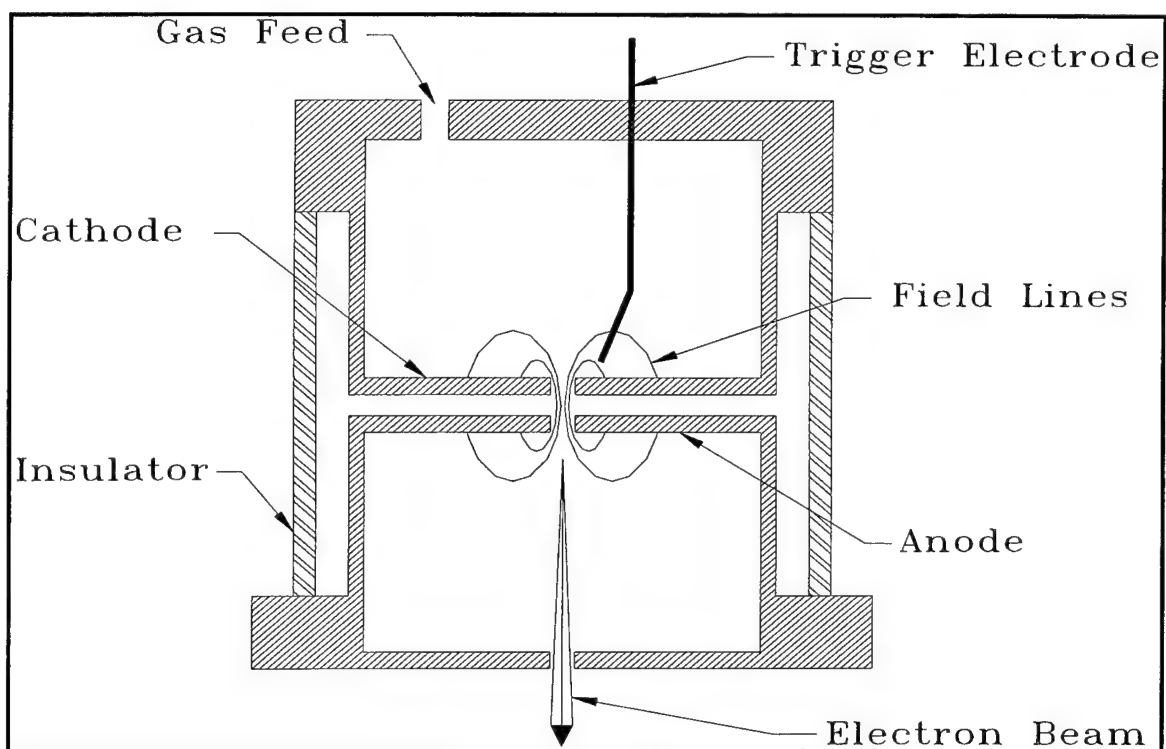
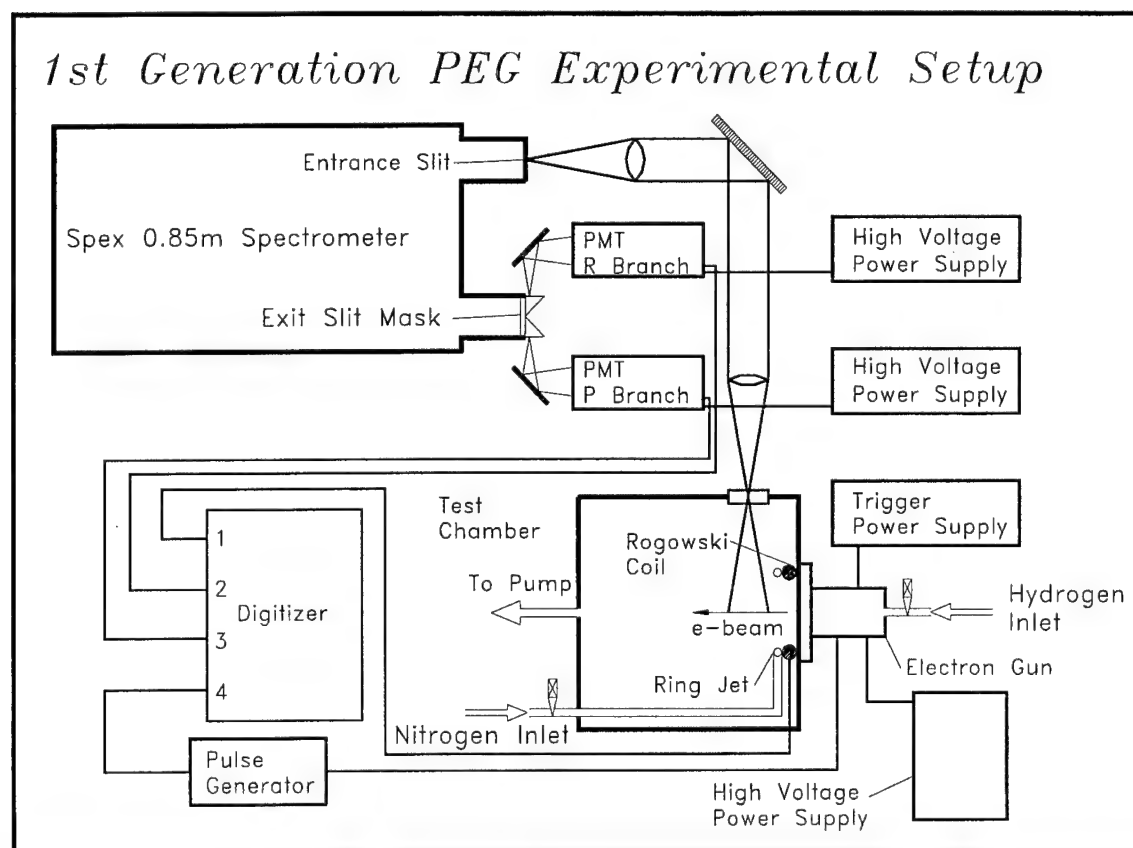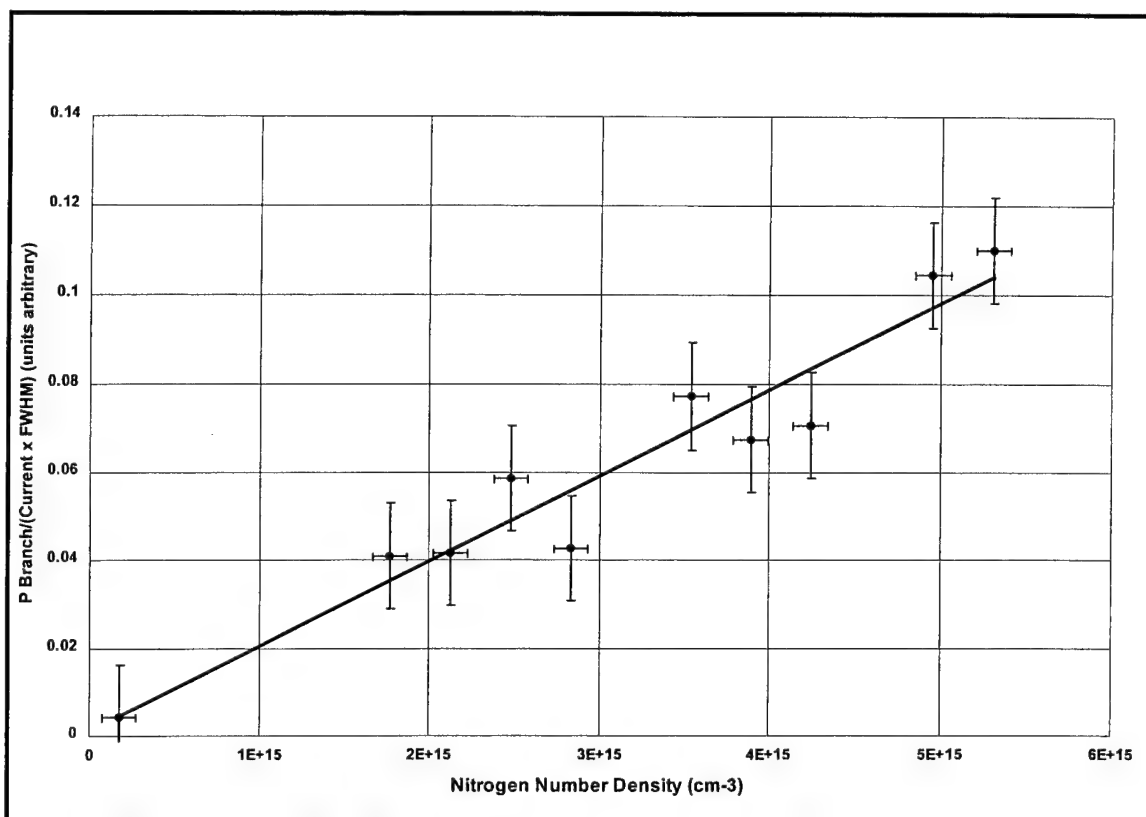**Figure 3: First generation PEG design.**

Figure 4: Initial experimental setup for PEBF studies utilizing single electrode pair PEG.

Figure 5: Linearity trend for first generation PEG generated nitrogen fluorescence.
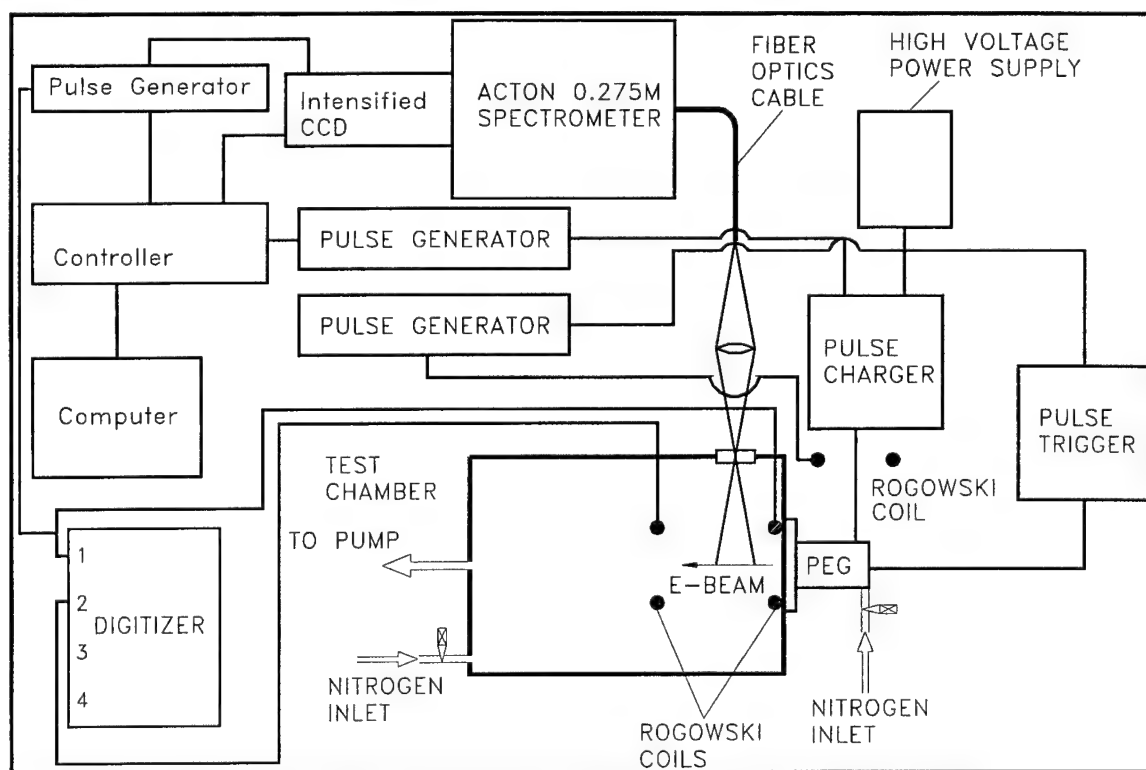

Figure 6: Experimental setup for second generation PEG apparatus mated with ICCD.

of view, occasionally exceeding it. The triggering variations caused a shot-to-shot jitter to be as high as ± 300 nsec. The PEG's instabilities were remedied by implementing a multi-electrode PEG design [Lutfy & Muntz, 1995; Benker et al, 1989; Frank & Christiansen, 1989]. The P branch signals for several test chamber densities are shown in Fig. 5 with corresponding 1 sigma error bars. Despite a significant amount of scatter due to the unpredictable firing characteristics of this first generation PEG, the linear trend is as expected for this pressure range. The rotational temperature was determined by averaging 34 firings. It is necessary to account for the N_2^+ (1,1) band centered at 388.4 nm since it is within the R branch wavelength range. After applying the PMT calibration factor of 2.0, a ratio of 0.18 ± 0.03 was found. The corresponding theoretical rotational temperature was 283 ± 30 K. The error specification of ± 30 K represents a 1 sigma spread due to data scatter. Since the nitrogen test gas was at a room temperature of 297 K, the known and measured temperatures are well within experimental uncertainty.

Because of uncertainty in the first generation PEG electron beam energy, it was of interest to compare the observed photon emission rate in the experiments to predicted values using a 33 keV electron beam. All of the following values are approximate estimates. The PMT had a gain of 1.6×10^6 and a quantum efficiency of about 30% at 391.4 nm. For a typical experiment, the P branch channel's measured voltage was 3.5 volts, which is equivalent to 2.9×10^{11} photoelectrons/sec. The observed photon count entering the PMT is thus 1×10^{12}.

Taking into account the limiting solid angle, the spectrometer, reflectance of the mirror, transmission efficiency of the lenses, and the efficiency of the grating, the overall optical transmission of the system was estimated to be 9×10^{-5}. A predicted photon output, after excitation to the v'=0 state of $N_2^+ \ B^2 \Sigma_u^-$, was estimated by integrating an initial population over a typical beam pulse that had 150amps peak current and 50 nsec FWHM. The optical system observed 0.04 cm of beam length and its entire width if the beam was within the field of view, so that the number of emitted photons in the P branch is predicted to be 1.25×10^{16} photons/sec. The experimental value of 1.1×10^{16} photons/sec is obtained after applying the optical transmission factor, assuming an emission spontaneous transition probability of $A_{B \rightarrow X} = 1.24 \times 10^7$ [Muntz, 1968].

The predicted and observed photon counts are in embarrassingly good agreement considering the uncertainty of the many assumptions necessary to generate the comparison. It does indicate that the pulsed electron gun produced beams with energies approaching 33 keV, which was the potential applied to the PEG.

The emission intensity varied linearly (within experimental uncertainty) with nitrogen pressure (Fig. 5). There was significant scatter in the data, undoubtedly due to the inconsistent discharge nature of the two-electrode first-generation PEG design. Estimates of observed photon counts compared to predicted values indicate that the beam energy in the experiment was near the accelerating potential applied to the PEG. With these encouraging results, the construction of a second generation multi-electrode PEG was initiated.

Concerns Regarding Nitrogen Gas Disturbance

Although the first generation PEG was not suitable for operational use since its beam was not well collimated and the triggering erratic, it did provide a proof of concept that was invaluable. Because of operational limitations of the first generation PEG previously discussed, a second generation variant was developed. However, since there was an expected gain factor of 10 in the second generation PEG beam currents, two processes were identified that could potentially complicate PEBF measurements. First, secondary electrons from ionized nitrogen gas molecules could change the comparative populations of the excited vibrational and rotational states. Some effects on rotation have been observed in EBF, but are not particularly significant at temperatures above 300 K [Muntz, 1968]. The effect of secondary electrons on vibration in EBF is far less well defined. Second, beam energy deposition could heat the nitrogen gas, leading to the observation of an artificially high rotational temperature. Obtaining accurate rotational and vibrational temperatures would alleviate the concerns listed above and significantly increase confidence in the PEBF technique. One of the main goals for the calibration tests of the second generation PEG was to determine any adverse impact that the PEG beam had on the integrity of the measurement. As discussed

below, the results of the PEBF research indicate that no significant disturbance exists at short gating times (~10 nsec) for rotational and vibrational population distributions (Figs 13-14).

Second Generation PEG

Design Overview

There has been an evolution in PEG design since PEBF research was initiated. The first generation PEG incorporated a single electrode pair. The initial design proved that PEBF was feasible, but the beam produced by this device was inconsistent and was not suitable for diagnostics in the LENS. A more consistent multi-electrode PEG was designed and built. The beam produced by the second generation PEG had 5-20 times the current of its predecessor with significantly improved collimation. The 30-40 keV electrons usually penetrate 5-8 cm downstream of the anode exit without a significantly altered spatial distribution ($\pm$ 1 mm). The beam is frequently observed to have more pronounced positional variations and sometimes quite dramatic directional changes at greater penetration depths, likely due to plasma instabilities associated with high current densities.

The application and evaluation of this multi-electrode PEG consisted of two distinct groups of experiments. First, a spectral survey was done for nitrogen using an intensified CCD array gated for 10 and 200 nsec windows for test gas pressures of 80 mTorr. Second, a series of Mylar penetration tests were carried out to achieve effective isolation between the PEG chamber and test cell. The experimental setup is shown in Fig. 6.

Experimental Setup for Second Generation PEG Calibration

Figure 6 shows a schematic of the PEG, supporting apparatus and detection equipment as it was set up for the calibration tests of the second generation PEG. The experimental arrangement differs from the previous calibration experiments (on the first generation PEG), as both an ICCD and a four-channel Tektronics digitizer were used in the data acquisition.

The trigger signal travels to the Princeton Instruments (PI) ST-130 controller box, which, in turn, sends a pulse to a Stanford Research (SR) 535 pulse generator, where the pulse is reconfigured to proper levels to initiate the pulse charger. The current rise from the pulse charger is detected by a Rogowski coil. The coil's signal is sent to a second SR 535 pulse generator, which introduces a delay to allow the PEG enough time to fully charge to 40 keV before activating the pulse trigger and initiating a discharge. The signal from the coil immediately behind the anode acts as a trigger event for both the Tektronics 644A digitizer and the PI PG-200 ICCD pulse generator. The digitizer records the current as registered by the coil, while the PG-200 activates the ICCD to capture a spectral signature. The optical system for the calibration tests performed recently consisted of a focusing lens (f# 2.5) placed to illuminate the aperture of a silica fiber optics bundle. The exit ferrule was mated to an Acton Research 0.275 m spectrometer and covered 6 mm of the entrance slit. The spectrometer was fitted with a 2400 grooves/mm grating blazed at 250 nm and the slit was set at 20 μm. The PI ICCD array was mated to the spectrometer to capture the spectral emissions. Data acquisition was completed as the PI ST-130 controller read out the pixel grid and transferred the information to the computer.

Results of Calibration Tests for Second Generation PEG Calibration

A spectral between 350 - 550 nm was explored at ICCD gate windows of 10 nsec and 200 nsec (Figs. 7-12) The data represented in Figs. 7 – 12 were used to measure both rotational and vibrational temperatures for nitrogen known to be at room temperature. The procedure for determining various population distributions, as well as number densities, has been outlined. Briefly, determining the rotational temperature involves capturing the P and R branches a band. As the rotational temperature increases, higher rotational levels became populated and the band will appear to spread in wavelength space. The intensity distribution in the rotational fine structure was used to measure the rotational temperature. The results of recent calibration tests for rotational temperature measurements in nitrogen are shown in Figs. 13 a,b. The temperature of the nitrogen test gas was 296 $\pm$ 3 K, and the corresponding theoretical ratio $\Re$ was 0.12. Experimental values varied from 0.15 (10 nsec case) to 0.21 (200 nsec case) (Figs. 13 a,b). The measured rotational temperature for the 10 nsec case was 333 $\pm$ 16 K and is close to the known value (296 $\pm$ 3 K). The temperature for the

200 nsec case was determined to be 451 ± 46 K. This result is evidence that a disturbance occurs during longer integration time scales.

The vibrational population distributions were determined by comparing the intensity of various bandheads with each other. Since higher temperatures will populate higher vibrational levels, intensity comparisons of carefully picked bandheads can be used to determine vibrational temperature or population distributions. The results for the measurement of vibrational band intensity ratios in nitrogen is shown in Fig. 14a. A representative linear relationship between integrated current and fluorescence intensity is displayed in Fig. 14b.

Comparing the emission intensities between the 10 nsec and 200 nsec gate windows for the First Negative System bands shows a marked increase in the signal strength of the higher vibrational levels. The Second Positive System bands agreed with previous experimental results for both gating times. The vibrational intensity ratios for the First Negative System for the (0,0)/(1,1) and (0,1)/(1,2) bands are in agreement with theoretical values within experimental accuracy for the 10 nsec case (Fig. 14). These ratios lose their correspondence to calculated for the First Negative System compared to longer gating times of 200 nsec. Short gating times (~10 nsec) are necessary for delaying the effects of collisional quenching and would be normal operating procedure. Also, the energy distribution of the beam is not known but is expected to fall off with time [Frank & Christianson, 1989]. The impact of the transient characteristics of the PEG on the excited state population level is not clear at this time. It would seem reasonable to conclude that gating windows should be located at the onset of the discharge to capture spectral signatures that are generated by higher electron energies. Complete exploration of proper gating and timing issues has not been performed. Since excitation of the Second Positive System is mainly due to secondary electrons or lower energy primary electrons, the intensity ratios for 10 nsec and 200 nsec windows did not vary significantly and are in good agreement with previous experimental work (Fig. 14a). The emission intensities of the Second Positive System bands compared to the First Negative System bands are larger than previously measured [Muntz, 1968] at both gating widths. Such comparisons are difficult to interpret, since a careful efficiency calibration of the optical system has not yet been made. However, it would seem that the Second Positive System bands appear more intense for PEBF than EBF when compared to the First Negative System. The vibrational band intensity ratios of these systems are in good agreement with both theoretical and previous experimental values for the 10 nsec gate. Errors associated with these results ranged from 5 - 18%. The values next to the peak numbers illustrated in Fig. 14 represent one standard deviation. The errors can be caused by a variety of sources including; optical system and ICCD setup, use of Franck-Condon factors instead of transition probabilities for the excitation and emission predictions and gas disturbances initiated by the beam itself.

Operational Constraints
The beam quality and reproducibility are highly dependent on the type of gas in the PEG chamber and its pressure. Chamber pressures of 20 mTorr of nitrogen produce the best results for the present multi-electrode PEG. Pressure variations of ± 10 mTorr have a significant negative impact on the beam's performance. In addition, the PEG is quite sensitive to contaminants (i.e. 5% oxygen). Therefore, it is critical for satisfactory operation to provide a high purity nitrogen environment in the PEG chamber at a known, controlled pressure.

Since the beam must propagate through number densities that are between 2 - 3 orders of magnitude greater than PEG chamber densities, a technique must be devised to effectively isolate the PEG chamber from the test section without significant beam attenuation. The PEG produces beams that are roughly 1 - 2 mm in diameter. However, the beam meanders somewhat (± 0.5 mm), which will govern the minimum orifice size (3mm diameter) that will allow the beam to propagate out of the PEG and into the diagnostic test volume without intolerable losses. Finally, the PEG's electrodes require varying degrees of conditioning (10 - 100 firings) before consistent beam formation is achieved. Hence, some form of protection for the PEG is mandatory. Several strategies have been considered.
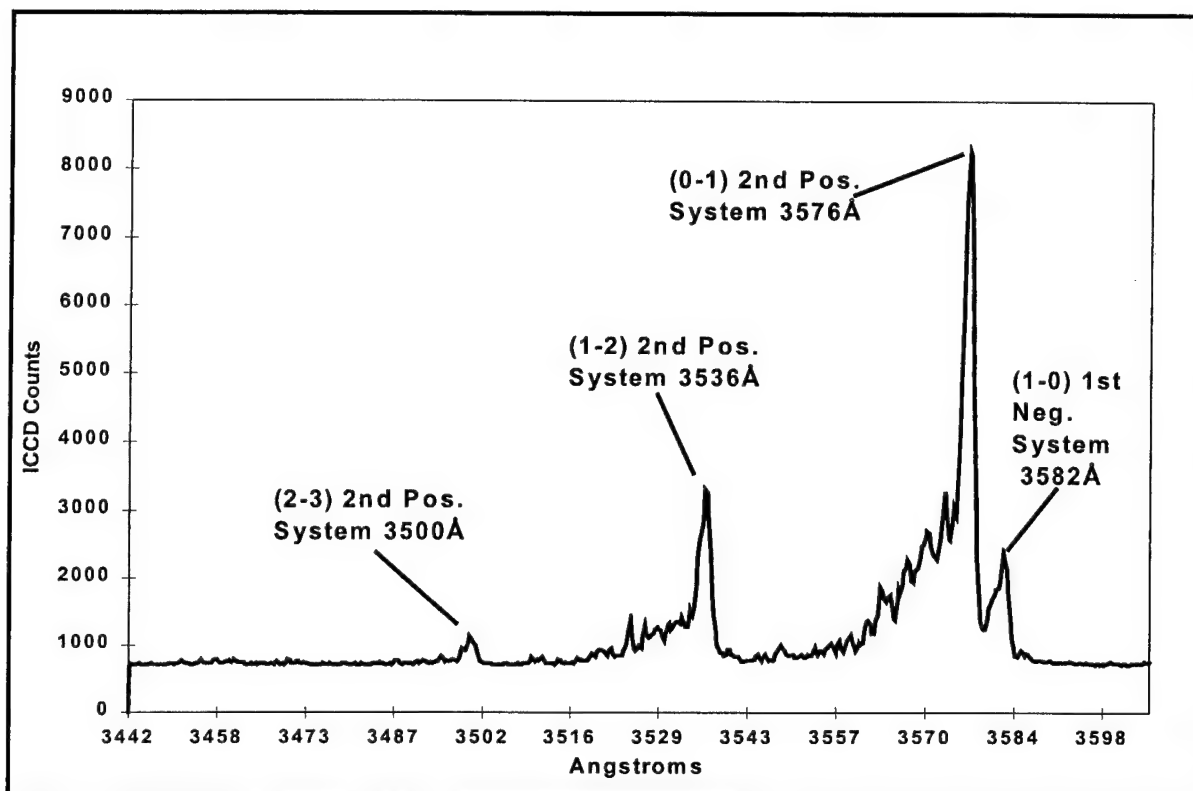
Figure 7: 10nsec gate window ICCD spectral trace for nitrogen gas.
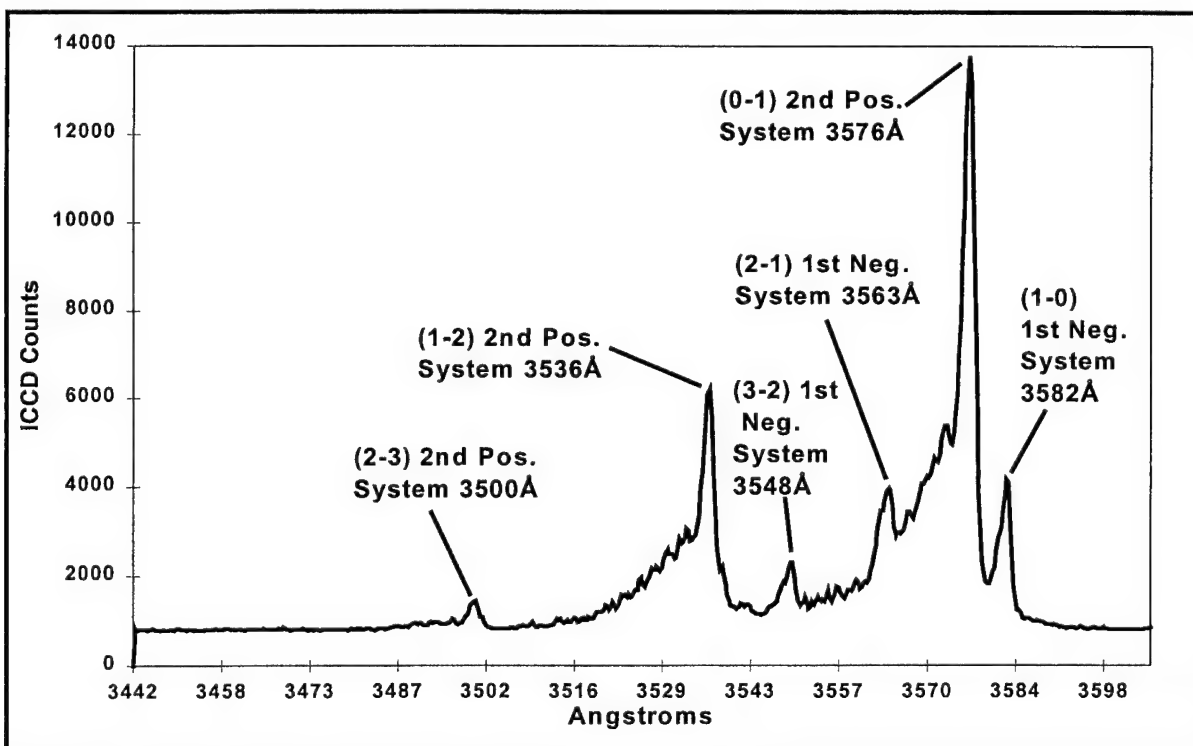
Figure 8: 200nsec gate window ICCD spectral trace for nitrogen gas.

178
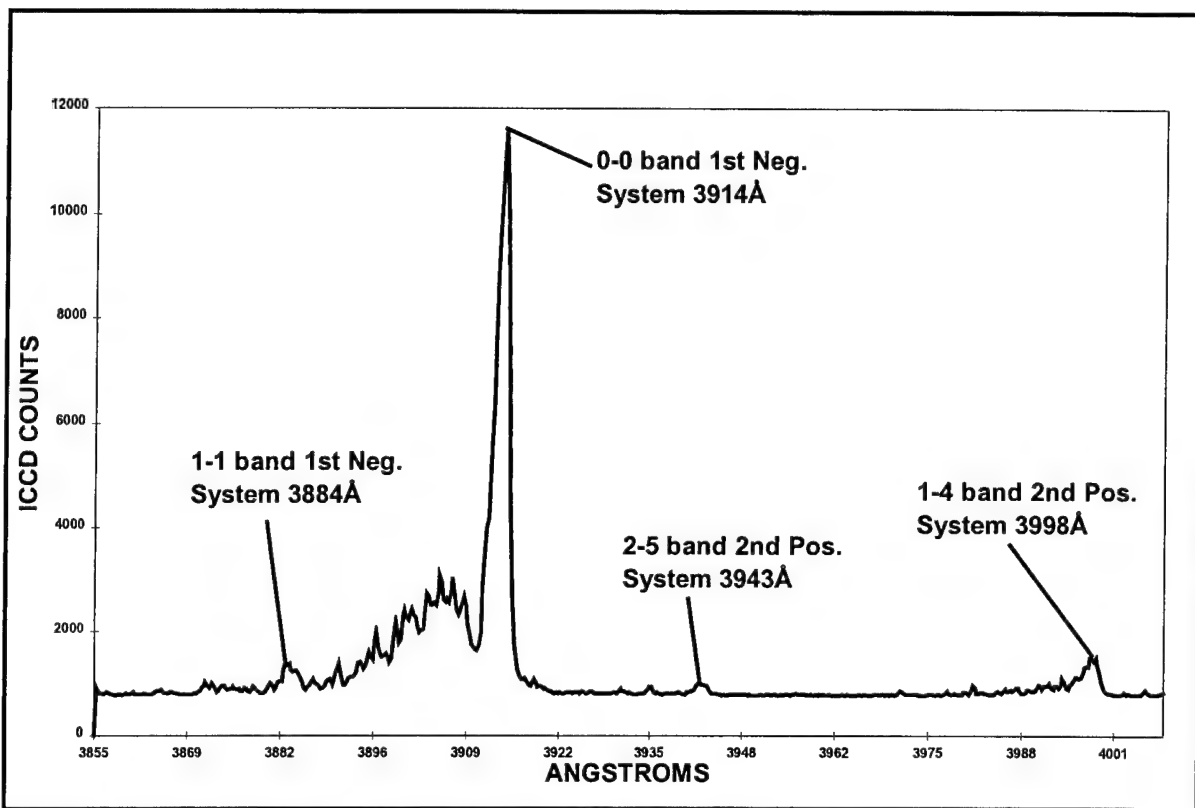
Figure 9: 10nsec gate window ICCD spectral trace for nitrogen gas.
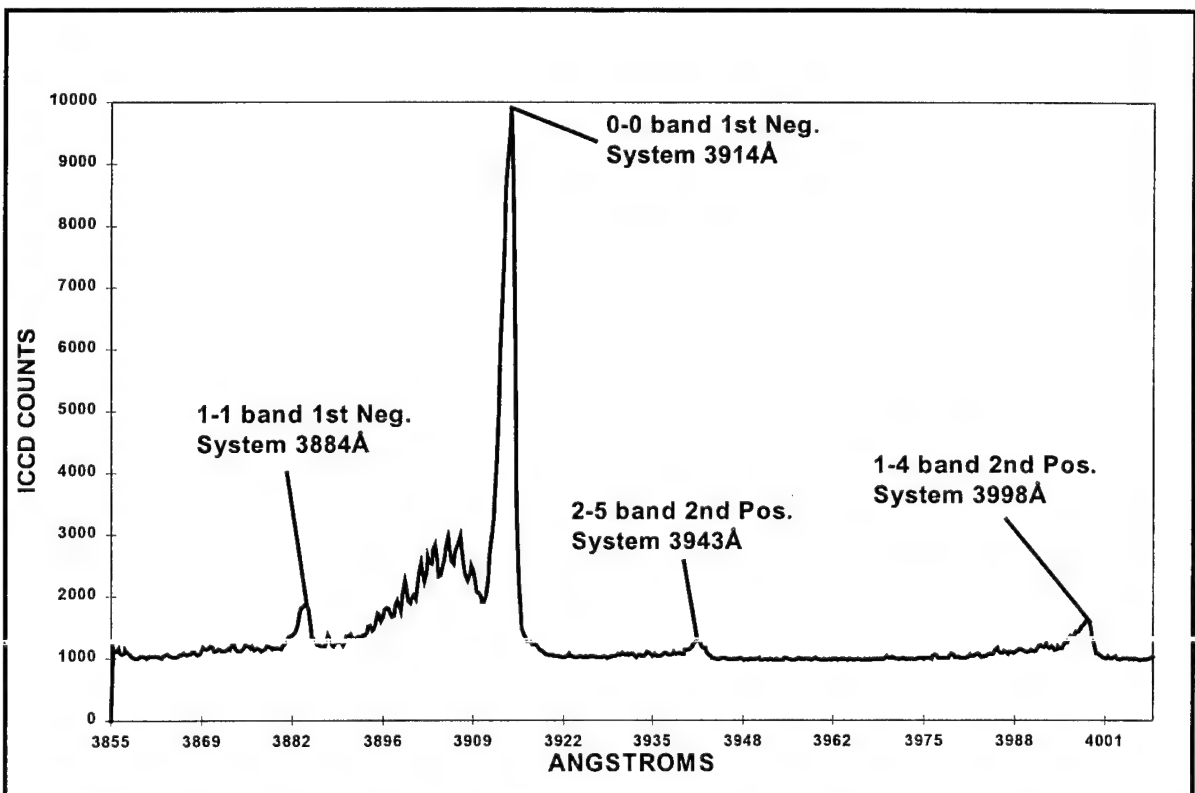
Figure 10: 200nsec gate window ICCD spectral trace for nitrogen gas.

Figure 11: 10nsec gate window ICCD spectral trace for nitrogen gas.
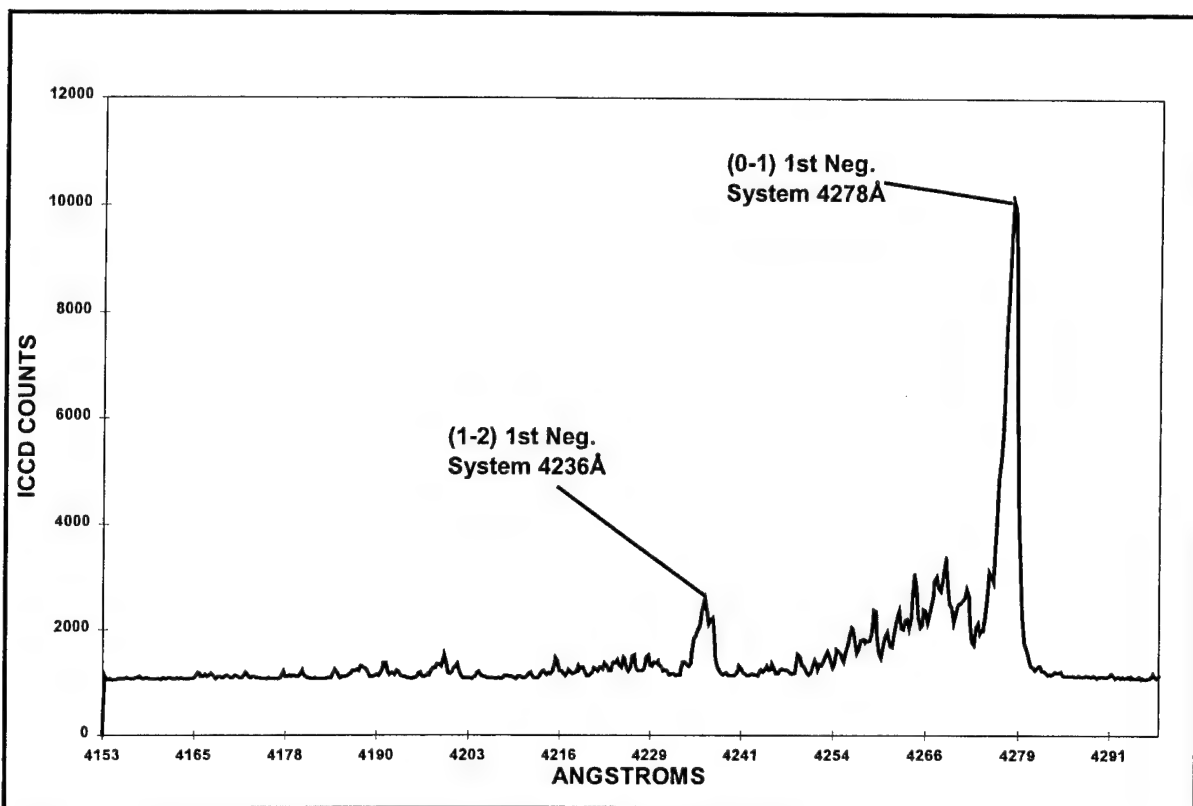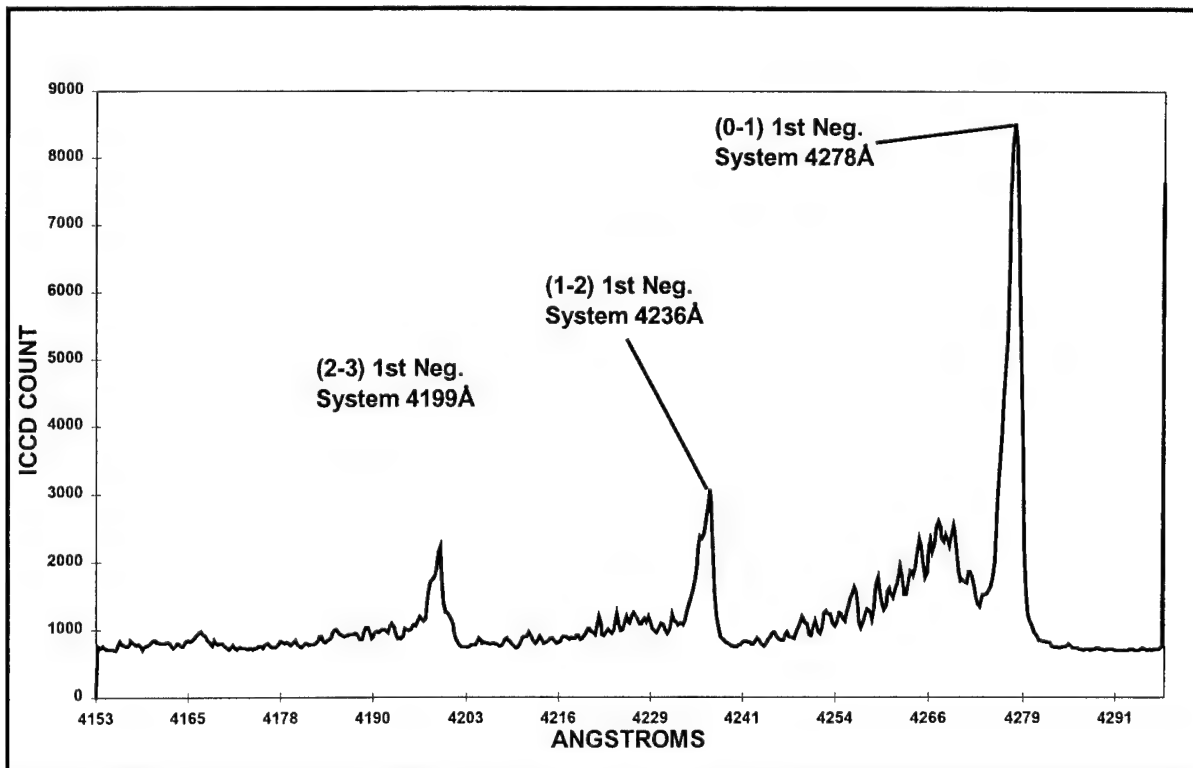

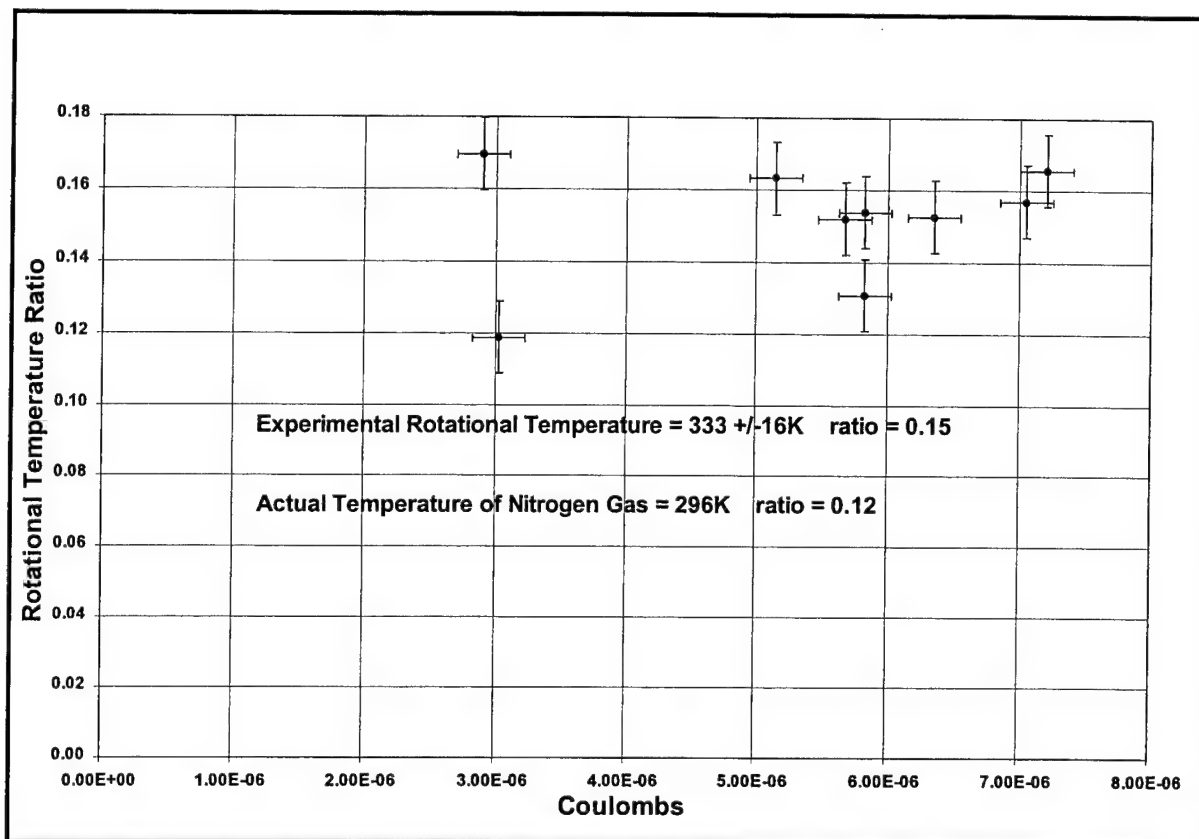Figure 12: 200nsec gate window ICCD spectral trace for nitrogen gas.

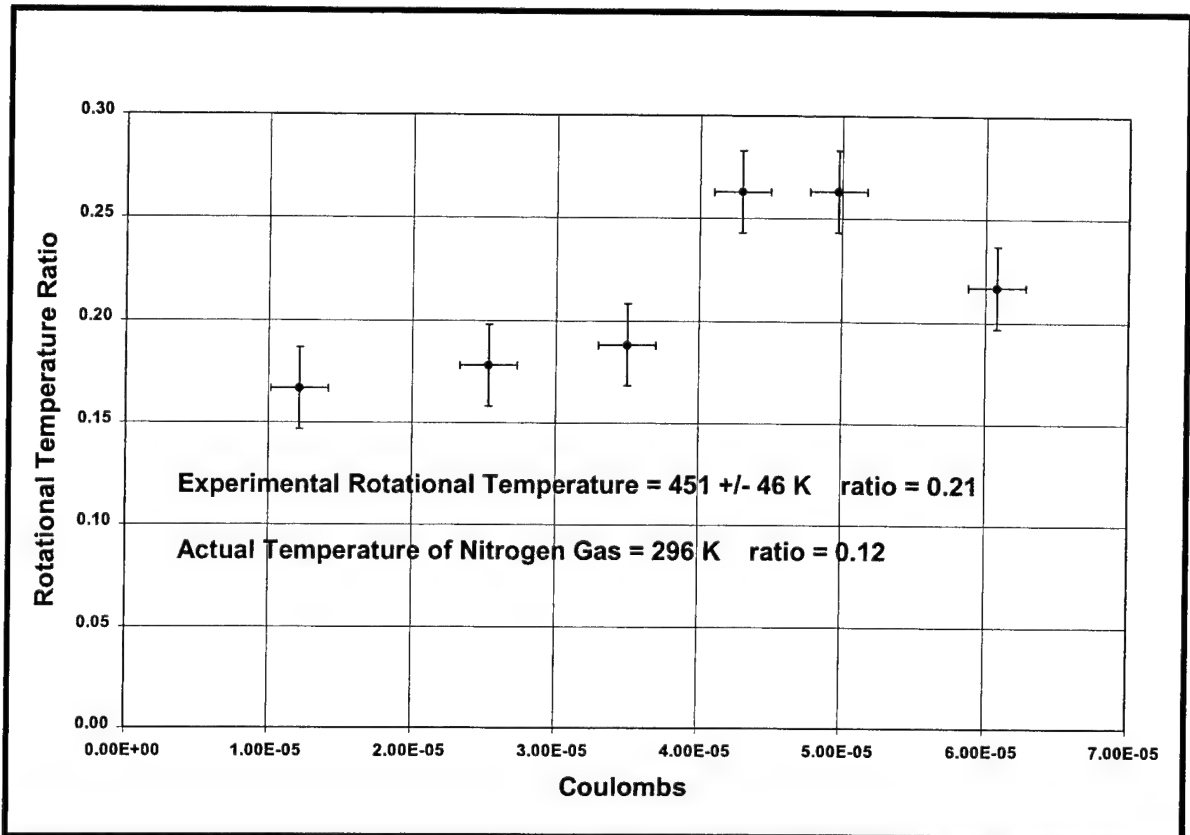**Figure 13a: Rotational temperature determination utilizing the multi-electrode PEG for 10 nsec gate.**

Figure 13b:Rotational temperature determination utilizing the 2nd generation PEG for 200 nsec gate.
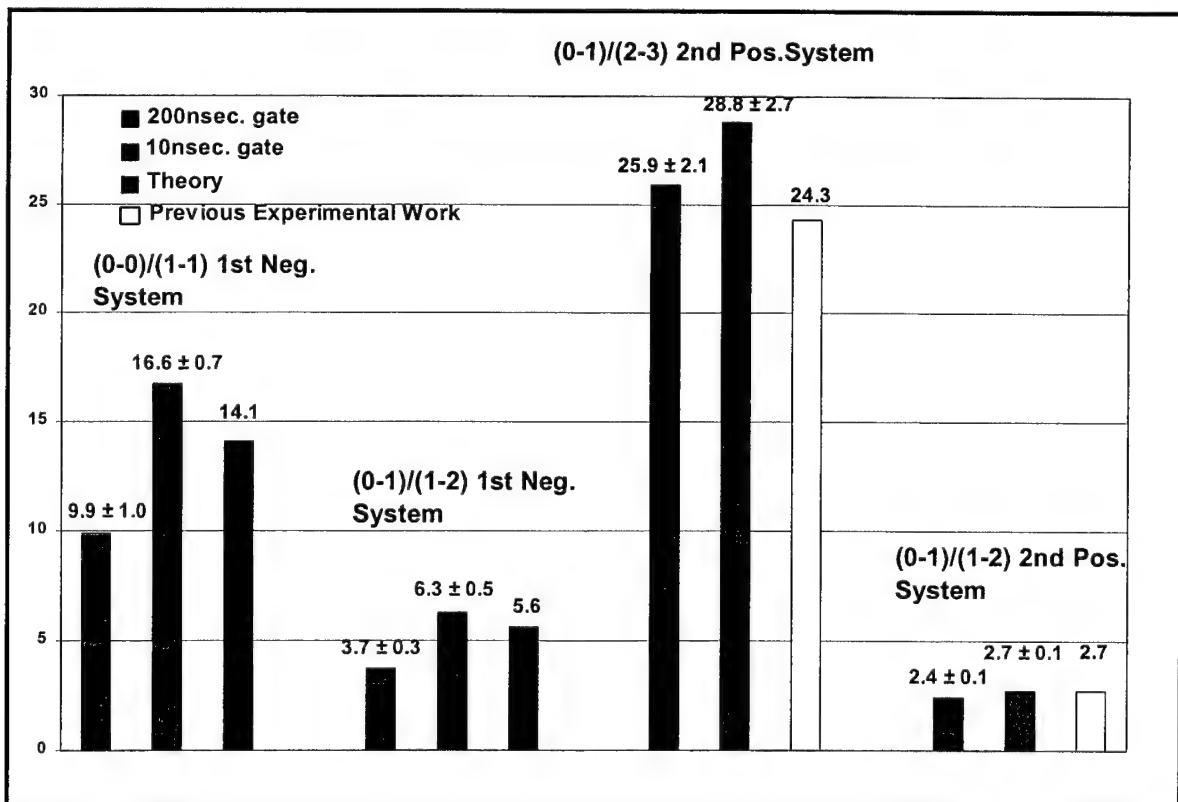

Figure 14: PEBF generated vibrational population measurements for nitrogen.

In order to measure the feasibility of various valving options, it is necessary to estimate the penetration distance of the test gas into the PEG cavity after valve opening. Based on the geometry of the PEG, a distance of 5 cm is considered a reasonable upper limit for foreign gas infiltration or for a density increase caused by a propagating shock wave. Assuming an effective test gas stagnation temperature of 2000 K, an allowed time for valve opening is about 50 μsec. A number of possible valving solutions were studied:

1) thin impermeable membrane that is penetrated and/or vaporized by the beam electrons.

2) a rotary valve capable of opening and closing in a few tens of μsec.

3) thin impermeable membrane that is vaporized μseconds before triggering the PEG.

4) differential pumping between the test section and PEG chamber.

The first solution was attempted initially because of its simplicity and apparent feasibility. Penetration tests were performed using 1.5 μm thick aluminized Mylar membranes. Calculations based on figures obtained from Attix et al [1968], yielded an average energy loss of 1.7 keV (at incident beam energy of 30 keV and Mylar density of 1.3 g/cm^3). Published results of multigap pseudospark systems used in material processing experiments supported these estimates [Benker et al, 1989]. An expected beam scattering half-angle of ~6° was calculated [Muntz, 1968]. No significant fluorescence signal was seen by eye nor detected with an intensified charge-coupled device (ICCD). In addition, a Rogowski coil placed 7 cm downstream of the anode failed to register any current. Holes averaging 2 mm in diameter were formed; however, this process appears to take too long and/or significantly interferes with the beam. Although this method seemed plausible at first, complications exist and another valving option was successfully deployed.

The second solution is more complicated but is an attractive alternative. Through the cooperation of GRC International, located in Santa Barbara, California, the proprietary design of a fast acting rotary valve will be modified and adapted to the PEG. This valving solution was tested, and exposure times of 60 μsec were achieved. This solution also addresses the stringent operational constraints previously discussed. The PEG chamber would not be exposed to the surroundings for any length of time, thus largely protecting the electrodes from contamination. A sketch of the apparatus is shown is Fig. 15.

The third possible solution was also considered, since the beam consistently bored holes in the Mylar. An inherent problem with both the first and third options is that it is difficult to accomplish PEG electrode conditioning. Assuming this problem could be managed, other issues remain. Vaporizing the membrane could be accomplished by double pulsing the PEG or vaporizing the Mylar through independent means (i.e. excimer laser or an electrical discharge). The PEG would be triggered a few μsec later. Both of these approaches would produce sufficiently instantaneous holes for the beam. However, the rapid fire of a PEG is limited by the inherent recovery time dictated by the diffusion of ions to the tube inner walls and electrode surfaces following a discharge. A typical recovery time for a hydrogen filled cavity is 100 μsec (e.g. thyratrons), which is driven by the mass of the ions involved. It would take significantly longer for the more massive nitrogen molecules. Hence, the double pulsing of the PEG could not be done fast enough to meet the stringent time constraint of 50 μsec or better. A general difficulty with the double pulsing approach is that the PEG chamber is necessarily exposed to the ambient environment after about 100 μsec. Serious contamination of the PEG electrodes would be expected from uncontrolled exposure to the high pressure in the shock tunnel. Another unknown effect has to do with the structure of Mylar ($C_{11}O_5H_{29}$). Vaporizing the Mylar with any kind of high energy discharge introduces the potential for molecular fragments and plasma affecting the beam propagation and quality.

The fourth option of differential pumping was also considered. As the pressure in the test section varied during the tunnel run, the back pressure in the PEG chamber would also surely fluctuate and there would be the risk of a misfire. To remover this risk would require the introduction of a two stage pumping scheme (Fig. 16). Such an arrangement would require that the beam pass through one constriction, travel several centimeters, and emerge from a 3mm orifice (Fig.16). Since the beam possesses some degree of instability,
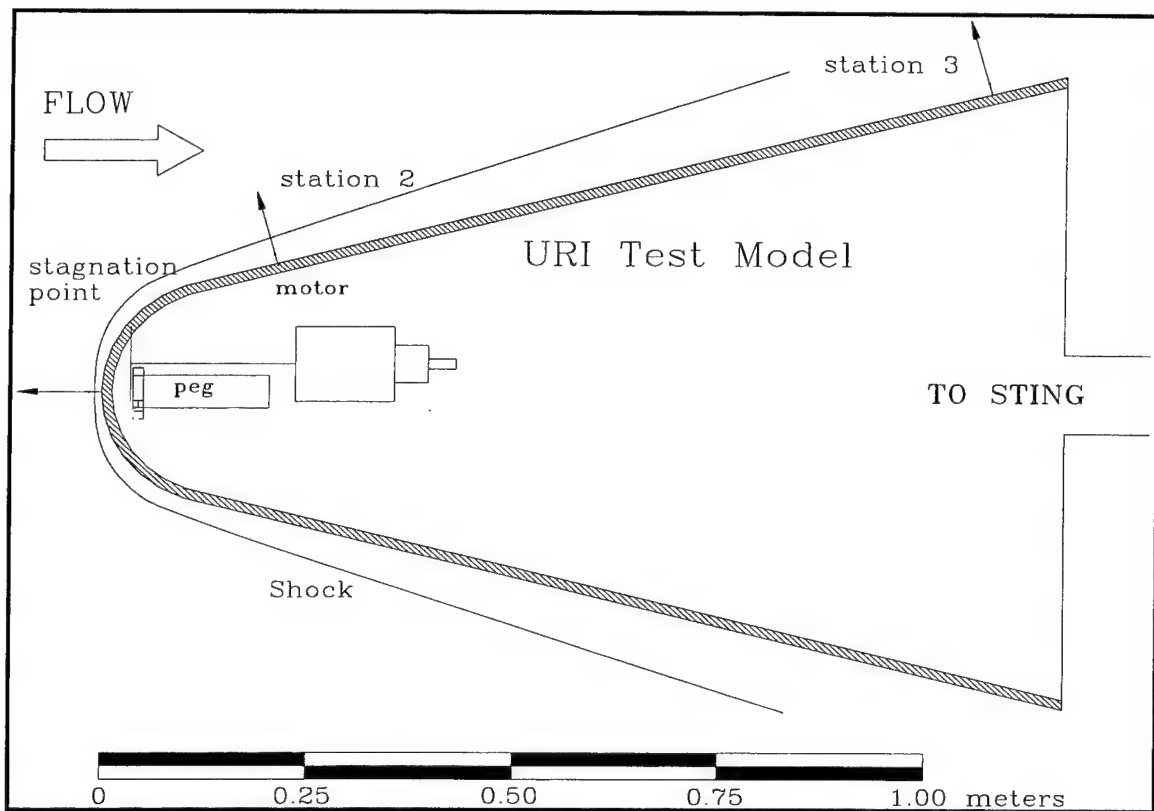
Figure 15: Fast-acting rotary valve apparatus installed with the PEG inside URI model.
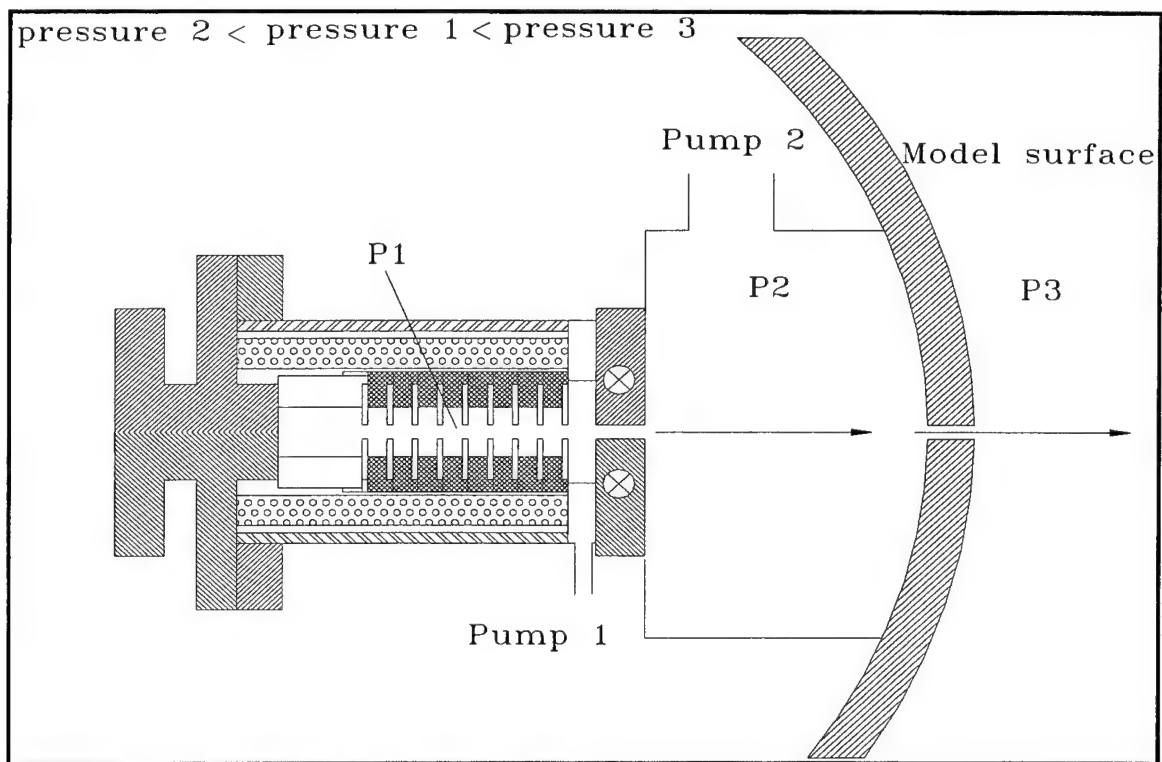

Figure 16: Two-stage differential pumping scheme.

it is not reasonable to expect that it could negotiate this obstacle with any degree of predictability. Furthermore, the fitting of pumps capable of handling the serious leak of a 3mm diameter orifice (see operational constraints) is difficult in the cramped space within the test model.

The rotary valve option has been developed and tested, with the successful results reported in F. Lutfy's PhD dissertation (to be published 2001).

Discussion of the CW Electron-Gun Measurement of the LENS Freestream

A series of tests using a CW electron gun was performed to characterize the LENS freestream, as well as to explore and compare expected fluorescent signals obtained using the CW EBF technique with respect to PEBF.

Fig. 17 is a schematic of the instrumentation installed in the LENS test section. Fig. 18 is a picture of the apparatus with the pmt package on the left and an optical multi-channel analyzer (OMA) fairing on the right. Also in view is the "shock diamond" (center) through which the electron beam was introduced perpendicular to the freestream flow. Fig. 17 is a simplified schematic of the experimental setup. The viewing region was 1" above the height of the shock diamond (i.e. in the freestream), and the emission volume was a sphere roughly 0.3" in diameter. The effective optical system f# was 3.4. The pmt package consisted of three pmts, which were coupled to bandpass filters. Two of the filters were tuned to the (0,1) and (1,2) bands of nitrogen's Second Positive System (357.7 and 353.7 nm respectively). The nitrogen filters both had a bandpass of 3 nm. These bands were chosen for their optimum separation and relative position with respect to the (0,0) bands of both the Second Positive and First Negative Systems of nitrogen. The pmt vibrational measurement would then be independently confirmed by utilizing the OMA/spectrometer to generate a spectrum with a range spanning 301.5-426.2 nm. The rotational measurement would be accomplished by switching gratings to resolve a range of 344.5-398.1nm. The (0,0) band of nitrogen's First Negative System, which lies at 391.4 nm, was targeted, since it has a relatively intense emission and is well documented. Finally, the third pmt was coupled to a bandpass filter centered at 501.6 nm with FWHM of 10 nm to detect driver gas arrival (i.e. helium).

An attempt was made to detect NO using this pmt arrangement mated with a filter centered at 256.1 nm with a bandpass of 47.1 nm following the research done by Petrie [1972]. Unfortunately, calibration complications relating to proper interpretation of the signal arose. Another interesting fact surfaced as CUBRC personnel later attempted to obtain a calibration for NO. As per Bergman [1997], they observed a positive NO signal when the electron beam was fired into air. Apparently, the beam caused some chemistry, and NO was produced, thereby nullifying the calibration.

The OMA fairing also housed a retractable Faraday cup. This device was extended to monitor and record the beam current as the test section was pumping down. With the retractable Faraday cup extended calibration readings of the pmts, as well as the OMA, were recorded simultaneously. These calibrations spanned from 7 to 0.7 Torr and would later be used to interpret the fluorescence traces obtained from the actual test runs. The test section's lowest pressure was 600 to 700 mTorr during the period of our tests. The Faraday cup was extended just prior the test run to confirm that the beam current was optimum and retracted moments before diaphragm rupture in the driver section (~tens of seconds). It was assumed that the last recorded current value was valid for the test run. It must be stated that the beam current at a given test section pressure remained remarkably consistent for given operational settings (within 3% for a 10-minute time frame). Consequently, the assumption that the current remained constant between time of last recording and test run (which spanned roughly a few tens of seconds) is reasonable.

Finally, a video system was used to observe the beam's condition during calibration tests and shock tunnel runs. The image was displayed on a monitor located a safe distance away from the LENS in a location which housed all power and data acquisition systems.

The CW electron gun was held at a pressure of 10^{-6} to 10^{-5} Torr. The system was differentially pumped using two turbomolecular, pumps and the beam was ejected out of a small graphite orifice 300-500 μm in diameter. Smaller diameters could have been achieved if the shock diamond apparatus was discarded,

since electromagnetic focusing was most effective at the exit plane of the electron gun. However, this would have forced the beam to propagate through both a boundary layer and Mach wave; it was believed that beam injection directly into the freestream was a more prudent approach. The use of a larger orifice introduced a complication with the static calibration measurements since the electron gun chamber pressure varied with the external pressure. Consequently, the beam current was not consistent as various pressures were sampled. The impact of this complication was minimized by normalizing the calibration signal to the current available. It was finally assumed that the beam current would not deviate during a test run from the final reading obtained prior to the run since test times are relatively short (~10msec). The video was used to fine-tune the beam's characteristics in order to negotiate the hole in the graphite plug with maximum efficiency.

The data acquisition was achieved by using a High-Techniques 600 digitizer that allowed capture of the pmt signatures along with displaying relevant trigger signals and stagnation pressure traces. The light from the emission volume was transmitted via a single fiber optics fiber 0.800 mm in diameter to the OMA/spectrometer unit. The OMA was terminated to a 286 PC that housed the necessary software to download spectral data.

Experimental Measurements

Figure 19 shows a calibration spectrum obtained in the LENS test section at an air density of 1.76×10^{17} cm^{-3} for an OMA exposure time of 3 msec. Displayed prominently are the (0,0), (0,1) and (1,2) bands of nitrogen's Second Positive System which were used for the density measurement and vibrational temperature determinations. Also appearing is the (0,0) band of nitrogen's First Negative System, which was used for the rotational temperature measurement.

Fig. 20 represents the spectrum obtained during a shock tunnel run for a nitrogen driven section at 5 MJ/kg enthalpy. By inspection of Fig. 20, it is quite apparent that a significant amount of contaminants is present.

Fig. 21 is an OMA trace used to determine rotational temperature and was obtained for a flow condition having air as the driven gas at 5 MJ/kg enthalpy.

Fig. 22 is a spectral trace obtained during a test run for a 10 MJ/kg enthalpy with air being the driven gas. Contamination is still evident in the latter as well.

Fig. 23 represents the overwhelming background light obtained during a 10 MJ/kg enthalpy run with air being the driven gas. All three pmts registered signals that would cripple any attempt to obtain CWEG generated signals.

The pmt signals are displayed in Fig. 24 and represent the conditions present during a 5 MJ/kg-enthalpy condition with air being the driven gas. The pmt traces for the (0,1) and (1,2) bands presented in Fig. 24 have had their corresponding background light signals subtracted. Also displayed is the background light trace for the helium pmt, as well as the actual helium signal obtained during active CW electron beam interrogation to obtain a measure of test time. Lastly, the stagnation pressure was also captured and is displayed in Fig. 24 as well.

Fig. 25 plots the ratio of the (0,1) and (1,2) bands of nitrogen as a function of time. This ratio represents a measure of the vibrational population level present in the freestream.

Finally, Table 1 summarizes the data obtained during the 5 test runs in the LENS facility.

Discussion of LENS CW EBF Tests

By comparing Figs. 19 and 20, it is readily evident that contamination levels are present. The most serious being CN. The source of CN was not known at the time of the test runs. Unfortunately, CN has broad emissions in the range of interest for our study. CN's violet system ($B\ ^2\Sigma - A\ ^2\Pi$) has band emissions at 358.4, 386.0, 387.1, 388.3, 419.7 and 421.6 nm. Since the (0,0) band of nitrogen's First Negative System is located at 391.4 nm, the rotational temperature measurements were not compromised. The degree of

186

interference is difficult to assess for the number density determination. However, number density measurements yielded values of 9 x 10^16 and 1.2 x 10^17 cm^-3 (± 20%) for the 5 MJ/kg and 10 MJ/kg air runs, respectively. As represented in Table 1, these values are within experimental uncertainty of the expected conditions. It would appear that CN contamination had minimal adverse impact on the number density measurement. However, recent CUBRC research indicates no significant CN contamination.

Test run numbers 8 and 9 had significant CN contamination (Table 1). However, the OMA trace for run 6 (Fig. 21) shows no significant contamination. The reason for the CN presence was not clear at the time of these tests. The vibrational temperatures for run 6 (i.e. 5 MJ/kg – air-driven) was found to be 3350 ± 1500 K using the OMA data and 3800 ± 600 K with the pmts. These measurements do not correspond to expected conditions. Possible quenching of the (0,1) band is unlikely since its lifetime is roughly half the lifetime of the (1,2) band. It is possible that the effective quenching cross section for these bands varied with temperature, but this would suggest a significant departure from expected freestream temperature. In light of the CN contamination, the vibrational temperature is uncertain. Table 1 highlights the test results for the LENS freestream.

TEST CONDITIONS	RUN 6	RUN 8	RUN 9
Driver Gas	Helium	Hydrogen	Helium
Mi	6.538	9.357	6.460
Driven Gas	Air	Air	Nitrogen
P_0 (psia)	7265	7413	7437
Calculated Freestream Velocity (km/sec)	3.2	4.5	3.3
Calculated Freestream Temperature (K)	241	680	246
Calculated Freestream Density (# - cm^-3)	1.23×10^{17}	1.72×10^{17}	1.20×10^{17}
Enthalpy MJ/Kg	5	10	5
EXPERIMENTAL RESULTS (EBF)			
Observed Test Time (msec) (preliminary)	2.5-3.3 +3/-1	--------	--------
Observed Rotational Temperature (K)	220 ± 60	--------	--------
Observed Vibrational Temperature (K) OMA	3350 ± 1500	4400 ± 900	1800 ± 1000
Observed Vibrational Temperature (K) PMT's	3800 ± 600	--------	--------
Observed Nitrogen Number Density (# - cm^-3)	9×10^{16} ± 20%	1.2×10^{17} ±20%	--------

Table 1: Summary of LENS freestream characterization tests.

The rotational temperature was measured to be 220 ± 60 K, which is within the expected value of 241K.

The observation of test time was also made uncertain due to the presence of significant background light levels. However, the test run trace shown in Fig. 24 appears to have an interesting series of inflexions at time indices of 6.5 and 10 msec and possibly due to driver gas arrival. Although absolute intensities vary, the background light signatures are remarkably self-similar up until those inflexion points are reached. However, the lack of OMA traces in the range of 500 nm combined with the limited number of test runs and the CN complications precludes any solid conclusions to be reached about test time issues.

Based on our experience from the LENS CW EBF study, the determination of vibrational population distributions was convoluted and very sensitive to interpretation of the data due to relatively weak signal strengths and poor resolution. In addition, the need to expand research to other gases which are present in significantly lower concentrations (NO, OH, etc.) require significantly greater signal strengths. Also, the need for accuracy puts greater demands on resolution of various trace signatures. Unfortunately, signal strengths are compromised as resolution is increased. The result is that the experimentalist is left with signals close to noise levels, which undermines quantitative analysis. The PEG generates beams that are roughly 6 orders of magnitude (~1000 A) greater than its CW cousin, with beam FWHM of tens of nanoseconds. The result is a signal that dominates the background light while ameliorating quenching difficulties. As a comparison, a CCD trace generated by firing the PEG into a static test cell with nitrogen is shown in Fig. 7. The reader will note that the nitrogen density represented in Fig. 7 was roughly 1/100th

that of the freestream density probed by the CW gun in the LENS tests. Also note that this trace was done with greater resolution than what was captured by the OMA in the LENS. This comparison dramatically illustrates the advantage of using the PEG as a diagnostic tool.

One drawback with the usage of a PEG is its limited firing rate. Anticipated frequencies of the PEG presently being developed range between one hundred to perhaps a thousand Hz. Although the CWEG generates limited signal strength when operated at elevated enthalpies and suffers from quenching effects, it does possess the powerful capability of generating time histories of critical parameters.

In addition, stagnation regions have significantly greater densities, and quenching difficulties are expected if using a CW electron gun. By being able to reference an emission of interest to a brief excitation event, the use of a PEG can delay the complications of quenching to number densities around 1×10^{18} cm^{-3} because of the very short pulse times. Figs. 2 and 26 show representations of the quenching issues relating to the use of both CW and pulsed electron guns.

A CUBRC 50 keV CW electron gun was installed in the test section of the LENS (Fig. 18). Diagnostics were achieved using an Optical Multichannel Analyzer (OMA) and three photomultiplier tubes (PMTs) which were coupled to bandpass filters (Fig. 17). Specifically, two of the filters were designed for the (0,1) and (1,2) bands of nitrogen's Second Positive System. These bands were chosen because they were ideally spaced (i.e. 4 nm apart) to allow easier deconvolution of the vibrational temperature with the optical equipment that was available. The third filter was centered on the 501 nm line of helium. It was used in an attempt to obtain a measure of test time for the facility by detecting driver gas arrival. In addition, since the concentration levels of NO are important for the study of high enthalpy flows, an attempt was made to capture an emission signature. However, for the optical package available, no results were obtained. A total of five runs were made with enthalpies of 5 and 10 MJ/kg in both air and nitrogen as test gases.

The results are shown in Figs. 20 - 25 and summarized in Table 1. It was noted immediately that an enthalpy of 10 MJ/kg generated considerable levels of background light, which nullified PMT effectiveness (Fig. 23). Using narrower bandpass filters could potentially ameliorate the background light problem. An enthalpy of 5 MJ/kg was more manageable, since background light levels were significantly lower (Fig. 24). The PMT traces represented in Fig. 24 have their associated background light levels already subtracted. Also included in Fig. 24 are the signal trace for helium detection and its corresponding background trace. The helium background is about equal to the signal and consequently made the determination of test time uncertain. However, the nitrogen pmts for this test condition were more readily interpretable, and a time history of the ratio of the (0,1)/(1,2) bands is shown in Fig. 25. It is quite apparent that the ratio before shock arrival is roughly 8% higher than the ratio after shock arrival. This change equates to a vibrational temperature of roughly 3800 ± 600 K. This result was quite surprising, since the corresponding rotational temperature was determined to be 220 ± 60 K. Quenching issues were investigated as possible error sources for the signal strengths, particularly for the (1,2) band. However, since the lifetime of the (1,2) band is roughly twice that of the (0,1) band, quenching should have reduced the (1,2) band intensity to a greater degree than that of the (0,1) band and, according to our results, the opposite happened. The nitrogen number density was determined by observing nitrogen's (0,0) band of the Second Positive System with the OMA. The density measurement agreed with expected results within experimental uncertainties (Table 1).

The OMA was used to derive rotational and vibrational population distributions and the number density of nitrogen as well as fingerprinting unknown species. A calibration trace obtained in the test section prior to a shock tunnel run is shown in Fig. 19. In sharp contrast, Fig. 20 represents a test run acquisition. It is immediately apparent that there was a significant degree of contamination (i.e. possibly due to CN gas). The source of this contamination was not known at the time. However, recent data from other CUBRC CWEBF tests shows no CN complications. Cleaning methods of the LENS could affect the formation of CN, but the reason explaining the discrepancy between CWEBF tests is not yet apparent. The vibrational temperature determination was achieved by making a ratio between the (0,1) and (1,2) bands of nitrogen, as previously mentioned. These OMA measurements yielded a somewhat lower temperature, 3350 ± 1500 K, than are obtained from the PMTs. The rotational temperature was determined by measuring the separation between the peaks of the P and R branches of the (0,0) band of nitrogen's First Negative System. The

rotational temperature was determined to be 220 ± 60 K for the 5 MJ/kg test run. Finally, using the (0,0) band of nitrogen's Second Positive System, the number density was found (Table 1).

Summary and Conclusions

There were two fundamental issues left to overcome so that the PEG could achieve operational status. First, consistency between pulses needed to be ameliorated. Second, a technique needed to be devised so as to allow beam propagation out from the tightly controlled environment of the PEG chamber and into the flowfields of interest.

As of two years ago, the PEG fired successfully 70% of the time. This figure was unacceptable due to the prohibitive cost of running hypervelocity test facilities. Therefore, diagnostic instrumentation has to be made to work on demand so as to take advantage of rare and expensive test runs. This point was addressed, and the present PEG achieves a success rate of 96% (based on 100 fires), with beam currents of ~ 1100 A.

Following a couple of iterations, a fast acting rotary valve has been designed and effectively seals the PEG chamber, while generating exposure times of <100 µsec. Issues relating to timing remain, but they should be resolved in the near future. This apparatus can be actuated with 5 msec of trigger lead time and lends itself quite well to shock tunnel applications.

The determination of vibrational and rotational population distributions for the LENS CW EBF study was uncertain due to low signals relative to background. In addition, the need to expand research to other gases which are present in significantly lower concentrations (NO, OH, etc.) requires greater signal strengths. Also, the need for accuracy puts greater demands on resolution of various trace signatures. Unfortunately, signal strengths are compromised as resolution is increased. The result is that the experimentalist is left with signals close to noise levels, which undermine quantitative analysis. The PEG generates beams that are roughly 6 orders of magnitude greater than its CW cousin with beam FWHM of tens of nanoseconds. The result is a signal that dominates the background light while ameliorating quenching difficulties. As an illustration, the reader should compare Figs. 7 and 20. The trace in Fig. 7 was generated using a PEG firing in a density that is two orders of magnitude lower than that of Fig. 20. Hence, for similar densities, the PEG could generate signals that totally dominate any background light. Therefore, determination of vibrational and rotational populations could be made with significantly greater certainty, as shown in Figs. 13 - 14. Number density measurements are also expected to be improved.

Alt. km	Number Densities (#/m³)				
	N2	O2	NO	N	O
40	6.0e22	1.4e22	5.0e21	1.5e12	3.3e20
50	1.9e22	3.7e21	1.6e21	6.6e12	1.4e21
Alt. km	Temp. (K)		Velocity (m/sec)		
40	303		4000		
50	468		4000		

Table 2: Expected freestream conditions.

The CW EBF technique was applied in the LENS freestream tests to help determine background light levels and ascertain strengths and weaknesses relative the PEBF technique. Based on the LENS tests, there is some concern that the freestream condition is in nonequilibrium (i.e. rotational temperature measured to be at 220 ± 60 K and vibrational temperatures varied between 3350 ± 1500 K and 3800 ± 600 K). However, since the signal strength was relatively low for the (0,1) and (1,2) bands of nitrogen's Second Positive System, there remains doubt about the accuracy of this result (as exemplified by the uncertainties associated with the measurements). In contrast, the PEBF technique did not significantly alter vibrational population ratios (as compared to theory and previous experimental work), with uncertainties of 5 - 19%. It is not possible to judge the validity of various CFD schemes if the boundary conditions (i.e. the freestream) are not correctly determined. For instance, the CFD results for the flowfield surrounding the stagnation region of a test cone are shown in Figs. 27 & 28 and Table 2 highlight the ideal anticipated freestream conditions [Muntz et al, 1996]. The LENS tests indicate that more definitive results would be possible using the PEBF technique to accurately specify the boundary conditions in the codes.
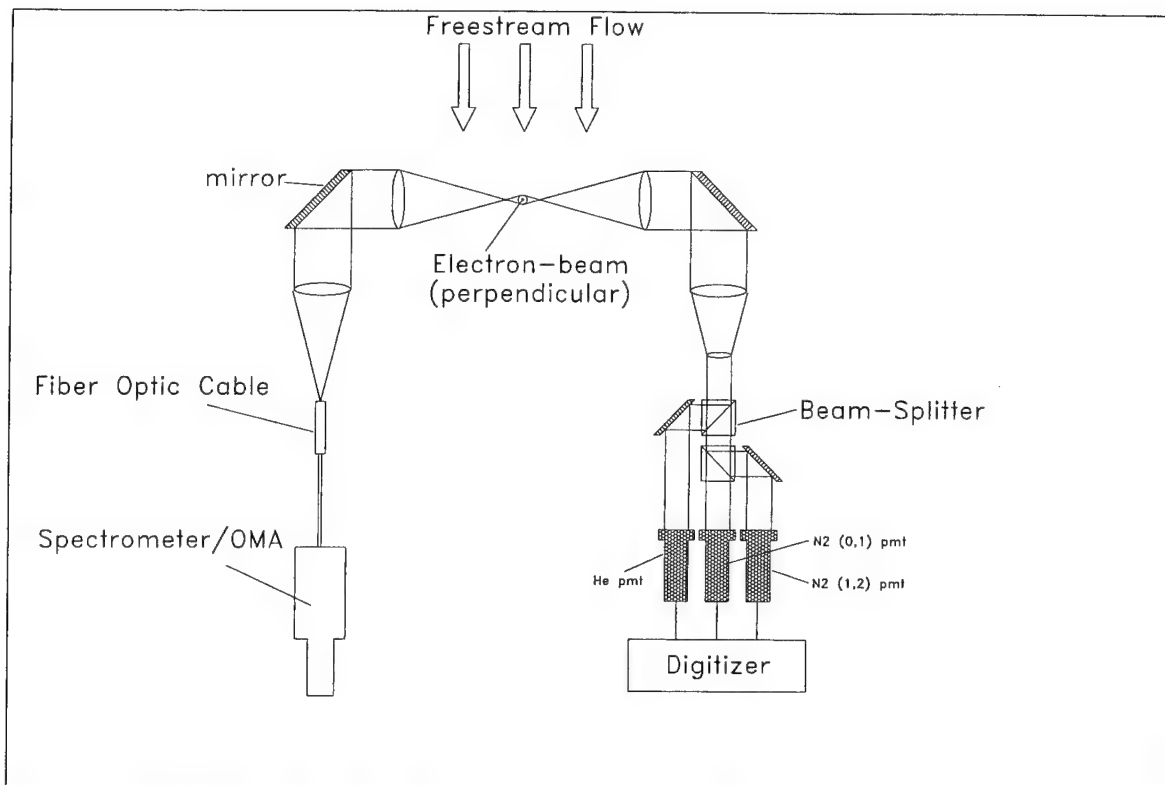
Figure 17: Schematic of experimental setup for CW EBF LENS freestream studies.
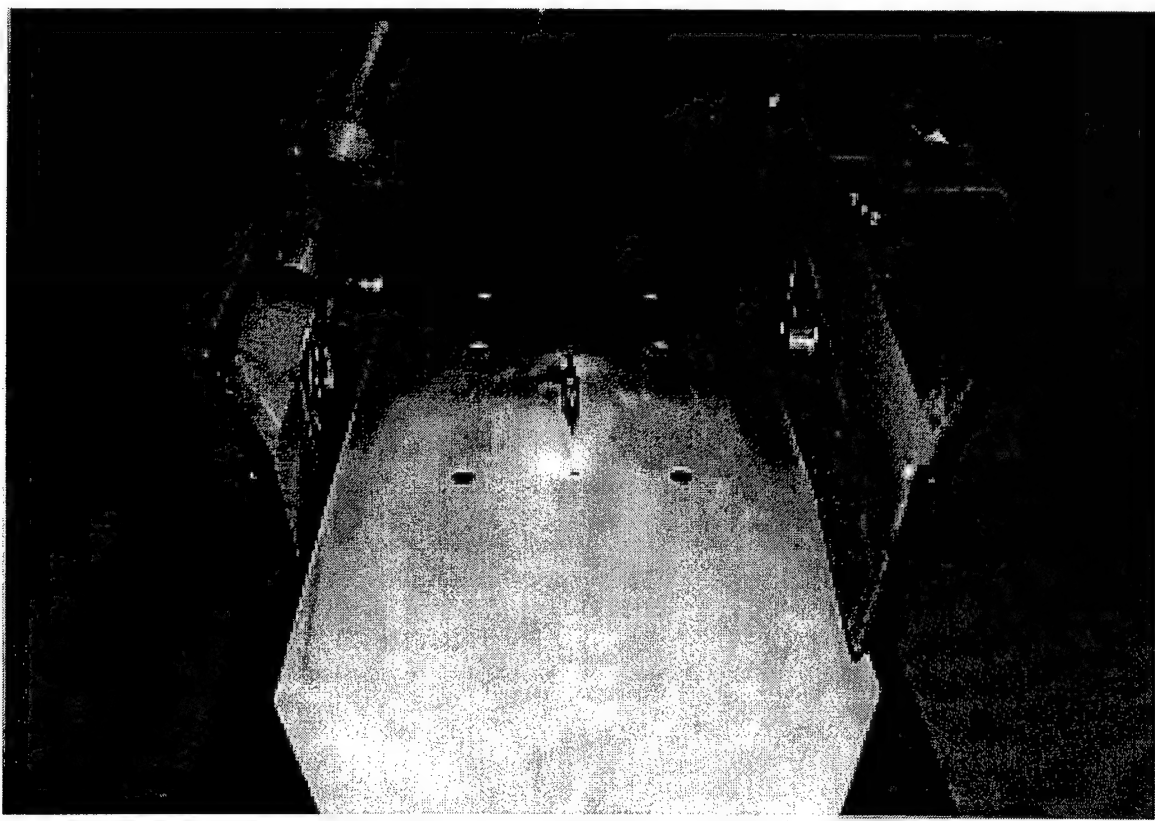
Figure 18: Installation of the CW electron gun in the LENS facility for freestream studies.
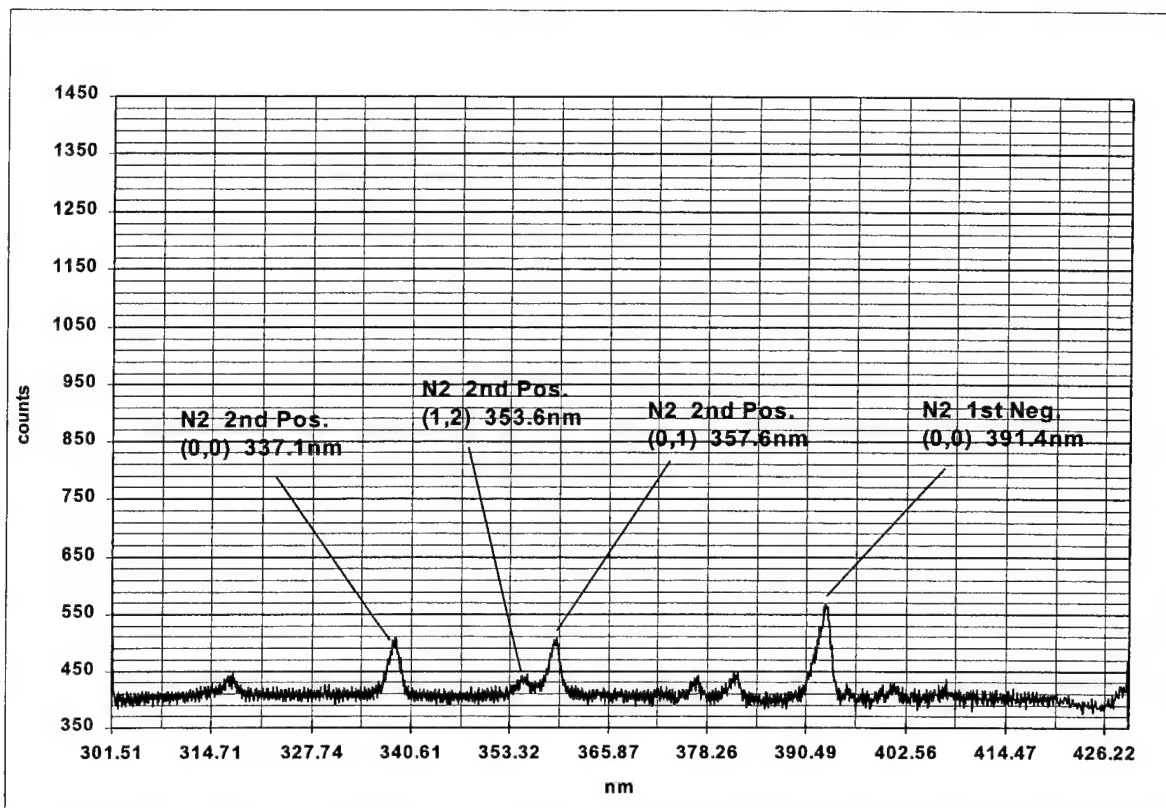
Figure 19: Calibration spectra obtained in air at a density of 1.76×10^{17} cm^{-3}.
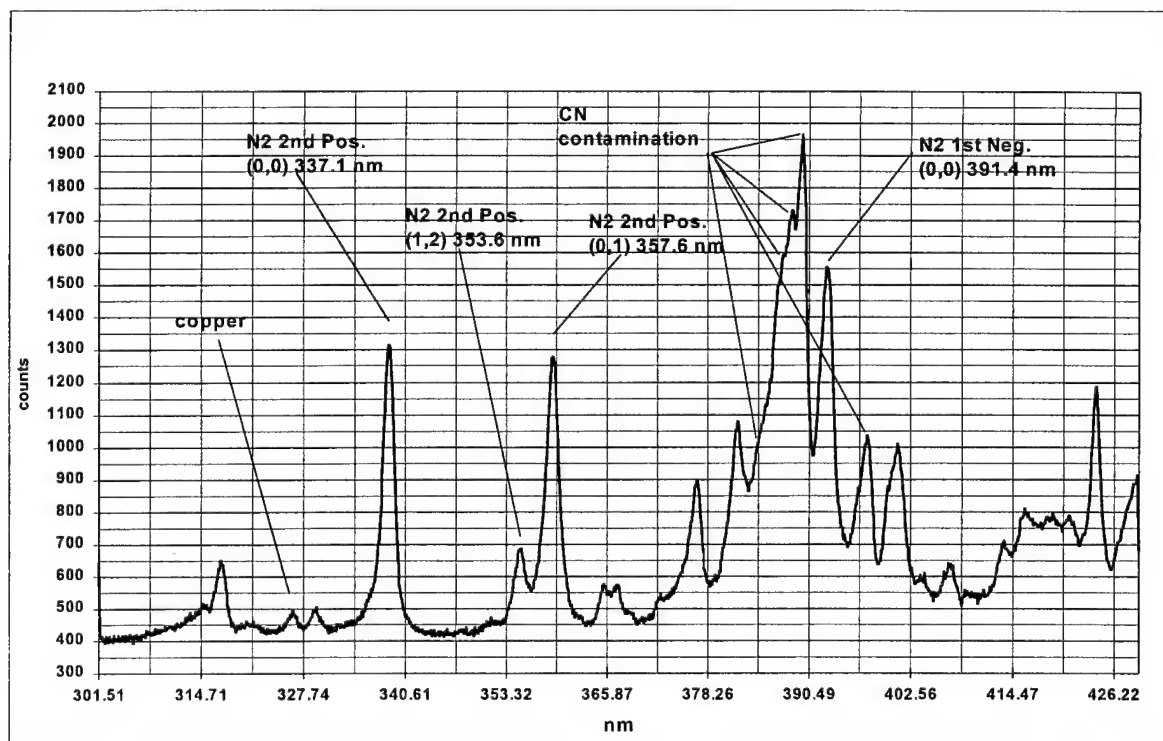
Figure 20: Trace for test run 8, 5MJ/kg enthalpy condition for a nitrogen driven section. Note CN contamination.
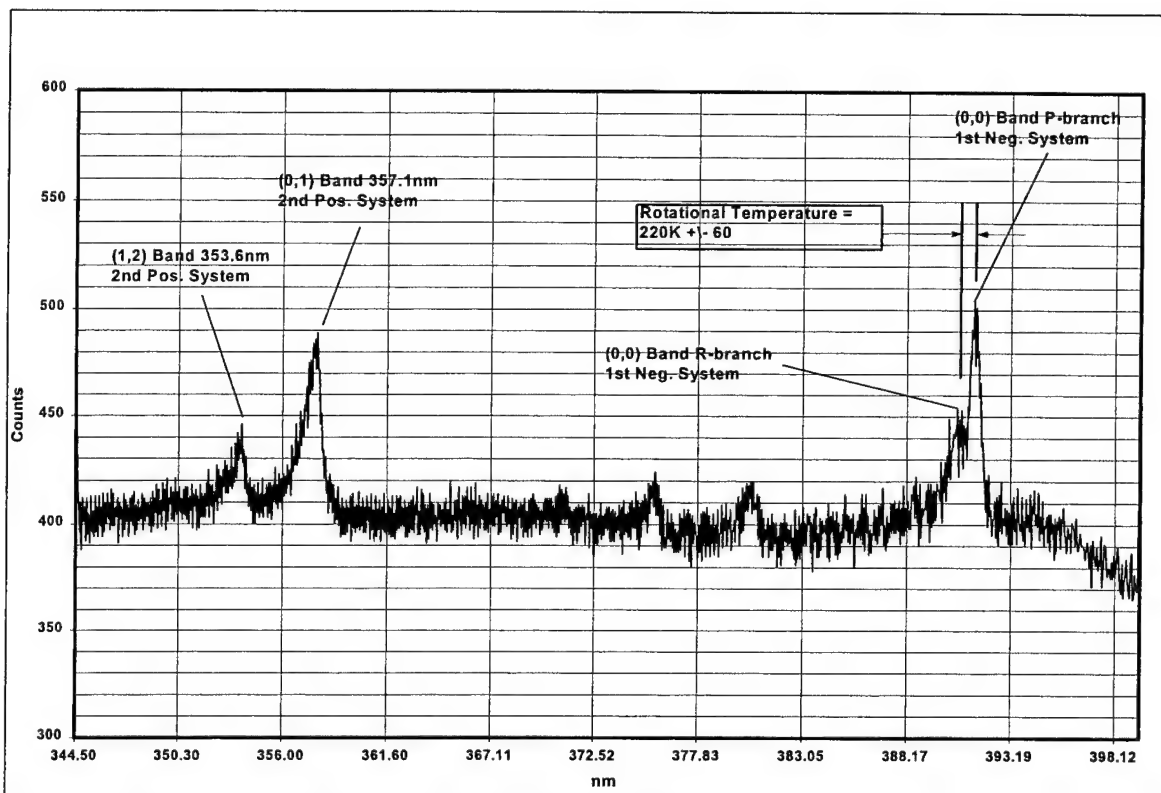
Figure 21: OMA generated spectra for a 5MJ/kg test run for air as driven gas.
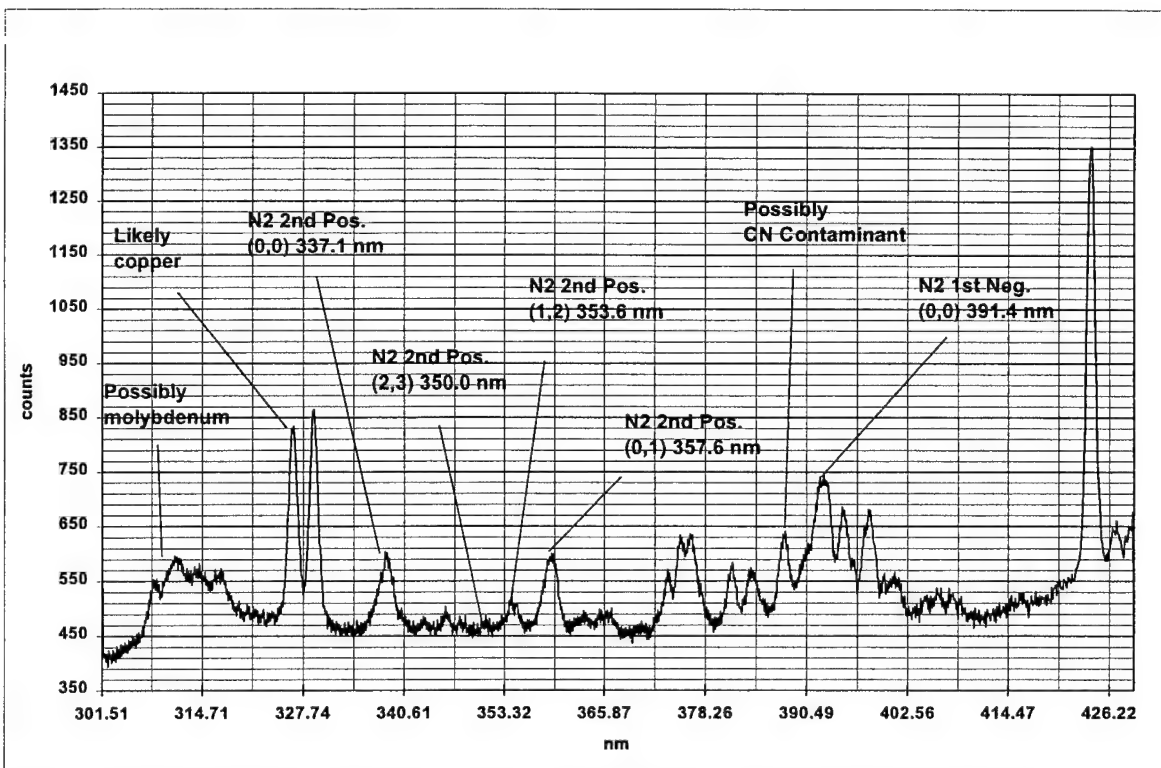
Figure 22: 10MJ/kg enthalpy test run with air as the driven gas. CN signature less intense.
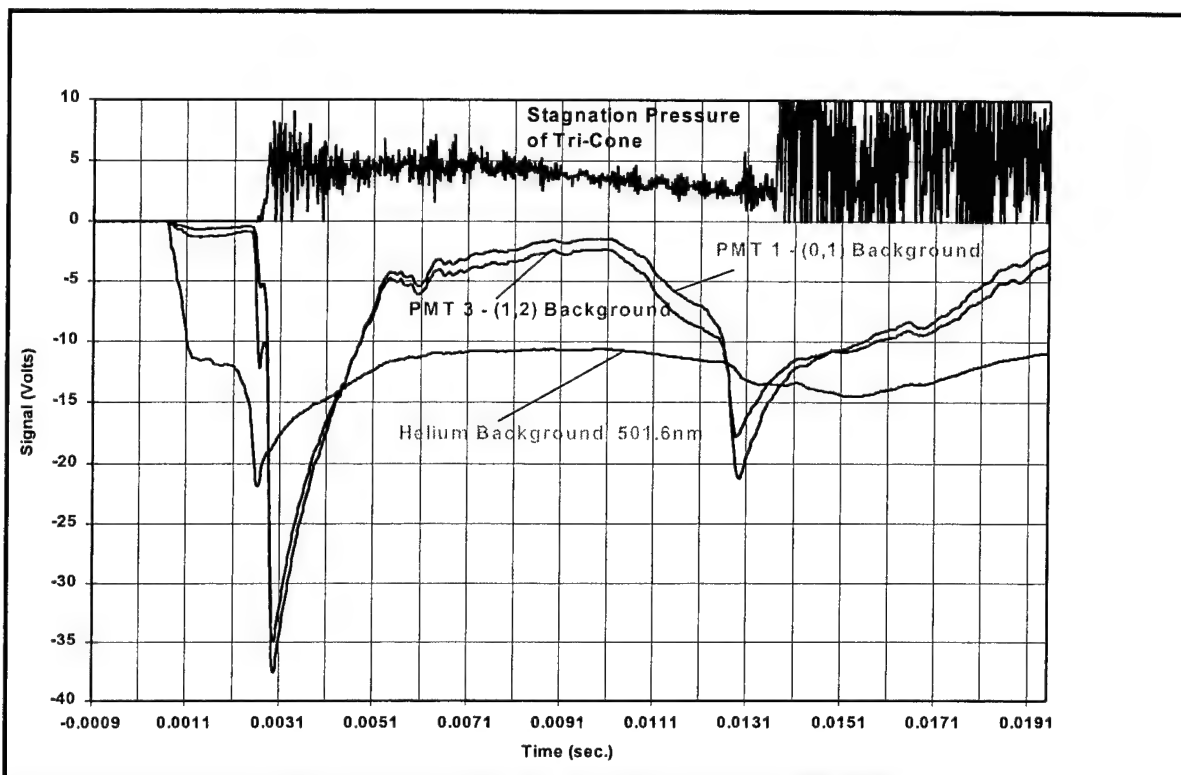
Figure 23: Background light traces for 10MJ/kg enthalpy in LENS freestream.
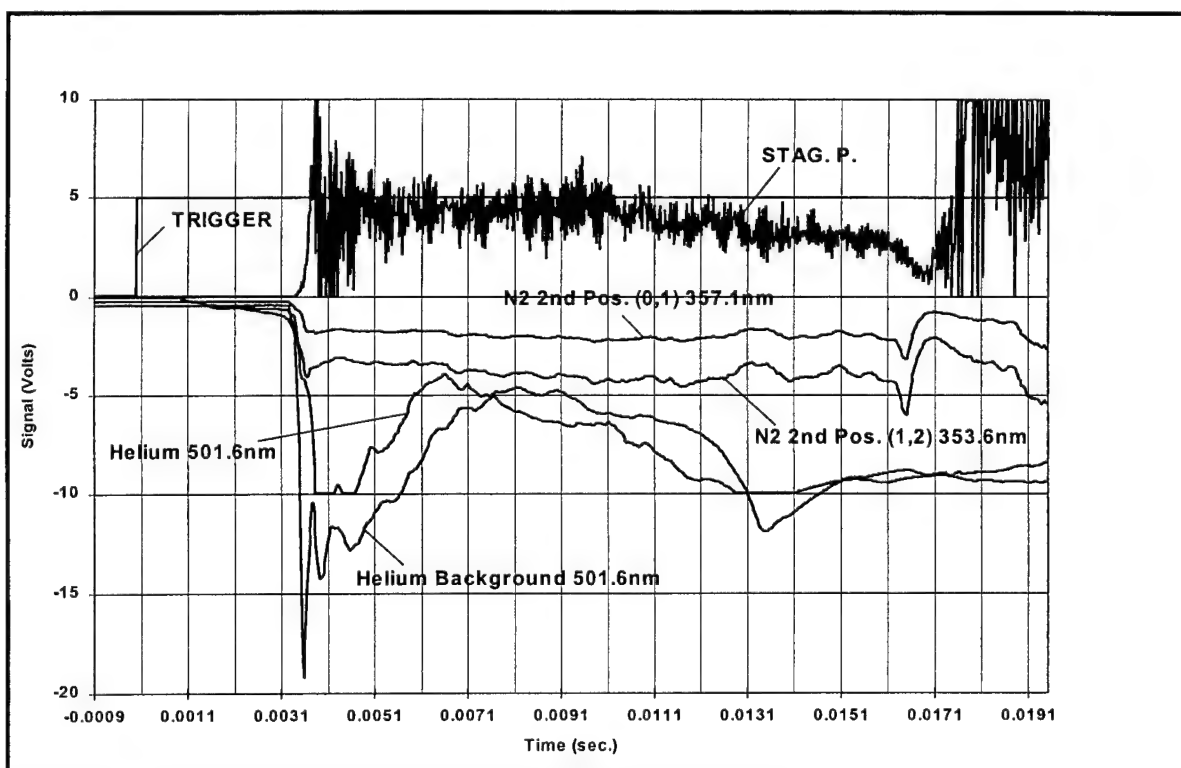
Figure 24: Test run traces for 5MJ/kg enthalpy in LENS freestream.
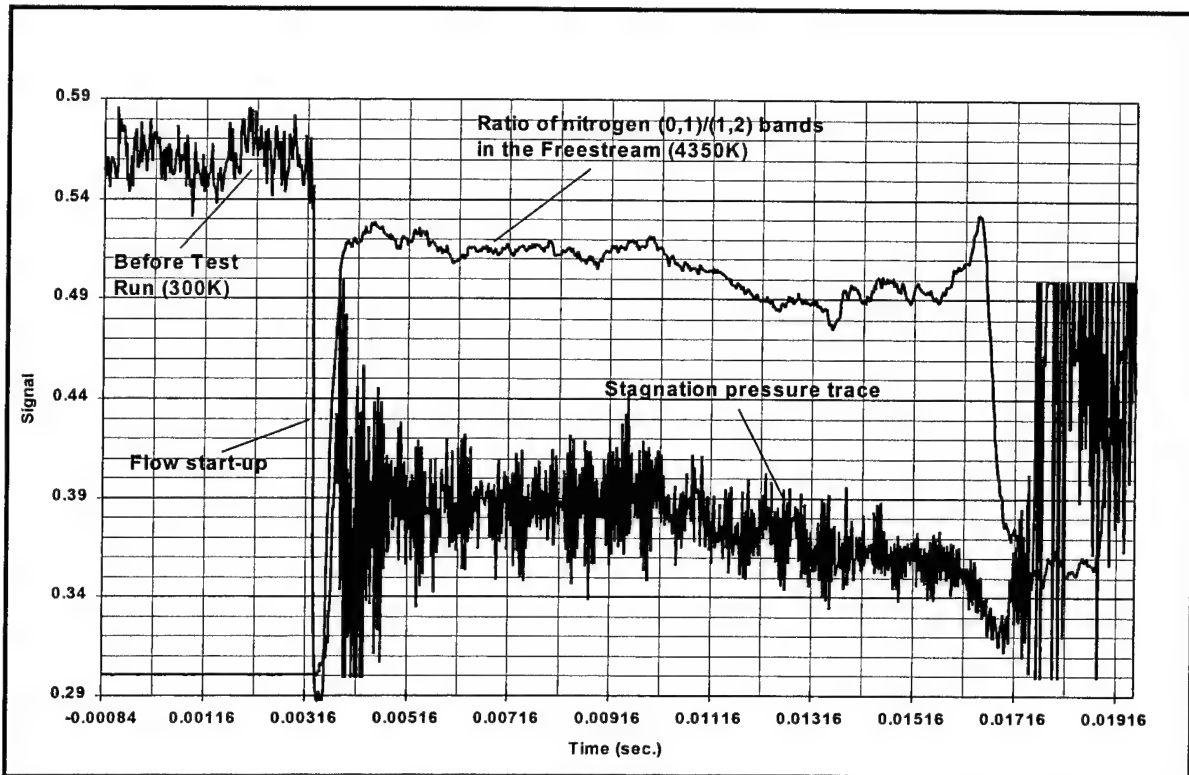
Figure 25: Ratio of (0,1)/(1,2) nitrogen bands for 5MJ/kg enthalpy.
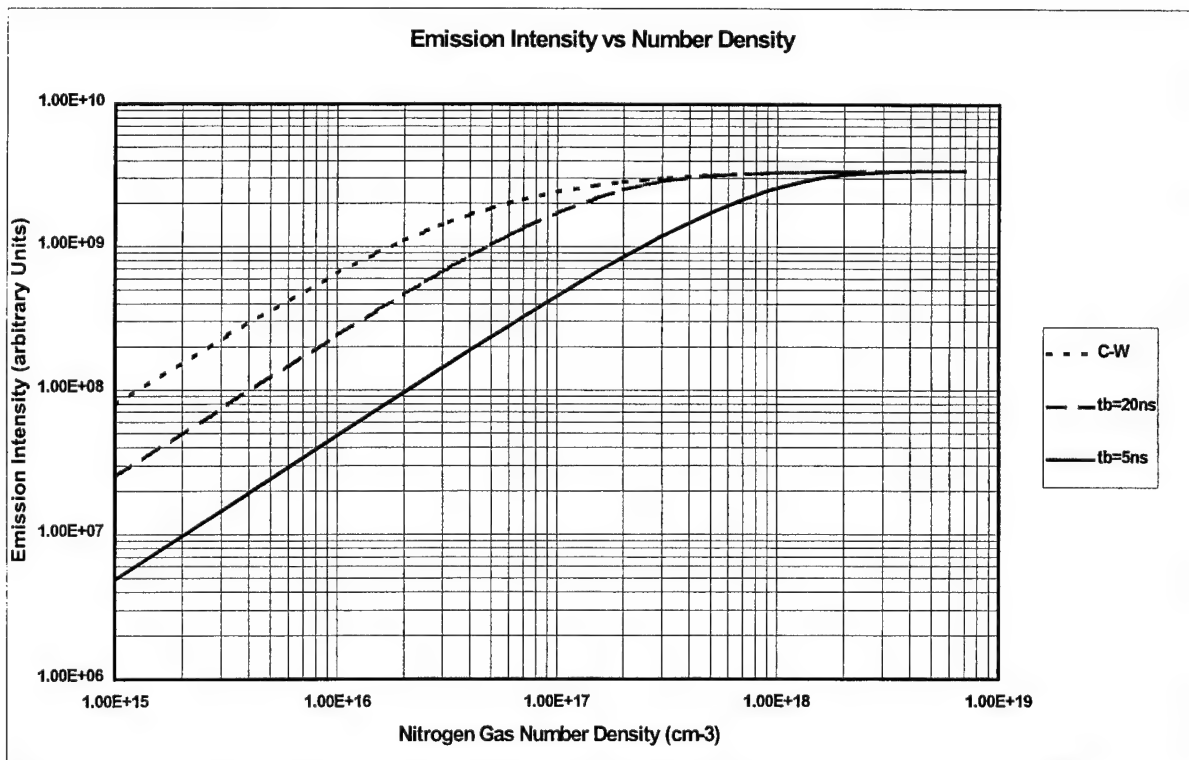
Figure 26: Quenching curves for PEG and CWEG generated beams.
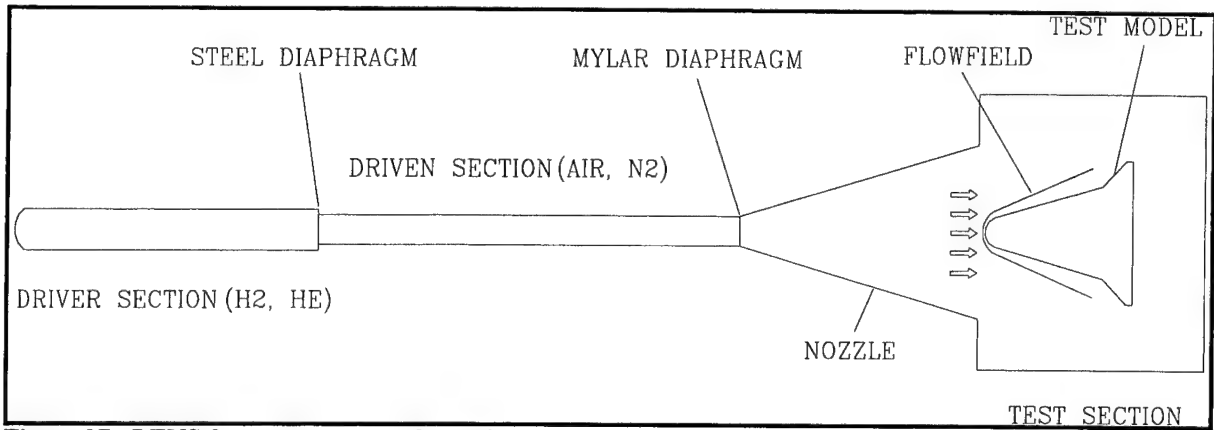
Figure 27: LENS freestream tests schematic.
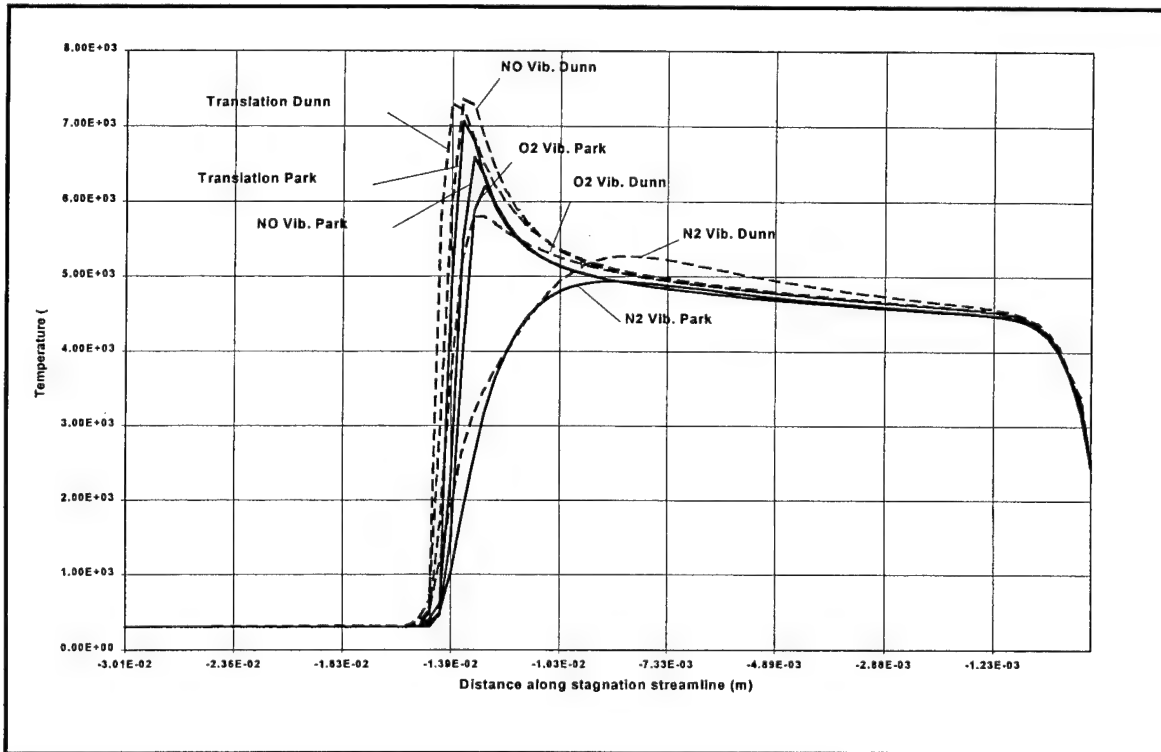
Figure 28: Stagnation streamline temperature profile for 40 km altitude.

195
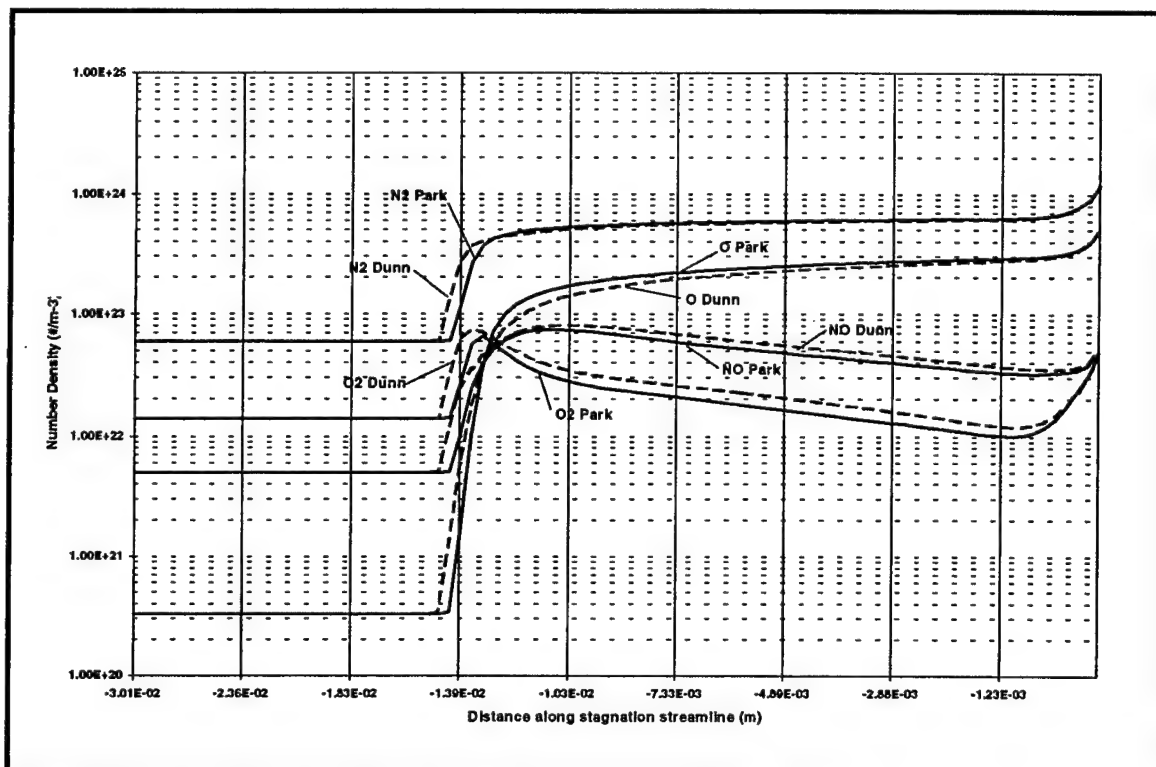
Figure 29: Number densities along stagnation streamline at 40 km altitude.
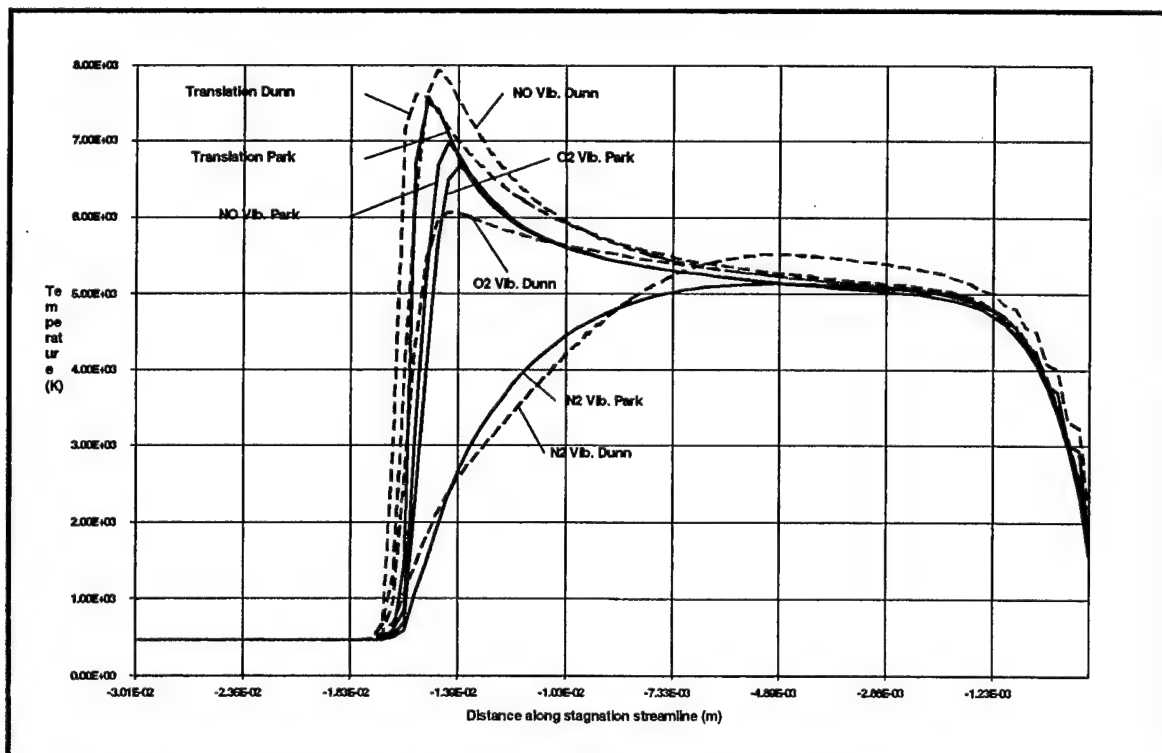
Figure 30: Temperature profile of stagnation streamline at 50km. altitude.

196
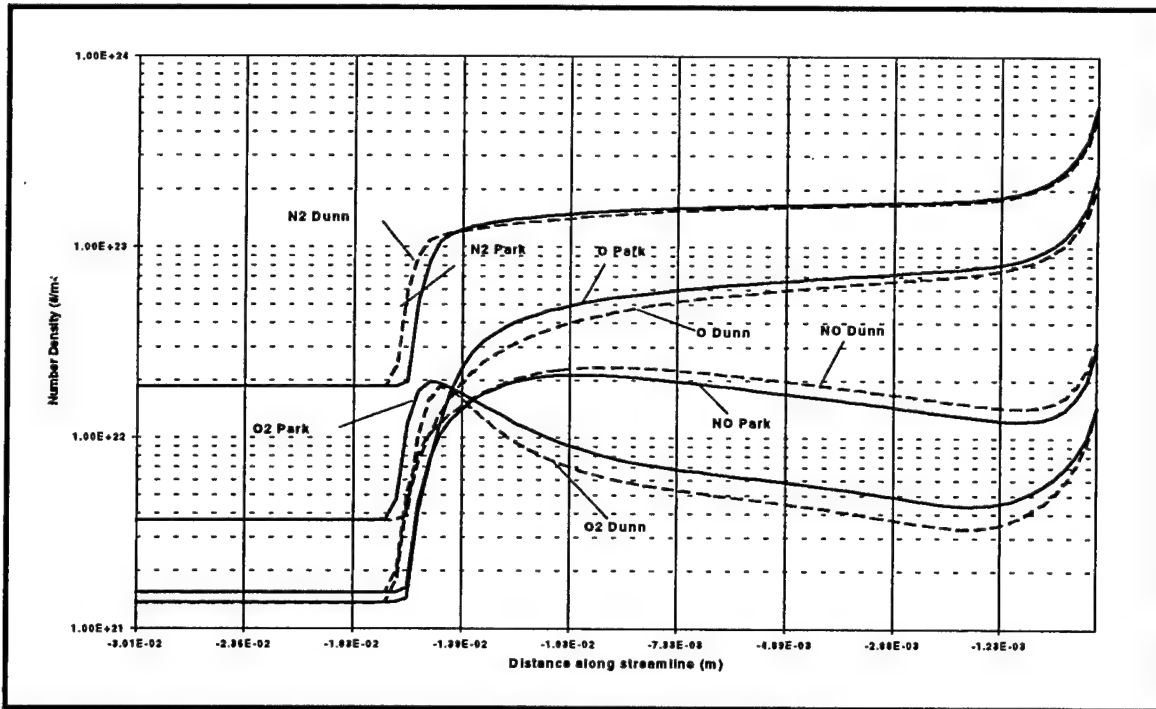
Figure 31: Number densities along stagnation streamline at 50km. altitude.
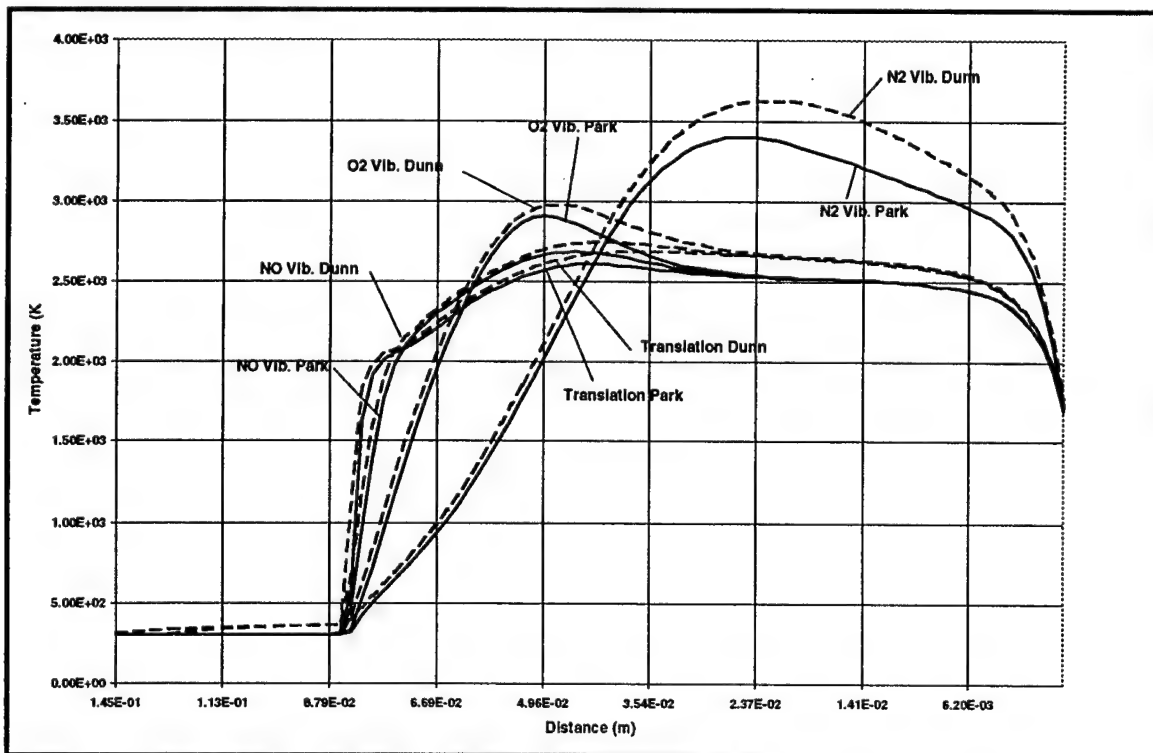
Figure 32: Temperature profiles for station 2 at 40km altitude.

197
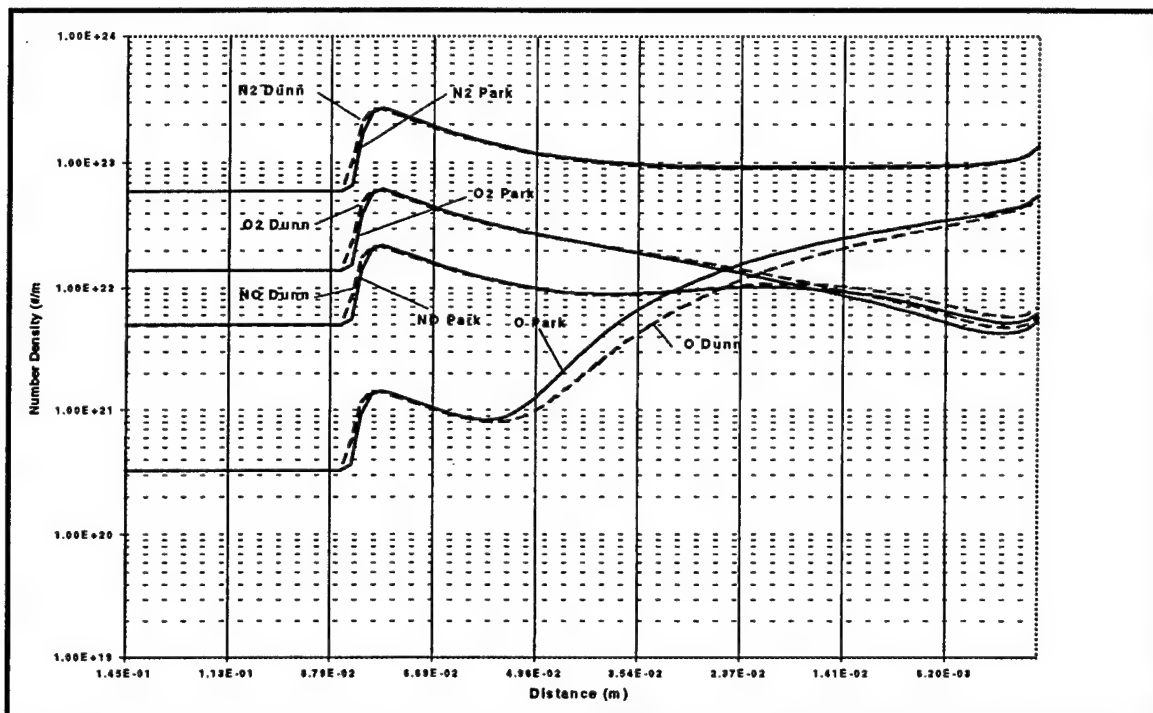
Figure 33: Number density profiles for station 2 at 40km altitude.

REFERENCES

Abel, S. & Muntz, E. P. 1964 The direct measurement of static temperatures in shock tunnel flows. *General Electric Technical Information Series* R64Sd25.

Attix, F., Roesch, W. & Tochilin, E. 1968 Radiation dosimetry. Academic Press Inc., New York, New York.

Baer, D.S., Hanson, R.K., Newfield, M.E., & Gopaul, N.K.L.M. 1994 Multiplexed diode-laser sensor system for simultaneous H_2O, O_2, and temperature measurements. *Opt. Lett.*, **19**, 1900.

Benker, W., Christiansen, J., Frank, K., Gundel, H., Hartmann, W., Redel, T., Stetter, M. 1989 Generation of intense pulsed electron beams by the pseudospark discharge. *IEEE Transactions on Plasma Science*, Vol. 17, No. 5, October.

Bergman, R., private communications, CALSPAN Corp., January, 1997.

Bortz, M.L., Arbore, M.A., & Fejer, M.M. 1993 Quasi-phase-matched optical parametric amplification and oscillation in periodically poled LiNb O_3 waveguides. *Optics Letters,* **20**, 1, 49.

Boutier, A (ed.) 1992 Laser-based diagnostics for Hypersonic flows. *New Trends in Instrumentation for Hypersonic Research*, NATO ASI, Series E-Vol. 224, Kluwer Academic Publishers.

Butefisch, K. A. & Vennemann, D. 1974 The electron-beam technique in hypersonic rarefied gas dynamics. *Progress in Aerospace Science*, **15** (5) 217.

Chang, H. A., Rea, E. C. & Hanson, R. K. 1987 Temperature measurements in shock tubes using a laser-based absorption technique. *Applied Optics*, Vol. 26, No. 5, March.

198

Chang, H.A., Baer, D.S., & Hanson, R.K. 1993 Semiconductor laser diagnostics for simultaneous determination of kinetic and population temperatures in high-enthalpy flows. *Proceedings of the 19th International Symposium on Shock Waves*, Marseilles, France.

Davis, L. & Wilson, J. L. 1969 Influence of reflected shock and boundary-layer interaction on shock-tube flows. *The Physics of Fluids Supplement I.* Shock Tube Symposium.

DiRosa, M.D., Chang, A.Y., & Hanson, R.K. 1993 CW dye laser technique for simultaneous, spatially-resolved measurements of temperature, pressure, and velocity of NO in an underexpanded free jet. *Applied Optics*, **32**, 4074.

Dunn, M. 1996 Nasa's ticket to the 21st century. Article published by the Associated Press.

Dyner, H. B. 1966 Density variation due to reflected shock-boundary-layer interaction. The Physics of Fluids, Vol. 9, No. 5, May.

Frank, K. & Christiansen, J. 1989 The fundamentals of the pseudospark and its applications. *IEEE Transactions on Plasma Science*, Vol. 17, No. 5, October.

Gadamer, E. O. & Schumacher, B. W. 1958 Electron beam fluorescence probe for measuring the local density in a wide field of observation. *Canadian Journal of Physics*, Vol.36.

Gadamer, E. O. 1962 Measurement of the density distribution in a rarefied gas flow using the fluorescence induced by a thin electron beam. University of Toronto Institute of Aerophysics, UTIA Report 83.

Garbuzov, D. Z., et al. 1995 2.7-μm InGaAsSb/AlGaAsSb laser diodes with continuous-wave operation up to -39 °C. *Proc. SPIE*, 2382, 250.

Glick, H. S., Hertzberg, A. & Smith, W. E. 1955 Flow phenomena in starting a hypersonic shock tunnel. *Cornell Aeronautical Laboratory* CAL No. AD-789-A-3.

Gochberg, L. A. 1994 The electron beam fluorescence technique in hypersonic aerothermodynamics. *AIAA* Paper 94-2635, June.

Goodfellow, K. D. 1995 Theoretical investigation of cathode operation in high-power arcjets. *AIAA Paper* 95-3061, July.

Guseva, L. G. 1964 Discharge striking in nonuniform fields at low gas pressures. *Investigations into Electrical Discharges in Gases*, ed. Cossutta, Macmillan, New York.

Hanson, R.K. 1986 Combustion diagnostics: planar imaging techniques. *Twenty-first Combustion symposium (International) on Combustion*, The Combustion Institute 1677.

Hanson, R.K., Baer, D.S., McMillin, B.K., & Arroyo, M.P. 1993 Multi-parameter and multi-point measurements. *International Journal of Physical Chemistry*, July.

Hanson, R.K., Kuntz, P.A., & Kruger, C.H. 1977 High-resolution spectroscopy of combustion gases using a tunable IR diode laser. *Applied Optics*, **16**, 2045.

Hanson, R. K., Seitzman, J. M. & Paul, P. 1990 Planar laser-induced imaging of combustion gases. *Applied Physics B*, **50**, 441.

Hertzberg, A., Wittcliff, C. E. & Hall, J. G. 1962 Development of the shock tunnel and its application to hypersonic flight. Hypersonic Flow Research, *Progress in Astronautics and Rocketry*, Vol. 7.

Herzberg, G. 1950 Spectra of diatomic molecules. Van Nostrand Reinhold Company Inc., Scarborough, Ontario, Canada.

Hiller, B. & Hanson, R. K. 1988 Simultaneous planar measurements of velocity and pressure fields in gas flows using laser-induced fluorescence. *Applied Optics*, Vol. 27, No. 1, January.

Ivanov, M., Gimelshein, S., Kashkovsky, A. & Markelov, G. 1993 Influence of real gas effects on control surfaces efficiency at high altitudes. AIAA Paper 93-5116, November.

Lee, M. P., McMillin, B. K. & Hanson, R. K. 1993 Temperature measurements in gases by use of planar laser-induced fluorescence imaging of NO. *Applied Optics*, Vol. 32, No. 27, September.

Lin, B. & Chow, Q. 1995 Breakdown voltages of pseudospark in He, A, and N_2 . *IEEE Transactions on Plasma Science*, Vol. 32, No. 3, June.

Liu, C. J. & Rhee, M. J. 1995 Experimental investigation of breakdown voltage characteristics of single-gap and multigap pseudosparks. *IEEE Transactions on Plasma Science*, Vol. 23, No. 3, June.

Lutfy, F. & Muntz, E.P. 1995 Initial calibration of a pulsed electron gun for hypersonic flow diagnostics. *AIAA* Paper 95-0292, January.

Lutfy, F. & Muntz, E.P. 1996 Calibration of a second generation pulsed electron gun for hypersonic flow diagnostics. *AIAA* paper 96-0178, January.

Maguire, B. L., Muntz, E. P. & Thomas, K. M. 1972 Simultaneous measurement of density and temperature fluctuations in a hypersonic wake. *AIAA* paper 72-118.

McCaa, D. J. & Rothe, D. E. 1968 Paper presented at Symposium on Molecular Structure and Spectroscopy, September.

McMillin, B. K., Lee, M. P. & Hanson, R. K. 1992 Planar laser-induced fluorescence imaging of shock tube flows with vibrational nonequilibrium. *AIAA Journal*, Vol. 30, No. 2, February.

McMillin, B.K., et al. 1993 Temporally resolved, two-line fluorescence imaging of NO temperature in a transverse jet in a supersonic cross flow. *Applied Optics,* **32**, 7532-45.

Mihalcea, R., Baer, D.S., & Hanson, R.K. 1996a Tunable diode laser measurements of NO_2 near 670 nm and 395 nm. *Applied Optics*, **35**, 21, 4059.

Mihalcea, R., Furlong, E.R., Baer, D.S., & Hanson, R.K. 1996b Multiplexed diode-laser absorption sensors for combustion monitoring. *Air & Waste Management Association Fifth International Symposium on Optical Sensing for Environmental and Process Monitoring,* Dallas, TX, November 6-8.

Miller, R. B. An introduction to the physics of charged particle beams. Plenum Press, New York, New York

Muntz, E. P. & Abel, S. J. 1964 The direct measurement of static temperature in shock tunnel flows. *Third Hypervelocity Techniques Symposium.*

Muntz, E. P. & Erwin, D. A. 1993 Rapid pulse electron beam fluorescence for flow field diagnostics. *New Trends in Instrumentation for Hypersonic Research*, ed. A. Boutier, p.265, NATO ASI Series, Series E: Applied Sciences, Vol. 21, Kluwer, Dodrecht.

Muntz, E. P. & Lutfy, F. M. 1996 The study of reacting, high energy flows using pulsed electron-beam fluorescence. *AIAA* Paper 96-1986, June.

Muntz, E. P. & Marsden, D. J. 1963 Electron excitation applied to the experimental investigation of rarefied gas flows. *Rarefied Gas Dynamics*, Vol. II, ed. J. A. Laurmann.

Muntz, E. P. & Softley, E. J. 1966 A study of laminar near wakes. *AIAA J.* 6, 961.

Muntz, E. P. 1968 The electron beam fluorescence technique. AGARDograph 132, December.

Muntz, E. P. 1981a Measurement of density by analysis of electron beam excited radiation. *Methods of Experimental Physics*, ed. R. J. Emrich, 434, Academic.

Muntz, E. P. 1981b Measurement of temperature by analysis of electron beam excited emissions. *Methods of Experimental Physics*, ed. R. J. Emrich, 489, Academic.

Muntz, E. P., Abel, S. J. & Maguire, B. L. 1965 The electron beam fluorescence probe in experimental gas dynamics. *IEEE Transactions on Aerospace*.

Muntz, E. P., Kunc, J. A. & Erwin, D. A. 1987 A pulsed electron-photon fluorescence technique for temperature and specie concentration measurement at points in relatively dense, unseeded air flows. *AIAA Paper* 87-1526, June.

Petrie, S. L. & Komar, J. J. 1972 Application of the electron beam fluorescence technique to the measurement of the properties of nitric oxide in nonequilibrium flows. *Air Force Flight Dynamics Laboratory* AFFDL-TR-72-144.

Petrie, S. L. 1966 Electron beam diagnostics. *AIAA* paper 66-747.

Petrie, S. L. 1968 Boundary layer studies in an arc-heated wind tunnel. *Ohio State University* R. F. Project 2033.

Philippe, L. & Hanson, R.K. 1991 Laser-absorption mass flux sensor for high-speed air flows. *Optics Letters,* **16**, 24, 2002.

Rhee, M. J. & Ding, B. N. 1992 Breakdown voltage characteristic of a pseudospark device. *The Physics of Fluids B*, Vol. 4, 764.

Rothe, D. E. & McCaa D. J. 1968 Emission spectra of molecular gases excited by 10keV electrons. *Cornell Aeronautical Laboratory* CAL No. 165.

Schilling, J., Pobst, J. & Erwin, D. 1993 The Use of pulsed electron beam fluorescence for arcjet plume diagnostics. *International Electric Propulsion Conference* Paper 93-130, September.

Schumaker, B. W. & Gadamer, E. O. 1958 Electron beam fluorescence probe for measuring the local gas density in a wide field of observation. *Canadian Journal of Physics* 36, 659.

Sebacher, D. I. & Duckett, R. J. 1964 A spectrographic analysis of a 1-foot hypersonic-arc-tunnel airstream using an electron beam probe. *NASA* TR R-114.

Sebacher, D. I. 1966 An electron beam study of vibrational and rotational relaxing flows of nitrogen and air. *Proceedings of the 1966 Heat Transfer and Fluid Mechanics Institute.* ed. M. A. Saad and J. A. Miller, Stanford University Press.

Spores, R. A., Hargus, W. A., Pobst, J. A., Schilling, J. H., Lutfy, F. M. & Erwin, D. A. 1994 Arcjet diagnostics for measuring velocity, density and temperature. *AIAA Paper* 94-2464, June.

Sweetman, B. 1993 Aurora. *Motorbooks International Publishers,* Osceola, WI.

Taylor, J. W. 1967 Jane's all the world's aircraft. McGraw-Hill Book Company, New York, New York.

"Thyratrons For Laser Applications - Users Guide", EG&G Publications & Media Center, Waltham, Massachusetts.

Wallace, J. E. 1968 Hypersonic turbulent boundary layer measurements using an electron beam. *Cornell Aeronautical Laboratory* CAL No. AN-2112-Y-1.

Wittcliff, C. E., Wilson, M. E. & Hertzberg, A. 1959 The tailored-interface hypersonic shock tunnel. *Journal of the Aero/Space Sciences*, April.

York, P. 1996 David Sarnoff Research Center, private communication.

York, P. et al. 1995 Recent Advances in III-V Diode Lasers for mid-infrared, single mode, continuously tunable laser operation. *AWMA/SPIE Optical Remote Sensing for Environmental and Process Monitoring*, September

Appendix II-1
PUBLICATIONS

Hanson, R.K., "Invited Paper", at AIAA 35th Aerospace Sciences Meeting, Reno, NV, January 1997.

Hanson, R.K., "Optical Diagnostics for Ground Testing", invites plenary paper at AIAA 19th Advanced Measurement and Ground Testing Technology Conference, New Orleans, LA, June 17-20, 1996.

Houwing, A.F.P., Kamel, M.R., Morris, C.I., Wehe, S.D., Boyce, R.R., Thurber, M.C., Hanson, R.K., "PLIG Imaging and Thermometry of NO/N_2 Shock Layer Flows in an Expansion Tube", AIAA-96-0537 at 34th Aerospace Sciences Meeting, Reno, NV, January 18, 1996.

Houwing, A.F.P., Palmer, J.L., Boyce, R.R., Thurber, M.C., Wehe, S.D., Hanson, R.K., "PLIF Imaging and Thermometry of NO/N_2 Shock Layer Flows in an Expansion Tube", presented at AIAA 34th Aerospace Sciences Meeting, Reno, NV, 1996.

Houwing, A.F.P., Palmer, J.L., Boyce, R.R., Thurber, M.C., Wehe, S.D., Hanson, R.K., "PLIF Thermometry in a High Temperature Shock Layer Flow on a Cylinder in a Supersonic Jet", AIAA-95-0515, 33rd Aerospace Sciences Meeting, Reno, NV, 1995.

Kamel, M.R., Morris, C.I., Hanson, R.K., "Simultaneous PLIF and Schlieren Imaging of Hypersonic Reactive Flows Around Blunted Bodies", presented at AIAA 35th Aerospace Sciences Meeting, Reno, NV, January 1997.

Kamel, M.R., Morris, C.I., Thurber, M.C., Wehe, S.D., Hanson, R.K, "Development of an Expansion Tube for Investigation of Combustion in Supersonic Projectile Flowfields", AIAA-95-2717, 31st Joint Propulsion Conference, San Diego, CA, 1995.

Kamel, M.R., Morris, C.I., Thurber, M.C., Wehe, S.D., Hanson, R.K., "New Expansion Tube Facility for the Investigation of Hypersonic Reactive Flow", AIAA-95-0233, 33rd Aerospace Sciences Meeting, Reno, NV, 1995.

Lutfy, F. & Muntz, E.P., "Calibration of a second generation pulsed electron gun for hypersonic flow diagnostics", AIAA-96-0178, presented at the 34th Aerospace Sciences Meeting, Reno, NV, January 1996.

Lutfy, F. M., Muntz, E.P., "CW electron gun measurement of vibrational and rotational populations, number density and contaminants in hypervelocity flows", paper to be presented at the 17th International Congress on Instrumentation in Aerospace Simulation Facilities (ICIASF), Monterey, CA, September 29-October 2, 1997.

Lutfy, F. & Muntz, E.P., "Initial Calibration of a Pulsed Electron Gun for Hypersonic Flow Diagnostics", AIAA-95-0292, San Diego, CA, June 1995.

Muntz, E.P., Boyd, Iain, Ketsdever, Andrew, "Rarefied Flow Testing in the 1990s: Measuring Those Phenomena that are Difficult to Calculate", AIAA-95-2631.

Muntz, E.P., Lutfy, F.M., Boyd, I.D., "The Study of Reacting High Energy Flows Using Pulsed Electron-Beam Fluorescence", AIAA-96-1986.

Nagali, V., Chou, S.I., Baer, D.S., Hanson, R.K., "Measurements of H_2O and Temperature in High-Pressure Environments using Near-IR Diode-Laser Absorption", AIAA-26-2225 at AIAA 19th Advanced Measurement and Ground Testing Technology Conference, New Orleans, LA, June 17-20, 1996.

Palmer, J.L., Houwing, A.F.P., Thurber, M.C., Wehe, S.D., Hanson, R.K, "PLIF Imaging of Transient Shock Phenomena in Hypersonic Flows", AIAA-94-2642, 30th Joint Propulsion Conference, Colorado Springs, CO, 1994.

Toshimitsu, K., Matsuo, A., Kamel, M.R., Morris, C.I., Hanson, R.K., "Comparison of CFD Calculations with PLIF Imaging Results of Hypersonic Flow Around Projectiles", presented at AIAA 35th Aerospace Sciences Meeting, Reno, NV, January 1997.

Wehe, S.D., Baer, D.S., Hanson, R.K., "Tunable Diode-Laser Absorption Measurements of Temperature, Velocity, and H_2O in Hypersonic Flows", AIAA-97-3267, at the 33rd Joint Propulsion Conference, Seattle, WA, July 1997.

SECTION III

FLOW FIELD ANALYSIS

This section authored by

I.D. Boyd

III.1 CONTINUUM COMPUTATIONS

A continuum code that solved the Navier-Stokes equations with coupled thermomechanical nonequilibrium was employed. In order to validate this code, it was applied to a flow over a planetary probe geometry that has been tested experimentally in LENS. Measurements of heat transfer and pressure coefficient along the surface of the body were obtained. Comparisons of the numerical results with the data gave generally good agreement (see Table 1, p 204a).

Studies for the design of interesting experiments in the LENS facility were completed. The investigations focused on a spherically capped cone geometry. Parametric studies of variation in cone angles, free stream velocity, and free stream density have been conducted. These revealed that a variety of physically interesting processes can be generated in LENS. These include: thermal equilibrium; thermal non-equilibrium where the transitional temperature exceeds the vibrational temperature; thermal non-equilibrium where the vibrational temperature exceeds the transitional temperature; chemical equilibrium; chemical non-equilibrium involving recombination (see Table 1, p 204a).

The results of the study suggested that experiments should be performed on a 10-15 degree cone, at free stream densities corresponding to the altitudes of 30, 40, and 50 km, and at free stream velocities of 3, 3.5, and 4 km/sec.

III.2 PARTICLE COMPUTATIONS

The direct simulation Monte Carlo method (DSMC) was also being applied to flows in LENS. A low density condition was tested experimentally for flow over the planetary probe geometry. Generally, the flows in LENS are in the near-continuum flow regime, which makes DSMC calculation numerically intensive. To address this issue, a new DSMC algorithm was developed for implementation on the IBM SP-2 parallel computer. The new data structure keeps information highly localized and used domain decomposition. A simulation was performed that used 100 million particles on 400 nodes of the BM SP-2 at Cornell Theory Center, probably the largest DSMC ever performed. Under these conditions, a parallel efficiency of 90% was attained. The code achieved a performance equivalent to 75 single processors of a Cray C90 vector supercomputer.

To verify the new DSMC code, it was applied to the planetary probe flow. Comparison was made with the measurements of heat transfer and pressure coefficients obtained in LENS. Generally, very good agreement was obtained (see Table 1, p 204a).

Use of Cornell Calculations

Section	Page	Subject
2.4.1	14	Navier-Stokes and DSMC
2.4.2	15	measure of heat transfer
2.4.3	16	Navier-Stokes
2.4.4	16	Navier-Stokes/DSMC hybrid
2.5	17	Conclusions
3.2.1	41	Blunted cone/flare
3.2.3.2	44	Blunted cone/flare
3.3.3.2	47	Pressure and heat transfer
3.3.3.3	47	Preliminary Navier-Stokes
3.3.3.3	47	Flowfield properties, Navier-Stokes
3.4	49	Shock layer nonequilibrium
4.2.2.1	74	Navier-Stokes, measure of heat transfer Figs. 3-34a,b
4.2.2.2	74	Blunted cone/flare
4.3.2	75, 76	Navier-Stokes, DSMC, Navier-Stokes/DSMC
5.2.2.2	103	Navier-Stokes flowfield
5.2.3.2	106	Navier-Stokes rotational temperature
5.2.3.3	109, 110	Vibrational temperature
5.2.3.5	111	Summary

Table 1. Use of Cornell (I.Boyd) calculations (DSMC, Navier-Stokes, Hybrid Navier-Stokes/DSMC)

Appendix III-1
PUBLICATIONS

Boyd, I.D., Kannenberg, K.C., and Dietrich, S., "Parallel DSMC Computation of Planetary Probe Flow Using an Adapted Unstructured Grid", in Aerothermodynamics for Space Vehicles and High-Velocity Flow Data Base, edited by W. Berry, J.A. Desideri, F. Grasso, J. Muylaert, and J. Periaux, Wiley, 1996 (in press).

Boyd, I.D., "Simulation of the SR3 Experiment Using a Vectorized DSMC Code", Fourth European High-Velocity Database Workshop, ESTEC, Noordwijk, The Netherlands, Nov. 1994.

Dietrich, S. and Boyd, I.D., "Parallel Implementation on the IBM SP-2 of the Direct Simulation Monte Carlo Method", AIAA Paper No. 95-2029, San Diego, CA, June 1995.

Srinivasan, A. and Boyd, I.D., "Design of Thermochemical Non-equilibrium Experiments for the LENS Hypersonic Facility", AIAA Paper No. 95-2006, San Diego, CA, June 1995.

Boyd, I.D., Srinivasan, A., Muntz, E.P., Hanson, R.K., and Holden, M.S., "Thermochemical Non-equilibrium Design Calculations for Detailed Hypervelocity Experiments in the LENS Facility", AIAA Paper No. 94-2097.

Section IV.
TRANSITION PROBABILITIES AND VISCOSITIES
This section authored by
J. A. Kunc

Abstract

The main goals of this part of the program were: 1) to obtain the state-to-state transition probabilities for molecular collisions (with the molecules in arbitrary vibrational-rotational states) resulting in vibration-translation (V-T) and vibration-vibration (V-V) exchange, and 2) to provide a general, comprehensive study of the effect of dissociation on the viscosity of high-temperature gases.

1. Dynamics of the V-T and V-V transitions is of fundamental importance in high-enthalpy flows because the vibrational excitation of molecules can cause serious imbalance in the distrubution of energy among the translational and internal modes of the gas molecules. In addition, vibrational excitation plays a crucial role in the efficiency of dissociation and of many chemical reactions. Therefore, this part of the program is devoted to evaluation of computationally efficient, preferably analytical, expressions for the cross sections and transition probabilities for the V-T and V-V processes defined above.

The initial and second phases of this part of the program have already been completed; see the Appendix. The initial phase resulted in analytical temperature-dependent first-order perturbation theory expressions for V-T transitions in collisions of oxygen and nitrogen molecules, while the second phase resulted in analytical energy-dependent infinite-order perturbation theory expressions for V-T transitions. The results obtained encourage the development of an approach yielding the transition probabilities for both the temperature-dependent and energy-dependent V-V transition probabilities in atmospheric gases such as nitrogen and oxygen. This development was the subject of the final part of the program. The approach was based on the same infinite-order perturbation scattering theory, because preliminary results indicated that this approach would lead to analytical V-V transition probabilities (see Ref. [1]).

2. Investigation of momentum transfer in dissociating gases is of primary importance for the physics of supersonic and hypersonic flows because the temperatures in these flows are usually high enough to cause significant dissociation. Theoretical models of the momentum transfer in dissociating gases are of special interest for description of the transport properties (viscosity, conductivity, and diffusion coefficient) in high-enthalpy flows because of the experimental difficulties involved in measuring these properties at high temperatures. Therefore, part of this program focuses on modeling of the transport of momentum and energy in high-temperature gases with significant dissociation.

The initial phases of this research, resulting in a study of the impact of dissociation on the viscosity of high-temperature iodine vapor, suggested that the impact of dissociation in other gases can also be profound. Therefore, significant effort was devoted to a general study of the viscosity of dissociating diatomic gases, especially atmospheric gases such as nitrogen and oxygen.

Theoretical work on high-temperature gas properties by Kunc and his collaborators has provided new insight into the viscosity of dissociating gases [6]; the effects of vibrational and rotational excitation on the diameters of high-temperature gas molecules has also been studied [7]. Finally, a new generalized hard-sphere interaction model has been formulated, which is of use in direct simulation Monte Carlo (DSMC) simulations of reacting gas flows [8]. Prof. Kunc has also pursued collisional vibration and dissociation probabilities between colliding diatomic molecules and atoms, for specific vibrational levels. One of his students,

206

R. Holbrook, has developed a technique for efficiently calculating dissociative collisions between homonuclear diatomic molecules in arbitrary vibrational states.

1   Introduction

Properties of rotationally and vibrationally excited diatomic molecules are of significant importance in studies of dissociation, chemical reactions, and rotation-vibration, vibration-vibration and vibration-translation transitions in high-temperature gases in material and plasma processing, supersonic and hypersonic flows, light sources and environmental studies. The properties depend on intramolecular potentials of the molecules, and many analytical expressions for the potentials have been proposed in literature (see Ref. [1] (hereafter called Paper I) and references therein). One of the most accurate of these potentials for vibrating and rotating diatomic molecules is the potential resulting from superposition of the Tietz-Hua potential[2, 3] (representing the 'vibrational' part of the atom-atom interaction in the molecules) and the centrifugal stretching term representing the 'rotational' part of the interaction. (The model of molecular rotational-vibrational motion driven by such intramolecular potential is called hereafter *the rotating Tietz-Hua oscillator*). However, the most commonly used intramolecular potential is a superposition of the Morse potential and the molecular centrifugal energy; the corresponding model of diatomic molecule is called *the rotating Morse oscillator*. The popularity of the latter model results from the fact that its rotational-vibrational energies $E_{v,J}$ can be given as a series expansion, and that the truncated form of the expansion (given in Eq.(2)) is very simple[4]. However, it is well known (see discussion in Paper I) that the truncated expansion has poor accuracy at moderate and high vibrational and rotational quantum numbers.

In Paper I we applied the Hamilton-Jacoby and the Bohr-Sommerfeld quantization rule[5] to the rotating Tietz-Hua oscillator and obtained expressions for rotational-vibrational levels which are much more realistic (when tested against the RKR (Rydberg-Klein-Rees) and *ab initio* calculations) at moderate and high quantum numbers than the corresponding levels obtained from equation (2). The main goal of this work is to derive, applying the approach of Paper I to the rotating Morse oscillator, energy expressions which are easy to use and highly accurate in the entire range of the vibrational and rotational quantum numbers of the O_2, N_2, NO and CO molecules in their ground electronic states. We focus in this work on these four molecules because of their importance in environmental, plasma processing and high-energy flow research and because the approach of Paper I is very accurate in the case of these molecules. (The approach of this work can also be applied to diatomic molecules other than the O_2, N_2, NO and CO, but in some diatomics the mathematical simplifications and physical approximations made in the approach may lead to less accurate energy levels than those obtained in this work).

We discuss below three expressions for rotational-vibrational levels of the four diatomic molecules under consideration. The first expression (representing our model A of molecular rotational-vibrational motion) is the truncated series expansion solution of the Schrödinger equation for the rotating Morse oscillator. The second expression is a relationship obtained from applying the approach of Paper I to the rotating Tietz-Hua oscillator (model B), and the third expression, the main result of this work, is obtained from applying the approach to the rotating Morse oscillator (model C).

2 Rotational-vibrational levels

2.1 Model A

In the model A, the intramolecular potential of the rotating oscillator representing diatomic molecule is

$$V_{ef}^A(R) = D \left[1 - e^{-\beta(R-R_e)} \right]^2 + \frac{L^2}{2\mu R^2}, \tag{1}$$

where D is the well-depth of the potential, R_e is the molecular bond length, R is the internuclear distance, β is the Morse constant, μ is the reduced mass and L is the angular momentum of the molecule. The first part of the sum in relationship (1) is the potential energy (the Morse potential) of the rotationless molecule, and the second part is the centrifugal energy of the rotating molecule (the rotating Morse oscillator).

The rotational-vibrational energies obtained from solution of the Schrödinger equation for diatomic molecule driven by the potential (1) can be given as a series expansion, and the most common (truncated) form of the expansion is[4],

$$E_{v,J}^A = \omega_e(v + \frac{1}{2}) - \omega_e x_e(v + \frac{1}{2})^2 + B_e J(1 + J) - D_e J^2(1 + J)^2, \tag{2}$$

where ω_e, $\omega_e x_e$, B_e and D_e are the usual spectroscopic constants, and J and v are the molecular rotational and vibrational quantum numbers, respectively. As mentioned earlier, equation (2) is inaccurate in diatomic molecules with moderate and high values of the rotational and vibrational quantum numbers.

Even though more accurate (higher-order) expansions of the solution of the Schrödinger equation for diatomic molecule have been discussed in literature, the expression (2) is the most common in applications (this is the main reason (see Paper I) why we compare below this expression (instead of a higher-order expansion) with the results of the present work). The popularity of the expression (2) results from the fact that the expression is simple and it predicts quite accurate values of the weakly-excited rotational-vibrational levels of diatomic molecules, and that reliable values of the molecular spectroscopic constants ω_e and $\omega_e x_e$ are available in literature (most of the other constants in the higher-order expansion representing the rotational-vibrational energies of the Morse oscillator are not available in literature, and calculation of their accurate values is not trivial).

One should also add that the vibrational constants of the Morse oscillator are:

$$\omega_e = \beta \left[\frac{D}{2\pi^2 c^2 \mu} \right]^{1/2}, \tag{3}$$

and

$$\omega_e x_e = \frac{h\beta^2}{8\pi^2 c\mu}, \tag{4}$$

where ω_e and $\omega_e x_e$ are in cm^{-1} and the rest of the quantities are in units of the c.g.s. system. However, it should be kept in mind that the constant β obtained from the expression (3) will differ from that resulting from the expression (4) if the spectroscopic constants ω_e, $\omega_e x_e$ and

D are taken as 'the best available in literature' because the latter constants (typically, the constants are obtained from measurements and *ab initio* calculations) are not consistent with the model of the Morse oscillator. In the present work we calculate β from the relationship (3) because the constants ω_e and D are usually more accurate than the constants $\omega_e x_e$. The anharmonicity constants $\omega_e x_e$ used in the present calculations (see Table I) are the 'best available in literature'.

2.2 Model B

The model B of the rotational-vibrational motion of diatomic molecule is based on a semi-classical formalism combining the Hamilton-Jacoby theory and the Bohr-Sommerfeld quantization rule (Paper I). The model (the rotating Tietz-Hua oscillator) assumes that the internuclear potential of diatomic molecule is:

$$V_{ef}^B(R) = D\left[\frac{1 - e^{-b_h(R-R_e)}}{1 - c_h e^{-b_h(R-R_e)}}\right]^2 + \frac{L^2}{2\mu R^2},\tag{5}$$

where c_h is an optimization parameter (see Table I) discussed in Paper I, and

$$b_h = \beta(1 - c_h).\tag{6}$$

The first part of the sum (5) is the potential energy of the rotationless oscillator (the Tietz-Hua potential), and the second part is, as in the case of the rotating Morse oscillator, the molecular centrifugal energy.

The approach of Paper I leads to the following expression for the rotational-vibrational energies of diatomic molecules according to the model of the rotating Tietz-Hua oscillator with the nomenclature following conventional spectroscopic convention, but also provided in Paper I:

$$E_{v,J}^B = D + L^2 B_J B_J'' - \left(F_o x_1 - F_1'' - F_2'' L^2 - F_3''' L^4\right)^2,\tag{7}$$

where

$$B_J = \frac{\omega_2}{(b_h R_*)^4},\tag{8}$$

$$B_J'' = (b_h R_*)^2 - b_h R_*(7u^2 + 2u + 3) + 15u^2 + 6u + 3,\tag{9}$$

$$u = c_h \xi_{e*},\tag{10}$$

$$\xi_{e*} = \exp[-b_h(R_* - R_e)],\tag{11}$$

$$R_* = R_e + (B_h C_J + D_h C_J^2)/b_h,\tag{12}$$

$$C_J = \frac{b_h^2 L^2}{2\mu D},\tag{13}$$

$$B_h = \frac{(1 - c_h)^2}{(b_h R_e)^3} \quad \text{and} \quad D_h = \frac{3}{2}B_h^2 - 3\frac{B_h^2}{b_h R_e} + 3\frac{B_h c_h(1 - c_h)}{(b_h R_e)^3},\tag{14}$$

$$F_o = \frac{\hbar b_h}{\sqrt{2\mu}}, \tag{15}$$

$$F_1'' = \sqrt{D}(1 + \omega_o x_1 + \omega_1 x_1^2), \tag{16}$$

$$F_2''' = A_J(1 + \omega_o x_2 + \omega_o^2 x_2^2)\left[-\eta_{1J} + \frac{\eta_{2J}}{\xi_{e*}\sqrt{D}}\sqrt{D}(1 + \omega_o x_2 + \omega_1 x_2^2)\right], \tag{17}$$

$$F_3''' = \frac{A_J\eta_{2J}}{\xi_{e*}\sqrt{D}}(1 + \omega_o x_2 + \omega_o^2 x_2^2)\left[F_2''' + \frac{A_J\eta_{2J}}{2\xi_{e*}\sqrt{D}}\sqrt{D}(1 + \omega_o x_2 + \omega_1 x_2^2)\right], \tag{18}$$

$$x_1 = v + 1/2, \tag{19}$$

$$x_2 = (v_{max}^{TH} + 1)/2, \tag{20}$$

$$\omega_o = \frac{\hbar b_h c_h}{\sqrt{2\mu D}}, \tag{21}$$

$$\omega_1 = \omega_o^2(1 - \frac{1}{2c_h}), \tag{22}$$

$$\omega_2 = \frac{b_h^2}{2\mu}, \tag{23}$$

$$A_J = \frac{\omega_2}{2\sqrt{D}\xi_{e*}(b_h R_*)^4}, \tag{24}$$

$$\eta_{1J} = b_h R_*(20u^2 + 6u + 4) - (42u^2 + 18u + 6), \tag{25}$$

$$\eta_{2J} = b_h R_*(18u^2 + 14u + 1) - (36u^2 + 30u + 3), \tag{26}$$

$$L^2 = \hbar^2[J(J + 1) - \Lambda^2], \tag{27}$$

Λ is the quantum number for the axial component of the molecular electronic angular momentum, and the maximum value v_{max}^{TH} of the vibrational quantum number in the Tietz-Hua oscillator is the integer nearest to, and smaller than,

$$v_{max}^{TH} = \frac{1 - c_h - (1 - 3c_h^2)^{1/2}}{\omega_o(2c_h - 1)} - \frac{1}{2}. \tag{28}$$

2.3 Model C

The intramolecular potential of diatomic molecules in the model C is the same as that given in the relationship (1). Applying the approach of Paper I to the model gives the following rotational-vibrational energies of diatomic molecule:

$$E_{v,J}^{C'} = D + \hbar^2 A_M J(J+1) - \left[\frac{\beta\hbar(v+1/2)}{(2\mu)^{1/2}} - \frac{2De^{u_e-u_*} - \hbar^2 B_M J(J+1)}{2[De^{2(u_e-u_*)} - \hbar^2 C_M J(J+1)]^{1/2}} \right]^2 . \quad (29)$$

where

$$u_e = \beta R_e \quad \text{and} \quad u_* = \beta R'_*, \quad (30)$$

$$\xi'_{e*} = \exp[-\beta(R'_* - R_e)], \quad (31)$$

$$R'_* = R_e + (B'_h C_J + D'_h C_J^2)/\beta, \quad (32)$$

$$B'_h = \frac{1}{(\beta R_e)^3} \quad \text{and} \quad D'_h = \frac{3}{2}B'^2_h - 3\frac{B'^2_h}{\beta R_e}, \quad (33)$$

$$A_M = \frac{1}{2\mu(R'_*)^2}\left[1 - \frac{3}{\beta R'_*}\left(1 - \frac{1}{\beta R'_*}\right)\right], \quad (34)$$

$$B_M = \frac{2}{\mu\beta(R'_*)^3}\left(1 - \frac{3}{2\beta R'_*}\right), \quad (35)$$

and

$$C_M = \frac{1}{2\mu\beta(R'_*)^3}\left(1 - \frac{3}{\beta R'_*}\right). \quad (36)$$

The expression (29) can be simplified by expanding the function

$$f(L^2) = \frac{2D\xi'_{e*} - B_M L^2}{2\sqrt{2D\xi'^2_{e*} - C_M L^2}} = \frac{2De^{u_e-u_*} - \hbar^2 B_M J(J+1)}{2[De^{2(u_e-u_*)} - \hbar^2 C_M J(J+1)]^{1/2}}, \quad (37)$$

into power series about $L^2 = 0$, which leads to

$$f(L^2) \simeq \sqrt{D} + F_m L^2 + G_m L^4 + ..., \quad (38)$$

where

$$F_m = \frac{1}{2\xi'_{e*}\sqrt{D}}\left[\frac{C_M}{\xi'_{e*}} - B_M\right] = \frac{\beta^2}{4\xi'^2_{e*}\mu u_*^3}\left[1 - 4\xi'_{e*} + \frac{3}{u_*}(2\xi'_{e*} - 1)\right], \quad (39)$$

$$G_m = \frac{C_M}{4\xi'^3_{e*} D\sqrt{D}}\left[-B_M + \frac{3C_M}{2\xi'_{e*}}\right] = \frac{\beta^4}{32\mu^2\xi'^4_{e*}D\sqrt{D}u_*^6}\left(1 - \frac{3}{u_*}\right)\left[3 - 8\xi'_{e*} + \frac{3}{u_*}(4\xi'_{e*} - 3)\right], (40)$$

212

and, subsequently, to

$$E_{v,J}^{C''} = D + A_M L^2 - \left[\frac{\beta\hbar}{\sqrt{2\mu}}(v+\frac{1}{2}) - \sqrt{D} - F_m L^2 - G_m L^4 \right]^2,$$ (41)

or

$$E_{v,J}^{C''} = f_b(v) + g_a(J) + g_b(J) + h(v,J),$$ (42)

where

$$f_b(v) = \frac{2\hbar\beta}{\sqrt{2\mu}}\sqrt{D}(v+\frac{1}{2}) - \frac{\hbar^2\beta^2}{2\mu}(v+\frac{1}{2})^2,$$ (43)

$$g_a(J) = \frac{L^2\beta^2}{2\mu u_*^2}\left[1 - \frac{3}{u_*}(1 - \frac{1}{u_*})\right] - 2\sqrt{D}f_a(J),$$ (44)

$$g_b(J) = \frac{-L^4\beta^4}{16\mu^2\xi_{e*}'^4 D u_*^6}\left(1 - \frac{3}{u_*}\right)\left[3 - 8\xi_{e*}' + \frac{3}{u_*}(4\xi_{e*}' - 3)\right] - f_a^2(J),$$ (45)

$$h(v,J) = \frac{2\hbar\beta}{\sqrt{2\mu}}(v+\frac{1}{2})f_a(J),$$ (46)

and

$$f_a(J) = \frac{L^2\beta^2}{4\xi_{e*}'^2\sqrt{D}\mu u_*^3}\left[1 - 4\xi_{e*}' + \frac{3}{u_*}(2\xi_{e*}' - 1)\right].$$ (47)

The expression (42) can be further simplified by taking into account the fact that the dependence of the function $h(v,J)$ on the vibrational quantum number is not strong, especially at moderate and high values of v. Thus, assuming in expression (46) that $v = v_{max}/2$, one has

$$E_{v,J}^{C'''} = f_b(v) + g_a(J) + g_b(J) + h_o(J),$$ (48)

where

$$h_o(J) = \frac{\hbar\beta}{\sqrt{2\mu}}(v_{max} + 1)f_a(J),$$ (49)

and where the maximum value of the vibrational quantum number of the Morse oscillator is obtained from the function (1) when $J = 0$. This value can be taken as the integer closest to, and smaller than,

$$v_{max} = \frac{\omega_e}{2\omega_e x_e} - \frac{1}{2}.$$ (50)

The expression (48) is very convenient in theoretical studies of molecular dynamics because it is quite accurate and because it is given as a sum of molecular rotational energy (which depends only on the rotational quantum number J) and molecular vibrational energy (which depends only on the vibrational quantum number v). However, even though the replacement of v in equation (46) by $v_{max}/2$ has little impact on the accuracy of the expression (48) at moderate and high vibrational quantum numbers, it does cause some meaningful inaccuracy of the expression at low values of the quantum numbers (see below).

213

3 Results and discussion

As discussed in Paper I, the rotating Tietz-Hua oscillator is one of the most realistic analytical representations of rotational-vibrational dynamics of diatomic molecules. Therefore, we test below the accuracy of the energy levels $E_{v,J}^A$, $E_{v,J}^B$, $E_{v,J}^{C'}$, $E_{v,J}^{C''}$ and $E_{v,J}^{C'''}$ of the O_2, N_2, NO and CO molecules against the corresponding levels obtained from numerical solution of the Schrödinger equation for the rotating Tietz-Hua oscillator. (The testing can also be done against the levels obtained from the analytical solution (7) for the oscillator because the numerical and analytical solutions are very close (see Paper I)).

In figures 1 - 6 we show the rotational-vibrational levels for all accessible quantum numbers of the O_2 and NO molecules. (The calculations of the levels were made for all four (O_2, N_2, NO and CO) molecules discussed in this work, and the results for the N_2 and CO molecules (not shown, in the figures) have accuracies which are very close to the accuracies of the results for the O_2 and NO molecules).

As can be seen in Figs. 1 - 2, the accuracy of the expression (29) obtained from the model C is very close, for all considered molecules and all molecular levels, to the accuracy of the expression (7) which was obtained from the model of the rotating Tietz-Hua oscillator. However, relationship (29) is more accurate than the 'truncated' expression (2) obtained from the model of the rotating Morse oscillator.

Relationships (7) and (2) are compared with relationship (41) (a simplified version of Eq. (29)) in Figs. 3 - 4. The comparison shows that expressions (7) and (41) have similar accuracies, and that these two expressions predict values of the moderate and high vibrational levels much more accurately than expression (2).

Comparison of equations (7), (2) and (48) is shown in Figs. 5 - 6. One can see there that substitution of $v_{max}/2$ for v in equation (42) (the substitution leads to equation (48)) works quite well for vibrational levels higher than about $v_{max}/3$.

In summary, the expression (41) (or (42)) of this work is a reliable analytical approximation of molecular rotational-vibrational energies. Its accuracy is acceptable in most applications and in the entire range of molecular vibrational and rotational quantum numbers. In the case of molecules excited to states with quantum numbers greater than about $v_{max}/3$, the expression can be replaced by the relationship (48). From practical point of view, the fact that the formula (48) works well only at moderate and high vibrational quantum numbers is not a significant limitation because one can use the formula at the moderate and high quantum numbers and the simple expression (2) (which also is a sum of a v-independent term and a J-independent term) at low quantum numbers.

Acknowledgements

Bibliography

References

[1] Kunc, J.A. and Gordillo-Vazquez, F.J., "The rotational-vibrational levels of diatomic molecules represented by the Tietz-Hua rotating oscillator" (Paper 1); accepted for publication in *Journal of Physical Chemistry*.

[2] Hua, W., *Phys. Rev. A* **42**, 2524 (1990).

[3] Natanson, G.A., *Phys. Rev. A* **44**, 3377 (1991).

[4] Pekeris, C.L., *Phys. Rev.* **45**, 98 (1934).

[5] Porter, R.N., Raff, L.M., and Miller, W.H., *J. Chem Phys.* **63**, 2214 (1975).

[6] Kunc, J.A., *Physics of Plasmas*, **2**, 4335 (1995).

[7] Gorbachev, Y.E., et al, *Physica A*, **287**, 108 (1997).

[8] Kunc, J.A., et al, *Physics of Fluids*, **7**, 5, 1173 (1995).

Table I: The molecular constants used in the present calculations: ω_e (the vibrational constant, in cm^{-1}), $\omega_e x_e$ (the anharmonicity constant, in cm^{-1}), R_e (the molecular bond length, in Å), μ (the reduced mass, in g), D (the well depth of the intramolecular potential, in cm^{-1}; note that in the text, D was used in c.g.s units. b_h is the parameter defined in Eq. (6).

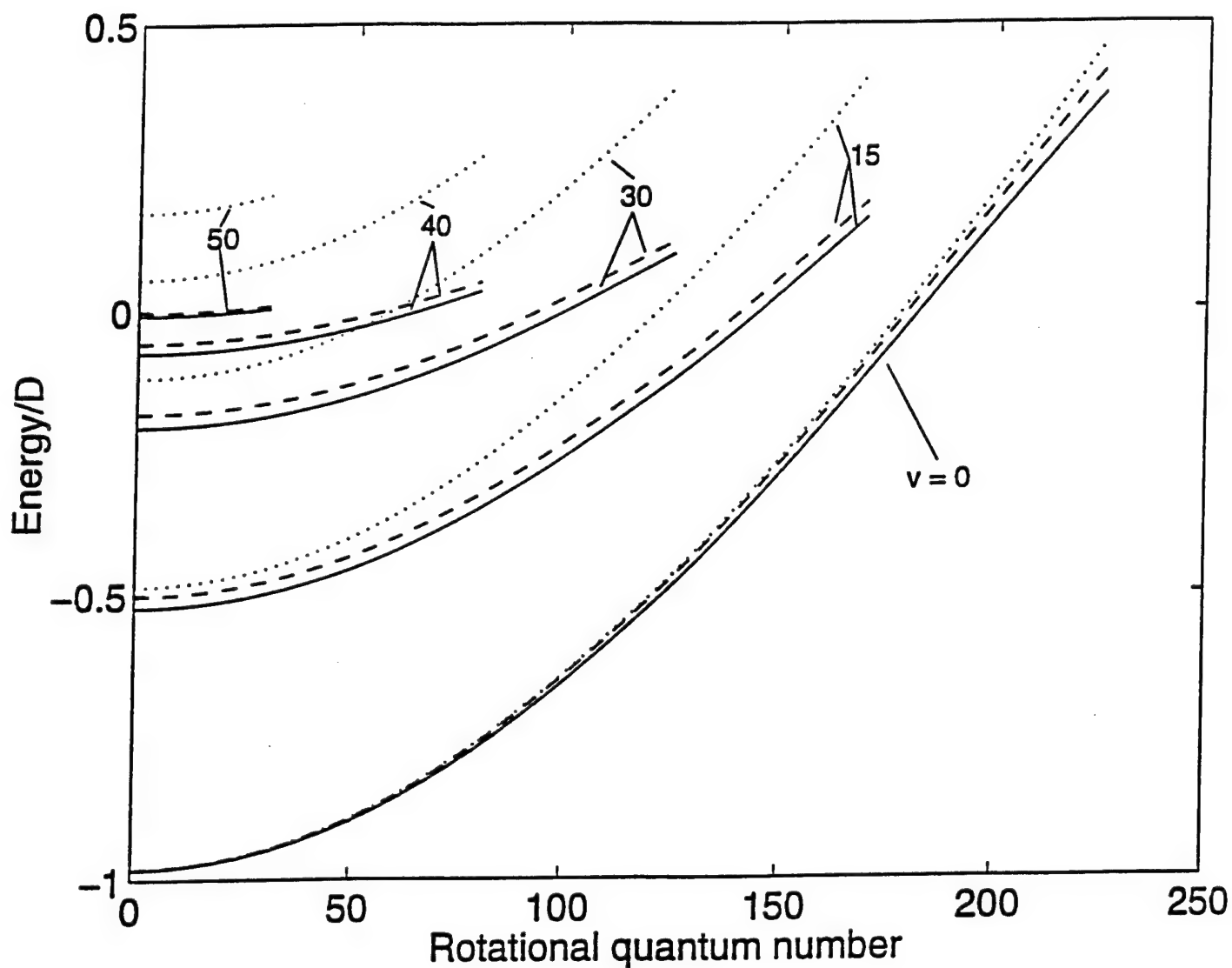| Molecule	ω_e	$\omega_e x_e$	R_e	$\mu/10^{-23}$	D	b_h
$O_2(X^3\Sigma_g^-)$	1580.2	11.98	1.207	1.337	42041	2.59103
$N_2(X^1\Sigma_g^+)$	2358.6	14.32	1.097	1.171	79885	2.78580
$NO(X^2\Pi_r)$	1904.2	14.07	1.151	1.249	53341	2.71559
$CO(X^1\Sigma^+)$	2169.8	13.29	1.128	1.146	90531	2.20481

Figure 1: The rotational-vibrational energies $E_{v,J}^B$ (solid line, Eq. (7)), $E_{v,J}^A$ (dot line, Eq. (2)) and $E_{v,J}^{C'}$ (dashed line, Eq. (29)) for the $O_2(X^3\Sigma_g^-)$ molecule. The zero rotational-vibrational energy corresponds to the dissociation continuum of the rotationless molecule. v and J are vibrational and rotational quantum numbers, respectively.
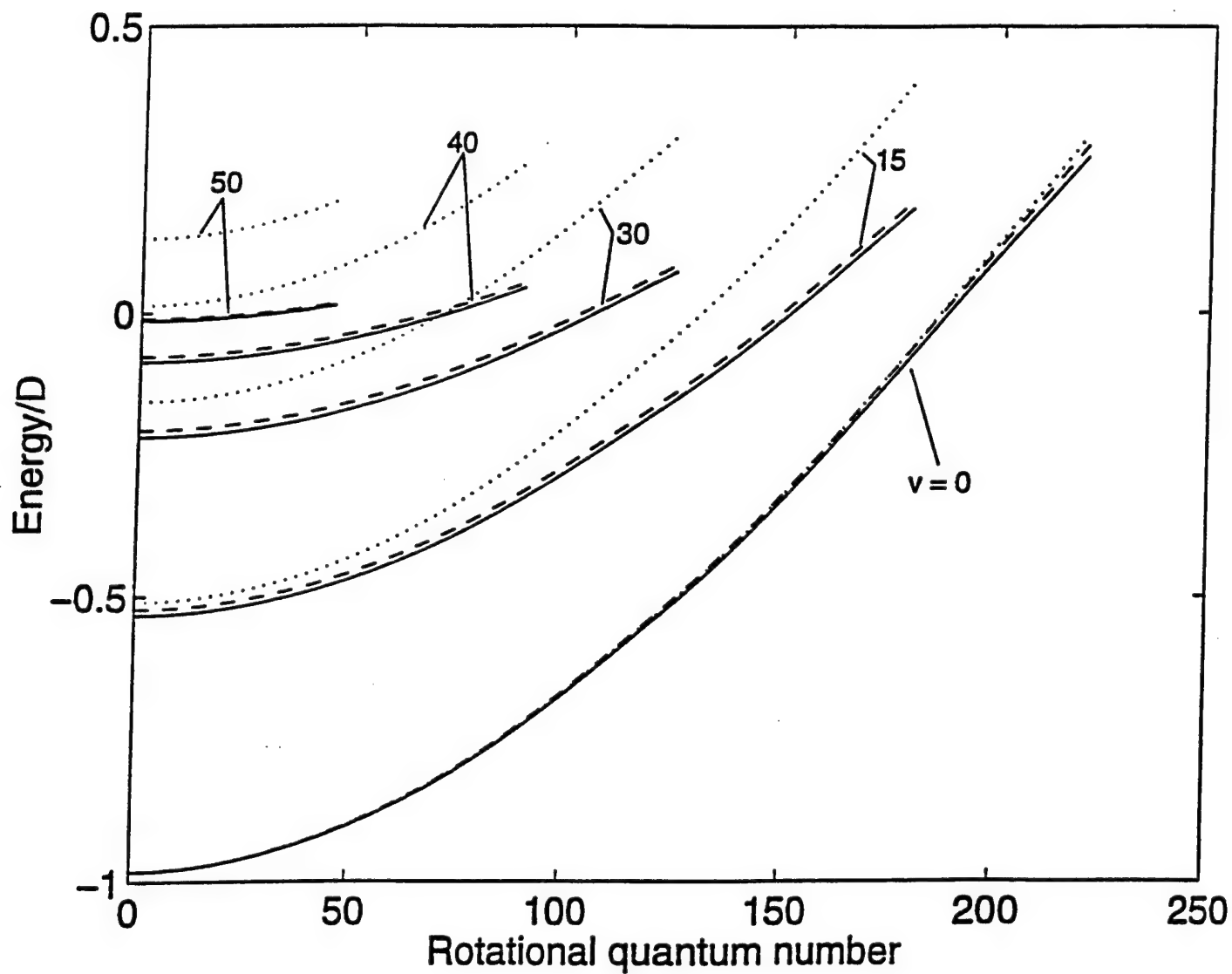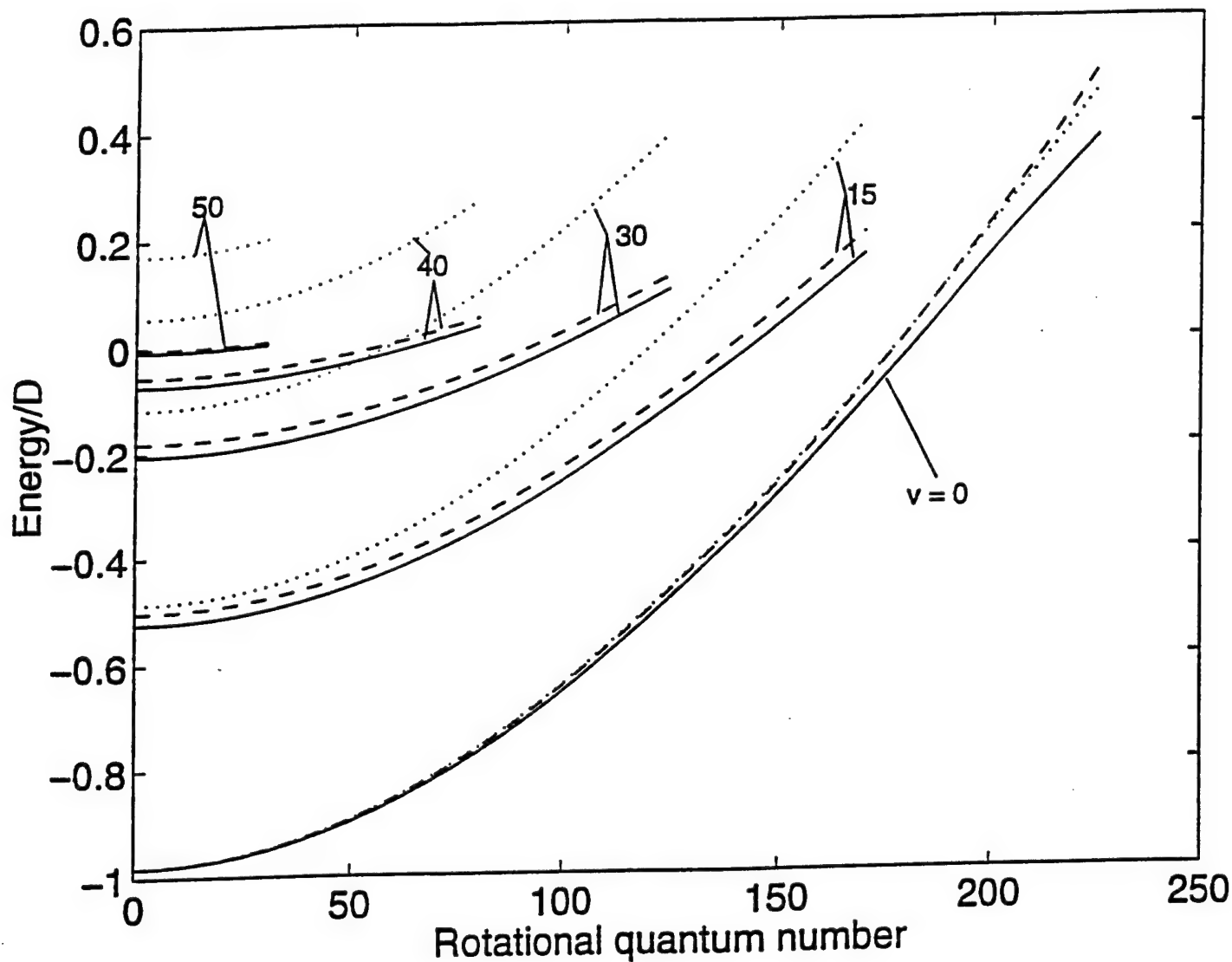
Figure 2: The rotational-vibrational energies $E_{v,J}^B$ (solid line, Eq. (7)), $E_{v,J}^A$ (dot line, Eq. (2)) and $E_{v,J}^{C'}$ (dashed line, Eq. (29)) for the NO($X^2\Pi_r$) molecule. Meaning of the symbols is the same as in Figure 1.

Figure 3: The rotational-vibrational energies $E_{v,J}^B$ (solid line, Eq. (7)), $E_{v,J}^A$ (dot line, Eq. (2)) and $E_{v,J}^{C''}$ (dashed line, Eq. (41)) for the $O_2(X^3\Sigma_g^-)$ molecule. Meaning of the symbols is the same as in Figure 1.
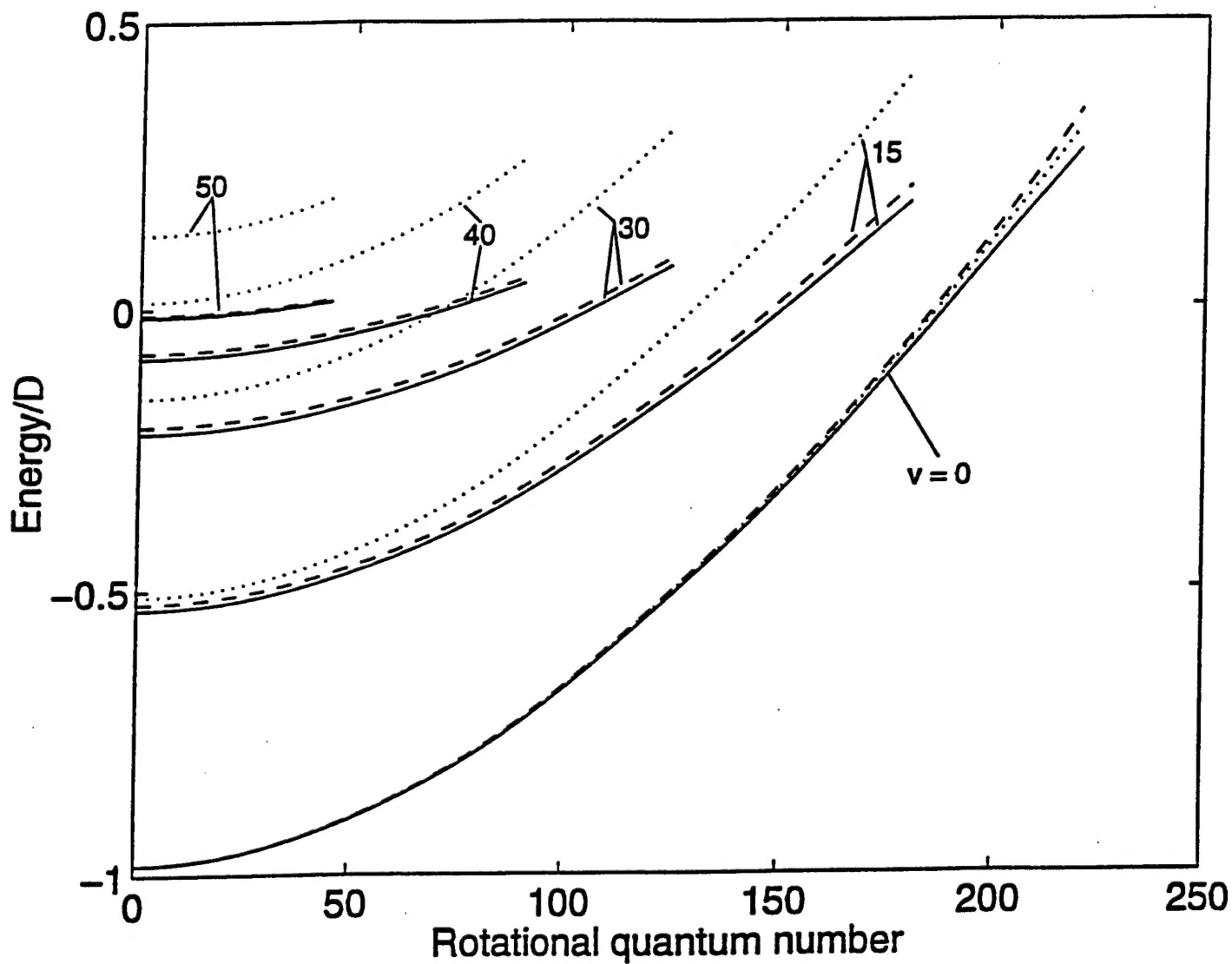
Figure 4: The rotational-vibrational energies $E_{v,J}^B$ (solid line, Eq. (7)), $E_{v,J}^A$ (dot line, Eq. (2)) and $E_{v,J}^{C''}$ (dashed line, Eq. (41)) for the NO($X^2\Pi_r$) molecule. Meaning of the symbols is the same as in Figure 1.
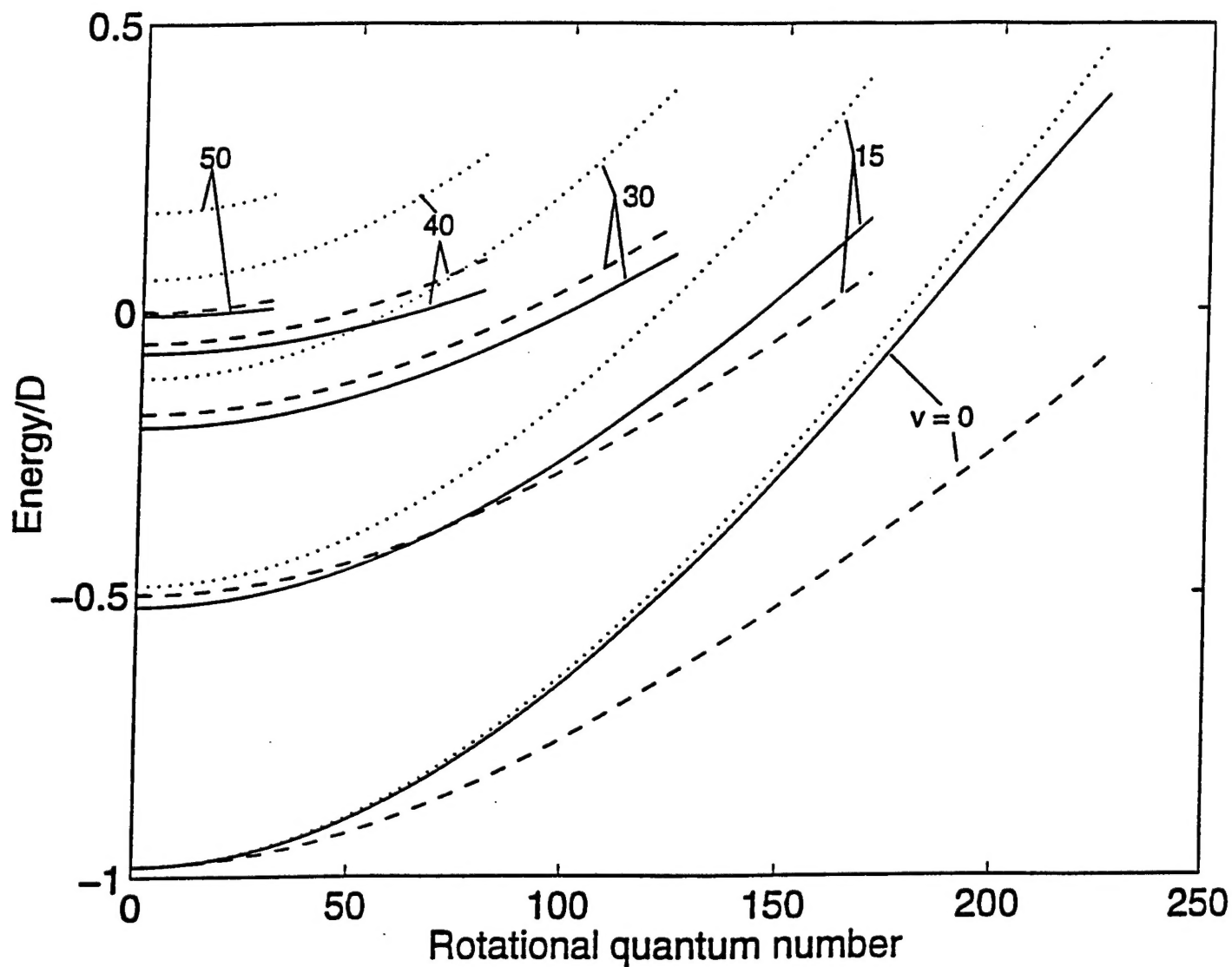
Figure 5: The rotational-vibrational energies $E_{v,J}^B$ (solid line, Eq. (7)), $E_{v,J}^A$ (dot line, Eq. (2)) and $E_{v,J}^{C'''}$ (dashed line, Eq. (48)) for the $O_2(X^3\Sigma_g^-)$ molecule. Meaning of the symbols is the same as in Figure 1.
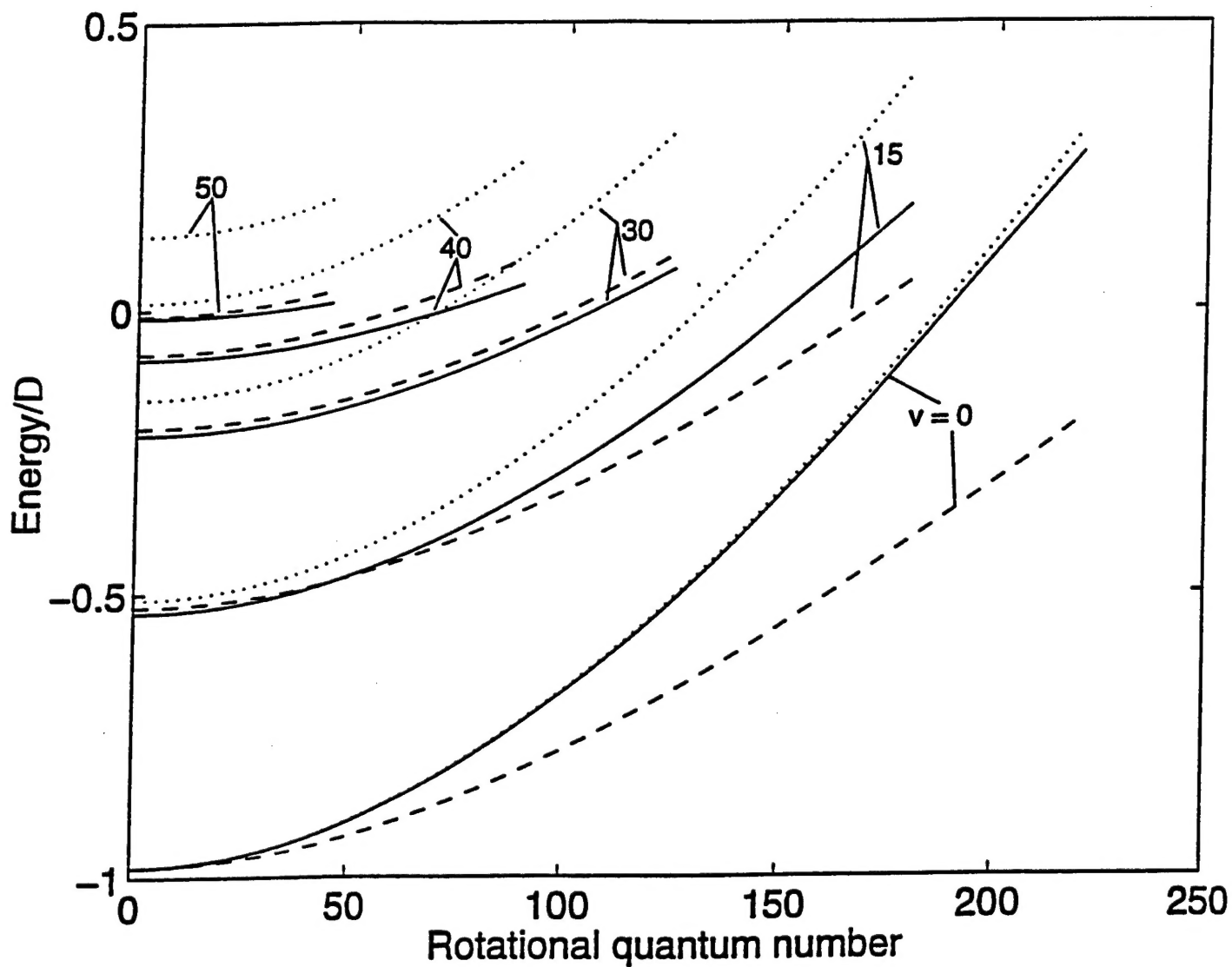
Figure 6: The rotational-vibrational energies $E_{v,J}^B$ (solid line, Eq. (7)), $E_{v,J}^A$ (dot line, Eq. (2)) and $E_{v,J}^{C'''}$ (dashed line, Eq. (48)) for the NO($X^2\Pi_r$) molecule. Meaning of the symbols is the same as in Figure 1.

Appendix IV-1
PUBLICATIONS

Gordillo-Vazquez. F.J., and Kunc, J.A., "Diagnostics of Plasmas with Substantial Concentrations of Atomic Oxygen", Phys. Rev. E. 51, 6, pp. 60110-6015, 1995.

Gobachev, Y.E., Gordillo-Vazquez, F.J., Kunc, J.A., "Diameters of Rotationally and Vibrationally Excited Diatomic Molecules, Physica A, 247, 108-120, 1997.

Holbrook, R., Kunc, J.A., Muntz, E.P., "Iodine: A Superior Gas for Modeling High Energy Flows", AIAA Paper No. 95-2119, San Diego, CA, June 1995.

Kang S.H. and Kunc J.A., "Energy Dependence of Vibration-Translation Transitions in Collisions of Neutral Particles", AIAA-94-2403.

Kunc, J.A., "Impact of Dissociation on Viscosity of Gases", Physics of Plasmas 2, 4355 (1995).

Kunc, J.A., Hash, D.B., Hassan, H.A., "The GHS Interaction Model for Strong Attractive Potentials", Phys. Fluids 7,5, 1173-1175, May 1995.

Vazquez F.G. and Kunc J.A., "Diagnostics of Plasmas with Substantial Concentrations of Atomic Oxygen", Physical Review, E51, 6010 (1995) and Physical Review, E52, 561 (1995).